Study of atmospheric neutrino oscillations with the deep-sea Cherenkov detector KM3NeT/ORCA and synergies with reactor neutrinos

Thien Nhan Chau

▶ **To cite this version:**

Thien Nhan Chau. Study of atmospheric neutrino oscillations with the deep-sea Cherenkov detector KM3NeT/ORCA and synergies with reactor neutrinos. Astrophysics [astro-ph]. Université Paris Cité, 2021. English. NNT : 2021UNIP7223 . tel-03999509

HAL Id: tel-03999509
https://theses.hal.science/tel-03999509

Submitted on 21 Feb 2023

HAL is a multi-disciplinary open access archive for the deposit and dissemination of scientific research documents, whether they are published or not. The documents may come from teaching and research institutions in France or abroad, or from public or private research centers.

L'archive ouverte pluridisciplinaire **HAL**, est destinée au dépôt et à la diffusion de documents scientifiques de niveau recherche, publiés ou non, émanant des établissements d'enseignement et de recherche français ou étrangers, des laboratoires publics ou privés.

Université de Paris

Ecole doctorale STEP'UP – ED N°560
Laboratoire AstroParticule et Cosmologie

Study of atmospheric neutrino oscillations with the deep-sea Cherenkov detector KM3NeT/ORCA and synergies with reactor neutrinos

CHAU Thien Nhan

sous la direction de

Antoine Kouchner
Véronique Van Elewyck

Thèse de doctorat de Physique de l'Univers

Présentée et soutenue publiquement le 16 novembre 2021

Devant un jury composé de

Pr. Antoine Kouchner, Université de Paris ..... *Directeur de thèse*
Pr. Corrine Augier, Université Claude Bernard Lyon 1 ..... *Rapporteur*
Dr. Marcos Dracos, Institut Pluridisciplinaire Hubert Curien ... *Rapporteur*
Pr. Sergio Navas, Université de Grenade ..... *Examinateur*
Pr. Thomas Patzak, Université de Paris ..... *Examinateur*
Pr. Lili Yang, Sun Yat-sen University ..... *Examinatrice*
Dr. Véronique Van Elewyck, Université de Paris ..... *Membre invité du jury*

Résumé en français

Contexte scientifique et méthode d'analyse

L'oscillation des neutrinos est le phénomène par lequel les neutrinos changent de saveur tout en se propageant. L'observation de ce mécanisme est jusqu'à présent l'un des rares indices de physique au-delà du modèle standard de la physique des particules et implique que les neutrinos sont massifs et mèlangés de telle sorte que les états propres de saveur ν_e, ν_μ, ν_τ (correspondant aux neutrinos qui participent à l'interaction faible) sont un mélange non trivial des états propres de masse ν_1, ν_2, ν_3. Dans le modèle standard du mélange à trois saveurs, les oscillations des neutrinos peuvent être caractérisées par trois angles de mélange $\theta_{12}, \theta_{13}, \theta_{23}$, les différences de masse au carré $\Delta m^2_{31}, \Delta m^2_{21}$ entre les états propres de masse, et une éventuelle phase de violation de la symétrie CP δ_{CP}. Ces paramètres d'oscillation des neutrinos sont mesurés de plus en plus précisément par de multiples expériences. Plusieurs questions restent malgré tout en suspens, notamment l'échelle de masse absolue des neutrinos, leur nature (particules de Dirac ou de Majorana), la valeur de la phase de violation de CP et l'ordre des masses des neutrinos (OMN), en l'occurrence s'il s'agit d'un ordre normal (ON, $m_1 < m_2 < m_3$) ou inversé (OI, $m_3 < m_2 < m_1$).

L'une des principales approches pour résoudre la question de l'OMN consiste à étudier les effets de la matière sur les neutrinos atmosphériques se propageant à travers la Terre. Les neutrinos atmosphériques sont créés dans les gerbes de particules induites par l' interaction des rayons cosmiques avec l'atmosphère. Lors de la propagation de ces neutri-

nos à travers la Terre, leur interaction avec la matière (de type diffusion élastique vers l'avant) induit des modifications d'oscillation différentes selon l'OMN. Cet effet, bien que sous-dominant, peut être observé par les grands détecteurs Tcherenkov à eau grâce à leur très grand volume cible pour l'interaction des neutrinos, et à leur haute sensibilité au signal de lumière Tcherenkov induit par les particules secondaires chargées produites par l'interaction, qui se propagent de manière ultrarelativiste dans un milieu transparent. La mesure de ces effets est l'objectif principal du détecteur de basse énergie de KM3NeT, appelé ORCA (pour Oscillation Research with Cosmics in the Abyss).

KM3NeT/ORCA est un détecteur Tcherenkov à eau de nouvelle génération en cours de construction dans les profondeurs de la mer Méditerranée. ORCA comprendra 115 Unités de Détection (UD) identiques, sous forme de lignes flexibles ancrées sur le fond marin et hébergeant chacune 18 modules optiques numériques qui constituent les composants élémentaires de détection de la lumière Tcherenkov. Chaque module optique se compose d'une sphère en verre de 43 cm de diamètre, résistante à la pression, et contenant 31 tubes photomultiplicateurs (PMT) ainsi que l'électronique associée. Le réseau d'UD est arrangé sous une forme cylindrique avec un rayon moyen de 115 m et une distance moyenne entre les lignes de 20 m. Sur chaque UD, l'espacement vertical entre les modules optiques est d'environ 9 m. Cette configuration est optimisée pour la détection des neutrinos atmosphériques d'énergie supérieure à 1 GeV, un domaine d'énergie intéressant pour les études d'oscillation. Six UD ont déjà été déployées sur le site d'ORCA et prennent des données depuis 2019.

Le détecteur observe les neutrinos via la lumière Tcherenkov induite par les particules chargées produites dans les interactions des neutrinos. La distribution en temps et en position des signaux numérisés, ou hits, enregistrés par les PMTs des différents modules optiques sont utilisés pour identifier les événements de neutrinos et reconstruire leur énergie et leur direction angulaire. Les événements détectés sont également classifiés en fonction de leur topologie qui permet d'inférer des informations sur la saveur du neutrino

ayant produit le signal.

La modélisation de la réponse du détecteur est un prérequis pour les analyses de physique avec ORCA. La collaboration KM3NeT a développé des chaînes de simulation Monte Carlo (MC) détaillées pour produire les échantillons de données utilisés pour évaluer la réponse du détecteur aux signaux de neutrinos. La simulation comprend plusieurs étapes : l'interaction des neutrinos dans l'eau, la génération et la propagation de la lumière Tcherenkov induite par les particules chargées produites dans l'interaction des neutrinos, la réponse des PMT aux signaux lumineux, la simulation du déclenchement du traitement de l'événement, la reconstruction et la classification topologique des événements.

Les analyses d'oscillation nécessitent la connaissance de la distribution attendue des neutrinos de différentes saveurs en fonction de leur énergie et de leur direction d'arrivée. La tâche nécessite l'utilisation de modèles de flux de neutrinos atmosphériques, des probabilités d'oscillation et des sections efficaces d'interaction des neutrinos, ainsi que du modèle de réponse du détecteur. Cette procédure a été développée et mise en œuvre dans un cadre logiciel KM3NeT appelé SWIM qui utilise une approche MC complète pour construire la réponse du détecteur. SWIM permet également l'évaluation de la sensibilité d'ORCA aux paramètres d'oscillation et à l'OMN par une méthode de minimisation du rapport de vraisemblance logarithmique. Un ensemble d'effets systématiques, considéré comme robuste et conservateur, a également été inclus. Tout au long de la thèse, nous adoptons pour l'analyse statistique l'approximation largement utilisée de la méthode d'Asimov, dans laquelle l'ensemble de données de toutes les quantités observées est supposé égal à leurs valeurs attendues.

Résumé des résultats

Cette thèse étudie le potentiel pour la physique des neutrinos du détecteur KM3NeT/ORCA. Les résultats peuvent être présentés en deux parties principales: les contributions aux

simulations MC d'événements neutrinos, et l'évaluation de la sensibilité aux paramètres d'oscillation des neutrinos et à l'ordre de masse à l'aide de SWIM.

Concernant les simulations MC, j'ai contribué à la production d'un échantillon d' événements de neutrinos à haute énergie (50-5000 GeV) pour un sous-réseau d'ORCA avec 7 DUs (ORCA7). Cet échantillon sera utile pour les recherches astrophysiques de neutrinos avec ORCA dans sa première phase de construction. Ce travail constitue ma tâche de service pour la Collaboration et j'ai également été chargé d'utiliser cette production pour vérifier la chaîne de simulation ORCA et pour effectuer le contrôle qualité standard à chaque étape de la production. Les contrôles de qualité ont confirmé le comportement attendu des outils de simulation et validé la production jusqu'à l'étape de déclenchement. Les performances d'ORCA7 à haute énergie sont également illustrées dans ma thèse en termes de surface effective et de résolution de reconstruction (énergétique et angulaire).

Une autre étude de simulation présentée dans cette thèse est la production d'échantillons avec différentes efficacités quantiques des PMT, pour étudier l'impact de telles incertitudes sur l'erreur systématique des mesures d'ORCA. Dans cette étude, l'échantillon MC nominal a été retraité à partir du niveau de déclenchement avec une efficacité quantique des PMTs modifiée de $\pm 10\%$ par rapport à l'échantillon standard. Ensuite, les fonctions de réponse du détecteur ont été évaluées et comparées pour les trois valeurs d'efficacité (une nominale et deux modifiées). Ces incertitudes conduisent à un décalage systématique de toutes les fonctions de réponse du détecteur en termes d'énergie vraie des neutrinos. Ces effets peuvent être capturés par l'introduction d'une erreur systématique dite d'*échelle d'énergie*. Cette étude a également montré que l'échelle d'énergie a un impact non négligeable sur la mesure du paramètre Δm^2_{31}, d'où la nécessité de l'inclure dans toutes les analyses de physique ORCA. En tant que responsable actuel de SWIM, j'ai également implémenté ces systématiques dans ce logiciel d'analyse.

Ce travail de thèse a également produit une nouvelle estimation de la sensibilité d'ORCA à l'ordre des masses et aux paramètres d'oscillation des neutrinos, et plus particulièrement

aux paramètres de mélange dans le secteur atmosphérique : Δm^2_{31} et θ_{23}. En termes de détermination de l'OMN, mon analyse confirme l'amélioration de sensibilité obtenue en densifiant la géométrie ORCA pour passer d'un espacement horizontal de 23 m (configuration choisie au départ du projet) à 20 m (configuration actualisée) entre les UD, grâce à l'amélioration connexe des performances d'identification et de reconstruction des événements. En résumé, un niveau de confiance de 5σ peut être atteinte en 3 ans sur la mesure de l'OMN, et en seulement 1 an de prise de données un niveau de 3σ peut déjà être obtenu dans le cas d'un ordre normal (ON) et en supposant une valeur de θ_{23} qui correspond au meilleur ajustement global. Dans le scénario d'un ordre inversé (IO), un niveau de confiance de 3σ peut être atteint après 4 ans mais un niveau de 5σ nécessitera plus de 10 ans de prise de données. Pour la mesure de Δm^2_{31} et θ_{23}, le détecteur ORCA complet avec 3 ans d'exposition pourra améliorer les contraintes actuelles des données mondiales. De plus, cette mesure peut déjà être réalisée (avec un niveau de confiance plus faible) avec la configuration ORCA7 dans une phase précoce de la construction.

Un autre résultat important de cette thèse est l'évaluation de la sensibilité à l'OMN attendue pour une analyse combinée des données d'ORCA et de JUNO, une expérience de nouvelle génération en cours de construction en Chine qui étudiera les $\bar{\nu}_e$ en provenance de réacteurs nucléaires. JUNO est sensible à l'OMN à travers l'interaction entre les oscillations rapides gouvernées par les paramètres Δm^2_{31} et Δm^2_{32} dans le canal de disparition de $\bar{\nu}_e$. La combinaison de JUNO et d'ORCA est motivée par l'augmentation de la sensibilité à l'OMN qui résulte de la tension attendue entre les deux expériences pour leur mesure du paramètre Δm^2_{31} dans le cas d'une hypothèse erronée sur l'OMN. Cette tension provient du fait que chaque expérience observe les oscillations des neutrinos à partir d'une saveur de neutrinos différente ($\bar{\nu}_e$ pour JUNO, principalement $\nu_\mu + \bar{\nu}_\mu$ pour ORCA). La fréquence d'oscillation effective est dès lors le résultat d'une combinaison différente des divers Δm^2_{ij} pour chaque expérience. Cet effet a été discuté théoriquement dans le passé dans le cadre d'une éventuelle combinaison de données de neutrinos atmosphériques et de réacteurs, et ORCA et JUNO pourraient être les premières expériences à en fournir une

confirmation expérimentale. Avec la combinaison des deux lots de données, le temps requis pour atteindre une détermination à 5σ de l'OMN est considérablement réduit, et ce pour toutes les valeurs plausibles des paramètres d'oscillation. Une significativité à un degré de confiance de 5σ peut ainsi être obtenue en 6 ans pour l'analyse combinée quelle que soit l'hypothèse sur l'OMN, alors que cela pourrait prendre plus de 10 ans en utilisant uniquement les données d'ORCA, en fonction de la vraie valeur de l'ordre des masses. En outre, l'étude montre que la combinaison peut déjà être réalisée dans la phase précoce de construction ORCA7 avec des résultats très prometteurs qui pourraient encore réduire le temps nécessaire à la détermination de l'OMN. L'influence des incertitudes systématiques et des effets de détecteur sur la combinaison a également été étudiée et une forte dépendance des résultats en la vraie valeur de θ_{23} a été observée. Dans le cas d'un ordre vrai normal et de θ_{23} dans l'octant supérieur, une détermination de l'OMN à 5σ serait faisable en moins de 2 ans de prise de données avec l'analyse combinée, c'est-à-dire avec un an d'avance sur l'analyse utilisant uniquement les données d'ORCA. Ce scénario favorable correspond également à la valeur de θ_{23} actuellement favorisée par les ajustements globaux des données d'expériences d'oscillations. Une autre observation importante est que l'approche utilisée pour le traitement de la systématique d'échelle d'énergie peut affecter de manière significative la puissance de la combinaison des données de JUNO et ORCA. Néanmoins, même dans une approche conservative de cette systématique une détermination de 5σ du OMN peut toujours être effectivement atteinte.

Enfin, la thèse présente les résultats d'une première mesure des paramètres d'oscillation θ_{23} et Δm^2_{31} avec KM3NeT/ORCA, utilisant l'échantillon de données des 6 UD actuellement déployées (ORCA6). Des critères de qualité des données ont été appliqués pour sélectionner un lot de données final approprié pour l'analyse physique, couvrant 91,9% du temps d'exposition total. Les échantillons Monte Carlo correspondants ont été produits selon une procédure de simulation dite "run by run", qui prend en compte les informations sur les conditions environnementales et l'état du détecteur au cours de chaque prise ("run") de données. Sur la base de l'échantillon MC, la sélection d'événements a été optimisée pour

rejeter le bruit de fond des muons atmosphériques tout en conservant une statistique suffisante d'événements neutrinos. Un très bon accord des données avec les prédictions MC a été obtenu, démontrant une bonne compréhension du détecteur. Ensuite, les données et le MC ont été traités par le logiciel SWIM pour l'évaluation de la sensibilité. Avec à peine 1 an de données d'ORCA6, une nette préférence pour le scénario d'oscillation a été obtenue, l'hypothèse d'une absence d'oscillations ayant été rejetée à un niveau de confiance de 6.7σ. De plus, le lot de données d'ORCA6 peut déjà fournir une contrainte sur θ_{23} et Δm^2_{31} qui est comparable à celle des mesures actuelles des autres expériences.

Abstract

KM3NeT/ORCA is a water-Cherenkov neutrino telescope being deployed in the depths of the Mediterranean Sea as part of the KM3NeT infrastructure. The detector is a tri-dimensional array of photomultipliers (PMTs) that detect the Cherenkov light induced by the charged particles produced when neutrinos interact with the surrounding matter. The configuration of the ORCA detector is optimized for the detection of atmospheric neutrinos with energies above 1 GeV.

This thesis focuses on the study of neutrino oscillations with the KM3NeT/ORCA detector. It presents first the results of Monte Carlo simulations that allowed the study and modeling of the impact of systematic uncertainties related to the PMT quantum efficiency on the ORCA performances. The thesis then presents an updated sensitivity study of ORCA for the neutrino mass ordering (NMO) and the oscillation parameters in the atmospheric sector: Δm^2_{31} and θ_{23}. A second study evaluates the gain in NMO sensitivity expected by combining the data of ORCA to those of JUNO, a next-generation reactor neutrino experiment being built in China. This gain results from the expected tension between the two experiments in the best-fit of Δm^2_{31} when assuming the wrong ordering. Finally, the thesis also presents the first measurement of the oscillation parameters in the atmospheric sector using data taken with ORCA in its current configuration with 6 lines deployed (ORCA6). This study already excludes the hypothesis of non-oscillation at a high confidence level, and provides a constraint on Δm^2_{31} and θ_{23} comparable to existing measurements from other experiments.

Keywords: Neutrino physics, oscillations, Cherenkov detectors, neutrino telescopes, KM3NeT.

Résumé

KM3NeT/ORCA est un télescope à neutrinos déployé dans les profondeurs de la mer Méditerranée dans le cadre de l'infrastructure KM3NeT. Le détecteur est formé d'un réseau tridimensionnel de photomultiplicateurs (PMTs) qui détectent la lumière Tcherenkov induite par les particules chargées produites lors des interactions de neutrinos avec la matière environnante. La configuration du détecteur ORCA est optimisée pour la détection des neutrinos atmosphériques d'énergie supérieure à 1 GeV.

Cette thèse porte sur l'étude des oscillations des neutrinos avec le détecteur KM3NeT/ORCA. Elle présente tout d'abord les résultats de simulations Monte Carlo d'événements neutrinos, qui ont notamment permis d'évaluer et de modéliser l'impact des incertitudes systématiques liées à l'efficacité quantique des PMTs sur les performances d'ORCA. La thèse présente ensuite une nouvelle estimation de la sensibilité d'ORCA à l'ordre de masse des neutrinos (OMN) et aux paramètres de mélange dans le secteur atmosphérique : Δm^2_{31} et θ_{23}. Une seconde étude porte sur l'évaluation du gain en sensibilité à l'OMN attendue en combinant les données d'ORCA avec celles de JUNO, une expérience de neutrinos de réacteurs de nouvelle génération en cours de construction en Chine. Ce gain résulte de la tension attendue entre les deux expériences pour leur mesure du paramètre de mélange Δm^2_{31} dans le cas d'une hypothèse erronée sur l'OMN. Enfin, la thèse présente les résultats d'une première mesure des paramètres d'oscillation du secteur atmosphérique avec ORCA dans sa configuration actuelle avec 6 lignes de détection déployées (ORCA6). Cette étude permet déjà de rejeter l'hypothèse de non-oscillation des neutrinos à un degré de confiance élevé, et fournit une contrainte sur les paramètres Δm^2_{31} et θ_{23} comparable à celle des mesures existantes d'autres détecteurs.

Mots-clés: Physique des neutrinos, oscillations, détecteurs Cherenkov, télescopes à neutrinos, KM3NeT.

Acknowledments

I would like to express my gratitude to my supervisors, Antoine and Véronique, for their support during the last three years. Without their help, this thesis might not be in reality or evolved to this level!

Thank you Simon and Christine for the very first guides on oscillation studies and SWIM during my master internship and at the beginning of my PhD. Besides, I am also grateful to Gwen, Marta, and Luigi for their help on the project of the ORCA7 simulation. Gwen, many thanks for always caring and giving advice on both my academic and personal life.

The whole KM3NeT collaboration would deserve great thanks, especially the oscillation group and the APC group! Thank you all for being part of this exciting journey of my life!

To my family, thank you for always being supportive on any of my decisions! Finally, I would like to thank Lien, my other half! Thank you for always by my side, patiently supporting me while we are doing long-distance as well as taking care of me during this year when we are together!

Contents

Introduction

Neutrino physics is one of the very active fields in particle physics. The discovery of neutrino oscillations implies that neutrinos are massive and mixed. This is so far one of the few hints for physics beyond the Standard Model. Multiple experiments have been providing increasingly precise measurements on the neutrino oscillation parameters. Even though there are still several remaining questions including the absolute mass scale of neutrinos, their nature to be Dirac or Majorana particles, the value of CP violation phase, and the neutrino mass ordering (NMO). One of the main approaches to resolve the NMO is by probing the matter effects on the atmospheric neutrinos propagating through the Earth. This is the main physics goal of the KM3NeT low energy branch called ORCA, which stands for Oscillation Research with Cosmics in the Abyss.

KM3NeT/ORCA is the next-generation water Cherenkov detector that observes neutrinos via the Cherenkov light emitted from charged particles induced by neutrino interactions. This detection is made possible by installing multiple optical sensors in the deep Mediterranean Sea. Currently, the detector is under construction with a small fraction that has been deployed and is taking data. This thesis is dedicated to the study of atmospheric neutrino oscillations with ORCA and the manuscript is organized in four parts as follows:

Part I: Scientific Context

The first part summarizes the scientific context of this work. An overview of neutrino oscillations is presented in Chap. 1. The chapter first gives a historical introduction and theoretical aspects of the neutrino oscillations in which the current status of the measurement of the oscillation parameters from global data is also discussed. Then it ends with the physics processes relevant to the atmospheric neutrino experiments, including the generation of the atmospheric neutrino fluxes, the oscillation of these neutrinos while propagating through the Earth, and finally the neutrino interactions in the energy range 1-100 GeV which is particularly interesting for oscillation studies. Chap. 2 describes the physics principles and technical design of the KM3NeT project with a focus on the ORCA

detector. The chapter also briefly summarizes the notable physics in addition to assessing the NMO.

Part II: Neutrino simulation with KM3NeT/ORCA

Modeling the detector response is a prerequisite for physics analyses. To serve this aim, the Monte Carlo (MC) simulation of neutrino signals and the response of the detector to such signals is vital and discussed in this part. Chap. 3 presents the most recent MC chain developed within the KM3NeT Collaboration for the ORCA detector. Then, Chap. 4 presents the production of a MC sample of neutrino events at high energy (50-5000 GeV) for a sub-array with 7 detection units (DUs) out of the 115 total expected (ORCA7). I was in charge of producing this MC sample as my service task for the Collaboration. I also used this subsample for checking the ORCA simulation chain and for performing the standard quality control of the production.

Part III: Analysis method for neutrino oscillation studies

This part presents the methodology and frameworks used for neutrino oscillation studies in this thesis. Chap. 5 describes the calculation of the expected neutrino distribution at the ORCA detector. The calculations have been developed and implemented in a KM3NeT software framework called SWIM which uses a full MC approach to build the detector response. I have been in charge of maintaining and developing this framework during the PhD. The framework has also been used to perform the physics studies presented in this work. A description of the sensitivity estimation for oscillation studies with ORCA is then described in Chap. 6. Finally, Chap. 7 presents the systematics considered in ORCA oscillation analyses. This chapter also discusses a particular study that I was involved in, which is the analysis of MC samples produced with different efficiencies of photomultiplier tubes (PMTs) used for characterizing the associated systematics called *energy scale*.

Part IV: Physics Results

This part shows the physics results of this thesis obtained with the SWIM analysis framework. Chap. 8 presents the updated sensitivity of the KM3NeT/ORCA detector to the NMO and the oscillation parameters in the atmospheric sector: Δm^2_{31} and θ_{23}. Those results have been used as an internal cross-check for the official KM3NeT results. In Chap. 9, a study on the combination of ORCA and JUNO for the NMO determination is discussed. This is a collaborative work with the JUNO group at the Hubert Curien Pluridisciplinary Institute

(IPHC) in which I was responsible for providing the ORCA analysis and the combination results. Finally, Chap. 10 presents the first oscillation measurement, in particular an estimation of θ_{23} and Δm^2_{31}, with KM3NeT/ORCA using the data sample from the current deployed 6 DUs.

Part I

Scientific Context

Chapter 1

An overview on neutrino oscillation physics

Contents

1.1 A historical introduction

1.1.1 Early history

The birth of the neutrino is strongly related to the history of weak interaction. Multiple milestones and historical events contributed to our current understanding of neutrinos; this section will only summarize the most important ones. A more complete review can be found in Ref. [1, 2].

The start of the story can be dated back to the investigation in β-decay that took place at the beginning of the XXth century, shortly after the discovery of radioactivity. In 1914, J. Chadwick observed a continuous energy spectrum for the electrons from β-decay which was in contrast with the discrete one observed in α- and γ-decays. This experimental result, subsequently confirmed by Ellis and Wooster in 1914, was puzzling at that time since the electron and the daughter nuclide were the only known products of the β-decay and the conservation of energy would imply that the emitted electron is monoenergetic. This observation triggered multiple interpretations. N. Bohr suggested that energy conservation might only be true in a statistical sense and that a violation could happen for any given decay. Another explanation relied on the emission of an additional, undetectable particle that would carry away part of the energy of the decay. Meitner demonstrated that this particle could not be neutral γ, providing a first hint that the process might relate to a new particle.

β-decay also raised another puzzle called the problem of spin statistics. It is observed that in β-decays, mother and daughter nuclides both have either an integer or a fractional spin, which means that the change in nuclear spin must be an integer. Since the electrons carry the spin of 1/2, the emission of an electron alone would violate the angular momentum conservation.

To solve the two mentioned problems, W. Pauli proposed the idea of a new particle produced along with the electron in β-decay. This particle must be neutral and weakly interacting, so that it could escape detection. Also, the particle had to be a fermion (spin 1/2) to preserve the angular momentum conservation. Pauli named his particle the *neutron*.

In 1932, Chadwick discovered the particle known today as the neutron, which proved to be too heavy to be Pauli's particle [3]. Fermi then renamed Pauli's particle the *neutrino* (the small neutral one in Italian), which is usually denoted as ν. The discovery of the neutron also led Fermi to develop his famous theory that proposes a formulation of the β-decay in analogy with quantum electrodynamics (QED) [4]. To that aim, he introduced an interaction (Fermi interaction) by directly coupling four fermions: neutron, neutrino,

proton, and electron. The theory thus described the β-decay as the process by which a neutron in a nuclide turns into a proton and emits an electron and a neutrino. Fermi also concluded that neutrinos should be extremely light and could be massless.

Despite the success of the Fermi theory, the existence of the neutrino was still in doubt for many years since no neutrino had been observed due to the extremely small interaction cross-section. In 1956, Reines and Cowan conducted an experiment using two water tanks with dissolved $CdCl_2$ surrounded by three scintillators, to measure the antineutrino flux from the Savannah nuclear reactor [5, 6]. The schematics of this experiment, which is known as the first reactor neutrino experiment, are depicted in Fig. 1.1. The detection principle relied on the inverse beta-decay (IBD) process when a neutrino interacts with a proton in the water tank:

$$\bar{\nu}_e + p \rightarrow e^+ + n. \tag{1.1}$$

The produced positron promptly annihilates with an electron of the medium, creating a pair of 511 keV photons. The neutron can be subsequently captured by a Cd nucleus in water, whose de-excitation will trigger the emission of a photon a few μs after the IBD. Both the photons from the positron annihilation and the one from the neutron capture can be detected in the scintillator. The coincidence within a few μs between these two signals provides a distinct signature of the neutrino detection. This discovery has given Reines a Nobel prize 40 years later.

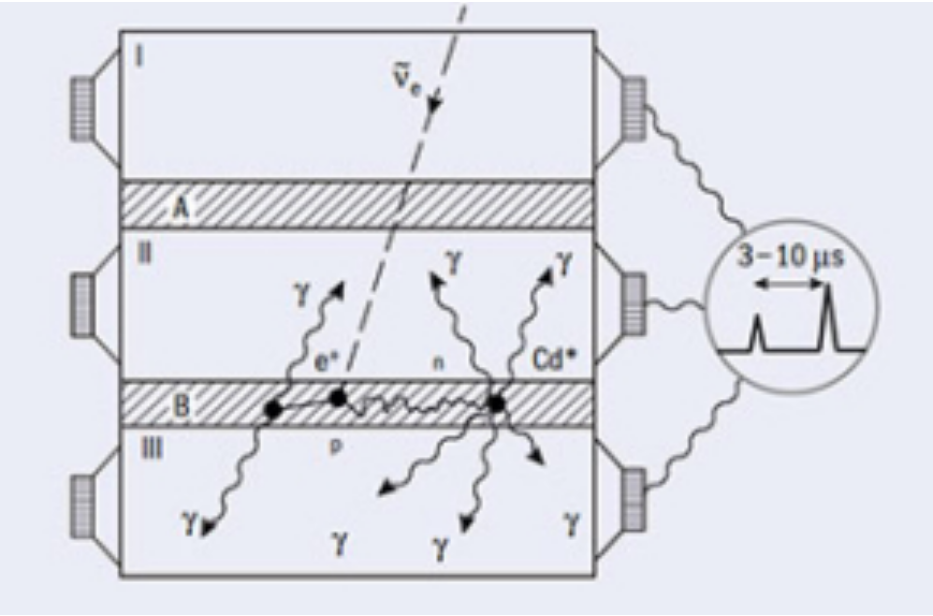

Figure 1.1: A schematic view of Cowan and Reines experiment on the discovery of the neutrino. The inverse beta-decay produces the coincidence signals of the 511 keV photons associated to the positron annihilation and the γ-rays emitted by the neutron capture on Cd. Figure taken from Ref. [7].

Another milestone in neutrino and weak interaction physics worth mentioning was

the discovery of parity violation. The parity symmetry is conserved if the probabilities of a process and its mirror process (obtained by applying the parity transformation as the flip of the sign of the spatial coordinates to the process) are equal. The first hint on parity violation was found in K^+ decay in cosmic ray experiments and later confirmed by accelerator experiments. The decays of K^+ happen in two modes with opposite parity: the K^+, once called θ, decays into two pions while the one called τ decays into three pions. Since both Kaon θ and τ have the same mass, spin, and charge, they must be the same particle which makes them the parity images of each other. Thus the two decay modes observed meant the violation of parity in weak interactions.

In 1956, C.S. Wu made the famous experiment of ^{60}Co decay. In this experiment, ^{60}Co was polarized and the angle of the electron emitted from ^{60}Co beta decay was measured [8]. The data showed that electrons were likely to be emitted in the opposite direction to the spin of the mother nucleus with the angle distribution of:

$$W(\theta) \sim 1 - 0.4 \cos\theta, \tag{1.2}$$

where θ is the angle between the electron momentum and the spin of mother nucleus. The parity transformation makes the electron momentum change sign while the nucleus spin remains identical, which causes $\theta \to 180^\circ - \theta$. This means $W(\theta)$ is not parity invariant and thus the β-decay of ^{60}Co does not conserve parity.

To account for parity violation, Fermi's theory has been reformulated in the form of the V-A theory (Vector - Axial). This was made possible with the assumption of a massless neutrino with a well-defined chirality (ν is left-handed and $\bar{\nu}$ is right-handed). In 1958, Goldhaber, Grodzin, and Sunyar made a direct measurement of the neutrino helicity (the projection of the spin onto the direction of momentum)[1] and they found out that neutrinos have the helicity of -1 which is in agreement with the V-A theory using massless, left-handed neutrinos [9].

In 1959, Pontecorvo suggested that the neutrino produced in pion decays is not the same as the one taking part in β decay, such that it can not produce electrons. In 1962, an experiment in Brookhaven National Laboratory (BNL), known as the first accelerator neutrino experiment, finally confirmed this and marked the discovery of ν_μ [10]. In this experiment, a 15 GeV proton beam was shot onto a beryllium target to produce secondary pions and kaons which later decayed and produced an almost pure ν_μ beam. The detector contained spark chambers shielded by iron to absorb all the hadrons and most of the primary muons. Once a neutrino interaction happened inside the detector, the produced muons or electrons could be distinguished using their topological properties (long tracks

[1] For massless fields, or in the ultrarelativistic limit, helicity coincides with chirality.

for muons and cascades for electrons). Muon-like events were dominant in the observed data which demonstrated that ν_μ is different from ν_e.

In 1967, another important breakthrough was made when S. Glashow, S. Weinberg, A. Salam proposed the theory of weak interaction based on an $SU(2) \times U(1)$ gauge theory [11–13], which put a crucial milestone for the Standard Model (SM) of Particle Physics. Multiple theoretical and experimental developments have since then completed the SM including the Higgs mechanism [14–17] confirmed experimentally by the discovery of the Higgs boson at CERN in 2012 [18,19] or the discovery of $Z, W^\pm$ bosons at CERN [20,21], ... In 1975, M. Perl discovered the third lepton τ [22] which directly implied the existence of third associated neutrino ν_τ. In July 2000, DONUT Collaboration announced the discovery of tau neutrino [23] which constituted the complete detection of 3 neutrinos in SM.

Neutrino has an interesting history and it played an important role in the foundation of SM, in particular, the understanding of the weak interaction. In the SM, neutrinos are massless. Nevertheless, in the past two decades, a variety of experiments has demonstrated the existence of neutrino flavour oscillations, which imply that neutrinos are massive. Thus, neutrinos now contain a hint to the physics beyond the SM, with many interesting questions to be investigated.

1.1.2 The discovery of neutrino oscillations

The concept of neutrino oscillations was first pioneered by Pontecorvo in 1957. Later on, the idea of oscillation stemming from ν_e and ν_μ are mixed states of two mass eigenstates was discussed by Maki, Nakagata, and Sakata. In 1967, Pontecorvo presented the first phenomenological model on two neutrino mixing and oscillation. The theory of neutrino oscillation was then completely developed in 1975-1976. Along with these theoretical developments, experiments have started to show growing evidence for the existence of neutrino oscillations. These early experiments revolve around the two observations called: the *solar neutrino problem* and the *atmospheric neutrino anomaly*.

Solar neutrino problem

The Sun, as a huge thermonuclear reactor, is a powerful source of neutrinos. Since these neutrinos are produced from the nuclear fusion processes, they are all electron neutrinos (ν_e) and have an energy of $\sim$ MeV.

From the early 1960s, progress in understanding of thermonuclear reactions in the Sun led to the construction of the standard solar model (SSM). According to the SSM, solar

neutrinos are produced by two series of nuclear reactions: the pp chain and the CNO cycle [24]. In both cases, the result is the conversion of four protons and two electrons into a Helium nucleus and two electron neutrinos:

$$4p + 2e^- \rightarrow^4 \text{He} + 2\nu_e \tag{1.3}$$

The solar neutrino spectrum for each reaction type of both pp chain and CNO cycle is shown in Fig. 1.2. In the pp chain, the main contribution comes from the proton-proton fusion (denoted in the figure as pp): $p + p \rightarrow^2 \text{H} + e^+\nu_e$. Nevertheless, the corresponding neutrino flux is at a very low energy (below 0.4 MeV). Above 0.4 MeV, the pp chain neutrino fluxes are mainly ^{7}Be and ^{8}B neutrinos which correspond to the reactions $^8\text{B} \rightarrow^8 \text{Be} + e^+ + \nu_e$ and $^7\text{Be} + e^- \rightarrow^7 \text{Li} + \nu_e$. The CNO neutrinos are produced by the β^+ decays of ^{15}O,^{13} N,^{17} F nuclei in the fusion chain.

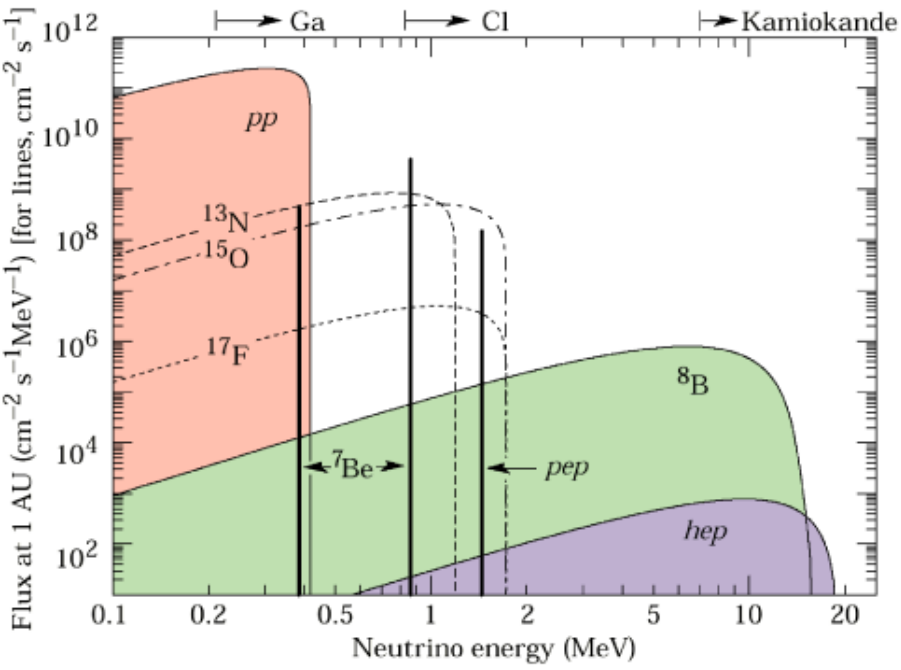

Figure 1.2: Energy spectra of neutrino fluxes for each of pp and CNO reactions as predicted by the Standard Solar Model. The fluxes are either discrete or continuous, depending on the nature of the corresponding reaction (2-body or 3-body decay). Figure taken from Ref. [25]

In 1965, R. Davis conducts the famous Homestake experiment to measure the solar neutrino flux. The detection principle, which was first proposed by Pontecorvo, was based on the neutrino capture reaction $\nu_e + ^{37}\text{Cl} \rightarrow^{37} \text{Ar} + e^-$. The reaction requires an energy threshold of about 0.814 MeV which causes the Homestake experiment to be insensitive to the pp neutrino flux; the dominant contributions to the detected flux come from ^{7}Be and ^{8}B solar neutrinos.

The experiment consisted of a tank containing 615 tons of perchloroethylene (C2Cl4)

installed deep underground. After some exposure time, the ^{37}Ar, induced by neutrinos interaction, was extracted by bubbling helium through the tank. Then, the number of ^{37}Ar was determined by a proportional counter which can detect the Auger electron from the electron capture of ^{37}Ar [2]. In such a way, the flux of detected neutrinos can be extracted. The result of the Homestake experiment was a neutrino flux amounting to just about 30% the prediction by the SSM [26].

This result was then confirmed by other experiments, including the water Cherenkov detector Kamiokande in the late 1980s. Kamiokande detected solar neutrino through the Cherenkov light from electrons induced by the neutrino elastic scattering (ES) interaction $\nu_\alpha + e^- \rightarrow \nu_\alpha + e^-$. This channel has a threshold of about 7 MeV, so that Kamiokande essentially detected the ^{8}B's neutrinos. The measurement resulted in 40% of the expected flux [27]. In the 1990s, SAGE (Soviet-American Gallium Experiment) and GALLEX (The Gallium Experiment) performed a similar radiochemical measurement as the Homestake experiment but using ^{71}Ga, whose lower threshold for neutrino capture allowed them to measure neutrinos in a wider energy range, including the *pp* flux. They obtained one-half of the expected flux from SSM [28, 29]. At about the same time, Super-Kamiokande (SK), the successor of the Kamiokande, performed again the measurement of ^{8}B neutrino flux and also confirm the observed deficit [30].

For several years, there was a debate on whether the solar neutrino deficit was due to neutrino oscillations (ν_e transforming into ν_τ and ν_μ that were not detected) or the SSM was incorrect. The puzzle was hard to solve because the radiochemical experiments (Homestake, SAGE, GALLEX) are only sensitive to ν_e flux, and the water Cherenkov detectors (Kamiokande, Super-Kamiokande), which use the ES interaction, are about six times more sensitive to ν_e than to ν_μ and ν_τ.

The breakthrough was made by the SNO (Sudbury Neutrino Observatory) experiment. SNO is also a Cherenkov detector like Kamiokande and Super-Kamiokande, but instead of water it makes use of heavy water (D_2O) which allows the detection of two other types of neutrino interactions (in addition to the mentioned ES):

- The Charged Current (CC): $\nu_e + d \rightarrow p + p + e^-$
- The Neutral Current (NC): $\nu_\alpha + d \rightarrow p + n + \nu_\alpha$.

The heavy water provides the deuterium (d) which is the target of the CC and NC inter-

[2] ^{37}Ar decays through the electron capture process in which the nucleus absorbs an electron from the atomic electron shell. After that, an outer electron replaces the "missing" electron, and photons with an energy equal to the energy difference between the two electron shells are emitted. These photons, in turn, can be absorbed by other electrons in the outer shells, which are then ejected from the atom. This is called the Auger effect and the emitted electrons are called Auger electrons.

actions that are possible for solar neutrinos of $\sim$ MeV energy. The CC interactions are detected through the Cherenkov light of the produced electron similar to the case of ES. For the case of NC interactions, the neutron capture on deuterium or ^{35}Cl (NaCl was doped into the heavy water in the second phase of the detector) induces a characteristic emission of γ-rays, which allows the detection as well as the discrimination with the Cherenkov signal associated to the electron produced in a CC interaction. While the measurement of CC interactions is sensitive to only ν_e, that of NC interactions is equally sensitive to all three active neutrinos which makes it important for measuring the total neutrino flux from the Sun.

In Fig. 1.3, SNO measurement for the flux of ^{8}B solar neutrinos is shown. The flux deduced from the NC measurement was in very good agreement with the SSM flux. Additionally, the CC measurement indicated that about two-thirds of ^{8}B solar neutrinos are converted into ν_μ and ν_τ as the measurement yielded $\frac{\phi_{CC}^{SNO}}{\phi_{NC}^{SNO}} = 0.340 \pm 0.023(stat.)^{+0.029}_{-0.031}(syst.)$. This result confirmed the validity of the SSM and proved that the solar neutrino deficit was due to neutrino oscillations [31].

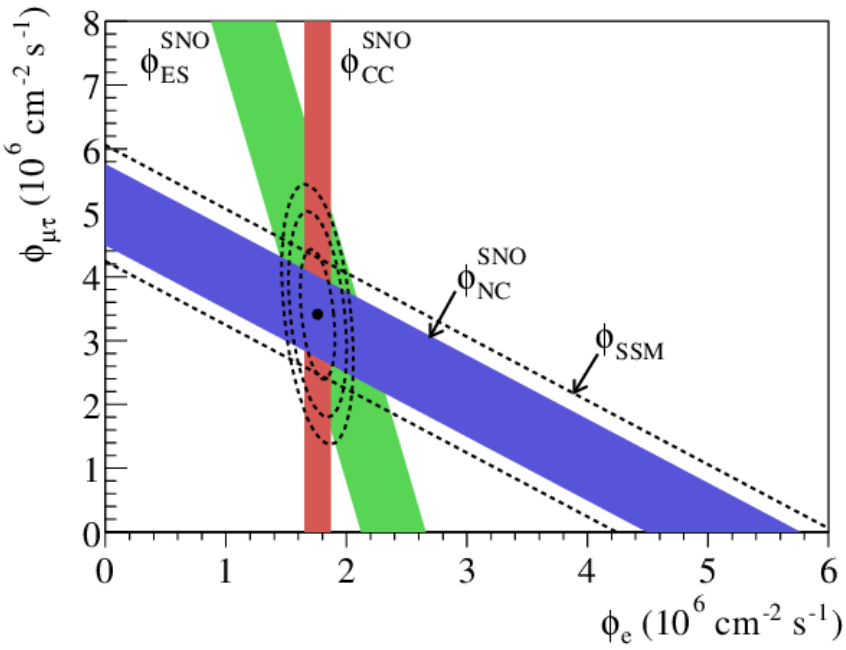

Figure 1.3: Flux of ^{8}B solar neutrinos as measured by SNO in the three different detection channels (ES, CC, NC). The bands represent the $\pm 1\sigma$ error. Figure taken from Ref. [31].

Atmospheric neutrino anomaly

The Earth is continuously bombarded by cosmic rays (CRs), which are mostly protons and light nuclei coming from the outer space. When such primary CRs interact with nuclei in

the Earth's atmosphere, they induce cascades of secondary particles usually called cosmic ray-induced air showers. Such air showers contain many hadrons, among which pions (and kaons) which mainly decay into muons and muon neutrinos:

$$\pi^+/K^+ \to \mu^+ + \nu_\mu, \quad \pi^-/K^- \to \mu^- + \bar{\nu}_\mu. \tag{1.4}$$

Many of these muons do not have sufficient energy to reach the ground and will decay in flight:

$$\mu^+ \to e^+ + \nu_e + \bar{\nu}_\mu, \quad \mu^- \to e^- + \bar{\nu}_e + \nu_\mu. \tag{1.5}$$

The neutrinos produced in these processes are called atmospheric neutrinos.

In the late 1980s, the Kamiokande and IMB (Irvine-Michigan-Brookhaven) detectors started to measure the atmospheric neutrino fluxes. They are both water Cherenkov detectors initially designed for the search of nucleon decay. Atmospheric neutrino interactions can produce charged particles which then create Cherenkov light detectable by these instruments. From the signature of the detected light, the information on the neutrino energy, direction, and interaction channels (interaction types, flavors) can be extracted. The interactions of atmospheric neutrinos at GeV scale are detailed in Sec. 1.3.3 and the light signatures of these interactions are discussed for the specific case of the ORCA water Cherenkov detector in Chap. 2.

According to the production of atmospheric neutrinos in Eq. (1.4) and (1.5), the measured ratio between muon neutrinos and electron neutrinos should be $R_{\mu/e} \simeq 2$ in the multi-GeV energy range. Nevertheless, both Kamiokande and IMB reported a large deficit such that $R^{Kamiokande}_{\mu/e} \simeq 0.60$ and $R^{IMB}_{\mu/e} \simeq 0.54$. This puzzle was called the atmospheric neutrino anomaly.

In 1998, the Super-Kamiokande experiment made a breakthrough for the solution of the atmospheric neutrino anomaly [32]. They reported the observation on the up-down asymmetry defined as:

$$A^{\text{up-down}}_\alpha = \frac{U_\alpha - D_\alpha}{U_\alpha + D_\alpha}, \tag{1.6}$$

where U_α and D_α are the number of up-going and down-going neutrino events of flavor α. The SK measurement for ν_μ in the multi-GeV energy range gave $A^{\text{up-down}}_\mu = -0.296 \pm 0.048(stat.) \pm 0.01(syst.)$ while the one for ν_e was consistent with zero. In the multi-GeV range of atmospheric neutrinos, the influence of the geomagnetic field on the primary CR is negligible, so that the rate and angular distribution of atmospheric neutrino fluxes are approximately isotropic. Furthermore, the Earth is transparent to neutrinos at these energies. This means that the up-down asymmetry observed by SK provided an indication for neutrino oscillations, with the main oscillation channel being in this case $\nu_\mu \to \nu_\tau$.

Interestingly, as depicted in Fig. 1.4, the SK measurement also showed that the number of 'missing' neutrinos due to oscillation depends on the ratio L/E where L is the reconstructed path length (extracted from the measured directions of the neutrinos) and E is the reconstructed neutrino energy. This dependence will be explained in more detail in the next section focusing on the theoretical foundations of neutrino oscillations.

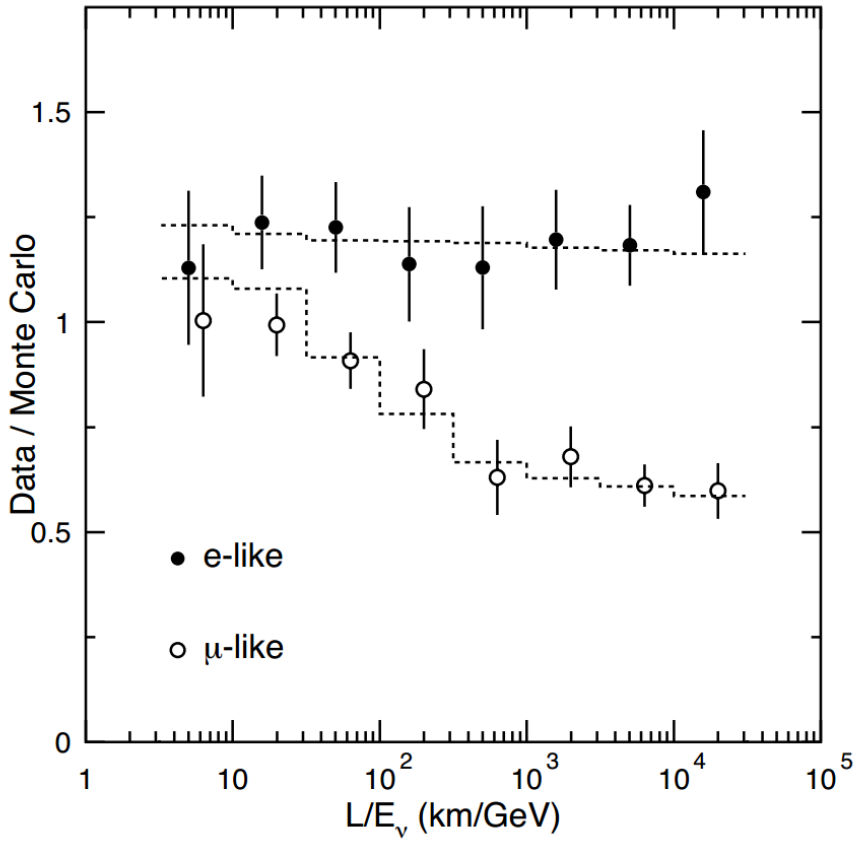

Figure 1.4: The ratio of the number of data events to Monte Carlo (MC) in Super Kamiokande as a function of reconstructed L/E. The dashed line show the expected Data/MC ratio in the oscillation hypothesis. Figure taken from Ref. [32].

1.2 Theoretical aspects of neutrino oscillations

1.2.1 Neutrino mixing and the PMNS matrix

Neutrino oscillations arise because the weak eigenstates (or flavor states) ν_e, ν_μ, ν_τ (neutrinos that participate in weak interaction) are a non-trivial mix of the mass eigenstates ν_1, ν_2, ν_3. As such, neutrino oscillations imply that not all neutrinos can be massless. The mixing can be described by the Pontecorvo-Maki-Nakagawa-Sakata (PMNS) matrix U. In the context of three flavor mixing, the PMNS matrix U is a 3×3 matrix which performs the mixing as follows:

$$\begin{pmatrix} \nu_e \\ \nu_\mu \\ \nu_\tau \end{pmatrix} = U \begin{pmatrix} \nu_1 \\ \nu_2 \\ \nu_3 \end{pmatrix} = \begin{pmatrix} U_{e1} & U_{e2} & U_{e3} \\ U_{\mu 1} & U_{\mu 2} & U_{\mu 3} \\ U_{\tau 1} & U_{\tau 2} & U_{\tau 3} \end{pmatrix} \begin{pmatrix} \nu_1 \\ \nu_2 \\ \nu_3 \end{pmatrix} \tag{1.7}$$

Since the matrix performs the change of basis, it has to be unitary and obey the unitarity relations:

$$U^\dagger U = \mathbf{1} \Leftrightarrow \sum_\alpha U^*_{\alpha i} U_{\alpha j} = \delta_{ij} \quad (\alpha = e, \mu, \tau; i = 1, 2, 3). \tag{1.8}$$

The PMNS matrix can be written as the product of three rotation matrices with mixing angles respectively θ_{23}, θ_{13}, θ_{12}, with the second rotation matrix containing a complex phase δ_{CP} (which causes the CP (charge parity) violation in neutrino oscillation as will be discussed later); and of a diagonal matrix P:

$$U = \begin{pmatrix} 1 & 0 & 0 \\ 0 & c_{23} & s_{23} \\ 0 & -s_{23} & c_{23} \end{pmatrix} \begin{pmatrix} c_{13} & 0 & s_{13} e^{-i\delta_{CP}} \\ 0 & 1 & 0 \\ -s_{13} e^{i\delta_{CP}} & 0 & c_{13} \end{pmatrix} \begin{pmatrix} c_{12} & s_{12} & 0 \\ -s_{12} & c_{12} & 0 \\ 0 & 0 & 1 \end{pmatrix} P, \tag{1.9}$$

where c_{ij} and s_{ij} are $\cos\theta_{ij}$ and $\sin\theta_{ij}$ respectively. The diagonal matrix P depends on the nature of neutrinos. P is the unit matrix if neutrinos are Dirac fermions, as it is the case for the other charged leptons (in such a case the neutrino and antineutrino are different particles). Neutrinos could also be Majorana fermions, a concept proposed by Majorana such that a particle and its antiparticle are identical [33]. In such case, P contains 2 Majorana phases $P = \text{diag}(e^{i\alpha_1}, e^{i\alpha_2}, 1)$. A review on Majorana neutrinos can be found in Ref. [34].

1.2.2 Neutrino oscillations in vacuum

Standard derivation of neutrino oscillation probability

The mixing of flavor states to mass states and vice versa is expressed as follows:

$$|\nu_i\rangle = \sum_\alpha U_{\alpha i} |\nu_\alpha\rangle \,, \tag{1.10}$$

$$|\nu_\alpha\rangle = \sum_i U^*_{\alpha i} |\nu_i\rangle \,, \tag{1.11}$$

where $\nu_\alpha = \nu_e, \nu_\mu, \nu_\tau$ are the flavor states and $\nu_i = \nu_1, \nu_2, \nu_3$ are three mass states. The two above formulas can be derived from each other thanks to the unitary relation (1.8).

When neutrinos propagate in vacuum, the mass states are the eigenstates of the free Hamiltonian:

$$\hat{\mathcal{H}} |\nu_i\rangle = E_i |\nu_i\rangle \,, \tag{1.12}$$

with the eigenvalues being the energies of the neutrinos:

$$E_i = \sqrt{|\vec{p}|^2 + m_i^2}. \tag{1.13}$$

The evolution of ν_i in time is governed by the Schrödinger equation:

$$i\frac{d}{dt} |\nu_i(t)\rangle = \hat{\mathcal{H}} |\nu_i(t)\rangle \,. \tag{1.14}$$

Then the plane wave solution of the equation yields:

$$|\nu_i(t)\rangle = e^{-iE_i t} |\nu_i(0)\rangle \tag{1.15}$$

In neutrino oscillation experiments, neutrinos are initially produced with a given flavor $|\nu_\alpha(t=0)\rangle = |\nu_\alpha\rangle$ which is the mix of mass eigenstates following Eq.(1.11). When neutrinos propagate the time evolution of each mass state follows Eq. (1.15). Hence, one can derive the time evolution of a neutrino initially produced with flavor α, $|\nu_\alpha(t)\rangle$, as:

$$|\nu_\alpha(t)\rangle = \sum_i U^*_{\alpha i} e^{-iE_i t} |\nu_i\rangle \,. \tag{1.16}$$

Substituting Eq. (1.10) into the above equation, we have:

$$|\nu_\alpha(t)\rangle = \sum_{\beta=e,\mu,\tau} \left(\sum_i U^*_{\alpha i} e^{-iE_i t} U_{\beta i} \right) |\nu_\beta\rangle \,. \tag{1.17}$$

One can see that if the neutrinos are mixed (i.e the mixing matrix U is not diagonal), the neutrino state after a time $t > 0$ is no longer a pure flavor state but rather a superposition of different flavor states. The probability for the initial flavor state ν_α to oscillate to ν_β at the time t is then given as:

$$P(\nu_\alpha \to \nu_\beta) = |\langle \nu_\beta | \nu_\alpha(t) \rangle|^2 = \left| \sum_i U_{\beta i} U^*_{\alpha i} e^{-iE_i t} \right| = \sum_{i,j} U^*_{\alpha i} U_{\beta i} U_{\alpha j} U^*_{\beta j} e^{-i(E_i - E_j)t} \tag{1.18}$$

Since neutrinos have a very small mass and usually travel in an ultra-relativistic regime, we can adopt an approximation:

$$E_i \simeq E + \frac{m_i^2}{2E}, \tag{1.19}$$

with $E = |\vec{p}|^2$. The oscillation probability can be rewritten as:

$$\begin{aligned} P(\nu_\alpha \to \nu_\beta) = \delta_{\alpha\beta} &- 4 \sum_{i<j} \mathrm{Re}\left[U_{\alpha i} U^*_{\beta i} U^*_{\alpha j} U_{\beta j}\right] \sin^2\left(\frac{\Delta m^2_{ji} L}{4E}\right) \\ &+ 2 \sum_{i<j} \mathrm{Im}\left[U_{\alpha i} U^*_{\beta i} U^*_{\alpha j} U_{\beta j}\right] \sin\left(\frac{\Delta m^2_{ji} L}{2E}\right), \end{aligned} \tag{1.20}$$

where $\Delta m^2_{ji} = m^2_j - m^2_i$ is the squared-mass difference, $L \simeq ct$ is the travel distance of the neutrino. For the case of anti-neutrinos, a similar derivation can be made and the probability can be obtained simply by replacing $U \rightleftharpoons U^*$ and inverting the sign of the last imaginary terms in Eq. (1.20) (see Ref. [1, 2] for the detailed derivation).

From the Eq. (1.20), we can see that neutrino oscillations can only happen in the case of non-degenerate masses ($\Delta m^2_{ji} \neq 0$) and non-trivial mixing ($U \neq \mathbf{1}$). For three flavor mixing, the oscillation is governed by six parameters: three mixing angles ($\theta_{23}, \theta_{13}, \theta_{12}$), two independent squared-mass splitting which can be chosen as Δm^2_{21} and Δm^2_{31} (Δm^2_{32} is then computed as $\Delta m^2_{31} - \Delta m^2_{21}$), and the CP phase δ_{CP}. The oscillation probability also depends on the ratio L/E. This dependence was first observed in the atmospheric neutrino data of SK as mentioned in Sec. 1.1.2.

The δ_{CP} phase enters the last term of Eq. (1.20) which causes $P(\nu_\alpha \to \nu_\beta) \neq P(\bar{\nu}_\alpha \to \bar{\nu}_\beta)$. Since $\nu_\alpha \to \nu_\beta$ and $\bar{\nu}_\alpha \to \bar{\nu}_\beta$ are the CP image of each other, this causes the CP-violation in neutrino oscillations. One can also notice that CP-violation only appears in the case of $\nu_\alpha \neq \nu_\beta$ (also called *appearance channel*) while it is not possible for $\nu_\alpha = \nu_\beta$ (also called *disappearance channel*) due to the vanishing of the last term of Eq. (1.20) in such case.

The Majorana phases do not contribute to the oscillation due to the combination of the form $U_{\alpha i} U^*_{\beta i}$ which cancels the diagonal matrix P in Eq. (1.9). Oscillation experiments are therefore not sensitive to the nature of Dirac or Majorana of neutrinos. This question can

be solved through experiments on the neutrino-less double beta decay of which a good review can be found in Ref. [35].

The approximation of two neutrino mixing

In the early time of neutrino experiments, most of them had not reached a sufficient sensitivity to the subdominant terms of Eq. (1.20) as, for example, in the case of early data of atmospheric neutrinos mentioned in Sec. 1.1.2. In such cases, the observed data can be sufficiently well described by the approximation of two neutrino mixing in which two flavor neutrinos ν_α and ν_β (α, β could be e, μ; e, τ; or μ, τ) are superposition of two mass states ν_1, ν_2:

$$\begin{pmatrix} \nu_\alpha \\ \nu_\beta \end{pmatrix} = U \begin{pmatrix} \nu_1 \\ \nu_2 \end{pmatrix} = \begin{pmatrix} \cos\theta & \sin\theta \\ -\sin\theta & \cos\theta \end{pmatrix} \begin{pmatrix} \nu_1 \\ \nu_2 \end{pmatrix}. \tag{1.21}$$

The mixing matrix U is now parametrized with just one mixing angle θ. Following the same procedure described above for the derivation of oscillation probability, one obtains:

$$\begin{aligned} P(\nu_\alpha \to \nu_\beta) &= \sin^2 2\theta \sin^2\left(\frac{\Delta m^2 L}{4E}\right) \\ P(\nu_\alpha \to \nu_\alpha) &= 1 - \sin^2 2\theta \sin^2\left(\frac{\Delta m^2 L}{4E}\right) \end{aligned} \tag{1.22}$$

The approximation to simplify from three to two flavor mixing works thanks to the fact that $|\Delta m^2_{21}| \ll |\Delta m^2_{31}|$ and the mixing angle θ_{13} is quite smaller than other two mixing angles. This is actually the case of our current knowledge from the global fit of neutrino oscillation experiments [36]. We present below how this approximation can be applied for some specific cases of neutrino experiments.

The atmospheric neutrino experiments (also long-baseline accelerator and short-baseline reactor experiments) turn out to be sensitive to the region such that the oscillation phase $\Delta m^2_{31} L/(2E) \sim 1$ which results in $\Delta m^2_{21} L/(2E) \ll 1$. Thus the terms containing Δm^2_{21} are subdominant and can be neglected. Applying to the three mixing cases, one can then deduce the oscillation probabilities for instance in the case of ν_μ oscillation as:

$$P(\nu_\mu \to \nu_e) \simeq \sin^2\theta_{23} \sin^2 2\theta_{13} \sin^2\left(\frac{\Delta m^2_{31} L}{4E}\right), \tag{1.23}$$

$$P(\nu_\mu \to \nu_\mu) \simeq 1 - (\cos^2\theta_{13} \sin^2 2\theta_{23} + \sin^4\theta_{23} \sin^2 2\theta_{13}) \sin^2\left(\frac{\Delta m^2_{31} L}{4E}\right), \tag{1.24}$$

$$P(\nu_\mu \to \nu_\tau) \simeq \cos^4\theta_{13} \sin^2 2\theta_{23} \sin^2\left(\frac{\Delta m^2_{31} L}{4E}\right). \tag{1.25}$$

Taking a further approximation $\theta_{13} \simeq 0$ (as θ_{13} is smaller than the other two mixing angles), we can neglect terms that are proportional to $\sin^2\theta_{13}$. The oscillation probabilities then read:

$$P(\nu_\mu \to \nu_e) \simeq 0, \tag{1.26}$$

$$P(\nu_\mu \to \nu_\mu) \simeq 1 - \sin^2 2\theta_{23} \sin^2\left(\frac{\Delta m^2_{31} L}{4E}\right), \tag{1.27}$$

$$P(\nu_\mu \to \nu_\tau) \simeq \sin^2 2\theta_{23} \sin^2\left(\frac{\Delta m^2_{31} L}{4E}\right). \tag{1.28}$$

One then recovers the formulas for two neutrino oscillation (1.22). Hence, the atmospheric ν_μ oscillation can be described as two neutrino oscillation between ν_μ and ν_τ. One can also derive that for $\nu_e \to \nu_e$, the approximation reads $P(\nu_e \to \nu_e) \simeq 0$. This explains the result of SK presented in Fig. 1.4 where only ν_μ disappearance is observed but not ν_e. θ_{23} and Δm^2_{31} govern the dominant terms of atmospheric neutrino oscillation so that they are also called the *atmospheric mixing angle* (θ_{atm}) and *atmospheric* Δm^2 (Δm_{atm}).

For low-energy solar neutrinos[3] (and also valid for long-baseline reactor neutrino), $\Delta m^2_{21} L/(2E) \sim 1$ while $\Delta m^2_{31} L/(2E) \gg 1$ which causes Δm^2_{31}-driven oscillation to be averaged out and Δm^2_{21}-driven terms to become dominant. Also neglecting $\sin^2\theta_{13}$ when compared with the two other mixing angles, one obtains:

$$P(\nu_e \to \nu_e) = P(\bar{\nu}_e \to \bar{\nu}_e) = 1 - \sin^2 2\theta_{12} \sin^2\left(\frac{\Delta m^2_{21} L}{4E}\right). \tag{1.29}$$

Similarly to the case of atmospheric neutrinos, we also usually call θ_{12} and Δm^2_{21} the *solar mixing angle* (θ_{sol}) and *solar* Δm^2 (Δm_{sol}).

Another case worth mentioning is the short-baseline disappearance of reactor anti-neutrinos, which yields:

$$P(\bar{\nu_e} \to \bar{\nu_e}) = 1 - \sin^2 2\theta_{13} \sin^2\left(\frac{\Delta m^2_{31} L}{4E}\right). \tag{1.30}$$

This means the experiments of this type are of particular interest for measuring θ_{13}.

One key observation from the aforementioned cases is that the ratio L/E can be chosen appropriately for each experiment such that it can access the sensitivity to different oscillation parameters. For $\dfrac{\Delta m^2 L}{2E} \sim 1$, the experiments can be sensitive to the given Δm^2 together with the related mixing angles coupled with it in the oscillation probability. For

[3] At low energies for solar neutrinos, the vacuum oscillations are dominant. When their energy increases, matter effects, which will be presented in the next subsection, come into play.

$\frac{\Delta m^2 L}{2E} \ll 1$, the associated oscillation terms are subdominant and give no sensitivity to the experiment. On the other hand, if $\frac{\Delta m^2 L}{2E} \gg 1$, the related terms oscillate rapidly and only the averages of them might be observed which give no sensitivity to Δm^2 but might give the information on the related mixing angles.

1.2.3 Neutrino oscillations in matter

When neutrinos propagate in matter, they can interact with both electrons and nucleons in a process called *coherent forward elastic scattering*. This type of interaction has no impact on the momentum and energy of the neutrinos and thus can interfere with the neutrino propagation in such a way that it modifies the flavor content of the propagating neutrino states and thus affects the oscillation process, as first pointed out by Wolfenstein [37]. This effect is called the *matter effect* and is discussed in this subsection.

To facilitate the study of the impact of matter effect, let us first reformulate the vacuum oscillations presented in the previous subsection. One can rewrite the vacuum Hamiltonian in the mass basis and in the ultra-relativistic approximation as follows:

$$\widehat{\mathcal{H}}_{0,mass} = \frac{1}{2E} \begin{pmatrix} 0 & 0 & 0 \\ 0 & \Delta m^2_{21} & 0 \\ 0 & 0 & \Delta m^2_{31} \end{pmatrix}, \tag{1.31}$$

where the common phase $E_1 = m_1^2/(2E)$ is factored out and subtracted since only relative phases between states are the physically meaningful. In the flavor basis, the Hamiltonian is obtained with the use of the PMNS matrix:

$$\widehat{\mathcal{H}}_{0,flv} = U \widehat{\mathcal{H}}_{0,mass} U^\dagger. \tag{1.32}$$

In the ultra-relativistic case $t \simeq x$ (with $c = 1$ in natural units), the Schödinger equation reads:

$$i\frac{d}{dx} |\nu_\alpha(x)\rangle = \widehat{\mathcal{H}}_0 |\nu_\alpha\rangle . \tag{1.33}$$

with the solution:

$$|\nu_\alpha(x)\rangle = \exp\left(-ix\widehat{\mathcal{H}}_0\right) |\nu_\alpha(x=0)\rangle = \widehat{\mathcal{U}}(x) |\nu_\alpha\rangle . \tag{1.34}$$

The operator $\hat{\mathcal{U}}(x) = \exp\left(-ix\hat{\mathcal{H}}\right)$ is called *evolution operator* since it transforms the initial neutrino state into the neutrino state after propagating on a distance x. Substituting this operator in terms of flavor basis, one obtains back the expression (1.16).

When neutrinos propagate in matter, the evolution is no longer described by the vacuum Hamiltonian. In this case, the Hamiltonian contains two terms: $\hat{\mathcal{H}}_0$ as the vacuum propagation and the potential term $\hat{V}$ induced by the interactions of neutrinos in the medium:

$$\widehat{\mathcal{H}} = \widehat{\mathcal{H}}_0 + \widehat{V}. \tag{1.35}$$

The processes of neutrino coherent forward elastic scattering are depicted in Fig. 1.5. In these processes, the NC interaction (through the exchange of Z boson) is present for all neutrino flavors while the CC interaction (through the exchange of $W^{\pm}$ boson) is possible only for ν_e. Since the potential term is induced by weak interaction processes, it should be diagonal in the flavor basis. A detailed derivation of the matter potential can be found in Ref. [38], which yields:

$$V_{\alpha\beta} = V_\alpha \delta_{\alpha\beta} = (V_{CC,\alpha} + V_{NC,\alpha})\delta_{\alpha\beta}, \tag{1.36}$$

$$V_{CC,\alpha} = \begin{cases} \sqrt{2} G_F n_e(x), & \alpha = e \\ 0, & \alpha = \mu, \tau \end{cases}; \quad V_{NC,\alpha} = -\frac{G_F}{\sqrt{2}} n_n(x),\ \alpha = e, \mu, \tau. \tag{1.37}$$

$G_F = 1.166 \times 10^{-5}\text{GeV}^{-2}$ is the Fermi constant. $n_e(x)$ and $n_n(x)$ are the densities of electrons and neutrons in the medium respectively. For antineutrinos, the potential terms are given with the opposite sign $V_\alpha(\bar{\nu}) = -V_\alpha(\nu)$. Due to the nature of the interaction as mentioned above, the CC potential is only present for the electron neutrinos while the NC potential is universal for all flavors. The latter generates a phase common to all neutrino flavors. Hence, it is not physical and one can eliminate it with a suitable global phase transformation applied to all neutrino fields [1]. The Hamiltonian for the case of propagation in matter can be finally written in the mass basis as:

$$\widehat{\mathcal{H}}_{M,mass} = \frac{1}{2E} \begin{pmatrix} 0 & 0 & 0 \\ 0 & \Delta m^2_{21} & 0 \\ 0 & 0 & \Delta m^2_{31} \end{pmatrix} + U \begin{pmatrix} V_{CC}(x) & 0 & 0 \\ 0 & 0 & 0 \\ 0 & 0 & 0 \end{pmatrix} U^\dagger, \tag{1.38}$$

and in the flavor basis: $\widehat{\mathcal{H}}_{M,flv} = U^\dagger \widehat{\mathcal{H}}_{M,mass} U$. The mass states are now no longer the eigenstates of the Hamiltonian since the Hamiltonian in the mass basis is not diagonal due to the appearance of the matter potential term. To find the eigenstates of neutrino propagating in the medium, one then has to diagonalize the Hamiltonian $\widehat{\mathcal{H}}_M$.

In practice, for numerical computation of oscillation probabilities, one can approximate the density profile along the neutrino path as a discrete series of N constant density layers $x_0, x_1, ..., x_N$. Then in each layer, the density and the Hamiltonian is independent of the

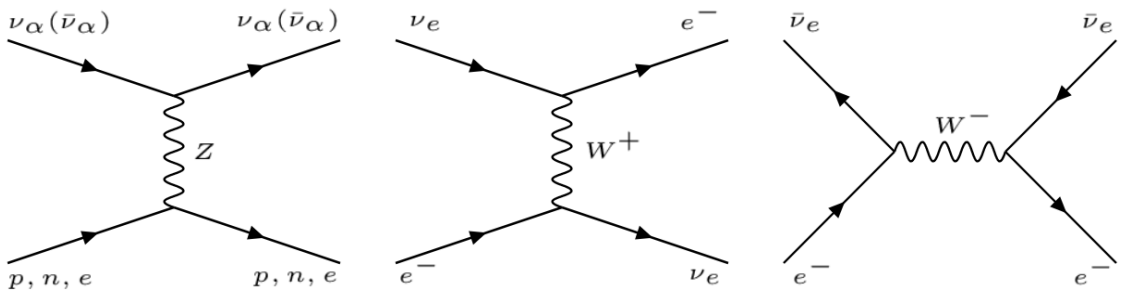

Figure 1.5: Possible processes in forward elastic scattering of neutrinos on ordinary matter (n, p, e^-). From left to right: NC interaction which appears for all flavors, CC interaction which is only present for electron neutrinos and antineutrinos.

position x:

$$\begin{cases} n_e(x) = n_{e,i} \\ \widehat{\mathcal{U}}_i(x) = \exp\left(-ix\widehat{H}_M(n_e, i)\right) \end{cases} \quad \text{for } x_i \leq x \leq x_{i+1}. \tag{1.39}$$

Using the evolution operator, one obtains the relation between the neutrino states at x_i and x_{i+1} which describes the evolution of neutrino in the layer $x_i \to x_{i+1}$:

$$|\nu_\alpha(x_{i+1})\rangle = \widehat{\mathcal{U}}_i(x_{i+1}) \, |\nu_\alpha(x_i)\rangle \, . \tag{1.40}$$

Consequently, the probability of transition for the full neutrino path can be computed as:

$$P(\nu_\alpha \to \nu_\beta) = |\langle \nu_\beta | \nu_\alpha \rangle|^2 = \left| \langle \nu_\beta | \, \widehat{\mathcal{U}}_{N-1}(x_N) ... \widehat{\mathcal{U}}_1(x_2) \widehat{\mathcal{U}}_0(x_1) \, |\nu_\alpha\rangle \right|^2 . \tag{1.41}$$

The evolution operator can be diagonalized by the specific effective mass states in each constant density layer and thus can give a straightforward calculation of the oscillation probability [39]. In fact, this formula is adopted for the numerical computation of oscillation probability of atmospheric traversing the Earth (see Chap. 5) which is used for the oscillation analysis with the ORCA detector presented in this thesis.

Matter effects in two neutrino mixing

As we have seen in the previous subsection, in many experimental contexts, neutrino oscillations can be effectively described in a two flavor oscillation scheme. Hence, it is worth considering the matter effect in this case. The matter Hamiltonian for the two flavor oscillation and in the flavor basis can be written as:

$$\widehat{\mathcal{H}}_{M,flv} = \begin{pmatrix} -\frac{\Delta m^2}{2E}\cos 2\theta \pm \sqrt{2} G_F n_e & \frac{\Delta m^2}{4E}\sin 2\theta \\ \frac{\Delta m^2}{4E}\sin 2\theta & 0 \end{pmatrix}, \tag{1.42}$$

where the sign $+(-)$ of the matter potential is for neutrinos (antineutrinos) respectively. For simplification, the electron density n_e is considered to be constant. The matter Hamiltonian can be diagonalized as follows:

$$\widehat{\mathcal{H}}_{M,flv} = U_M \begin{pmatrix} E_1^M & 0 \\ 0 & E_2^M \end{pmatrix} U_M^\dagger, \qquad U_M = \begin{pmatrix} \cos\theta_M & \sin\theta_M \\ -\sin\theta_M & \cos\theta_M \end{pmatrix}, \tag{1.43}$$

where E_1^M and E_2^M are the two eigenstates of the matter Hamiltonian. θ_M is the effective mixing angle. These parameters are defined as:

$$E_2^M - E_1^M = \frac{\Delta m^2}{2E}\sqrt{\left(1 \mp \frac{n_e}{n_{res}}\right)^2 \cos^2 2\theta + \sin^2 2\theta}, \tag{1.44}$$

$$\sin 2\theta_M = \frac{\sin 2\theta}{\sqrt{\left(1 \mp \frac{n_e}{n_{res}}\right)\cos^2 2\theta + \sin^2 2\theta}}, \tag{1.45}$$

$$\cos 2\theta_M = \frac{\cos 2\theta}{\sqrt{\left(1 \mp \frac{n_e}{n_{res}}\right)\cos^2 2\theta + \sin^2 2\theta}}, \tag{1.46}$$

where $n_{res} = \frac{\Delta m^2 \cos 2\theta}{2\sqrt{2} G_F E}$ is called the *resonance density*. The $-(+)$ sign is for neutrino and antineutrino respectively. One can further define the effective squared mass difference:

$$\Delta^M m^2 = \Delta m^2 \sqrt{\left(1 \mp \frac{n_e}{n_{res}}\right)^2 \cos^2 2\theta + \sin^2 2\theta}. \tag{1.47}$$

Then the oscillation probability can be given in a similar form as in vacuum:

$$P(\nu_\alpha \to \nu_\beta) = \sin^2 2\theta_M \sin^2\left(\frac{\Delta^M m^2 L}{4E}\right) \tag{1.48}$$

We can see that the oscillation probability can become resonant: $\sin^2 2\theta_M = 1$ under given circumstances. If the neutrino energy is at the value such that $n_{res} = n_e$, then the resonance happens for neutrinos in the case of $\Delta m^2 \cos 2\theta > 0$ and antineutrinos in the case of $\Delta m^2 \cos 2\theta < 0$. This resonance was first discussed by Smirnov and Mikheev in 1985 [40] and is called the MSW resonance (named after Mikheev, Smirnov, and Wolfenstein). In the two flavor framework, one can choose the convention so that $0 \leq \theta \leq \frac{\pi}{4}$. Then the sign of $\Delta m^2 \cos 2\theta$ is also the one for Δm^2 which causes the matter oscillation to be sensitive to the sign of Δm^2 (or the *mass ordering* which will be further discussed in Sec. 1.2.4).

Matter effects in solar and atmospheric neutrino oscillations

Matter effects play an important role when neutrinos travel for a large distance through the dense medium for instance the cases of solar and atmospheric neutrinos that traverse the Sun and/or the Earth. Nevertheless, in these two cases, the matter effects are somewhat different due to the difference in density profile of the Sun and the Earth.

In the case of solar neutrinos, the electron density of the Sun is not a constant but varies as a function of position x. In such a case, the effective mixing angle θ_M is also position-dependent and induces off-diagonal components as $\dot{\theta}_M(x)$ in the Hamiltonian. In fact, the Sun density varies slowly so that the position dependence of the effective mixing angle $\theta_M(x)$ is also slow enough ($\dot{\theta}_M(x) = 0$). Then one can make the approximation that the evolutions of effective eigenstates are decoupled. Such regime is called the $adiabatic$ regime and results in the *MSW effect* in the Sun. Combining data from SNO, SK, and KamLAND (a reactor neutrino experiment) had also lead to the determination of the LMA (Large Mixing Angle) solution for solar neutrino oscillations [41]. A more detailed description of this mechanism can be found in Ref. [42, 43]. The MSW effect observed in solar neutrino data also points out that $\Delta m^2_{21} \cos 2\theta_{12} > 0$. With the convention that $\theta_{12} \leq \pi/4$ (equivalent to choosing that ν_1 (ν_2) is composed mainly from ν_e (ν_μ) respectively), this observation fixes the sign of Δm^2_{21} to be positive.

In the case of atmospheric neutrinos crossing the Earth, the oscillations have not only the MSW resonance but also the *parametric enhancement*. This effect appears when neutrinos travel through a periodic variation of the electron density, which is the case for atmospheric neutrinos traversing the Earth with a spherical distribution of density. This mechanism will be discussed in more detail in Sec. 1.3.2.

1.2.4 Recent experiments and current status of three neutrino oscillation picture

The important measurements in the solar and atmospheric neutrino sectors presented in Sec. 1.1.2 have shown profound evidence for the concept of neutrino oscillations. Multiple experiments following up in the past two decades have provided more and more accurate measurements of the oscillation parameters and extended further our understanding of the neutrino sector. In this subsection, we first briefly review the contributions made by recent experiments, then the current status and prospects for neutrino experiments are also discussed.

Solar and reactor neutrino experiments

Apart from the discovery of neutrino oscillation, SNO and SK have also provided the measurement of the oscillation parameters in the solar sector i.e the θ_{12} and Δm^2_{21}.

The solar sector can also be accessed by a reactor neutrino experiment called KamLAND [44] which collected data at a very long baseline (~ 180 km). Including KamLAND's data with those from solar experiments had helped improve the constraints on θ_{12} and Δm^2_{21} as well as confirming the MSW LMA mechanism [41, 45]. As mentioned in the previous section, the sign of Δm^2_{21} was found to be positive thanks to these experiments.

The decoupling between early atmospheric and solar data, such that each of them can be approximately well described by two flavor oscillations, has shown that $\Delta m^2_{21} \ll \Delta m^2_{31}$ and that θ_{13} is small as discussed in Sec. 1.2.2. Since θ_{13} governs the subdominant terms in these observation, determining this parameter is important for the precision measurement of next generation experiments. The reactor neutrino experiments play an important role in the determination of θ_{13}. Three reactor experiments have contributed significantly to establishing the current value of θ_{13}: Daya Bay [46, 47], DoubleChooz [48, 49], and RENO [50, 51]. They measured the $\bar{\nu}_e \to \bar{\nu}_e$ transition at a baseline of ~ 1 km. At this baseline, the dominant oscillation probability follows Eq. 1.30 and thus provides sensitivity to both θ_{13} and Δm^2_{31}. The measurement of θ_{13} has shown that this parameter is non-zero and in fact has a "relatively large" value: $\theta_{13} = 8.57°$ (assuming normal mass ordering $\Delta m^2_{31} > 0$) from the current global fit result [36]. This is an asset for later experiments measuring the remain unknown parameters δ_{CP} and the question of *neutrino mass ordering* (NMO) i.e whether the sign of Δm^2_{31} is positive (*normal ordering* - NO) or negative (*inverted ordering* - IO).

Accelerator neutrino experiments

Accelerator neutrino experiments measure the neutrinos created from the decay of mesons (pions and kaons) produced by shooting protons to a target. These neutrinos have an energy of ~ 1 to few GeV. A typical accelerator neutrino experiment usually has two detectors: the *near detector* that is close to the neutrino source and measures the initial neutrino flux, and the far detector that measures the oscillated flux. The distance between them is about $10^2 - 10^3$ km (Long baseline). Long-baseline (LBL) accelerator experiments can measure the disappearance of ν_μ as well as the appearance of ν_e from the initial ν_μ flux. With these channels and considering the mentioned energy and baseline, the LBL accelerator experiments have a good sensitivity to the atmospheric parameters θ_{23} and Δm^2_{31}, and some sensitivity to θ_{13}. They are also expected to solve the remaining question on δ_{CP} and,

Parameter	Main contribution	Other contributions
Δm^2_{21}	KamLAND	SOL
$\lvert\Delta m^2_{31}\rvert$	LBL+ATM+REAC	-
θ_{12}	SOL	KamLAND
θ_{23}	LBL+ATM	-
θ_{13}	REAC	(LBL+ATM) and (SOL+KamLAND)
δ_{CP}	LBL	ATM

Table 1.1: Contribution of different types of neutrino experiments to the measurement of oscillation parameters. The used acronyms for type of experiements: LBL (long baseline accelerator), ATM (atmospheric), SOL (solar), REAC (reactor). Table extracted from Ref. [57].

in principle, also the neutrino mass ordering. The top current experiments are NOνA [52] and MINOS [53] that use a beam from Fermilab; and T2K [54] which uses a beam created at the J-PARC accelerator facility in Japan, and aimed at the Super-Kamiokande detector.

Atmospheric neutrino experiments

Atmospheric neutrino experiments can measure the atmospheric neutrino flux produced by the cosmic-ray induced air showers as briefly presented in Sec. 1.1.2. The energy range of interest for oscillation studies is typically from ∼0.1 GeV to ∼ 100 GeV. Current active experiments are Super-Kamiokande [55] and IceCube DeepCore [56]. They contribute to the measurement of θ_{23} and Δm^2_{31}. The NMO is also expected to be resolved with the next generation of atmospheric neutrino experiments thanks to the matter effects in the Earth which will be explained in more detail in Sec. 1.3.2.

Current status and future prospects

Tab. 1.1 summarizes the different contributions from different types of experiments to the measurement of neutrino oscillation parameters. The current status of these measurements as inferred from global data is discussed e.g. in Refs. [36, 57].

Among all 6 oscillation parameters, θ_{31} and $|\Delta m^2_{31}|$ are measured to a really good precision. Constrains from θ_{31} dominantly come from reactor experiments while for $|\Delta m^2_{31}|$ accelerator, atmospheric and reactor experiments are all important and make quite comparable contributions. The solar parameters θ_{12} and Δm^2_{21} are measured by KamLAND and solar experiments but there is still room for improvement in the precision and the future reactor experiment JUNO is expected to provide improved constraints on these parameters [58]. Currently, in the picture of three neutrino oscillations, three main issues remain

to be solved: the precise measurement of θ_{23}, the measurement of the CP violation phase δ_{CP}, and the determination of the neutrino mass ordering.

θ_{23} is the least constrained mixing angle and measuring it to a very good precision is one of the main goals for neutrino physics at the moment. Whether θ_{23} is maximal mixing ($\theta_{23} = \pi/4$), in the upper octant ($\theta_{23} > \pi/4$) or in the lower octant ($\theta_{23} > \pi/4$) would be a theoretical interest since it would help to constrain a number of theoretical models which implies the maximal mixing of θ_{23}. Accelerator and atmospheric experiments probe the oscillation process of ν_μ disappearance, whose dominant term is proportional to $\sin^2 2\theta_{23}$. This results in a degeneracy of the two octants of θ_{23}. The degeneracy can only be lifted thanks to the sensitivity to the matter effect and the ν_e appearance which are subdominant in the oscillation. Thus, the θ_{23} octant question requires good precision and high statistics measurement. Currently, global analysis of neutrino oscillation data yields a best fit value of θ_{23} in the upper octant, while the lower octant is slightly disfavored with $\Delta\chi^2 \geq 5.8(6.4)$ for normal (inverted) mass ordering while that for disfavoring maximal mixing is $\Delta\chi^2 = 7.8(8.5)$ [57].

The measurement of δ_{CP} is based on the sensitivity to the difference between oscillation probabilities of $\nu_\mu \to \nu_e$ and $\bar{\nu}_\mu \to \bar{\nu}_e$. At the time of writing this thesis, such measurement is mainly done at the long baseline accelerator experiments T2K and NOνa, while atmospheric data can also provide a small contribution. The global data is currently disfavoring the CP-conserving value $\delta_{CP} = 0$ with a quite notable $\Delta\chi^2 = 9.1(11.3)$ for NO (IO). The other CP-conserving value $\delta_{CP} = \pi$ is still allowed with $\Delta\chi^2 = 0.4$ in NO, while it is disfavored in the case of IO with $\Delta\chi^2 = 14.6$ [57].

For the time being, the question on the NMO has not been answered explicitly yet. Recent data from the current long-baseline accelerator experiments T2K and NOνa alone do not give any clear preference for the NMO yet ($\Delta\chi^2 \sim 0.4$ in favor of NO for each experiment). However, a combination of these two experiments gives a preference of IO with $\Delta\chi^2 \simeq 2.4$ due to the tension in δ_{CP} measurement which is observed in the NO case but not in the IO one. Nevertheless, after combining with reactor and atmospheric experiments, a preference for NO with $\Delta\chi \simeq 6,4$, corresponding to a significance of 2.5σ, is observed. This is mainly due to the atmospheric data which by themselves favor NO, and to the tension in the Δm^2_{31} measurement between the reactor and atmospheric experiments that appears for the case of IO but not for NO.

Together with the current active experiments, a new generation of experiments is being planned and built, which aims at resolving the abovementioned questions. The next generation of long-baseline experiments is being designed to be dedicated to the precise measurement of δ_{CP}. The two main projects in this line are DUNE (Deep Underground Neutrino Experiment) [59] in the USA and T2HK in Japan [60]. JUNO, the medium base-

line reactor experiment, is also in construction and it is expected to improve the precision on the oscillation parameters (Δm^2_{31}, θ_{12}, Δm^2_{21}) as well as to determine the NMO. The atmospheric experiments are also an appealing option for the determination of the NMO. Two next-generation atmospheric neutrino detectors are being built for this goal: ORCA (Oscillation Research with Cosmics in the Abyss) - the low energy branch of the KM3NeT telescopes [61] and PINGU (Precision IceCube Next Generation Upgrade) - a low-energy upgrade of the IceCube neutrino telescope [62]. Recently, the idea of enhancing the NMO sensitivity through a combination of next-generation atmospheric and reactor experiments has been proposed [63–65]. One such study for the combination of JUNO and ORCA is presented in Chap. 9 of this thesis.

1.3 Oscillation physics with atmospheric neutrinos

In this section, the underlying physics for the atmospheric neutrino experiments are presented. We first summarize the properties of the atmospheric neutrino fluxes in the energy range of interest for the oscillation studies ($\sim 1 - 100$ GeV). Then the phenomenology of the atmospheric neutrino oscillations is briefly discussed with the emphasis on the determination of the NMO. Finally, the neutrino interactions in the energy range 1-100 GeV are also presented.

1.3.1 Flux of atmospheric neutrinos

As mentioned in Sec. 1.1.2, atmospheric neutrinos are created in cosmic-ray induced air showers through the processes:

$$\pi^+/K^+ \to \mu^+ + \nu_\mu, \quad \pi^-/K^- \to \mu^- + \bar{\nu}_\mu. \tag{1.49}$$

$$\mu^+ \to e^+ + \nu_e + \bar{\nu}_\mu, \quad \mu^- \to e^- + \bar{\nu}_e + \nu_\mu. \tag{1.50}$$

In the energy range of interest here, the contribution of tau neutrinos is negligible as they are heavier than pions and kaons.

The production mechanisms of atmospheric neutrinos determines the characteristics of their fluxes, including the composition (in flavors and polarization) as well as the energy and angular spectra. These features have been discussed in the early of 1960s [66, 67]. The energy spectrum of atmospheric neutrinos follows a power law similar to the spectrum of primary cosmic-rays. The other main effect is the decays of muons, which causes a zenith dependence of the neutrino fluxes. Since the muon path lengths are typically longer

close to the horizon than the vertical directions, more neutrinos are produced from muon decays in the horizon compared to the vertical directions at the same energy. Other factors affecting the energy and angular dependence of atmospheric neutrinos are related to the decays of pions and kaons, the dependence of atmospheric density with altitude as well as the development of the air shower.

The flavor ratio $(\nu_e + \bar{\nu}_e)/(\nu_\mu + \bar{\nu}_\mu)$ is $1/2$ (as expected from the decay processes (1.49) and (1.50)) only at low energy (≤ 1 GeV). When going to higher energy, this ratio decreases because some of the energetic muons reach the ground before decaying, therefore reducing the proportion of ν_e. This effect is less pronounced for horizontal neutrinos than for vertical ones due to the aforementioned typically longer path length of muons close the horizon. In the high energy part of the spectrum, kaons also have other decay channels with the corresponding ratios:

$$K^+ \to \pi^0 + \mu^+ + \nu_\mu \ (3.4\%), \tag{1.51}$$

$$K^+ \to \pi^0 + e + \nu_e \ (5.1\%). \tag{1.52}$$

In the case of the second decay channel, only ν_e is produced from kaon decays. Thus the flavor ratio also depends on the ratio of pions to kaons in the air shower.

In the primary cosmic-rays and also in the air showers, the amount of matter is larger than the one of antimatter which causes more ν_e and ν_μ to be produced than $\bar{\nu}_e$ and $\bar{\nu}_\mu$; i.e the ratios are $\nu_e/\bar{\nu}_e > 1.0$ and $\nu_\mu/\bar{\nu}_\mu > 1.0$. While $\nu_e/\bar{\nu}_e \simeq 1.3$ and does not depend much on energy and zenith angle, the $\nu_\mu/\bar{\nu}_\mu$ ratio increases with energy and zenith angle. This is because the muon decays, which contribute more at low energy and in horizontal directions, tend to reduce the asymmetry between ν_μ and $\bar{\nu}_\mu$, as can be seen from Eq. (1.49) and (1.50).

The geomagnetic field of the Earth induces a shielding effect on the cosmic rays interacting with the atmosphere. This results differences of up to $\sim 10\%$ in the flux of neutrinos at different locations [68], in particular its zenith dependence, despite the very isotropic distribution of primary cosmic-ray. A slight dependence on the azimuth angle is also raised due to the geomagnetic field.

All these effects can be precisely accounted for thanks to detailed 3D simulation of atmospheric neutrino fluxes [68–70]. A very recent and popular simulation widely used is the one provided by Honda group in Ref. [68]. The sources of uncertainties in the numerical computation of atmospheric neutrino fluxes, which are mainly related to the primary fluxes and to the hadronic shower induced by the primary cosmic-ray interaction, are also discussed explicitly in Ref. [71]. These two results are important for evaluating the measured neutrino rates as well as for studying the effects of flux uncertainties on the sensitivity

of atmospheric neutrino experiments. They are used for the works in this thesis and the detail will be presented in Chap. 5 and Chap. 7.

1.3.2 Atmospheric neutrino oscillations

From the matter oscillations presented in Sec. 1.2.3, assuming $\frac{\Delta m^2_{21}}{\Delta m^2_{31}} \ll 1$ and $\sin^2\theta_{13} \ll 1$, one can compute the atmospheric oscillation probabilities to the first order expansion as (see also Ref. [72] for the derivation):

$$P(\nu_\mu \to \nu_e) \simeq \sin^2\theta_{23}\sin^2 2\theta^M_{13}\sin^2\left(\frac{\Delta^M m^2_{31} L}{4E_\nu}\right) \tag{1.53}$$

$$\begin{aligned} P(\nu_\mu \to \nu_\mu) \simeq 1 &- \sin^2 2\theta_{23}\cos^2\theta^M_{13}\sin^2\left(\frac{(\Delta m^2_{31} + \Delta^M m^2_{31})L}{8E_\nu} + \frac{V_{CC}L}{4}\right) \\ &- \sin^2 2\theta_{23}\sin^2\theta^M_{13}\sin^2\left(\frac{(\Delta m^2_{31} - \Delta^M m^2_{31})L}{8E_\nu} + \frac{V_{CC}L}{4}\right) \\ &- \sin^4\theta_{23}\sin^2 2\theta^M_{13}\sin^2\left(\frac{\Delta^M m^2_{31} L}{4E_\nu}\right). \end{aligned} \tag{1.54}$$

with the effective parameters defined as:

$$\Delta^M m^2_{31} = \xi \Delta m^2_{31}, \quad \sin^2 2\theta^M_{13} = \frac{\sin^2 2\theta_{13}}{\xi^2}, \tag{1.55}$$

$$\xi = \sqrt{\sin^2 2\theta_{13} + \left(\cos 2\theta_{13} - \frac{A_{CC}}{\Delta m^2_{31}}\right)^2}, \tag{1.56}$$

where $V_{CC} = \pm 2\sqrt{2} E G_F n_e$, $A_{CC} = 2EV_{CC}$. In these formulas, we have also assumed a constant electron density in matter for simplicity.

One can see that the $\nu_\mu \to \nu_e$ transition is enhanced in the MSW resonance region ($\sin^2\theta^M_{13} \to 1$). This channel also gives the sensitivity to the octant of θ_{23} thanks to the proportionality of the oscillation probability to $\sin^2\theta_{23}$. In the case of $\nu_\mu \to \nu_\mu$ transition, the first term in Eq. 1.54 is dominant in the non-MSW resonance region while the second term becomes dominant in the MSW resonance region. The third term is the only term that gives sensitivity to the θ_{23} octant but it is subdominant in both cases. Thus $\nu_\mu \to \nu_\mu$ would give a minor contribution to the sensitivity of θ_{23} octant.

As pointed out in Sec. 1.2.3 and as can also be seen from the above formulas, the MSW resonance occurs for neutrinos (antineutrinos) in the case of NO (IO) respectively and thus provides sensitivity for the determination of the NMO. From the MSW resonance

$\sin^2\theta_{23} \to 1$, one can derive the energy at which the resonance occurs as:

$$E_{res} = \frac{\Delta m^2_{31}\cos 2\theta_{13}}{2\sqrt{2}G_F n_e} \simeq 7 \text{ GeV} \left(\frac{4.5 \text{ g/cm}^3}{\rho}\right)\left(\frac{\Delta m^2_{31}}{2.4\times10^{-3} \text{ eV}^2}\right)\cos 2\theta_{13}, \tag{1.57}$$

where we adopt the approximation for the electron density such that $n_e = \frac{Z}{A}\frac{\rho}{m_p} \simeq 0.5\frac{\rho}{m_p}$ with the matter density ρ, the proton mass m_p and the proton-to-nucleon ratio Z/A which is generally close to 0.5 in the case of the Earth. The Earth's core density is $\sim$ 12 g/cm^3 while that of the mantle is ~ 4.5 g/cm^3. These densities correspond to a resonance energy of 2.5 and 7 GeV respectively, which are in the energy range of atmospheric neutrinos.

Another resonance also occurs in the case of atmospheric neutrinos, which is called parametric enhancement. In this effect, the transition probability becomes maximal due to a match of the matter density variation with the phase of neutrino oscillations [73,74]. This means the resonance can happen even far from the MSW region. This effect turns out to be present for neutrinos that cross the mantle-core-mantle density profile corresponding to the cosine zenith angle range: $-1 \leq \cos\theta_z \leq -0.84$.

1.3.3 Neutrino interactions in the energy range 1-100 GeV

In the energy range 1-100 GeV, neutrino interactions are dominated by the scattering on nuclei via CC (by exchanging $W^\pm$ bosons) or NC (by exchanging Z bosons) interactions:

$$\text{CC}: \overset{(-)}{\nu} + \text{nucleon} \to l^\mp + H; \tag{1.58}$$

$$\text{NC}: \overset{(-)}{\nu} + \text{nucleon} \to \overset{(-)}{\nu} + H; \tag{1.59}$$

where the two observable products are a lepton (in the case of CC interaction) and the final hadronic state H. In the high energy region, the lepton direction is almost aligned with that of neutrino so that it can be used as an estimator for the neutrino direction. The neutrino energy can be estimated from the reconstructed energy of the produced lepton and hadronic states $E_\nu = E_l + E_H$. We also define the inelasticity y (or Bjorken-y) as:

$$y = 1 - \frac{E_l}{E_\nu} = \frac{E_H}{E_\nu}, \tag{1.60}$$

which corresponds to the fraction of neutrino energy transferred to the hadronic system in the interaction.

Based on the hadronic products of the interactions, one can also categorize the neutrino interaction as follows:

- *Elastic and quasi-elastic scattering (QE)*: the hadronic products contain one or multiple nucleons(s) from the target. The term elastic is for NC while quasi-elastic is for CC (CCQE) due to the production of charged leptons.
- *Resonant production (RES)*: this type of interaction creates a baryonic resonance state which then decays into mesonic final states including nucleons and mesons (mainly pion and kaons).
- Deep inelastic scattering (DIS): the energy transferred is high enough such that it breaks the nucleons and produces hadronic showers.

Fig. 1.6 shows the total neutrino CC cross-sections as well as the contribution from three types of interaction: QE, RES, and DIS. The neutrino cross-section is about two times larger than the one for antineutrino. The QE is only dominant in the sub-GeV domains while RES is the main contribution in the energy range 1-10 GeV. Above 10 GeV, QE, and RES cross-sections decrease while DIS increases and becomes the dominant process. The detection of the signal from neutrino interactions will be discussed explicitly in the case of the ORCA detector in the next chapter.

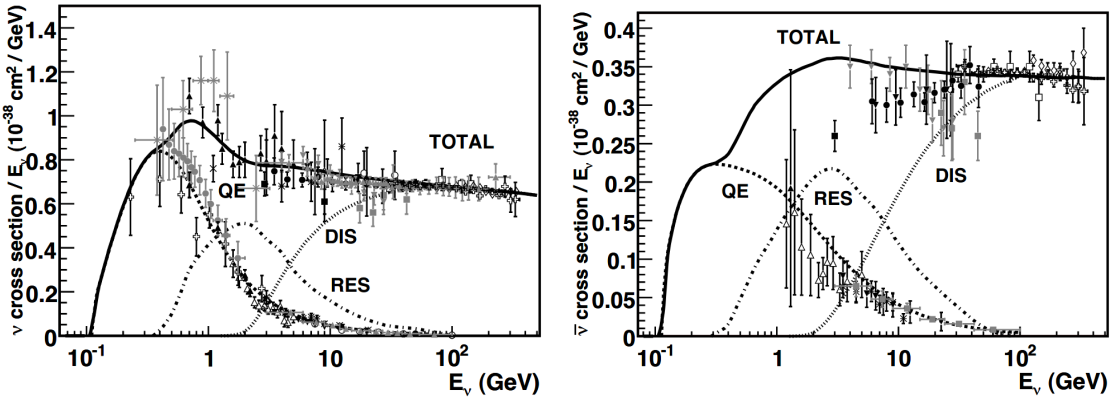

Figure 1.6: Total neutrino and antineutrino per nucleon CC cross-sections for an isoscalar target. Figure taken from Ref. [75].

Chapter 2

The KM3NeT/ORCA detector

Contents

In 1960, M. A. Markov proposed the idea of detecting high energy atmospheric neutrinos using the Cherenkov effect with photosensitive devices installed deep underwater [67, 76]. The proposal was meant for serving the studies on neutrinos properties. In the same year, K. Greisen also discussed the detection of neutrinos from cosmic sources with the suggestion of using a large underground water-Cherenkov detector surrounded by photomultipliers. The advantage of such approaches is to achieve an efficient neutrino detection due to the very large target volume and the high sensitivity to the signal of Cherenkov light induced by the relativistic propagation in a transparent medium (water, or ice) of charged particles produced by a neutrino interaction in or around the detector. Pioneering underground water-Cherenkov experiments have been built, including the currently operating Super-Kamiokande detector [55]. In addition, neutrino telescopes instrumented huge volumes of naturally abundant ice or water have also been deployed, with the main purpose of detecting and studying high-energy astrophysical neutrinos: ANTARES [77], Baikal [78], and IceCube [79].

In this context, the KM3NeT Collaboration is building a set of next-generation water-Cherenkov neutrino telescopes in the depth of the Mediterranean Sea. The design and technology benefit from the experience acquired in the successful deployment of the first deep-sea neutrino telescope ANTARES [77]. The KM3NeT telescopes consist of two tridimensional arrays of photomultiplier tubes (PMT), that will be deployed on distinct sites: ARCA and ORCA (for Astroparticle and Oscillation Research with Cosmics in the Abyss, respectively). ARCA is a gigaton-scale detector that will mainly focus on neutrino astronomy in the TeV–PeV energy range. ORCA is a denser and smaller array (Mton-scale) optimized for oscillation physics with atmospheric neutrinos at energies above 1 GeV.

This chapter describes the physics principles and technical design of the KM3NeT project, with a focus on the ORCA detector, the main subject of this thesis. Sec. 2.1 presents the detection principles of neutrino events in deep-sea Cherenkov telescopes, also discussing the different sources of background. Then, Sec. 2.2 describes the KM3NeT design and technology. Finally, the science prospects of ORCA are summarized in Sec. 2.4.

2.1 Neutrino detection in water-Cherenkov detectors

2.1.1 Cherenkov radiation

When a charged particle moves through a dielectric medium, it polarizes the medium along its trajectory and creates a time-dependent dipole field which emits in a spherical wave with the phase velocity of light in the medium c/n, where n is the refraction index, c is

the light velocity in vacuum. If the particle velocity is greater than the light velocity in the medium, these spherical wavelets can interfere constructively and form a coherent wavefront propagating at a well-defined angle with respect to the direction of the particle. This emission, dubbed as Cherenkov radiation [80], is illustrated in Fig. 2.1.

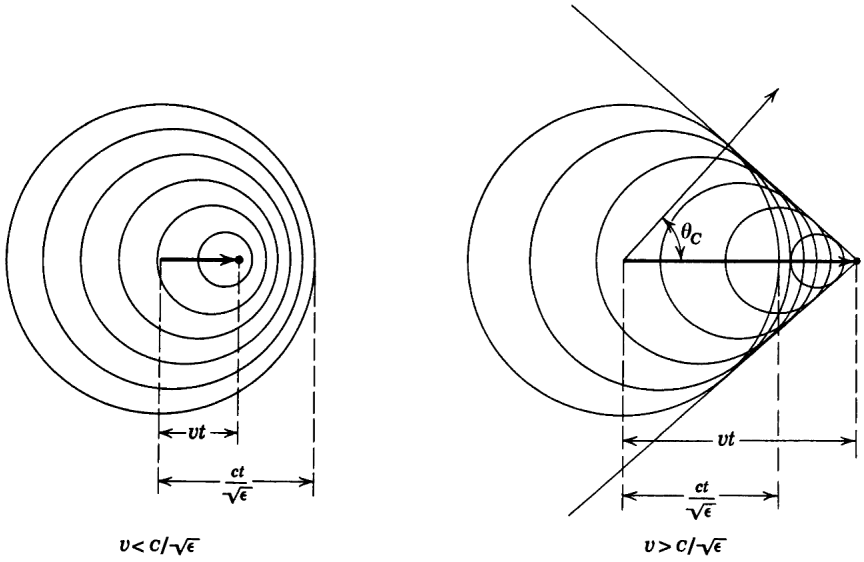

Figure 2.1: An illustration of Cherenkov radiation. The Cherenkov radiation is formed and emitted in the Cherenkov angle θ_c when a particle travels faster than the velocity of light in medium $c/\sqrt{\epsilon}$ (where ϵ is the dielectric constant which relates to the refractive index as $n = \sqrt{\epsilon}$). Figure taken from Ref. [81].

From this figure, one can derive the Cherenkov angle, defined as the angle between the particle trajectory and the direction of light emission:

$$\cos\theta_c = \frac{1}{\beta n}, \tag{2.1}$$

where $\beta = v/c$ is the ratio of particle speed v to light speed c. For ultra-relativistic particles, which is usually the case for secondary particles emitted in the interaction of neutrinos with energies in the GeV to PeV region, as typically detected by the KM3NeT detectors, one can approximate $\beta \simeq 1$. With the seawater refractive index being $n \simeq 1.35$, the Cherenkov angle is computed as $\theta_c \simeq 42°$, independent of the particle energy. Seawater is transparent in the ultraviolet to visible band from 300 nm - 600 nm, which is also the detection band of Cherenkov detection. In this band, a particle with a unit charge can yield about 340 photons per cm of path length.

2.1.2 Neutrino event signatures

As discussed in Sec. 1.3.3, neutrino interactions in the energy range relevant for ORCA include quasi-elastic (QE), resonant (RES) and Deep Inelastic Scattering (DIS) processes. They can be classified into 4 interaction channels depending on the weak-interaction process and neutrino flavor: NC, ν_e CC, ν_μ CC, ν_τ CC as summarised in Fig. 2.2. The light signatures for each channel are described as follows:

- **NC**: The NC interaction is flavor-insensitive and the only detectable light signal comes from the hadronic shower. The particles in a hadronic shower usually have a small interaction or decay length which results in a typical $\lesssim 10$ m extension of the shower. The associated light signatures thus mimic a cascade emission from a single point. Such kind of event topology is called ***shower-like*** (or *shower* for short, or also called sometimes *cascades*). It is worth noticing that a hadronic shower is produced in all 4 mentioned channels and it carries the inelastic fraction y (also called Bjorken-y) of the neutrino energy.

- $\nu_\mathbf{e}$ **CC**: $e^\pm$ have a short (~ 36 m) radiation length in water [82] so they cannot travel far and lose their energy rapidly via a cascade of electromagnetic processes including Bremstrahlung:

  $$e^- \rightarrow e^- + \gamma \tag{2.2}$$

  and pair production:

  $$\gamma \rightarrow e^+ + e^-. \tag{2.3}$$

  This produces an electromagnetic shower, and the corresponding events are also shower-like. The electromagnetic showers are usually a few meters extension but yield $\sim$ 20% times more light per unit energy in the few-GeV range as compared to hadronic showers [83].

- ν_μ **CC**: This interaction channel produces a charged (anti)muon, $\mu^\pm$, a long-lived particle which can travel a significant distance and will produce a ***track-like*** (or *track*) signature in the detector. For the energies up to $\sim$10 GeV, muons can be approximated as *minimum ionizing particles*. In this regime, most of the energy losses occur through ionization with a rate of about 4 GeV per meter of track length, independent of the muon energy. Therefore, the measured track length of the muon can also be used as an energy proxy for estimating its energy.

- ν_τ **CC**: The $\tau^\pm$ have the short lifetime of about 2.9×10^{-13}s and mostly decay right after the production. Most of the tau decays produce hadronic showers ($\sim$65%) and sometimes electromagnetic showers ($\sim$17%) which lead to the dominance of shower-

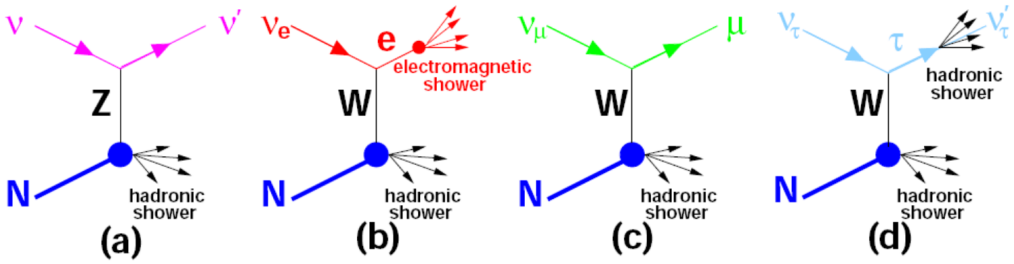

Figure 2.2: Summary of DIS neutrino event classes in neutrino telescopes: (a) NC, (b) ν_e CC, (c) ν_μ CC, (d) ν_τ CC. In the case of CCQE and RES, the hadronic component might include one or multiple nucleons or pions. Figure taken from Ref. [84].

like signals in this channel. Nevertheless, about 17% can produce $\mu^\pm$ which results in the track-like signature.

2.1.3 Optical Background in the deep-sea

Apart from the neutrino signals, water-Cherenkov detectors in the deep-sea are also sensitive to multiple sources of background light: radioactive decay, bioluminescence, dark pulses, and atmospheric muons. They are described in this subsection.

The dominant source of radioactivity in the deep-sea is the potassium isotope ^{40}K, which is naturally present at ∼0.04% in seawater. The ^{40}K radioactive decays happen through β^- process:

$$^{40}\mathrm{K} \rightarrow {}^{40}\mathrm{Ca} + \bar{\nu}_e + e^- \tag{2.4}$$

or electron capture:

$$^{40}\mathrm{K} + e^- \rightarrow {}^{40}\mathrm{Ar}^* + \bar{\nu}_e \rightarrow {}^{40}\mathrm{Ar} + \bar{\nu}_e + \gamma \tag{2.5}$$

In the β decay, the energy of the electrons produced is about 1 MeV, which is already enough for generating Cherenkov light. In the case of electron capture, the photons emitted from the excited states ^{40}Ar* have an energy of 1.460 MeV which is enough to produce electrons via Compton scattering. These electrons in turn can be energetic enough to emit Cherenkov radiation [85].

Bioluminescence is another important optical background in the deep sea, which is continuously produced by some species of living organisms [86]. The light is normally emitted in the blue or green visible wavelength to which the seawater is transparent. These

emissions are naturally not time-correlated on a nano-second basis. Their signature is a slowly time-varying rate extending over a large part of the detector. Also observed are bright bursts that can increase significantly the local rate on a DOM and last up to several seconds. Bioluminescent activity is also correlated with the sea current and has seasonal variations [87, 88].

Since the deep-sea neutrino telescopes use PMTs for the detection of the Cherenkov radiation, they are also affected by the dark pulses which are internal signals recorded by the PMTs without any external light sources. This type of noise can be generated by spontaneous thermal emission of electrons in PMT's photocathodes and dynodes, or radioactive decay inside the PMT structure [89].

Atmospheric muons are produced in cosmic-ray air showers alongside neutrinos. Unlike neutrinos, they cannot traverse the Earth and can only reach the detector from above. Even so, most of the down-going atmospheric muons are absorbed in the water or the surrounding rock before reaching the deep-sea detector and only observed in the detector if their energies are $\sim$ 1 TeV and above, hence creating track-like signals. Even though a large part of the muon flux is absorbed before reaching the detector, the abundance of atmospheric muons is such that their rates in the detector still dominate those of neutrinos by a factor of $\sim 10^4$.

To achieve data samples with an acceptable neutrino purity for physics analyses, a performant rejection of these backgrounds is required. The first three mentioned types of background are mostly uncorrelated in time and space, and thus can be reduced significantly using trigger algorithms based on suitable space and time causality conditions which will be described in Sec. 2.3. The Additional rejection methods include the vetos applied on the PMTs if the baseline rate is too high (e.g. due to episodes of high bioluminescence), and the fine-tuning of the PMT threshold which specifically aims at reducing the dark pulses.

Atmospheric muons are a physical background whose signature in the detector is very close to the one associated to some neutrino event classes, therefore they cannot be efficiently filtered out at the trigger level. One way to remove atmospheric muons at the analysis level is to introduce a cut on the reconstructed direction in order to reject all down-going muons that would come from the atmosphere above the detector. Nevertheless, this cut cannot reject the down-going atmospheric muons that are misreconstructed as up-going. Additional cuts on the reconstruction quality combined with machine learning-based classifiers are necessary to sufficiently reject the atmospheric muon background. The efficiency of these suppression methods will be briefly discussed in Chap. 3, 8, and 10.

2.2 The KM3NeT/ORCA detector design and technology

As mentioned previously, the KM3NeT project involves two detectors, ORCA and ARCA, searching for neutrinos in different energy ranges. Nevertheless, both are built and operated with the same technology which aims at the detection of Cherenkov light induced by charged particles produced by neutrino interactions in water. This section presents a brief description of the main technological components of the KM3NeT detectors.

2.2.1 Digital Optical Modules

The main detection element of the KM3NeT telescopes is the Digital Optical Module (DOM). A DOM consists in a spherical pressure-resistance glass of 43cm diameter housing 31 3-inch Hamamatsu PMTs and related electronics. The PMTs are distributed over the sphere, pointing towards all directions (except vertically upwards) to obtain a close to uniform angular acceptance. More specifically, on each DOM, 2 rings of 6 equally spaced PMTs point to the upper hemisphere while the remaining 19 PMTs are distributed on 3 other rings of 6 PMTs, plus one vertically downwards, in the lower hemisphere. A reflector ring is installed around the bulb of each PMT to increase the photon collection efficiency. The space between the PMT cathodes, reflector rings, and glass sphere is also filled with an optical gel to ensure good optical contact. A DOM and a PMT with its reflector ring are shown in Fig. 2.3.

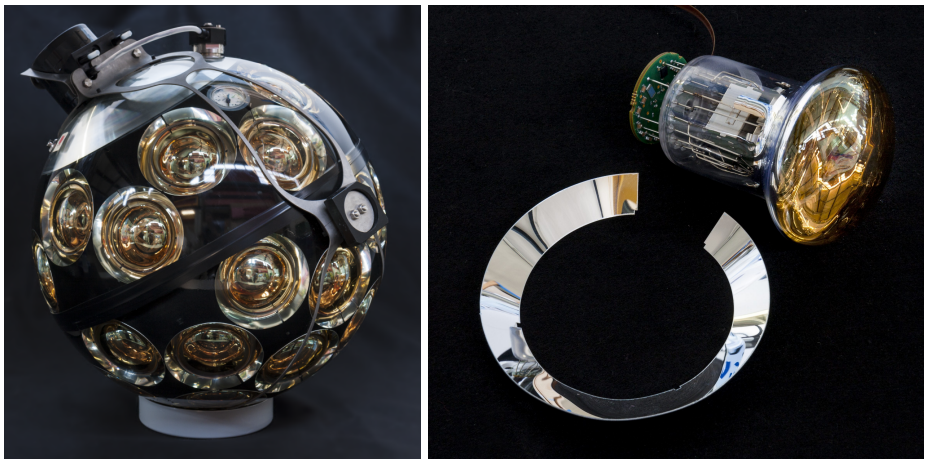

Figure 2.3: KM3NeT DOM (left) and PMT with its reflector ring (right). Pictures taken from Ref. [90].

The design of the DOMs is one of the signature technological features of the KM3NeT project in comparison with other, past and existing Cherenkov neutrino telescopes (e.g ANTARES, IceCube, and Baikal-GVD), which have used optical modules with one single large PMT. The multi-PMTs design of KM3NeT is advantageous in several aspects [91]. On

the one hand, this design yields a larger photocathode area per optical module: the photocathode area of one KM3NeT DOM is about three times larger than that of one ANTARES optical module, while the cost per unit of photocathode area is reduced. On the other hand, the uniform distribution of PMTs on the DOMs helps improve the angular acceptance to approximately 4π coverage while only around 2π was reached with single PMT modules. The segmentation of the photocathode area also helps preserve the directional information of detected photons as well as better identifying local coincidences on the same DOM. These features are important for event reconstruction and background suppression.

This multi-PMT approach is now being considered by other future Cherenkov detectors, including the upgrade of the IceCube detector [92] and the future Hyper-Kamiokande experiment [93].

2.2.2 The Detection Units

In the deep sea, DOMs are installed on vertical structures called Detection Units (DU). Each DU comprises two parallel Dyneema®[1] ropes on which the DOMs are attached using a titanium collar. The ropes are attached to an anchor laid on the sedbed, while at the top, an additional buoy is used to keep the DU straight close to the vertical. Each DU supports 18 DOMs.

For ORCA and ARCA, the distribution of DUs on the seafloor and of DOMs along the DUs are different, which leads to the different geometries that are suitable for the target energy range of the detector. ARCA, which aims at detecting high-energy astrophysical neutrinos in the TeV–PeV energy range, has a vertical spacing between DOMs of ~ 36 m and a horizontal spacing between DUs of ~ 95 m. In the case of ORCA, the lower targeted neutrino energy range (at the GeV scale) leads to a denser distribution which is ~ 20 m inter-DU and ~ 9 m inter-DOM.

The ORCA detector, the subject of this thesis, will comprise 115 DUs whose layout is illustrated in Fig. 2.4, together with the related seabed infrastructure. The DUs are connected to two main electro-optical cables (MEOCs) through five nodes. Each node connects 6 chains of 4 DUs. The MEOCs runs from the shore to the detector site in order to supply power for the detector as well as transmit data from each individual DOM to the shore station. A Calibration Unit will also be installed at the detector site, comprising a Base with calibration instruments and an Instrumented Unit to monitor the environmental parameters around the detector.

[1] Dyneema® is an UHMwPE (Ultra High Molecular weight Polyethylene) or HMPE (High Modulus Polyethylene) fiber which is particularly strong and light.

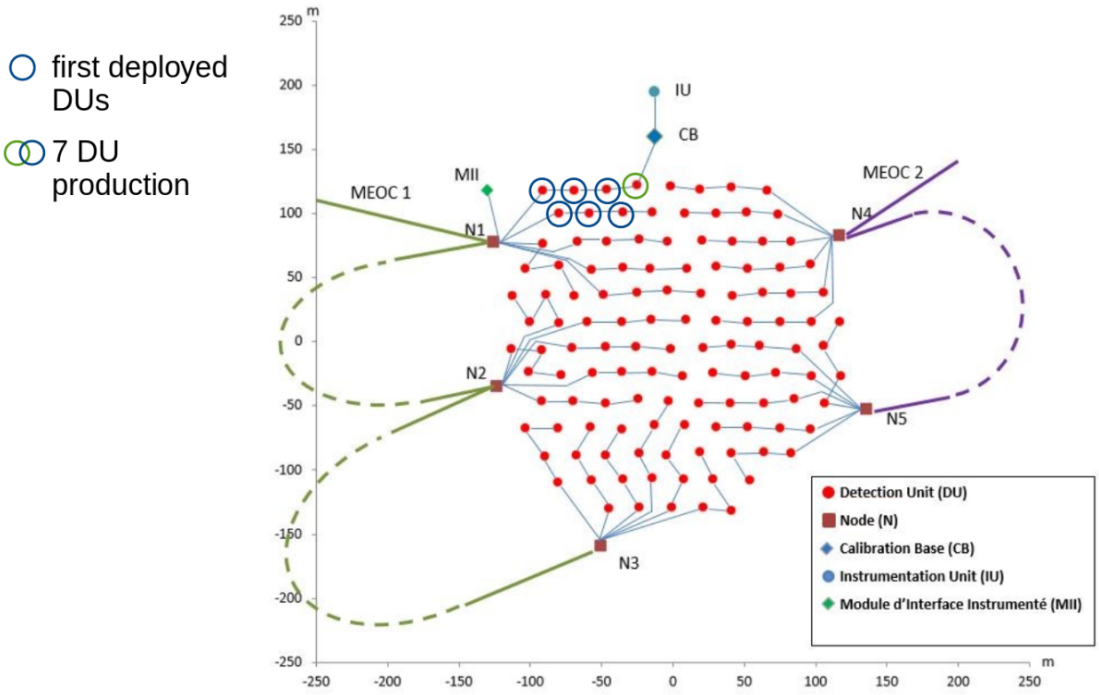

Figure 2.4: The planned layout of the ORCA detector. The figure also shows the 6 DUs which are currently in operation (with blue circles) and the ORCA7 sub-array of 7 DUs (with blue and green circles) that will be used for sensitivity studies presented later in this manuscript. The figure is taken from Ref. [94].

2.2.3 Calibration

Achieving an accurate reconstruction of neutrino events requires a precise knowledge on the evolution of the data-taking conditions, which include the optical properties of the seawater, DOMs, PMTs as well as the timing and positioning of optical modules. In order to achieve the desired reconstruction performances, the timing accuracy has to be at ns level [95] and about 10cm is necessary for position accuracy [96].

On each DOM, multiple calibration instruments are installed. They include the sensors for monitoring the pressure, temperature, and humidity; a LED beacon that can send signals to neighbouring DOMs for time and position calibration; a compass and tilt meter for monitoring the orientation of the DOM; and a digital acoustic receiver used for acoustic positioning.

A Calibration Unit, which comprises a Calibration Base and Instrumentation Unit, will be installed in the vicinity of the ORCA array as shown in Fig. 2.4 and will also participate in the time and position calibration of the detector elements. The Calibration Base hosts a Laser Beacon, a hydrophone and an acoustic emitter. The Laser Beacon is meant to illuminate the whole array of DUs and will be used for inter-DU time calibration, to complement the inter-DOM calibration performed with the LED beacons installed on each DOM. Additionally, it can also be used for measuring water transparency. The hydrophone and acoustic emitter are part of the long-baseline acoustic positioning system of the detector. The Instrumentation Unit is a recoverable inductive line supporting instruments used for the monitoring of water properties, which serves in particular to compute the speed of sound in water, an important factor for acoustic positioning calibration.

Apart from the aforementioned calibration instruments, the data taken by the DOMs themselves can offer a method of intrinsic detector calibration. Single decays of ^{40}K occurring in the vicinity of the DOMs can produce a genuine coincidence between signals on different PMTs in a time window of $\sim$25 ns [97]. At this level of coincidence, the ^{40}K decay is the dominant rate, which allows an easy extraction of this signal from the data. Additionally, the ^{40}K concentration in seawater is very stable and can be precisely simulated. Therefore, the detected ^{40}K signals are sensitive to water optical parameters and individual PMT efficiencies. Furthermore, the ^{40}K coincidences on PMTs of the same DOMs can be used for determining the relative time offset between PMTs in a DOM and their time spreads as already demonstrated in ANTARES [85]. Another method including the use of atmospheric muon tracks for calibrating the inter-DOMs time offset can also be performed. These possibilities are discussed explicitly in Ref. [97].

2.3 Data processing and event triggers

2.3.1 Digital signal and data transmission

When a photon hits a PMT on one of the ORCA DOMs, it can create a photoelectron (p.e) release from a photocathode due to the photoelectric effect. This p.e is then accelerated to the series of dynodes thanks to a high voltage applied. More electrons are released when a dynode is hit and thus an electron cascade is formed. A voltage pulse is created when the electron cascade hits the final anode and this signal is recorded if it exceeds a certain threshold which is normally set to be 30% of the amplitude expected from a single initial p.e. The registered signal, called ***hit***, includes the PMT identifier, the start time of the pulse, and the time-over-threshold (ToT), which is related to the total charge of the pulse. These bare PMT hits are also called ***L0 (level zero) hits***.

The KM3NeT project follows the so-called 'all data to shore' approach in which the data processing and filtering are performed at the shore station. This helps minimize the amount and complexity of the data acquisition system installed in the deep-sea. Following such an approach, all L0 hits from DOMs are transferred to the shore station via the optical fibers running along the DUs. In each group of 4 chained DUs (72 DOMs in total), the signals from each DOM are assigned a different wavelength so that they can be transmitted together over a single fiber. The transferred data is chunked in time slices of 100 ms, which results in a data transfer rate of $\sim$25 Gb/s for the full detector.

Since most of the optical background hits are uncorrelated in space and time, it is necessary to define higher-level hits, called L1 and L2 hits, for the sake of event triggering. They are so-called ***L1 and L2 hits***. An L1 hit is defined if two L0 hits on the same DOM are coincident within a short time window of < 10 ns. L2 hits also follow the L1 condition but with an additional constrain that the two L0 hits have to be on two separate PMTs with the directions forming an open-angle $< 90^{\circ}$.

At the moment, L0 and L2 coincidences are used for event triggering. Instead of writing full L0 data, only writing L0 when the trigger conditions are met can reduce the amount of data written by a factor of $\sim 10^3 - 10^5$. The next section will present more about the event triggers used in ORCA.

2.3.2 Event triggers in ORCA

A trigger algorithm has been developed to target clusters of hits that are causally connected. Once the trigger is activated, all of the hits in the detector within a timeslice are

saved and such a snapshot is called an 'event'. Those triggered events are likely to be physical and will be reconstructed for analysis. The timeslice chosen for saving an event normally spans from the first to the last triggered hit with an additional expanding margin to make sure all of the related hits are recorded. This margin is safely chosen as $\sim 1\ \mu s$ which is the time required for a photon to traverse the detector.

At the moment, it exists three trigger algorithms for ORCA namely: ***3DMuon, 3DShower,*** and, ***MXShower***. The first two algorithms, also called 3D triggers, cover the two expected topologies of events which are long muon tracks (track-like) with 3DMuon and spherical emission from a single point (shower-like) with 3DShower. MXShower is designed in addition to the 3D triggers for lowering the energy threshold to target a few GeV events. The criteria for these triggers are presented as follows:

- **3DMuon:** This trigger algorithm scans over 200 equally sampled test directions and per each test direction, it looks for at least 4 causally connected L2 hits on different DOMs within a cylinder centered on the test direction and having the predefined radius $R_{3\mathrm{D}\mu}$. Assuming emission from track-like hypothesis, the causality condition for the two hits reads

$$c|t_i - t_j| < (z_i - z_j) + n \sin\theta_c \sqrt{(x_i - x_j)^2 + (y_i - y_j)^2} + c\delta t, \tag{2.6}$$

  where (x_i, y_i, z_i, t_i) is the coordinate of the hit, θ_c is the Cherenkov angle, n is the refractive index. The z-axis is aligned with the defined cylinder. δt is the additional tolerance time window which is currently set to 10 ns. This is to accommodate the uncertainties in time and position calibration.

- **3DShower:** This trigger algorithm assumes the spherical emission from a single point. It looks for at least 3 causally connected L2 hits on different DOMs of the maximal predefined distance $D_{3\mathrm{DSh}}$. The causality condition is as follows:

$$c|t_i - t_j| < n|\vec{r}_i - \vec{r}_j| + c\delta t, \tag{2.7}$$

  where $\vec{r}_i$ is the position vector of the hit.

- **MXShower:** The few GeV neutrinos often can not produce even two L2 coincidences. Thus the MXShower algorithm is used in addition with the two above 3D triggers in order to keep the faint events from few GeV neutrinos. The algorithm starts with 1 seed of L2 hit and then looks for the around L0 hits that satisfy the 3DShower causality condition in Eq. 2.7.

The trigger parameters; including the number of coincidence hit, $R_{3\mathrm{D}\mu}$, $D_{3\mathrm{DSh}}$, or δt; are optimized such that it produces the maximal efficiency to a neutrino signal while still

fast enough for real-time application. The current requirement is that after the trigger, the rate inferred by the pure noise should not exceed the rate from atmospheric muons. Such optimization is reported in Ref. [61] and Ref. [94].

2.4 Physics with the ORCA detector

The first DU of the ORCA detector has been deployed in September 2017. Then 4 DUs have been installed in July 2019. Since the sea operation end of January 2020, 2 more DUs were successfully deployed and the detector is currently operating with 6 DUs. ORCA will grow quickly in size and targeting a rich science program. This section summarizes the notable physics objectives of the ORCA detector.

The main physics target of ORCA is to determine the unresolved question on the neutrino mass ordering. As described in Sec. 1.3, matter effects result in a different pattern of atmospheric neutrinos traversing the Earth with different NMO scenarios and thus help to solve the NMO. ORCA, which is designed for detecting atmospheric neutrinos above $\sim$ 1 GeV, relies on such effects for the determination of NMO. The sensitivity to the atmospheric neutrino oscillation also helps ORCA to provide the measurement on θ_{23} and Δm^2_{31}, one of the currently least well-measured oscillation parameters in the neutrino sector. Another important subject is the detection of tau appearance, the phenomena in which the atmospheric ν_μ oscillates into ν_τ with a maximum around 24 GeV (well above ORCA energy threshold). This detection helps to test the unitarity of the PMNS matrix which is currently only tested at the 20%-40% level. These studies are reported in Ref. [98].

ORCA also offers sensitivity to the extensions of the standard 3ν oscillation framework including non-standard interactions (NSI) and the sterile neutrino. The effects of these models are also enhanced thanks to the matter effects experienced by atmospheric neutrinos during their passage through the Earth. This is discussed in Ref. [99] and Ref. [100] which provides competitive results compared to the leading experiments in the field.

Other topics comprise Dark Matter and Earth tomography. A theoretically well-motivated dark matter candidate so-called Weakly Interacting Massive Particle (WIMP) could be captured in the Sun and then can decay or annihilate into standard model particles including also neutrino fluxes detectable by ORCA [101]. Since ORCA is sensitive to the Earth matter effect on atmospheric neutrinos, it can also provide tomographic information of the Earth, particularly the electron density and the proton-to-nucleon (Z/A) ratio [102].

Furthermore, ORCA can also contribute to astrophysics studies. One such study is the detection of core-collapse supernova (CCSN). Even though the CCSN neutrino energy is at

the MeV scale (below the ORCA energy threshold), the burst of such neutrinos from CCSN reaching the detector can cause a population of coincidences in excess over the background expectation, taking into account all the DOMs in the detector [103]. In addition, the potential of ORCA toward the search for low energy astrophysical neutrinos is also discussed in Ref. [104] and Ref. [105].

This thesis works are dedicated to oscillation physics with ORCA which focuses on the determination of NMO and oscillation parameter measurement. The physical results are reported in Part III of the thesis. The potential of ORCA to the determination of NMO and oscillation parameter measurement is presented in Chap. 8. Chap. 9 discusses a combination of ORCA and JUNO, a reactor neutrino experiment in construction, which enhances the NMO determination. Finally, Chap. 10 shows the first results on oscillation measurement with the very first data from the current 6 DUs of ORCA.

Part II

Neutrino simulation with KM3NeT/ORCA

Chapter 3

Neutrino simulation with KM3NeT/ORCA

Contents

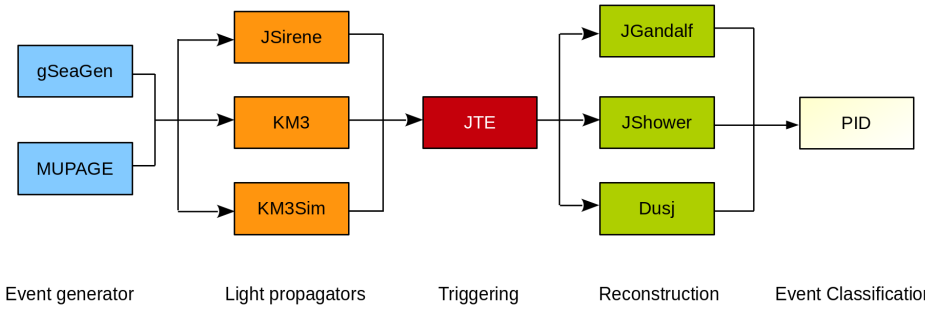

Figure 3.1: Flowchart for the neutrino simulation chain. Labels in the blocks indicate the used softwares.

This chapter presents the Monte Carlo (MC) simulation chain for characterizing the detector response to the incident neutrino events. This MC scheme is adapted from the ANTARES one which is described in Ref. [106]. The simulation consists of multiple stages which are illustrated in the flowchart of Fig. 3.1. First, neutrino interactions are simulated by an event generator described in Sec. 3.1. The output of the generator is the list of particles that emerge from the neutrino interaction, with their kinematical properties. They will be used as input for the light propagators in which the Cherenkov light induced by the propagating charged particles is simulated. Sec. 3.2 describes in detail the light simulation packages developed within the KM3NeT Collaboration. After the light simulation stage, the events that produce at least 1 hit on one PMT are stored. Then, the PMT response, readout and triggering are simulated by a custom KM3NeT software (JTE, or JTriggerEfficiency). From the detected signals, the energy and direction of the events are reconstructed with KM3NeT reconstruction softwares. Finally, a classifier (or particle identification - PID) algorithm is used for the determination of event topologies (shower-like or track-like). A brief description of the triggering, reconstruction, and PID is provided in Sec. 3.3.

This simulation chain has served to produce the MC event samples that are currently used in the collaboration to perform physics analyses with ORCA, which are described in Sec. 3.4. During my PhD, I have also contributed to the production of additional MC samples that were tailored for two specific studies, that will be described respectively in Chap. 4 (production of a sample of high-energy neutrino events in a subarray configuration of ORCA) and Chap. 7 (production of samples with different PMT efficiencies to study the impact on ORCA systematics).

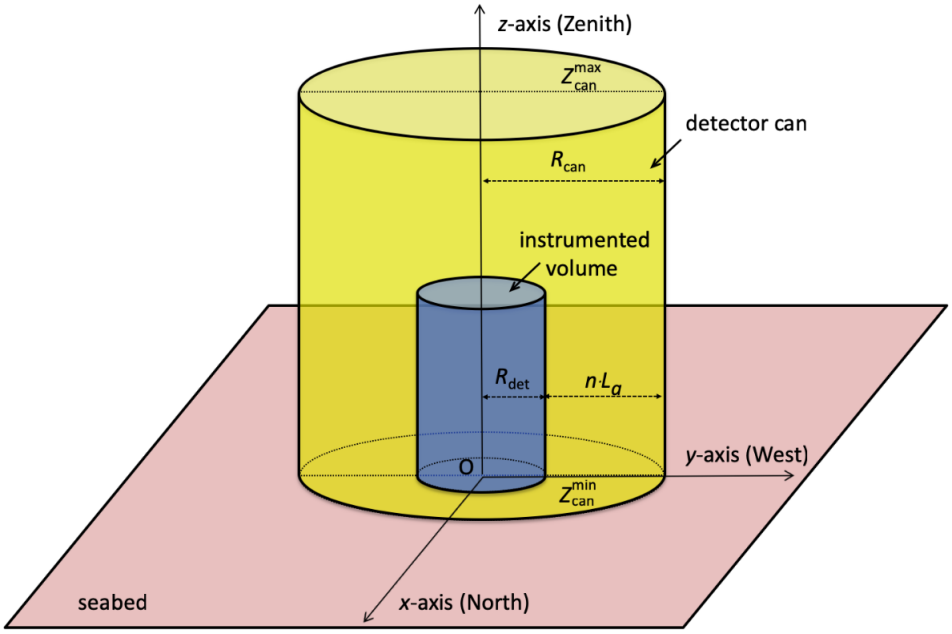

Figure 3.2: Geometry of the can definition in gSeaGen. The detector can is defined with the sizes Z_{can}^{min}, Z_{can}^{max} and R_{can}. The radius R_{can} is extended from the instrumented volume with the radius R_{det} by n times the light absorption length L_a. Figure taken from Ref. [107]

3.1 Event generators

The generation of neutrino interactions in seawater is performed using gSeaGen [107], a GENIE [108]-based code developed within the KM3NeT collaboration.

In particular, gSeaGen defines a cylindrical *detector can* surrounding the instrumented volume, which is in principle large enough to contain all events that are susceptible to emit Cherenkov light that will reach the detector. Fig. 3.2 illustrates a default geometry configuration of the detector can. From the input detector geometry file, gSeaGen constructs a cylindrical instrumented volume (in blue) which contains all PMTs and is centered at the gravity center of the detector. The detector can (in yellow) is then created as an extension of the instrumented volume, with the bottom surface lying exactly at the sea bed while the height and radius are a multiple of the absorption length ($L_a \sim 70$ m [109, 110]). It should be noted that the can dimensions presented here can be completely defined by the user. The choice of the can size for a given production should be large enough to include all events that might produce detectable Cherenkov light, ie. light that will reach the instrumented volume. One specific example of choice of can dimension will be discussed in Chap. 3.

Based on this can, the *interaction volume* is defined which contains neutrino interactions simulated by GENIE. The interaction products as well as their kinematic profiles then

can be recorded for the next simulation stages.

As described in Sec. 2.1.2, neutrino interactions will produce different types of event topologies (track-like and shower-like) which results in different simulation needs, reflected in the introduction of the so-called *interaction volume*. For ν_e and NC interactions which produce shower-like events, the interaction volume coincides with the detector can. All events are generated homogeneously within the can and only the events that generate charged particles reaching the instrumented volume will be stored after the simulation. In the case of ν_μ CC and ν_τ CC, the interactions can produce long muon tracks which can reach the detector even from very large distances, depending on their energy. Thus, the interaction volume for these interaction types no longer coincides with the detector can, but is further extended in all directions by a length that corresponds to the maximum muon range in material (water and rock), evaluated at the highest simulated muon energy. The interactions are generated homogeneously in this extended volume and the events producing muons that reach the detector are kept.

Another event generator worth mentioning here is MUPAGE [111, 112] which is an atmospheric muon bundle generator developed specifically for water/ice-based neutrino telescope. It uses the parametrization model extracted from the full Monte Carlo simulation of muon bundles generated from cosmic ray air showers. The code is used for the separate study of background contamination of atmospheric muons which is not relevant for the Monte Carlo-based study presented in Chap. 4 and 7 that in fact focus on the neutrino detection. This is due to the fact that the muon contamination can be negligible after the selection cuts which will be mentioned later for specific analyses in this work.

3.2 Light and secondaries propagation

The event generator gSeaGen gives output all of the events that create secondary particles reaching the detector can. It also provides kinematic information on all products of the interactions. KM3NeT collaboration has developed packages for simulating Cherenkov light emerging from these secondary products: KM3Sim, KM3, and JSirene.

The package KM3Sim [113] based on GEANT4 [114] simulates and propagates each individual secondary particle as well as the photons induced by the Cherenkov effect accounting for the effect of light absorption and scattering. Then, the hits generated by photons reaching the PMTs are also simulated based on the PMT and DOM characteristics e.g photocathode area, angular acceptance, quantum efficiency, and photon transmission through DOM glass and optical gel.

KM3 and JSirene on the other hand are based respectively on precomputed tables (from KM3Sim) or analytical expressions for the probability distribution functions that provide the probability of detecting a Cherenkov photon on each PMT as a function of the position and orientation of the PMT with respect to the emission point. Hence, KM3 and JSirene yield a much better performance in terms of computation time and resources compared to KM3Sim. As a consequence, they are generally preferred to be used for light simulation from high-energy neutrino interaction or atmospheric muon bundles since such kinds of events produce a huge amount of light and secondary products.

A comparison between KM3Sim and KM3 can be found in Ref. [61]. The study compared the total number of hits on PMTs and DOMs produced by a muon in the case such that almost all light produced is inside the instrumented volume. This comparison showed that KM3Sim and KM3 agree very well with different muon energy. In Chap. 4, another effort of comparison between the light propagators is shown for the specific case of high energy production for ORCA7 which focuses more on KM3 and JSirene.

After the light simulation, the events that produce at least 1 hit on one PMT are stored. These events are the input for the next stages of the simulation chain which are triggering, reconstruction, and classification. These are summarized in the next section.

3.3 Triggering, Reconstruction and Event classification

3.3.1 Triggering in ORCA

At the light simulation stage, the quantum efficiency of the photocathode is taken into account. Thus, the next step is simulating the PMT response. The KM3NeT package for handling PMT response simulation up to triggering is JTriggerEfficiency (JTE). First, JTE converts the photon hits resulting from the light simulation stage into L0 hits similarly to the real data acquisition procedure described in Sec. 2.3. At this level, the package also introduces the optical noise due to the β-decays of ^{40}K in the seawater which is simulated as random uncorrelated hits with a rate of 10 kHz per PMT and time-correlated hits on inter-PMT on each DOM with the rates of 600 Hz twofold, 60 Hz threefold, 7 Hz fourfold, 0.8 Hz fivefold, 0.08 Hz sixfold. The simulated time-correlated noise rate has been extracted from the data taken by the first ORCA DUs [115].

In the final step, JTE uses dedicated triggering algorithms, which are described previously in Sec. 2.3, to select the events induced from energetic particles (neutrinos and atmospheric muons). Compared to the trigger setup presented in the LoI [61], the algo-

rithm has been improved for triggering on faint events with just a few tens of detected photons, which results in a significant increase in the efficiency of neutrino detection in the few-GeV energy range. This trigger setup is designed optimally for oscillation studies at low (< 10 GeV) energies where the NMO signal is expected to be strongest. It leads to a trigger rate of 8 mHz for atmospheric neutrinos, 50 Hz for atmospheric muons, and 54 Hz for pure noise events.

3.3.2 Reconstruction for track-like and shower-like events

The energy and direction of the triggered events are then reconstructed using dedicated algorithms developed for shower-like and track-like event topologies. The track reconstruction, which is called JGandalf, is designed to extract the length and direction of the elongated track assumed to be muon induced from neutrino interaction. The shower reconstruction, referred to as Dusj, works by determining the interaction vertex assuming spherical light emission and then extracts the information on energy and direction from the angular light distribution of ν_e CC events. The detailed steps and explanation of both reconstruction tools can be found in Ref . [83] and Ref . [116].

The JGandalf track reconstruction follows these stages:

- First, the algorithm performs a pre-fit step which starts with a direction scan over hypothetical tracks spread over the sky with a 5 degree spacing. For each of the selected hits belonging to an event, the photon emission point along a hypothetical muon track is determined assuming light emission at the Cherenkov angle and ignoring photon scattering. After that, the time residuals, defined as the difference between the recorded hit time and the predicted hit time assuming a given hypothetical track, can be calculated. The likelihood for each hypothetical track is built based on the time residuals and used to rank the tracks. The best ranking track is passed to the next step.

- The more correct likelihood fit is performed with the accurate probability density functions (PDFs) of the time residual distribution. The PDFs take into account the PMTs orientation, light emission of muons, and photon scattering in water, as well as the area, angular acceptance, and quantum efficiency of the photocathodes. After maximizing this likelihood, the position and direction are obtained.

- The hits that pass a certain likelihood threshold are considered to be signal-like and projected back to the reconstructed track. The length of the reconstructed track is then defined from the first and last projected hit along the track. Since for the mini-

mum ionizing μ (below 100 GeV), the track length linearly scales with the energy, it can be used as a good estimator for reconstructed track energy.

- Finally, an energy correction is applied for fixing the systematic offset observed between simulation and reconstruction energy distributions.

The shower reconstruction with Dusj includes these stages:

- The reconstruction tool performs the first vertex fit using hit time residual distribution and also accounting for PMT directionality. This first step mainly focuses on suppressing the noise hits and avoiding bad starting fit points.
- The next step is to check if the found vertex matches the hit distribution of point-like emission or if the event is too bright with too many photons. These events that do not pass this check are likely to be atmospheric muons and it can be decided to not be processed further.
- A second vertex fit is performed which uses the information on the most accurate signal of hits. This includes the selection of hits on PMTs facing the vertex and using time residuals PDFs which account for distance-dependent noise levels. The second fit helps refine the vertex reconstruction.
- The final fit uses the PDFs of expected photon detected for each DOMs under shower-hypothesis. The fit estimates the remaining event parameters: energy, direction, and Bjorken-y.

Another shower reconstruction called JShower has been in development with the full detail presented in Ref. [117]. The tool also uses basic processes like Dusj but the main difference is the energy and direction reconstruction performed with parameterized PDF at PMT level instead of DOM level. This algorithm leads to an improvement in the reconstructed energy, especially in the low energy region. Considering that JShower has been developed within the current official framework for data processing and event reconstruction in KM3NeT, this reconstruction package will be used as the official one for ORCA in the near future. At the time of writing this thesis, Dusj is still the standard one and used for all oscillation analyses in ORCA as well as for the works presented in this manuscript.

3.3.3 Event classification

In both oscillation or astrophysics analyses, the information on the flavor of the interaction plays a vital role in extracting the desired physics signature. Once an event passed the

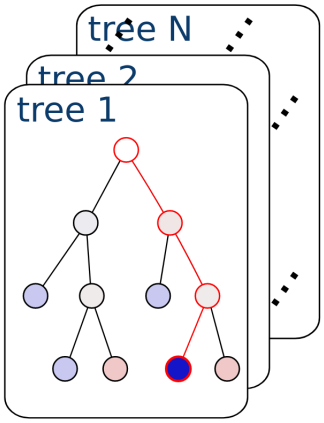

Figure 3.3: A schematic representation of Random Decision Forest technique. Figure taken from Ref. [94]

reconstruction step, it is injected into the stage of the event classifier (also called particle identification - PID) which is capable of determining the event topologies to be shower-like or track-like, or whether it is neutrino-like or background-like (atmospheric muon and pure noise). Multiple machine learning-based tools have been developed within the KM3NeT Collaboration to fulfill this aim. This section presents an event classification based on Random Decision Forest (RDF) which has been developed specifically for oscillation analysis. This classifier is used for most of the oscillation studies in ORCA including the latest sensitivity study on the NMO [98] as well as the oscillation studies of this work presented in Chap. 8, 9. The detail of this classifier can be found in the work in Ref. [94].

An RDF is a set of decision trees that are made from a random subset of available training events and available *features*. Training events are available as input from MC data while features are categorical variables derived from the characteristic parameters of the input. A schematic representation of RDF is described in Fig. 3.3. Events pass through the trees from top to bottom where at each node the tests based on the defined features are performed which results in the events being classified into one of the two child nodes. The flows end at the bottom of the trees where events are assigned with specific class labels. The trees are trained with simulated data so that the assignment of features to nodes and the classification processes at each node are adjusted to achieve the best separation between classes of events at the end of the procedure.

In the current ORCA standard PID procedure, each RDF model is trained to make a binary decision among two classes of events only. Then an output score (also called PID score) is computed that describes the likeliness of an event to be in one class instead of another, as the fraction of trees voting for such class. Three output scores, which scale from 0 to 1, have been trained and used:

- *atmospheric_muon_score*: whether the event is likely to be atmospheric muon.
- *pure_noise_score*: whether the event is likely to be pure noise i.e bioluminescence or K40 decay.
- *track_score* : whether the event is track-like or shower-like.

The first two scores are used for the suppression of background and for obtaining a pure neutrino event sample, while the last one is for classifying events into topologies which preserve (partially) the information of interaction flavor. One can set cuts on these variables and optimize them for specific analyses. At the moment, the official cuts on the *track_score* are such that 3 classes of events, also called PID classes, are defined:

- **Tracks**: $0.7 <$ *track_score* ≤ 1.0.
- **Intermediate**: $0.3 <$ *track_score* ≤ 0.7

  Showers: $0.0 <$ *track_score* ≤ 0.3

These cuts have been optimized for the NMO sensitivity of ORCA as the best compromise between a good event purity level and a sufficient statistics of events in the extreme classes [118].

Compared to the past published results, a major update in this classifier regards the inclusion of new features related to the hit PDF on PMTs around the reconstructed position and direction of neutrino events. This results in an improvement of the PID performance as pointed out in Ref. [119] and will also be illustrated later in Sec. 5.2.1.

3.4 The 'ORCA115_20x9_190222', 'ORCA115_23x9_190222' and 'ORCA7_23x9_190222' Monte Carlo samples

In this part, we describe the latest MC samples used for the analyses on the ORCA potential for oscillation physics, which have been produced in 2019 with the standard simulation chain described in this chapter. They will also be used for the analyses presented in Chap. 8 and Chap. 9.

Historically, the first MC sample generated for a full ORCA detector was produced with a configuration with 115 DUs with an average inter-DU spacing of 23 m and inter-DOM spacing of 9 m. This layout was first adopted as the most suitable spacing for ORCA to

	ORCA115_20x9		ORCA115_23x9		ORCA7_23x9
# of events ($\times 10^6$)	Generated	Selected	Generated	Selected	Selected
$\nu_e + \bar{\nu}_e$ CC	24.1	2.1	30.0	3.5	0.21
$\nu_\mu + \bar{\nu}_\mu$ CC	44.2	4.8	31.6	3.7	0.24
$\nu_\tau + \bar{\nu}_\tau$ CC	13.6	2.5	45.3	2.1	0.16
$\nu + \bar{\nu}$ NC	30.5	0.7	206.6	2.9	0.17

Table 3.1: Statistics of 'ORCA115_20x9_190222', 'ORCA115_23x9_190222' and 'ORCA7_-23x9_190222' MC productions. The ORCA7_23x9 is the masked production from the ORCA115_23x9 and thus uses the same generated sample.

determine the NMO [61] while satisfying conservative deployment constraints, and it has been used for the previous results in Ref. [120]. Nevertheless, based on the experience acquired with the deployment of the first detection lines, a slightly denser configuration with 20 m inter-DU spacing has turned out to become technically feasible. Additionally, this configuration has been proven to achieve more sensitivity to the NMO thanks to the slightly denser DU population (20 m vs 23 m) which allows a more efficient detection in the low-energy (few GeV) region. Thus, the 20m x 9m configuration has now been chosen as the official one. A comparison between the performances achieved with the two horizontal spacings for the determination of NMO will be discussed in Chap. 8.

In order to study the physics potential of a sub-array of ORCA detector (that would correspond to an early construction stage), the collaboration has also produced a simulated sample with just 7 DUs installed. At the time this production was started, only the full production with 23 m configuration was available. Thus, this sample was obtained by re-running the old production with the 23 m $\times$ 9 m configuration from the trigger level, but removing all DUs other than the 7 desired DUs in the detector configuration file. This is a so-called masking technique.

Tab. 3.1 shows the statistical size of the aforementioned MC productions in terms of the number of generated events (at gSeaGen level) and the selected events (passing the light and trigger stages, without further quality cuts on the reconstruction). All these productions were processed with the latest RDF-based event classifier as described in Sec. 3.3.3.

Chapter 4

High energy simulation for ORCA7

Contents

The main physics target of ORCA is the neutrino oscillation in the GeV energy domain. The three MC samples for ORCA presented in Sec. 3.4 serve this goal and cover the energy range of 1-100 GeV. Nevertheless, ORCA can also detect neutrino events above 100 GeV, a region that is interesting for astrophysics. Thus, there is a strong interest to explore the potential of ORCA in the higher (> 100 GeV) energy range.

In this context, I was in charge of producing a Monte Carlo simulation extended to high energies (from 50 GeV up to 5 TeV) for the ORCA7 subarray, that could be exploited in particular for astrophysical neutrino searches. This work constitutes my service task for the Collaboration and I have also been in charge of using this specific production for checking the ORCA simulation chain as well as performing standard quality control of the production.

This chapter presents the checks and quality control that have been done at each stage of the simulation chain, as a preparatory work for a fully automated quality check procedure. To this aim, some test samples with small statistics have been produced. In the next sections, the quality checks on both test samples and final samples are presented. The workflow is as follows:

- Produce samples with small statistics in order to be quickly produced and suitable for testing purposes with multiple changes in the configuration. The test production is on three energy ranges 30-70 GeV + 180-220 GeV + 1800-2200 GeV with 3 channels (ν_e CC, ν_μ CC, NC) along with 3 light propagators (KM3Sim, KM3, JSirene). These samples will be used for checking the consistency of gSeaGen (Sec. 4.1.1) and cross-checking among the 3 light simulators (Sec. 4.1.2).
- For the full production, a more realistic sample with energy ranges of 50-500 GeV + 500-5000 GeV is used. The tests at this stage will be presented in Sec. 4.2. After these checks, the configuration of the production is almost set. Any other changes or re-optimisation, such as trigger set up, statistics,..., will be analysis-driven.

This chapter also reports some first investigations into the performance of ORCA7 in terms of response functions such as effective area, energy and angular resolution at high energy, and comparison with the existing low energy production that have been used for the oscillation studies. They are presented in Sec. 4.3. Further studies regarding the selection and event classification for astrophysics analysis with this detector sub-array are being carried on within the collaboration based on the MC production in this work.

4.1 First test production

The first check for the production is performed with small statistics for the three different energy ranges: 30-70 GeV, 180-220 GeV, 800-1200 GeV. These samples are used for checking the consistency of gSeaGen and cross-checking within 3 light propagators. The summary table of these test productions are shown in Table 4.1.

Table 4.1: Summary table for the testing samples. The following informations are shown:
N^{in}_{GsG} - number of total events simulated by gSeaGen,
N^{out}_{GsG} - number of output events by gSeaGen (input to light simulation),
N^{out}_{light} - number of events output after light simulation,
T_{GSG}, T_{Light} - time for processing each step: gSeaGen and light propagation respectively.
v [s/evt] - time to process 1 event from gSeaGen to light simulation.
The values are averaged over 10 produced files.

ν_eCC 30 - 70 GeV				ν_eCC 180 - 220 GeV			ν_eCC 800 - 1200 GeV		
Light	KM3Sim	KM3	JSirene	KM3Sim	KM3	JSirene	KM3Sim	KM3	JSirene
Spectrum	E^{-1}	E^{-1}	E^{-1}	E^{-1}	E^{-1}	E^{-1}	E^{-1}	E^{-1}	E^{-1}
N^{in}_{GSG}	1.0E4	1.0E6	1.0E5	1.0E4	1.0E5	1.0E5	1.0E3	1.0E5	1.0E5
N^{out}_{GSG}	1.92E3	1.49E5	1.49E4	2.16E3	2.03E4	2.03E4	2.16E2	1.9E4	1.9E4
N^{out}_{light}	105.6	16265.6	1620	230.9	3496.2	4070	42.9	4634	6870
$T_{GSG}[h]$	0.0858	0.139	0.128	0.086	0.198	0.198	0.081	0.159	0.159
$T_{Light}[h]$	20	0.084	0.013	32	0.177	0.016	48	0.230	0.026
$v_{light}[s/evt]$	8	0.002	0.003	30	0.031	0.003	75	0.255	0.013

ν_μCC 30 - 70 GeV				ν_μCC 180 - 220 GeV			ν_μCC 800 - 1200 GeV		
Light	KM3Sim	KM3	JSirene	KM3Sim	KM3	JSirene	KM3Sim	KM3	JSirene
Spectrum	E^{-1}	E^{-1}	E^{-1}	E^{-1}	E^{-1}	E^{-1}	E^{-1}	E^{-1}	E^{-1}
N^{in}_{GSG}	1.0E5	1.0E5	1.0E6	1.0E5	1.0E5	1.0E6	1.0E4	1.0E5	1.0E6
N^{out}_{GSG}	4.13E3	2.9E3	2.89E4	3.61E3	3.25E3	3.24E4	2.69E2	2.18E3	2.19E4
N^{out}_{light}	232.81	291.6	2590	400.1	499.3	4940	44.58	428.4	4580
$T_{GSG}[h]$	0.161	0.158	0.761	0.198	0.219	1.244	0.218	0.219	1.401
$T_{Light}[h]$	24	0.108	0.024	36	0.177	0.229	52	0.228	0.028
$v_{light}[s/evt]$	10	0.134	0.006	38	0.255	0.005	100	0.376	0.005

4.1.1 gSeaGen checks

Fig. 4.1 shows the weighted energy distribution for three energy ranges and the unweighted one for ν_e CC 800-1200 GeV as an example. Firstly, the weighted distributions of the three energy ranges all match each other and following the power spectrum. For the unweighted distribution, the ν_e CC depicts a flat (slightly decreasing) feature while the ν_μ CC shows a steep increase as the energy increases. To explain these behaviors, we note that two factors affect the trend of such distribution: first - the unweighted generation spectrum E^{-1} as the input for these test samples, i.e more interaction generated at low energy, second - the fact that the higher the energy of the interaction is, the higher the probability that the event will be kept after gSeaGen simulation.

For ν_e, most interactions produce shower-like events with short-ranged charged particles. The probability that events produced outside of the instrumented volume is selected increases at high energy. This effect roughly compensates for the decreasing generation spectrum. For the ν_μ CC interactions, the long propagation length of the muon makes the track-like events easier to detect even when they occur outside of the instrumented volume. This effect increases with energy and supersedes the effect induced by the generation spectrum, therefore leading to a positive slope in the ν_μ CC unweighted distribution.

Other useful plots to verify the gSeaGen simulation are the spatial distributions of the output events. In Figure 4.2, we show the spatial distribution of ν_e CC and ν_μ CC 180-220 GeV at gSeaGen level. An equal binning in R^2 is chosen in order to have the same volume for each bin. One can see that the features are consistent with the mechanism of the simulation, which is described in Sec. 3.1, such that all the ν_e events are homogeneously distributed inside the can. The ν_μ distribution is homogeneous inside the can and gradually decreases at larger distances. One can also see the effect of the seabed which induces a higher absorption of events below Z=0. In general, the mentioned checks just showed the consistency and expected behaviors of this simulation at gSeaGen stage.

4.1.2 Light propagation comparison

The cross-checks between three light propagators (KM3Sim, KM3, JSirene) are also performed with the test samples of three different energy ranges: 30-70 GeV, 180 - 220 GeV, 800 - 1200 GeV.

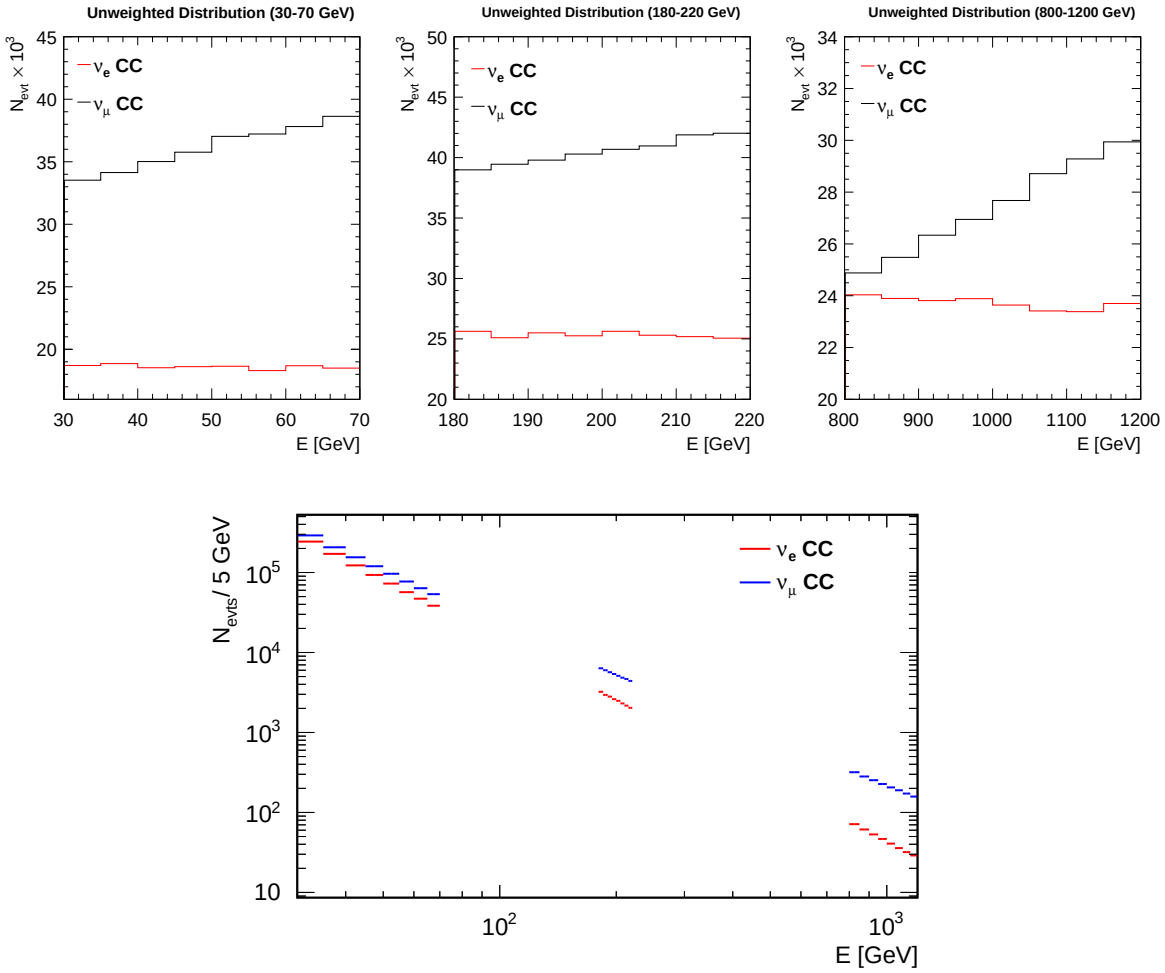

Figure 4.1: Energy distribution for output events of gSeaGen. Upper panel: Unweighted distribution for ν_e & ν_μ CC test samples. Lower panel: Distribution for all three test samples weighted with $E^{-3.5}$ spectrum.

Computation time

From the summary tables, we make the comparison in CPU times as follows:

Table 4.2: Average time (second) to process 1 event through light simulation.

		KM3Sim	KM3	JSirene
ν_e CC	30-70 GeV	8	0.02	0.03
	180-220 GeV	30	0.03	0.003
	800-1200 GeV	75	0.255	0.013
ν_μ CC	30-70 GeV	10	0.134	0.006
	180-220 GeV	38	0.255	0.005
	800-1200 GeV	100	0.376	0.005

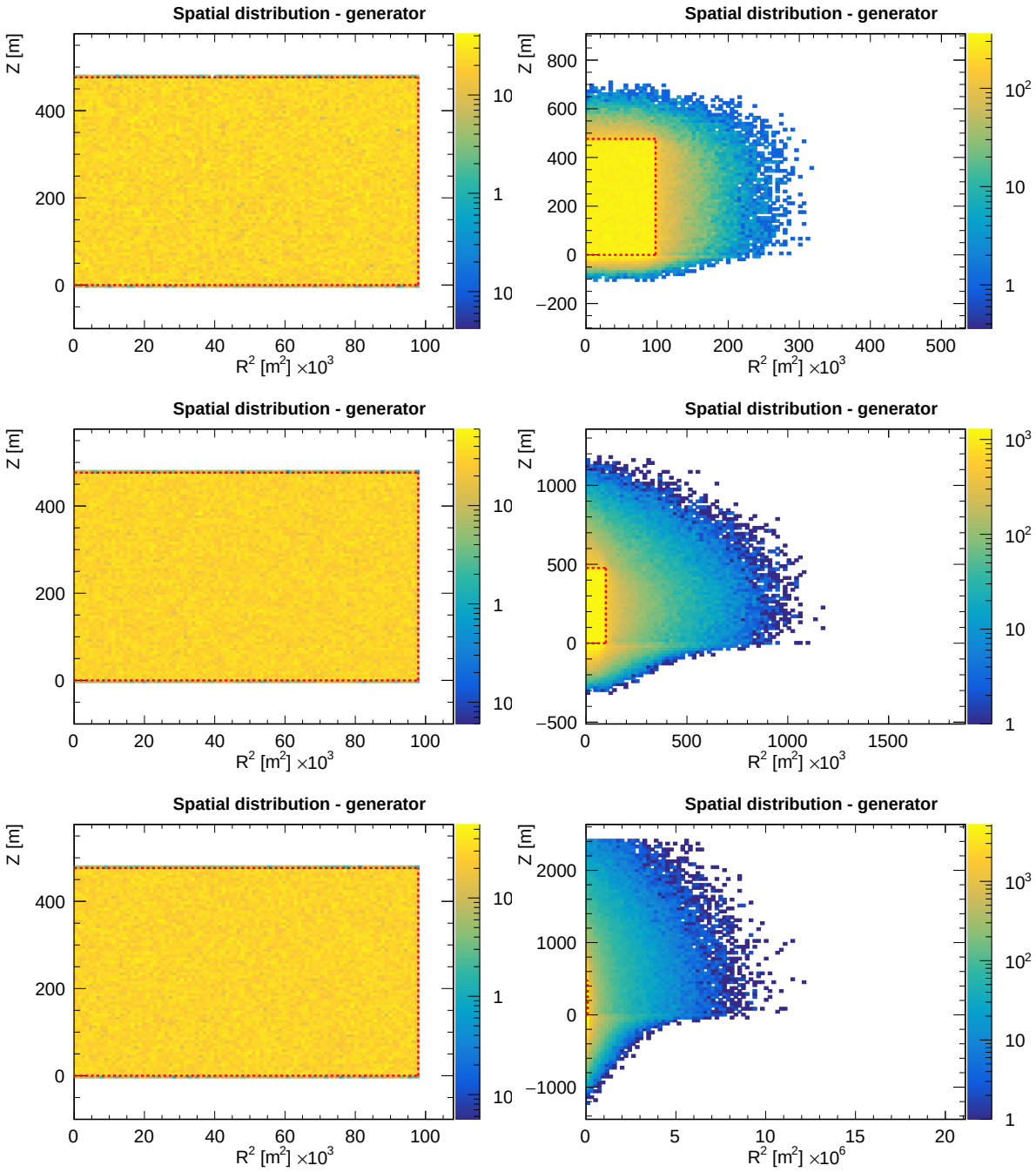

Figure 4.2: Spatial distribution (Z [m], R^2 [m^2]) of gSeaGen output for ν_e CC (left) and ν_μ CC (right). From above to below: 30-70 GeV, 180-220 GeV, 800-1200 GeV. Red dashed lines indicate the detector can.

From Tab. 4.2, one notices that KM3Sim takes much more time (1-2 order of magnitude) to process compared to KM3 and JSirene. This is expected since KM3Sim simulates every particle generated from neutrino interaction while KM3 and JSirene are based on precomputed tables and the p.d.f functions for calculating directly the probability of detecting Cherenkov photon on each PMT. Especially, for ν_μ events and at high energy, JSirene is way faster than the two others ($\sim$ 0.02 s/evt compared to 0.3 s/evt for KM3 and 100 s/evt

for KM3Sim) which leads to the decision to use it for the real production.

Light Efficiency

Table 4.3: Light efficiency of each propagators.

		KM3Sim	KM3	JSirene
ν_e CC	30-70 GeV	10.4%	10.9%	10.9%
	180-220 GeV	19.09%	17.3%	20.08%
	800-1200 GeV		24.4%	36.2%
ν_μ CC	30-70 GeV	9.3%	10.1%	8.9%
	180-220 GeV	15%	15.4%	15.2%
	800-1200 GeV		19.6%	20.9%

Tab. 4.3 shows the comparison in the efficiency defined as ratios between the number of events after light simulation and number of events after gSeaGen - input to the light simulation. One can notice that there is a good agreement among the three light propagators except for the ν_e CC 800-1200 GeV samples. The light efficiency in KM3 for this sample is 24 $\%$ while it is 36 $\%$ in the case of JSirene (10% of difference). Below we will present the checks that have been performed in order to understand better these discrepancies as well as spot potential problems related to them.

In Fig. 4.3, a deeper investigation into JSirene - KM3 discrepancies is performed by plotting the spatial distribution of the neutrino events after each simulation step. At gSeaGen level, all the events are distributed uniformly inside the can, which is expected for the simulation of ν_e events. At light level, one can clearly see that JSirene has more events at far distances while KM3 shows a clear cut in the shape of the distribution. This can be explained by the fact that KM3 has light tables up to 200m from the particle while JSirene uses the p.d.f, which can be extended indefinitely. However, at the trigger level, the two chains show similar shapes which says that we are still safe after JTE.

Such kind of spatial distribution plots also suggest that a 4-absorption-length extension in gSeaGen can (used for this test production) might be inefficient since a lot of events being simulated by gSeaGen and the light propagators do not appear at the trigger level. To optimize this, we have created various test samples with reduced can (2, 3 absorption lengths) and looked at the spatial distribution at the trigger level to find out the suitable can size. We would want the can size to be small enough to avoid wasting time simulating a lot of events that will never be triggered and large enough so that we do not lose events. The suitable can size is reported and discussed in Sec. 4.2.

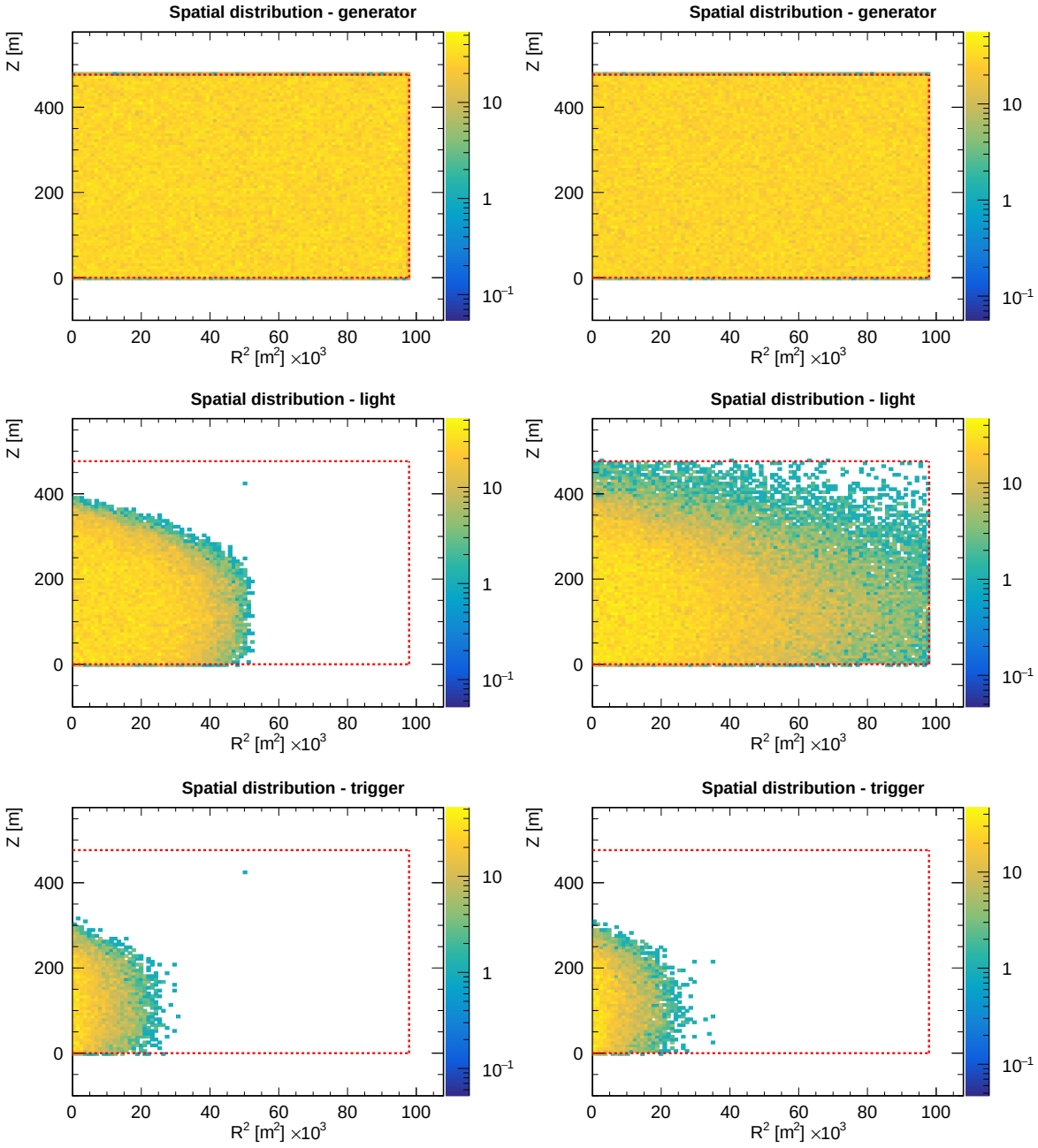

Figure 4.3: Spatial distribution (Z[m], R^2[m^2]) of neutrino events ν_e CC 800-1200 GeV at each steps of the simulation with two different light simulators. Left: KM3, Right: JSirene. The red dashed lines depict gSeaGen can.

JDomino's plots - Comparison at photo-electron level

Another comparison is made with the tool called JDomino developed to easily extract information on photo-electrons detected from the results of the light simulators. Two example plots are shown in Fig. 4.4 and 4.5 which are respectively the number of hits as a function of the numbers of photo-electrons and the distribution of photo-electrons against the photon emission angle with respect to the charged particle direction. The last is divided into subplots by distance from the emission points to the PMTs in the range from 0 to 240 m (20 m for each subplot).

The JDomino plots show that both JSirene and KM3 have the same shape over all distributions. Both light propagations depict a peak at the Cherenkov angles in the emission angle distribution. Nevertheless, there are still differences of $\sim 1\%$ in the number of photo-electrons between the predictions of the two light simulators. Also one can see that KM3 table ends up at 200 m which verifies again the difference in light efficiency reported above.

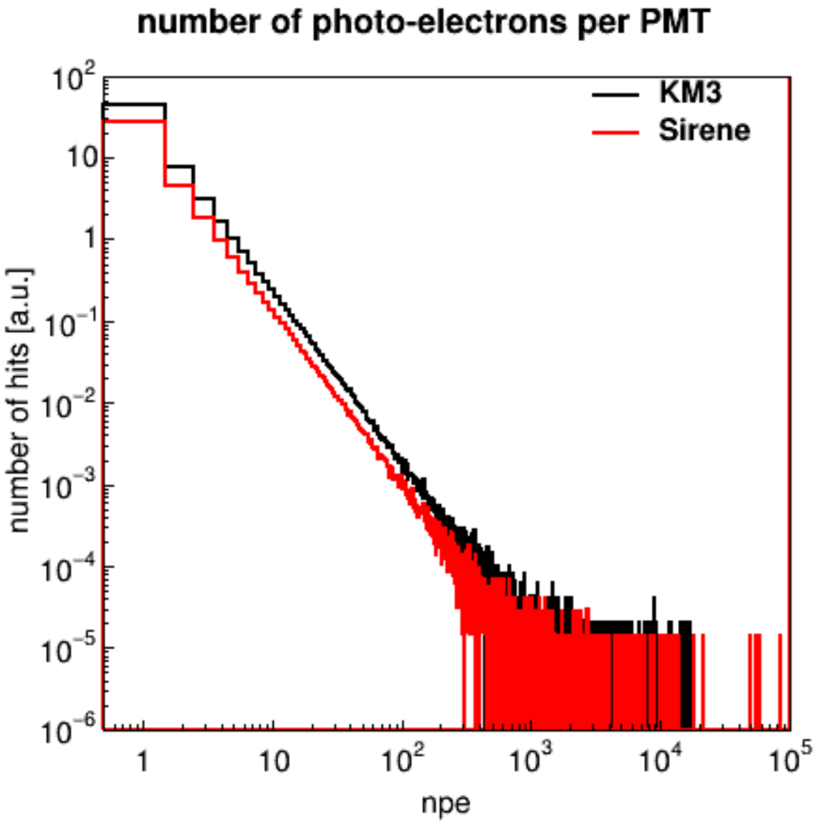

Figure 4.4: Number of hits as the function of numbers of photo-electrons (npe) for KM3 and JSirene.

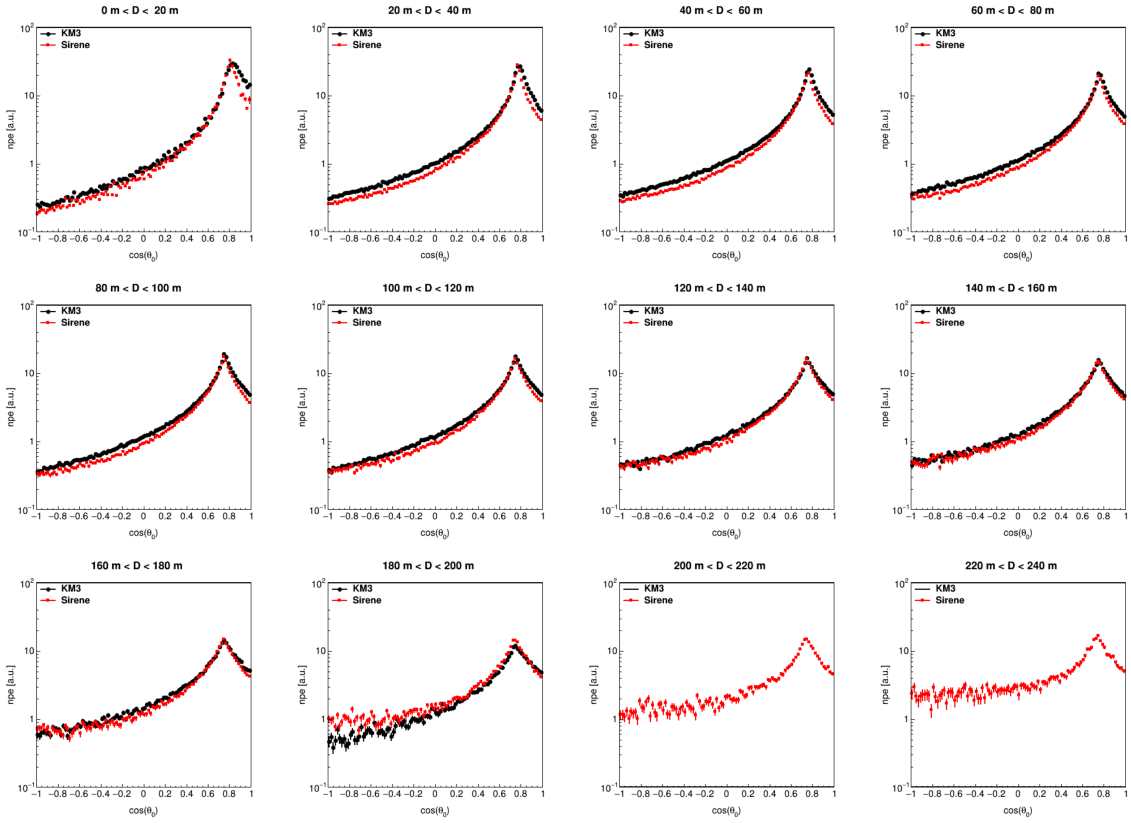

Figure 4.5: Emission angle distributions of the numbers of photo-electrons (npe) for KM3 and JSirene.

4.2 The full production

This production is divided into two energy ranges: 50-500 GeV and 500-5000 GeV. We will use JSirene as light simulator as it will save us a lot of computation time. The summary table for the full production is shown in Tab. 4.4.

Table 4.4: Summary table for the full production. The values are evaluated for each run. 10 runs have been performed in total.

	50 - 500 GeV			500 - 5000 GeV		
	ν_e CC	ν_μ CC	ν_e NC	ν_e CC	ν_μ CC	ν_e NC
Spectrum	E^{-1}	E^{-1}	E^{-1}	E^{-1}	E^{-1}	E^{-1}
Number of GSG bin	1	10	1	1	10	1
N^{in}_{GSG}	7.5E5	3.7E6	1.5E7	3.6E5	3.7E6	4.5E7
N^{out}_{GSG}	62324.3	84988.5	8574.6	34002.1	62913.9	9502.5
$N^{out}_{JSirene}$	44149.9	34049.5	4297.3	25425.5	32093.1	5284.8
N^{out}_{JTE}	7904.4	5955.4	609.8	5236.2	7211.3	877.6

For ν_μ CC events, the gSeaGen generation is done with 10 bins of energy instead of 1.

The reason is that gSeaGen will simulate ν_μ events which are far away from the can and the furthest distance depends on the highest energy in each defined energy bin. Bearing that in mind, dividing the generation energy of ν_μ into multiple bins helps not to simulate low energy events at too far distance and thus improves the efficiency of the simulation as well as the statistics of ν_μ CC events.

4.2.1 Quality checks at trigger level

This full production also went through quality checks at gSeaGen and light stages as mentioned in the previous section. In this section, we present the quality checks for this full production at trigger level.

In Fig. 4.6, the energy distributions (weighted and unweighted) of the samples are shown. The distributions do not show anomalies and the weighted distributions for the two energy ranges perfectly match.

Fig. 4.7 shows the spatial distribution of the current setup of the simulation. The distribution has a clear and good shape - densely distributed at the center and decreasing to 0 at far distances from the detector, which means that we did not miss high energy and far-away events. For this simulation, the can is reduced to 2 absorption length extensions for better efficiency (except for ν_e events at 500-5000 GeV where the extension is 3 absorption lengths in order not to miss high energy events). Compared to the $\nu_e CC$ events distribution in Fig. 4.3, this reduction helps not to waste time on a lot of events that may never pass the trigger. The efficiency of the simulation, which can be roughly described by N_{JTE}/N_{GSG}, has also improved to $\sim 10\%$ compared to $\sim 1\%$ in the test sample with 4 absorption length extension.

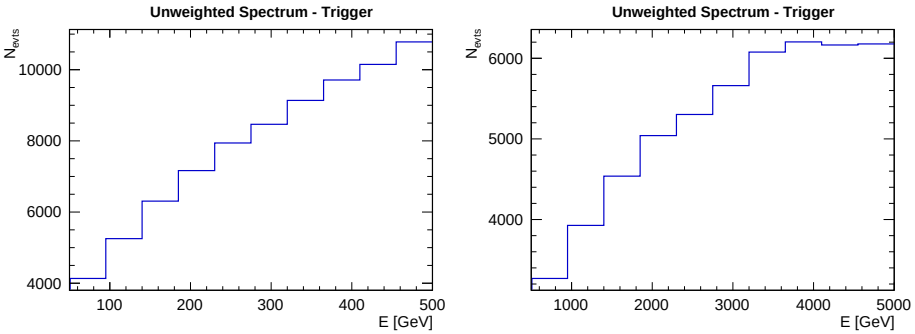

ν_e CC

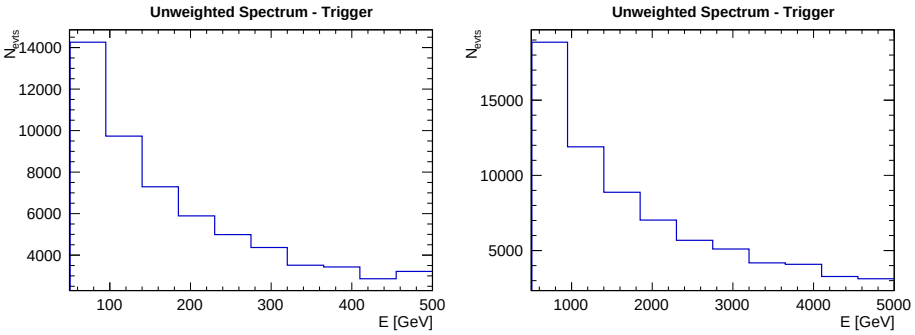

ν_μ CC

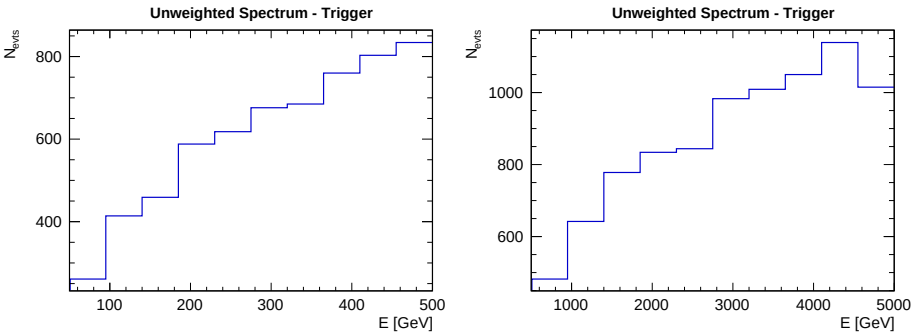

ν_e NC

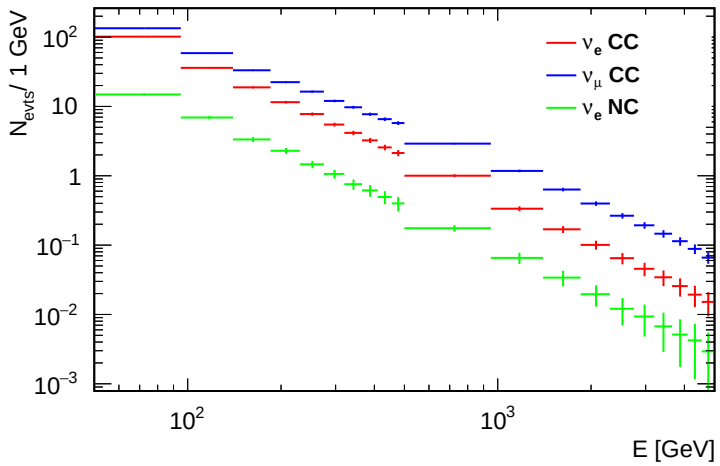

Weighted distribution for all samples

Figure 4.6: Energy distribution (weighted and unweighted) of the full production at trigger level, for ν_e CC (top plots), ν_μ CC (middle plots) and ν_e NC (bottom plots).

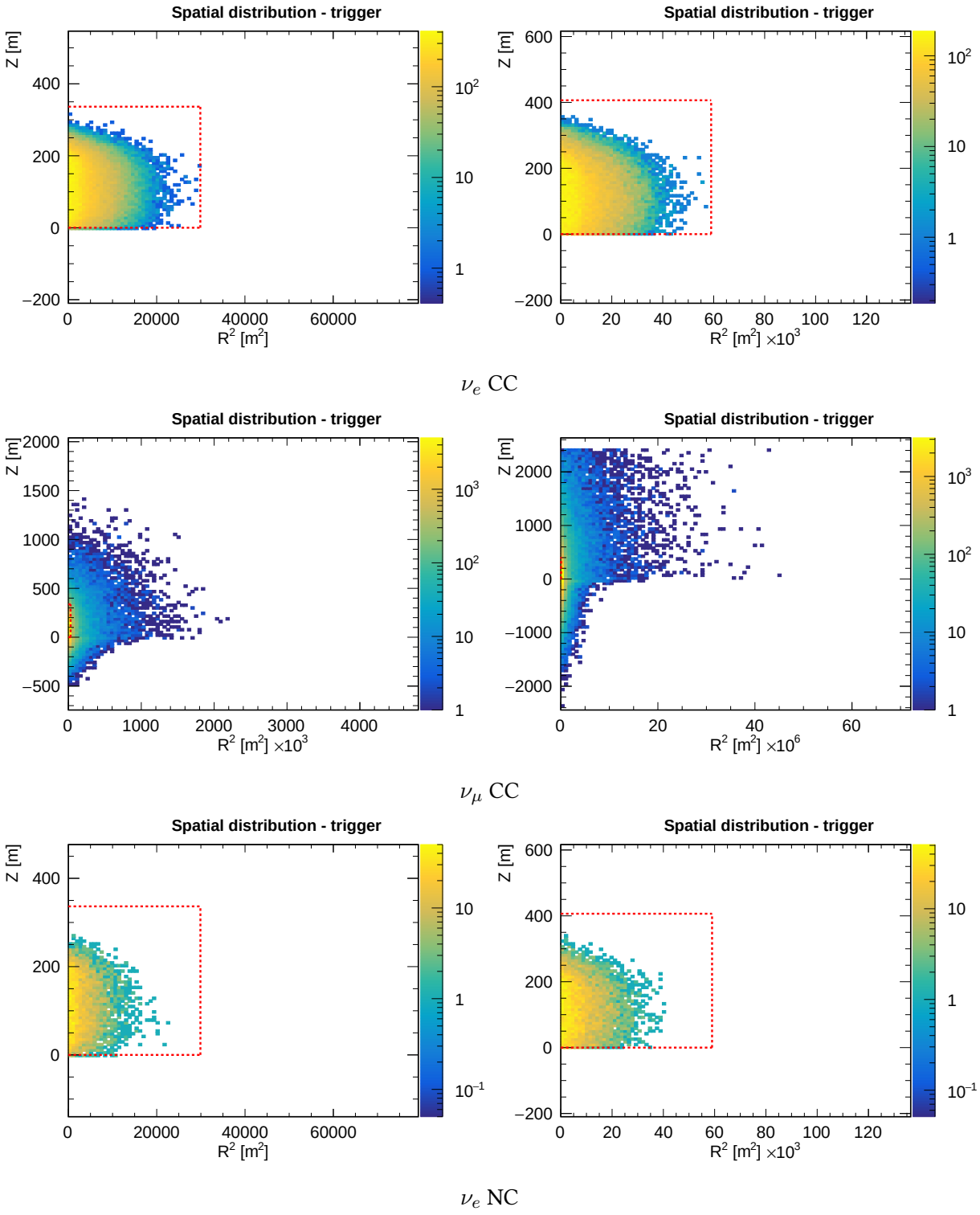

Figure 4.7: Spatial distribution for samples of 50-500 GeV (left) and 500-5000 GeV (right) at trigger level, for ν_e CC (top plots), ν_μ CC (middle plots) and ν_e NC (bottom plots).

4.3 Performance of ORCA7 at high energy

This section presents the performance of ORCA7 at high energy based on the produced MC sample. For ensuring consistency, the cross-check with the ORCA7 low energy sample is also performed. This low-energy MC sample has been produced in the previous work within the Collaboration for oscillation studies by re-running the existing production of the full detector at the trigger level with the masked-detector configuration as mentioned earlier in Sec. 3.4. The energy range of this sample is 1-100 GeV which provides a cross-range of 50-100 GeV with the high-energy sample presented here.

One response function often used for describing neutrino telescope performances is the effective area, which is calculated as the ratio between a trigger rate $R_{trig}[\mathrm{s}^{-1}\mathrm{GeV}^{-1}]$ and the corresponding flux $\phi[\mathrm{m}^{-2}\mathrm{s}^{-1}\mathrm{GeV}^{-1}]$. The effective area captures the information on the neutrino cross-section and the detector efficiency on detecting neutrinos for some given selection cuts. In Fig. 4.8, the effective areas of all flavors are presented with both low and high energy MC production. The effective areas of the high energy sample match well with the low one and also show a good agreement in the overlapping energy range (50-100 GeV). This indicates the consistency between the two production samples up to the trigger stage. The figure also shows the effective area for point source (PS) searches in ANTARES [121] as a reference. With only 7DUs, ORCA can already have a comparable effective area with ANTARES. Nevertheless, it should be noted here that the ORCA7 effective areas presented here do not apply any selection yet. A selection, which will be carried out in the future, could potentially reduce the shown effective areas.

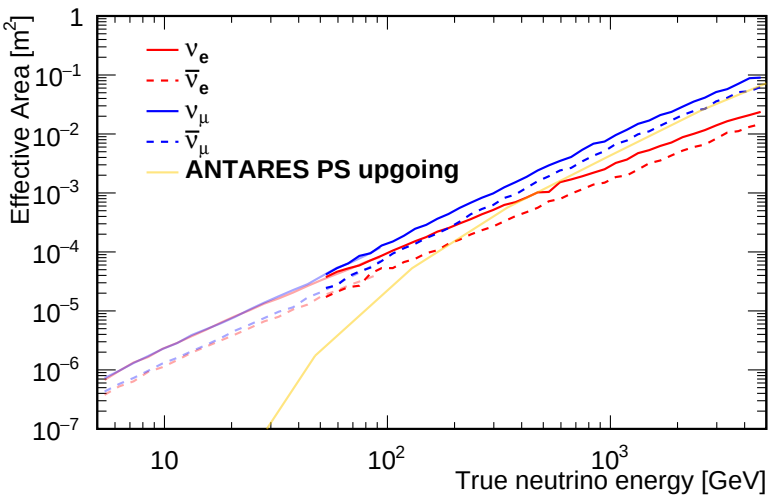

Figure 4.8: Effective area of ORCA at trigger level for all neutrino flavors. Both low (1-100 GeV) and high (50-5000 GeV) energy sample are shown in light and dark line respectively. The effective area for point source (PS) searches in ANTARES [121] is shown as a reference.

To explore the reconstruction ability of ORCA7, the production is also run up to the reconstruction stage with 2 reconstruction algorithms: JGandalf and Dusj as described in Chap. 3. Fig. 4.9 presents the energy and angular resolutions of track and shower reconstruction for ν_e CC and ν_μ CC with both the low and high energy productions. At the time this production was performed, the implementation of JGandalf did not allow for reconstructed energy values above 100 GeV. Thus, the energy reconstruction from Dusj is considered here for both ν_e and ν_μ CC events.

One can notice that the angular resolutions of the track reconstruction (JGandalf) are in good agreement and match in the median, 68% and 90% quantiles of the distributions and the median kinematic angle for both low and high energy productions. Nevertheless, the plots exhibit systematic shifts in the high energy production compared to the low energy one for the energy and angular resolutions of the Dusj shower reconstruction.

At the moment, the reason for the offset shown in Fig. 4.9 is still not identified, and possible explanations are under investigation. One notable difference between the two MC samples is the used light propagator. The low energy sample uses KM3Sim while the high energy one adopts JSirene. Thus, a more detailed comparison between these two light propagators might be required to improve the consistency at high energy. The second one is that the low energy production has been generated with a smaller can size using a ~ 1 absorption length extension which is already sufficient for the NMO sensitivity region of few GeV but might not be enough around 100 GeV. Additionally, the low energy sample has been implemented with a specific selection which includes extra containment cuts and an energy correction (as discussed in Sec.3.3.2), while the high energy sample does not go through the same process yet. Fig. 4.10 shows the distributions of reconstructed vs true energy of the ν_e CC and ν_μ CC events. These indicate that the high energy production generated in this work still selects a lot of faraway events, which leads to an underestimation of the reconstructed energy. For the track-like events (ν_μ CC), the reconstruction ability of the ORCA7 sub-array is saturated because the long track length of high energy events exceeds by far the spatial extension of the sub-array. For the shower-like events (ν_e CC), the shape of the distribution when increasing true energy suggests that a good selection and appropriate energy correction should help remove badly reconstructed events and improve the energy resolution of the high energy production to match the low energy one. Such selection and further investigations on this topic are in development by another PhD student in the collaboration, based on the sample produced in this work.

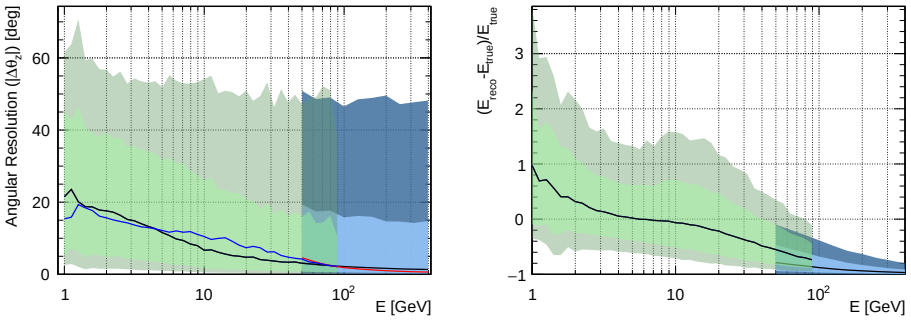

ν_μ CC

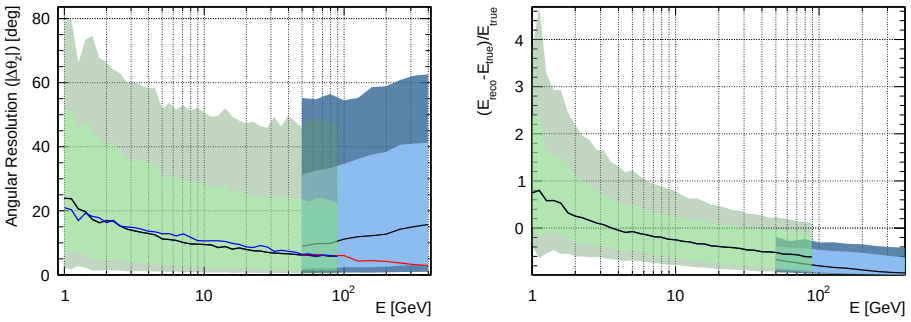

ν_e CC

Figure 4.9: Zenith angle resolution (left) and energy resolution (right) for ORCA7 from low energy production (blue) and high energy production (green) for ν_μ CC (top) and ν_e CC (bottom) samples. JGandalf is used for the ν_μ CC direction reconstruction while Dusj is used for the rest. Black lines show the median while light and dark bands depict resepctively the 68% and 90% quantiles of the distributions. The blue and red lines represent, for each sample, the median kinematic angle between the neutrino and the associated charged lepton.

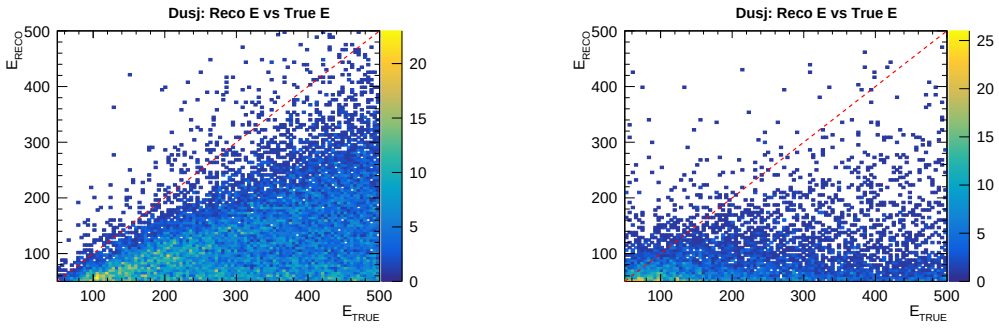

(a) ν_e CC (b) ν_μ CC

Figure 4.10: Number of event as a function of reconstructed and true energy for Dusj reconstruction

4.4 Conclusion

This chapter presented my service task for the Collaboration which consisted in the generation of a MC production of high energy (50-5000 GeV) neutrino events for the ORCA7 sub-array, together with the quality checks performed for this production. This work will help investigate the potential of ORCA7 for astrophysical neutrino searches. The quality checks have confirmed the expected behavior of the simulation tools and validated the production up to the trigger stage.

In order to further investigate the properties of the production, the energy spectrum and spatial distribution at different stages of the simulation have been studied. Furthermore, based on the spatial distribution of events, a suitable can size for the simulation was identified with the aim of achieving a sufficient efficiency to minimize the number of events that would never pass the trigger while ensuring that the detectable high energy and far-away events are not lost. The cross-checks performed between the current three light simulators have shown a good agreement. The whole checking procedure developed in this work is an important step towards the collaboration objective to develop a standard and fully automated set of scripts for producing the quality checks.

A comparison with the ORCA7 low energy sample has also been performed thanks to the overlap energy range (50-100 GeV) between the two productions. The effective areas computed from the two production match well, which indicates the consistency up to the trigger stage. Nevertheless, some offsets at the reconstruction level between the two samples are also observed. Possible causes might come from the simulation settings (light propagators, can size) or the selection and energy correction applied after the reconstruction step for the low energy sample but not yet developed for the high energy sample. This issue will require more investigation in the future.

Part III

Analysis method for neutrino oscillation studies

Chapter 5

Calculation of the neutrino event rates in ORCA

Contents

In this chapter, the calculation of the expected neutrino distribution at the ORCA detector is described. One first needs to compute the expected neutrino interaction rate at the detector site without accounting for the detector effects. This will be referred to as *interaction rate* (or *interacting event rate*) in the rest of the thesis. This task, presented in Sec. 5.1, requires the use of atmospheric neutrino flux, oscillation probabilities, and cross-section models. The second step is to compute the predicted event distribution in the measured parameter space, i.e. the number of detected and classified events as a function of reconstructed variables which will be referred to as *expected rates*. To this aim, a model of the detector response to the neutrino interactions is built from the Monte Carlo sample as described in Sec. 5.2.

These calculations have been developed and implemented in a software framework called SWIM, which is the result of a previous work described in Ref. [122]. I have been working as a maintainer and developer of SWIM since 2018. In this context, I have been in charge of producing neutrino mass ordering and oscillation parameter sensitivities with this framework and compare with the results produced by other frameworks developed in the Collaboration as a pre-publication cross-check for several official KM3NeT results [98, 119, 123]. These works are discussed in Chap. 8. I have also used the framework for performing the study of combining NMO sensitivity between JUNO and ORCA which is presented in Chap. 9.

5.1 Calculation of interaction rate

The very first step is to calculate the interaction rate at the detector. ORCA measures the atmospheric neutrinos produced in the atmosphere, oscillating along the propagation path, and then interacting in the detector. Therefore, the information on the atmospheric neutrino flux, oscillation probability, and neutrino cross-section in water is required. They are taken as inputs from external models which are presented below.

5.1.1 Atmospheric neutrino flux

The atmospheric neutrino flux is taken from Ref. [68], subsequently referred to as the Honda flux. The results are stored in form of pre-computed and tabulated values of differential flux (in units $m^{-2} \cdot s^{-1} \cdot GeV^{-1} \cdot sr^{-1}$) on a grid of energies and cosine zenith angles. The flux is computed for each neutrino flavor ($\overset{(-)}{\nu}_e$, $\overset{(-)}{\nu}_\mu$) averaged over years and azimuth angles. The ν_τ fraction is negligible in atmospheric neutrino flux in the GeV energy region thus it is not considered for this input.

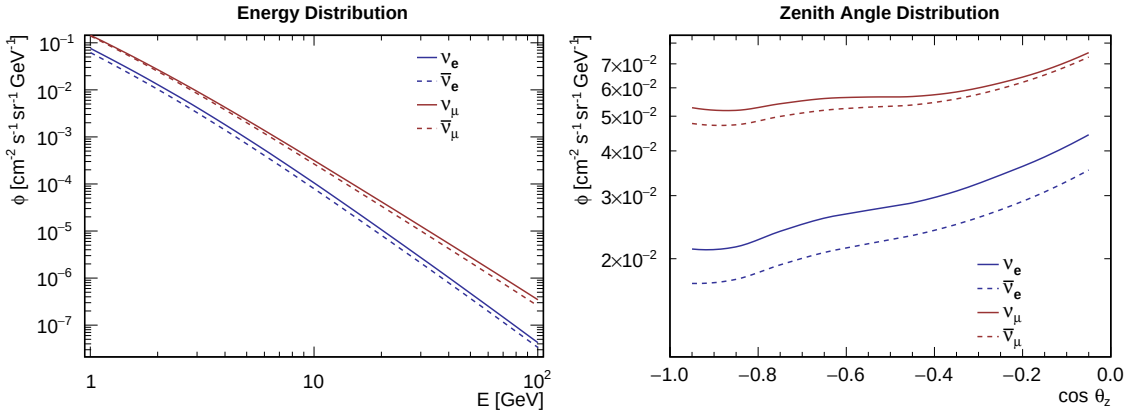

Figure 5.1: Atmospheric neutrino flux as the function of energy (left) and cosine zenith angle (right). The plots are presented for upgoing neutrinos since this sample is of interest for the oscillation studies.

The chosen flux has been computed for the Gran Sasso site which is located in the neighbor of the ORCA detector. In the case of SWIM framework, the tabulated fluxes are transferred into the form of 2D histograms then one can use bilinear interpolation to extract the flux values of any user-defined bins and apply them into Eq. (5.4). Fig. 5.1 shows all flavors of atmospheric neutrino flux as a function of energy and cosine zenith angle.

5.1.2 Oscillation probability calculator: OscProb

The probabilities are computed using the custom-built software OscProb [124], which uses a radial model of the Earth with 42 concentric shells of constant electron density, for which mass density values are fixed and follow the Preliminary Reference Earth Model (PREM) [125]. To reflect the location of the ORCA detector, 3 km deep under the sea, the outermost shell (with radius between 6368 km and 6371 km) has been set to the density of water. Since most of atmospheric neutrinos are produced at an altitude of about 15 km in the atmosphere [68], an additional shell of atmosphere with the corresponding depth is added to the model, with the assumption that all the neutrinos are created at the top of this shell.

Each shell is characterized by a given chemical composition described in terms of the weight fraction w of each chemical element, and of the corresponding proton-to-nucleon ratio Z/A where Z and A are the atomic number and atomic weight of the element. Based on this, the electron number density (in units m^{-3}) for each shell can be computed as:

$$n_e = \left(\sum_i w_i \frac{Z_i}{A_i} \right) \times \frac{N_A}{10^{-3}\text{kg.mol}^{-1}} \times \rho, \tag{5.1}$$

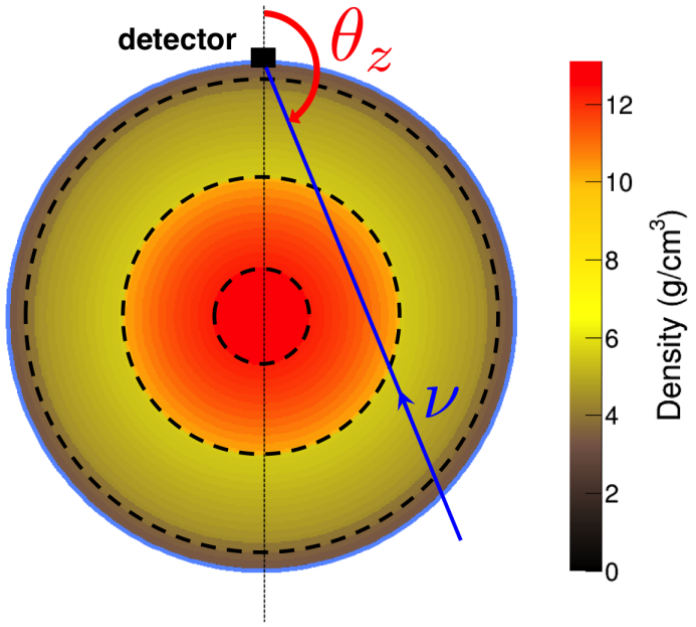

Figure 5.2: Skematic of an atmospheric neutrino transversing through the Earth in PREM model and coming to the detector.

where the index i runs over all elements in the shell. N_A and ρ are respectively the Avogadro number and the mass density in kg.m^{-3}.

For a given zenith angle, the package can determine the trajectory of the neutrino traversing the Earth and reaching the detector as depicted in Fig .5.2. Then by knowing the neutrino energy and electron density of each shell, the transition probability of the neutrino can be determined by diagonalizing the evolution operator in each constant density layer of the PREM model following the oscillation formula presented in Eq. (1.41).

5.1.3 Neutrino cross-section

In the SWIM framework, it requires the elasticity differential cross section, which can be computed as:

$$\frac{d\sigma_{\nu_x}}{dy}(E, y) = \sigma_{\nu_x}(E) \cdot P_E(y) \tag{5.2}$$

where $\sigma_{\nu_x}(E)$ is the total cross-section as a function of the neutrino energy and $P_E(y)$ is the probability distribution of an interaction of inelasticity y (or Bjorken-y) at the neutrino energy E. The total cross-section can be extracted from the mentioned neutrino interaction generator GENIE as the weighted sum of neutrino-nucleon cross-sections for each water

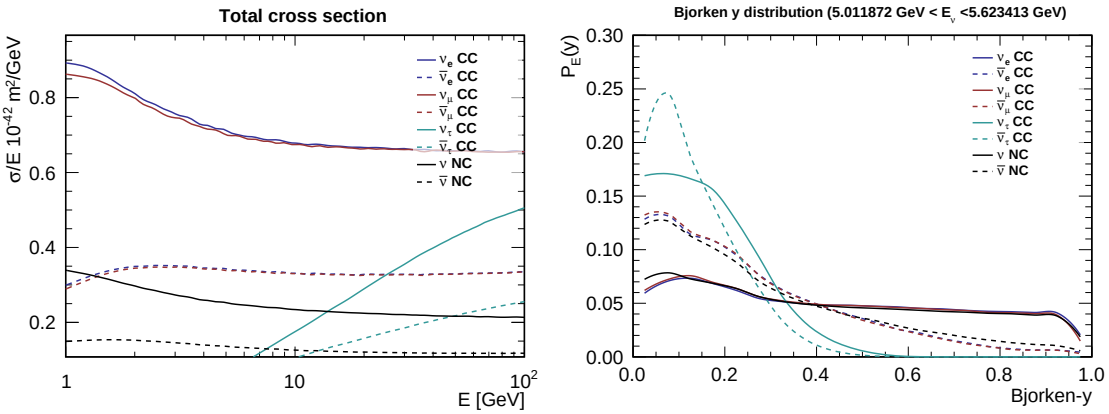

Figure 5.3: Total cross-section as a function of energy (left) and the normalized Bjorken-y probability distribution in one slice of energy (right).

molecular component:

$$\sigma_{\nu_x}(E) = \frac{2\sigma(^1_1\mathrm{H}) + \sigma(^{16}_8\mathrm{O})}{18}. \tag{5.3}$$

The 2D probability distribution of Bjorken-y $P_E(y)$ is then obtained from the ORCA Monte Carlo sample. Since the gSeaGen package stores the true energy and Bjorken-y of every neutrino interaction, one can extract $P_E(y)$ by filling a histogram of neutrino events in 2 dimensions of energy and Bjorken-y then normalizing the whole distribution by the total number of filled events. In Fig. 5.3, the total cross-section and Bjorken-y distribution used in SWIM are shown.

5.1.4 The interacting event distribution

For oscillation analyses, the measurement of the energy and baseline (equivalent in this case to the zenith angle) of the events is of particular interest. Another valuable parameter is the Bjorken inelasticity (or Bjorken-y) which describes the fraction of neutrino energy transferred to the hadronic shower. Because the cross-section as a function of Bjorken-y is different for neutrino and anti-neutrino, measuring y would lead to the ability of separating statistically the polarization information of neutrinos. The interacting event rate is therefore computed as a binned distribution on three variables: the energy, the zenith angle and the Bjorken-y, following the formula taken from Ref. [122]:

$$\frac{dn^{\nu_x}_{int}}{dMdt}(E,\theta,y) = \Delta y \cdot \frac{d\sigma_{\nu_x}}{dy}(E,y) \cdot \sum_{\nu_\alpha} 2\pi \cdot \Delta E \cdot \Delta(\cos\theta) \cdot P_{osc}(\nu_\alpha \to \nu_x) \cdot \frac{d\Phi_{\nu_\alpha}}{dEd(\cos\theta)d\phi}(E,\theta), \tag{5.4}$$

where E, θ, y are respectively the true energy, zenith angle and inelasticity of the neutrino interaction. The components of the formula are defined as follows:

- ν_x is the interaction channel which is one of 8 channels:
  - 6 charged current interaction channels: $\overset{(-)}{\nu_e}$ CC, $\overset{(-)}{\nu_\mu}$ CC, $\overset{(-)}{\nu_\tau}$ CC
  - 2 neutral current interaction channels: $\overset{(-)}{\nu}$ NC (resulting from the fact that NC interaction is insensitive to the neutrino flavor).
- ν_α is the initial atmospheric neutrino flavor. $\nu_\alpha \in \{\nu_e, \nu_\mu\}$ since the atmospheric ν_τ component is negligible in the range of energies probed by ORCA.
- $\frac{d\Phi_{\nu_\alpha}}{dEd(\cos\theta)d\phi}(E, \theta)$ is the differential of atmospheric neutrino flux by energy (E), cosine zenith angle ($\cos\theta$), and azimuth angle (ϕ).
- $P_{osc}(\nu_\alpha \to \nu_x)$ is the probability of oscillation from ν_α to ν_x along their path through the Earth. For saving computational time, this quantity is set to 1 for NC interaction channels because of their insensitivity to the neutrino flavor.
- $\frac{d\sigma_{\nu_x}}{dy}(E, y)$ is the differential cross-section with respect to the Bjorken-y for a neutrino of energy E and inelasticity y interacting in the ν_x channel.
- Δy, ΔE, $\Delta(\cos\theta)$ represent the bin width in E, θ and y, accounting for the integration on these three variables. The factor 2π comes from the integration on azimuth angles which is factored out because there are no dependence of oscillation probability and cross-section on this variable as well as it gives no sensitivity to the oscillation.

The rate here is computed as the number of interacting events per unit exposure, which is defined as the product of target mass by the duration of the experiment (usually expressed in units *Megaton* $\times$ *years* for ORCA).

From the described external input, one can then compute the interacting event rate following the formula (5.4). In Fig. 5.4, the distributions of the neutrino event rate as the function of true E and $cos\theta$ are shown for 4 combined channels: $\nu_e + \bar{\nu}_e$ CC, $\nu_\mu + \bar{\nu}_\mu$ CC, $\nu_\tau + \bar{\nu}_\tau$ CC, $\nu + \bar{\nu}$ NC. The ν_τ CC events only appear above ~ 3 GeV due to the threshhold energy of creating τ particles. In these distribution, one can also notice the effect of the discontinuity in matter distribution at the core-mantle boundary of the Earth as a discrete pattern observed at $\cos\theta \sim -0.85$.

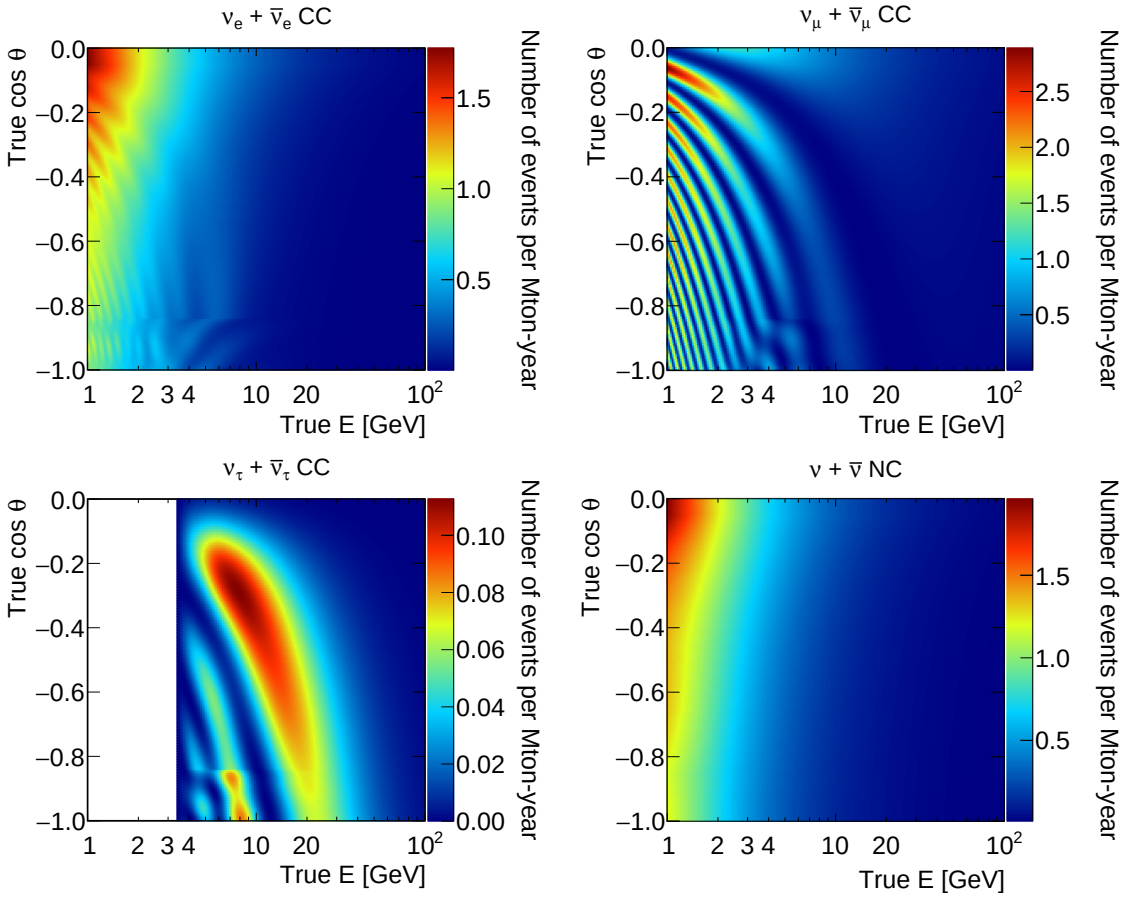

Figure 5.4: True $(E, \cos\theta)$ distribution of neutrino events in 4 combined channels: $\nu_e + \bar{\nu}_e$ CC, $\nu_\mu + \bar{\nu}_\mu$ CC, $\nu_\tau + \bar{\nu}_\tau$ CC, $\nu + \bar{\nu}$ NC

5.2 Detector response model in SWIM

The previous section describes the computation of the interaction rate. The next step is to transfer these interacting event distributions into the measured distribution detected by the detector. This requires the response model of the detector. In the case of SWIM, a full Monte Carlo approach is adopted to build the detector response in which the whole detector response information is taken directly from a MC simulated sample.

This approach is different from the one developed in other frameworks of the collaboration such as paramNMH and MONA which have been used for published results in Refs. [98, 123]. paramNMH models the detector response as parametrized functions and then fits them with the given MC sample [116]. MONA uses a full MC approach similar to SWIM, but with a different implementation based on RooFit [126] and a different treatment of some systematics. Keeping a good agreement between frameworks is an important validation step for all official physics results to be issued on behalf of the KM3NeT

Collaboration. During my PhD, I was in charge of producing the corresponding results with SWIM and I took an active part in the comparison and cross-checking process between analysis framework. A specific comparison between SWIM and paramNMH for the oscillation analysis is presented in Chap. 8.

5.2.1 The Response Matrix

Once obtained the MC samples, they can be injected into SWIM for building the detector response model and finally obtaining the expected event distribution as observed by the detector. SWIM uses a binned detector response matrix built from the MC sample that maps the events generated with interaction type ν_x and true variables (E, θ, y) into the corresponding reconstructed variables (E', θ', y') and PID classes denoted here as index i. This matrix, as is defined in Eq. (5.5), is calculated using the number of generated events ($N^{\nu_x}_{gen}(E, \theta, y)$) for a given true energy, zenith angle, inelasticity and interaction type ν_x ($\overset{(-)}{\nu}_e$ CC, $\overset{(-)}{\nu}_\mu$ CC, $\overset{(-)}{\nu}_\tau$ CC, $\overset{(-)}{\nu}$ NC) and the number of those events $N^{\nu_x \to i}_{sel}(E, \theta, y; E', \theta', y')$ that were reconstructed with a given E', θ', y' and into a specific PID bin i (i = Track, Shower, Intermediate).

$$R^{[\nu_x \to i]}(E, \theta, y; E', \theta', y') = \frac{N^{\nu_x \to i}_{sel}(E, \theta, y; E', \theta', y')}{N^{\nu_x}_{gen}(E, \theta, y)}. \tag{5.5}$$

The 8-dimensional matrix is built using MC-generated events and the outcome of their processing through the reconstruction and classification algorithms so that the ensemble of matrices account for detection and reconstruction efficiencies, misidentification probabilities, and errors on reconstructed variables (including all correlations). By using the response matrix to convolute the interaction event rate, the final detected event distribution is obtained as follows:

$$n^i_{reco}\underbrace{(E', \theta', y')}_{\text{reco variables}} = T \sum_{\nu_x, E, \theta, y} R^{[\nu_x \to i]}(E, \theta, y; E', \theta', y') \times M_{ref} \times \frac{dn^{\nu_x}_{int}}{dMdt}\underbrace{(E, \theta, y)}_{\text{true variables}}, \tag{5.6}$$

where $n^i_{reco}(E', \theta', y')$ is the number of events in the bin of reconstructed (E', θ', y') and classified into the PID class i. T is the exposure time and $\frac{dn^{\nu_x}_{int}}{dMdt}$ is the interaction rate described in Eq. 5.4. M_{ref} is so called the reference mass which is the mass associated to a reference volume used for the selection of generated events. The reference volume should be chosen to be equal or smaller than the generation volume of the MC simulation, so that the ratio $M_{ref}/N^{\nu_x}_{gen}$ does not depend on the size of the volume.

The response matrix can also be factorized into 3 components as follows:

$$R^{[\nu_x \to i]}(E, \theta, y; E', \theta', y') = p_{reco}^{\nu_x \to i}(E, \theta, y, E', \theta', y') \cdot P_{PID}^{\nu_x \to i}(E, \theta, y) \cdot \frac{M_{eff}^{\nu_x}(E, \theta, y)}{M_{ref}}, \tag{5.7}$$

They are correspondingly:

- The *effective mass* which describes the efficiency of the detector towards neutrino detection. It represents the mass of the target volume where neutrino interactions will generate events successfully passing the trigger, selection, and reconstruction stages.

$$M_{eff}^{\nu_x}(E, \theta, y) = M_{ref} \frac{\sum_{i,E',\theta',y'} N_{sel}^{[\nu_x \to i]}(E, \theta, y; E', \theta', y')}{N_{gen}(E, \theta, y)} \tag{5.8}$$

- The *reconstruction probability* which tells us the probability of a selected event in PID bin i with true information (E, θ, y) to be reconstructed with the values (E', θ', y').

$$p_{reco}^{\nu_x \to i}(E, \theta, y; E', \theta', y') = \frac{N_{sel}^{[\nu_x \to i]}(E, \theta, y; E', \theta', y')}{\sum_{E',\theta',y'} N_{sel}^{\nu_x \to i}(E, \theta, y; E', \theta', y')} \tag{5.9}$$

- The *PID probability* which presents the probability of an event with true information (E, θ, y) to be classified into a PID class i.

$$P_{PID}^{\nu_x \to i}(E, \theta, y) = \frac{\sum_{E',\theta',y'} N_{sel}^{[\nu_x \to i]}(E, \theta, y; E', \theta', y')}{\sum_{i,E',\theta',y'} N_{sel}^{[\nu_x \to i]}(E, \theta, y; E', \theta', y')} \tag{5.10}$$

Fig. 5.5 shows the effective mass after trigger and selection cuts as a function of neutrino energy for different neutrino flavors and interaction channels obtained from the MC sample 'ORCA115_20x9_190222'. The effective masses all start at zero for low energy $\sim$ 1 GeV and increase with the energy of the neutrinos. For the ν_e, ν_τ, and ν NC events, it reaches a plateau at high energy as there are containment conditions for the shower events. For ν_μ CC events, as they produce longer tracks and looser containment conditions are applied, the effective mass for this type of event can still increase with the ν_μ energy. The effective masses of the $\bar{\nu_\mu}$ and $\bar{\nu_e}$ are larger than the ones of ν_μ and ν_e for the CC interaction type. This is due to the Bjorken-y distribution of anti-neutrinos being more peaked towards low value of Bjorken-y than the one of the neutrinos, as shown in Fig. 5.3. Since the Bjorken-y represents the inelasticity of the interaction, this means that a $\bar{\nu}_{e/\mu}$ CC tends to transfer less

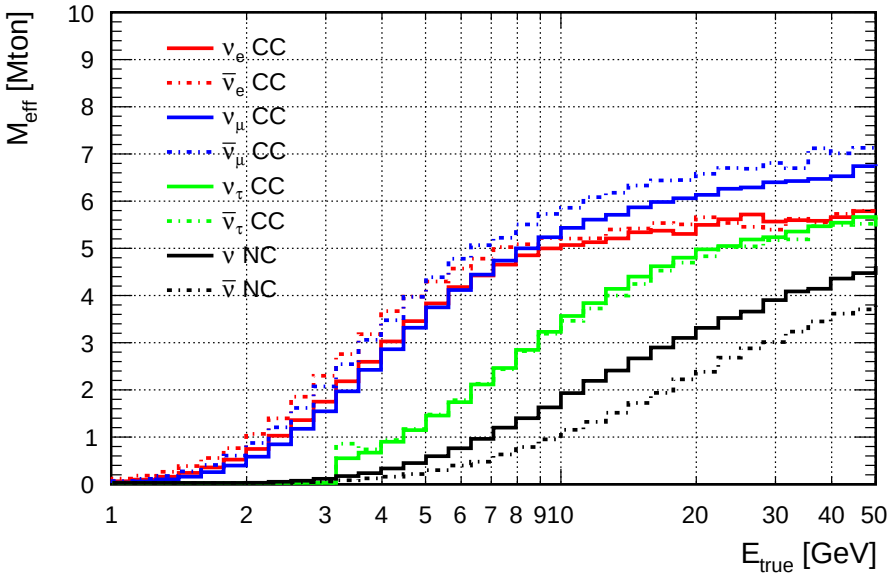

Figure 5.5: Effective mass of the detector obtained from the 'ORCA115_20x9_190222' MC sample as the function of neutrino energy for different neutrino flavours and interactions.

energy to the hadronic shower than a $\nu_{e/\mu}$ CC and thus produces in average a lepton with a higher energy, hence also a higher amount of emitted light. The feature is reversed for NC interactions because the higher energy transferred to an outgoing antineutrino (as opposed to neutrino) does not translate into any increase in the light signal. On the contrary, the lower inelasticity of the antineutrino interaction will result in less light produced by the hadronic shower.

In Fig. 5.6 and Fig. 5.7, an example of PID and reconstruction probability (for Dusj as an example) is shown with the cut at *track_score* > 0.5 to be defined as *tracks* and *track_score* ≤ 0.5 as *showers*. Both figures are extracted directly from the MC sample 'ORCA115_20x9_190222'. The classifier (or PID) guarantees $\sim 60\%$ of muon neutrinos classifed as *tracks* at low energy and $> 80\%$ above 10 GeV while the electron neutrino contamination in *tracks* sample is below 20% in the whole energy range of interest. The accountance of the hit-based PDF improves the performance of the classification as mentioned in the previous section. For the reconstruction probability, the figures depict the energy resolution to be Gaussian-like with a saturation observed for muon neutrinos at high energy due to most of the muon tracks are not fully contained in the detector instrumented volume.

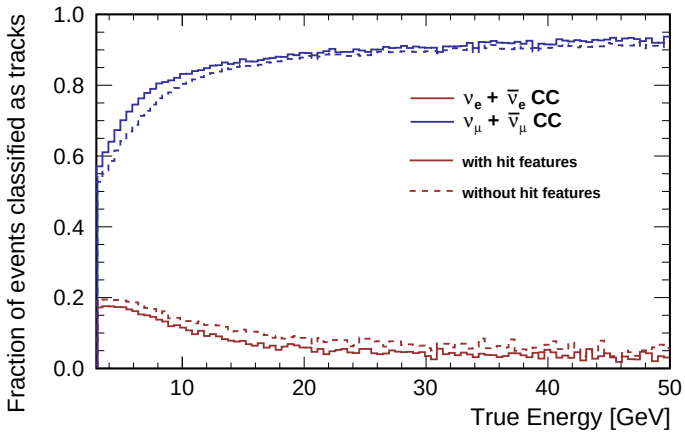

Figure 5.6: PID probability of electron and muon neutrino CC events classified as tracks obtained from the MC sample 'ORCA115_20x9_190222'. The performance is improved when including the hit-based PDF (solid) compared to the previous one without the hit-based features (dashed).

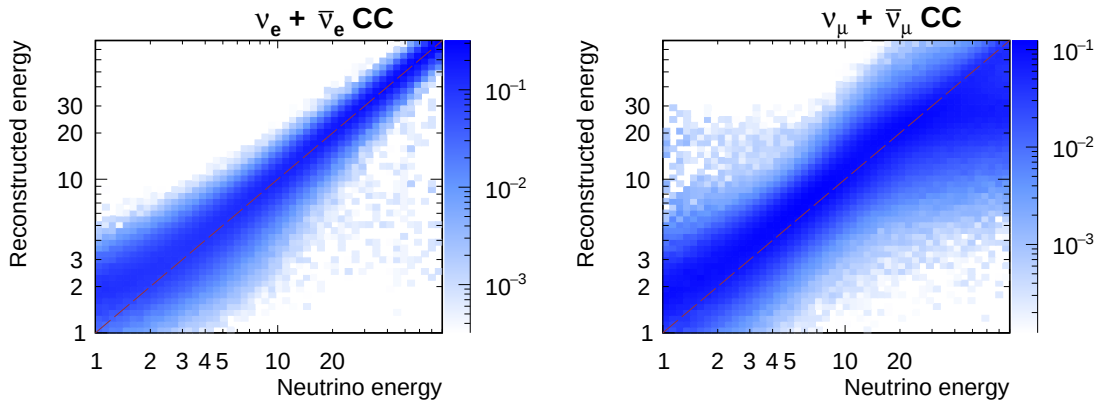

Figure 5.7: Reconstruction probability as a function of reconstructed and true neutrino energy for electron-neutrino CC events classified as showers (left) and muon-neutrino events classified as tracks (right) using the Dusj algorithm, as obtained from the MC sample.

While the response matrix method of SWIM ensures that all the information on the detector response is taken into account as obtained from the MC simulation, its accuracy depends on the size of the MC sample. A detailed study of the effects of MC fluctuation to oscillation analyses with ORCA can be found in Ref. [120]. This study leads to the account for statistical fluctuations in the MC production using the Beeston-Barlow light method [127], that will be described in the next chapter.

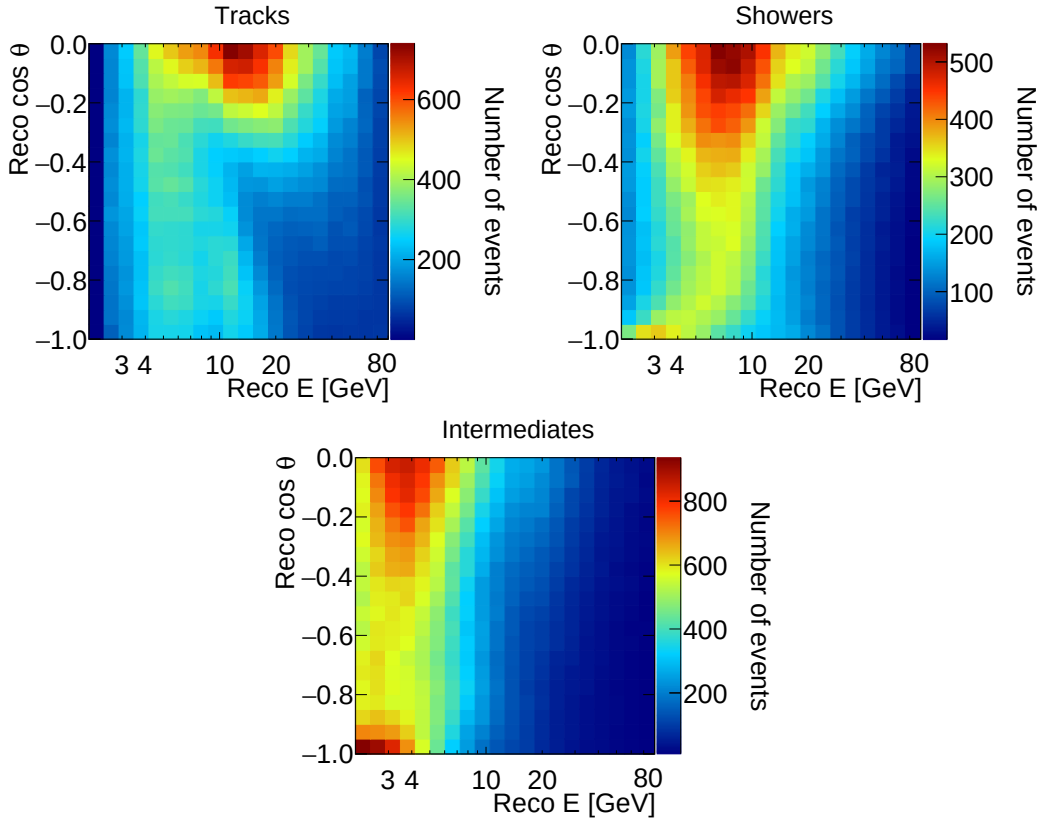

Figure 5.8: Expected event distributions for ORCA in the 3 PID classes for 3 years of exposure and true NO assumption, with the oscillation parameter values from Ref. [128].

5.2.2 Expected event distributions

The expected event distribution can then be computed following Eq. (5.6). Fig. 5.8 shows an example of the expected event distributions in the 3 PID classes as presented in Sec. 3.3.3 for 3 years of data taking assuming normal ordering and oscillation parameters from the global fit of Ref. [128]. Compared with the distribution shown in Fig. 5.4, one can see the effect of applying the detector responses to the interaction rate. The features of the interaction distributions are smeared out due to the reconstruction resolution of the detector. For example, the ripple structure in $\nu_\mu + \bar{\nu}_\mu$ CC channel is no longer visible in the Track class. Additionally, in the interaction rates, the highest event population is in the low energy region of $\sim$ 1 GeV while in the expected event distribution, the most populated region is shifted to the higher energy. This is due to the fact that the efficiency of the detector is very low in the few-GeV region and only increases at higher energy, as depicted in the effective mass plot shown in Fig. 5.5.

Chapter 6

Statistical method for the sensitivity evaluation

Contents

The previous chapter describes how one can obtain the expected event distributions measured by the detector under a given set of hypotheses regarding the underlying physical model (e.g., NO or IO) and input parameters (e.g., neutrino fluxes, oscillation parameters,...). The next step is to fit the hypothesis to measured data and extract the sensitivity of the data towards the desired physics phenomena, which in the context of this work are the neutrino mass ordering and the oscillation parameters, as presented in Part IV.

A detailed description of the sensitivity estimation in the case of oscillation studies with ORCA can be found in Ref. [122]. In this chapter, we summarize the statistical method which is used in SWIM and applied throughout this thesis. This Chapter presents the mathematical basis for the computation of the ORCA sensitivity to the NMO and the oscillation parameters that will be performed in the final Part of this manuscript. It also includes a discussion about the method to account for uncertainties due to MC statistical fluctuations.

6.1 Calculation of the neutrino mass ordering sensitivity

6.1.1 A brief review on frequentist hypothesis testing

In the concept of hypothesis testing, we want to decide whether a hypothesis is accepted or rejected with an observation or a set of data. The hypothesis under test is called the *null hypothesis* H_0. Additionally, we can only accept or reject a hypothesis by saying whether it is favourable or unfavourable in comparison with an *alternative hypothesis* H_1.

One first has to define a *test statistic* T which is a function of data and of the expectation from a given hypothesis. The test statistic is defined such that the larger (or smaller) the value of T, the more powerful the outcome of rejecting the null hypothesis. Since the measurement from an experiment usually involves multiple random processes as well as statistical fluctuations, the expectation from a hypothesis is also a set of random numbers, which implies that the test statistic is a random number as well. Under an assumed hypothesis H, the PDF of the test statistic, denoted as $p(T|H)$, can be completely defined.

Knowing the PDF of the test statistic, one then defines a critical value T_c^α such that if the observation yields a value $T_{obs} > T_c^\alpha$, then the null hypothesis is rejected. For a given value of T_c^α, the probability α that a random observation will fall into the critical region $T_{obs} > T_c^\alpha$ is computed as:

$$\alpha = \int_{T_c^\alpha}^{\infty} p(T|H_0)dT. \tag{6.1}$$

α is called the probability of error of the first kind (i.e., rejecting H_0 when it is true) or *significance level* of the test on H_0. The probability $1-\alpha$ is the *confidence level* (CL) of accepting H_0 if it is true, also called *size* of the test. In particle physics, it is the convention to convert α into a number of Gaussian standard deviations such that α represents the integral from $S\sigma$ away on one side of the standard Gaussian function. Such conversion reads:

$$\alpha = \frac{1}{\sqrt{2\pi}} \int_S^\infty dx\, e^{\frac{-x^2}{2}} = \frac{1}{2}\text{erfc}\left(\frac{S}{\sqrt{2}}.\right), \tag{6.2}$$

where erfc is the complementary error function. The significance in terms of σ then yields:

$$S = \sqrt{2}\,\text{erfc}^{-1}(2\alpha). \tag{6.3}$$

According to this relation, the corresponding CL $(1-\alpha)$ for $1,2,3\sigma$ is respectively 84.14%, 97.73%, and 99.87%[1].

Another quantity of interest is the probability to accept H_0 when the alternative hypothesis H_1 is true instead of H_0:

$$\beta = \int_{-\infty}^{T_c^\alpha} p(T|H_1)dT. \tag{6.4}$$

β is the probability of error of the the second kind and $(1-\beta)$ is called the *power* of the test.

Fig. 6.1 shows an illustration of the PDFs of the test statistic under the assumption of the null hypothesis H_0 and the alternative hypothesis H_1 together with the probabilities of making an error of the first kind α and second kind β. It is notable that both the size (α) and the power $(1-\beta)$ of the test depend on the choice of the critical value T_c^α. In particle physics, we usually adopt the concept of *median sensitivity* in which the critical value T_c^α is chosen as the median of the test statistic assuming true alternative (H_1) hypothesis. This results in the power of the test to be 50%.

6.1.2 Test statistic definition for the determination of NMO

Before presenting the NMO sensitivity evaluation, it is necessary to describe the test statistic used in this work. Assuming a predicted event distribution η under a given hypothesis and Poisson statistics for each bin of the measured event number, the likelihood for ob-

[1]Sometimes the two-sided Gaussian convention is also used which leads to a different correspondence of $1,2,3\sigma$ with 68.27%, 95.45%, and 99.73%.

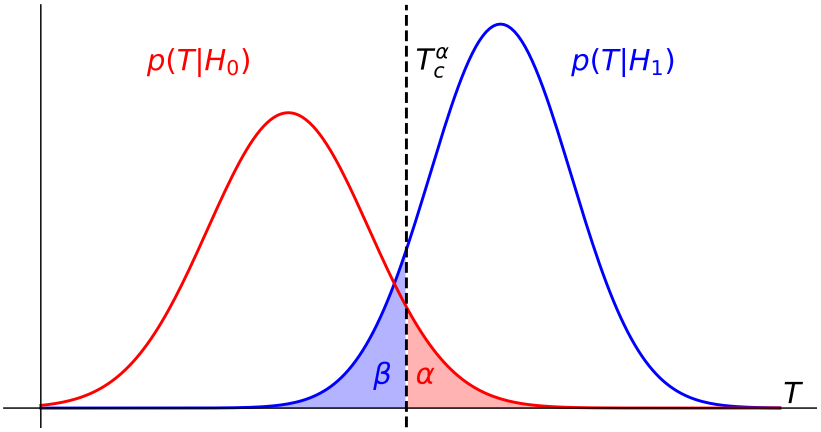

Figure 6.1: An illustration of the PDFs of the test statistic under the assumption of the null hypothesis H_0 and the alternative hypothesis H_1. The probabilities of making an error of the first kind α and second kind β corresponding to a critical value T_c^α are also shown.

taining the observed data d is given by:

$$\mathcal{L}_{\text{stat}}(d|\eta) = \prod_i \exp(\eta_i) \frac{\eta_i}{d_i!}, \tag{6.5}$$

where d_i, η_i are correspondingly the observed data and expectation under a hypothesis at bin i. In the case of ORCA, the data and expectation are binned under the PID classes and three reconstructed variables: energy, cosine zenith angle, and inelasticity, yielding distributions as shown in Fig. 5.8. The expression (6.5) is usually referred to as the *statistical likelihood*. In reality, the expected distribution can be affected by other parameters that are not of interest for the measurement, referred to as the *systematics parameters* and which will be discussed in Chap. 7. They are also called the *nuisance parameters* (denoted here as p) and sometimes are constrained by other experiments. To account for this, a second factor dubbed as *prior likelihood* is introduced, so that the complete likelihood reads:

$$\mathcal{L}(d|\eta) = \mathcal{L}_{\text{stat}}(d|\eta) \times \mathcal{L}_{\text{syst}}, \tag{6.6}$$

where $\mathcal{L}_{\text{syst}}$ is defined as:

$$\mathcal{L}_{\text{syst}} = \prod_j \frac{1}{\sqrt{2\pi\sigma_j^2}} \exp\left(-\frac{(p_j - p_j^0)^2}{2\sigma_j^2}\right). \tag{6.7}$$

This factor constrains each nuisance parameter p_j by a Gaussian PDF with mean value p_j^0 and variance σ_j. One can see that the larger the likelihood, the better agreement between

the data and the hypothesis.

In the case of testing the NMO hypothesis, one considers one ordering as the null hypothesis and the other ordering as the alternative one, or vice-versa. As an example, to determine whether we can reject IO (as the null hypothesis) when assuming NO (as the alternative one), the chosen test statistic is the so-called $\Delta\chi^2$ which is defined based on the log-likelihood ratio as follows:

$$\Delta\chi^2_{NO} = -2\ \ln\left(\frac{\max_\eta \mathcal{L}_{IO}(d|\eta)}{\max_\eta \mathcal{L}_{NO}(d|\eta)}\right) \tag{6.8}$$

$$= \min_\eta[-2\ln\mathcal{L}_{IO}(d|\eta)] - \min_\eta[-2\ln\mathcal{L}_{NO}(d|\eta)]. \tag{6.9}$$

One would then try to find the parameter configuration η of the hypotheses that minimizes the terms in brackets in eq. (6.9). In the SWIM framework, this is done through the implementation of a fitting procedure based on the MINUIT2 library [129]. The definition of $\Delta\chi^2$ is conventional such that it follows the χ^2 distribution and can be converted directly into a significance level as will be discussed later.

In practice, in the case of testing IO (NO) with respect to NO (IO) the $\Delta\chi^2$ is reformulated as follows:

$$\Delta\chi^2_{NO(IO)} = \min_\eta\left[\chi^2(d|\eta_{IO(NO)})\right] - \min_\eta\left[\chi^2(d|\eta_{NO(IO)})\right], \tag{6.10}$$

where the $\chi^2(d|\eta)$ reads:

$$\chi^2(d|\eta) = -2\sum_i\left(d_i - \eta_i - d_i ln\frac{d_i}{\eta_i}\right) + \sum_j \frac{(p_j - p_j^0)^2}{\sigma_j^2}, \tag{6.11}$$

as obtained from the expressions of the statistical likelihood (first term) and the prior likelihood (second term) given in Eq. 6.5 and 6.7. A detailed derivation from Eq. (6.9) to Eq. (6.10) can be found in Ref. [122].

6.1.3 Evaluation of NMO sensitivity with pseudo-experiments

Following the procedure in Sec. 6.1.1, the PDFs of the test statistic (6.10) under the NO and IO hypothesis need to be calculated in order to quantify the NMO sensitivity. In practice, it can be done by generating a large number of pseudo-experiments (PEs) to simulate as much as possible all the possible outcomes of the real measurement. The procedure can be as follows:

- For a given hypothesis (NO or IO), one first defines the corresponding true parameters that represent the hypothesis. Then these parameters can be allowed to vary following Gaussian constraints based on external measurements from other experiments. This is to take into account the uncertainties in the theoretical models.
- Then using the fluctuated true parameters, the expected event distributions are computed following the procedure described in Chap. 5.
- The expected event numbers in each bin are then redrawn following Poisson distribution with the mean equal to the expected value computed in the previous step. This step is to account for the statistical fluctuations in the measurement. The obtained event distribution then represents for one PE.
- A large number of PEs is produced following the above steps. For each PE, the test statistic $\Delta\chi^2$ is computed and then the distribution of $\Delta\chi^2$ can be obtained.

As pointed out in Ref. [130] and shown for the case of ORCA in Ref. [122], the test statistic $\Delta\chi^2$ follows a normal distribution in both cases of NO and IO. Therefore, the corresponding PDFs obtained with the PEs can be fitted with a standard normal distribution to obtain the mean $\mu_{IO(NO)}$ and the variance $\sigma_{IO(NO)}$ corresponding to the IO (NO) assumption respectively. One can then compute the significance level for rejecting IO (NO) with the alternative hypothesis of NO (IO) following Eq. 6.1 as:

$$\alpha = \int_{T_c}^{\infty} p\left(T = \Delta\chi^2 | IO(NO)\right) dT = \int_{T_c}^{\infty} \frac{1}{\sqrt{2\pi\sigma^2_{IO(NO)}}} e^{-\frac{\left(T-\mu_{IO(NO)}\right)^2}{2\sigma^2_{IO(NO)}}} dT. \tag{6.12}$$

As mentioned in Sec. 6.1.1, the median sensitivity is obtained with the critical value chosen as the median of the test statistic distribution assuming true alternative hypothesis which in this case is also the mean: $T_c = \mu_{NO(IO)}$. Thus, one can rewrite the integration in Eq. (6.12) as:

$$\begin{aligned} \alpha &= \int_{\mu_{NO(IO)}}^{\infty} \frac{1}{\sqrt{2\pi\sigma^2_{IO(NO)}}} e^{-\frac{(T-\mu_{IO(NO)})^2}{2\sigma^2_{IO(NO)}}} dT \\ &= \int_{\frac{\left(\mu_{NO(IO)}-\mu_{IO(NO)}\right)^2}{2\sigma^2_{IO(NO)}}}^{\infty} \frac{1}{\sqrt{\pi}} e^{-x^2} dx. \end{aligned} \tag{6.13}$$

Comparing with Eq. (6.2), one can derive the significance in terms of number of σ for excluding IO (NO) with a given assumption NO (IO) as:

$$S_{NO(IO)} = \frac{\mu_{IO(NO)} - \mu_{NO(IO)}}{\sigma_{IO(NO)}} [\sigma] \tag{6.14}$$

The test statistic values T_{obs} for the observation (or data) can then be computed and compared with the critical value T_c. If $T_{obs} > T_c$, we can conclude the rejection of the ordering under test, with a significance computed as (6.14).

For the case of a full ORCA detector (ORCA115) or the sub-array of 7DUs (ORCA7), since the data d is not available yet, one can replace it by pseudo-data in order to predict the physics potential of the detector before the actual experiment is realized. This is done by first simulating the expected distribution under the alternative hypothesis (which is now assumed to be the true one). After that, to mimic the statistical fluctuations, the values at each bin are randomly resampled following Poisson distribution with mean values equal to the computed expectation value.

6.1.4 The Asimov dataset approach

The above method of PEs would be CPU-expensive to precisely define the PDFs of the test statistics. Throughout this thesis, we adopt instead an alternative method which is called the *Asimov dataset*. In this approach, the fluctuated pseudo-data d is replaced by the expectation of a true assumption η_{NO} or η_{IO}. This results in the second term of (6.10) to vanish as the pseudo-data matches exactly with the correct assumed hypothesis. Then, the $\Delta\chi^2$ for the Asimov dataset, which is usually denoted as $\overline{\Delta\chi^2}$, reduces to one single term:

$$\overline{\Delta\chi^2}_{NO} = \min_{\eta_{IO}} \left[\chi^2(\eta_{NO}|\eta_{IO})\right], \text{with NO true assumption.} \tag{6.15}$$

$$\overline{\Delta\chi^2}_{IO} = \min_{\eta_{NO}} \left[\chi^2(\eta_{IO}|\eta_{NO})\right], \text{with IO true assumption.} \tag{6.16}$$

In this case, the significance in terms of number of σ to exclude the wrong ordering assuming a given true ordering is commonly estimated as:

$$S_{Asimov} = \sqrt{\overline{\Delta\chi^2}}\ [\sigma]. \tag{6.17}$$

This estimation is based on Wilk's theorem which states that if the alternative hypothesis is true, the $\Delta\chi^2$ would follow a χ^2 distribution with a single degree of freedom [131, 132]. Thus, from Eq. (6.1) and Eq. (6.2), one can derive the above formula (6.17).

Nevertheless, as discussed in Ref. [133, 134], the condition for Wilk's theorem might not hold due to the discrete nature of the NMO. According to Ref. [135] and [130], the test statistic in this case follows a normal distribution: $\mathcal{N}(\pm\overline{\Delta\chi^2}, 2\sqrt{\overline{\Delta\chi^2}})$ with $+(-)$ for true NO (IO). Following Eq. 6.3, one can then derive the significance for rejecting IO(NO) in the

case of true NO(IO):

$$S_{NO(IO)} = \sqrt{2}\text{erfc}^{-1}\left[\text{erfc}\left(\frac{\overline{\Delta\chi^2}_{IO} + \overline{\Delta\chi^2}_{NO}}{\sqrt{8\overline{\Delta\chi^2}_{IO(NO)}}}\right)\right]. \tag{6.18}$$

This formula is different from Eq. (6.17) and only yield the same value if $\overline{\Delta\chi^2}_{IO} \simeq \overline{\Delta\chi^2}_{NO}$. As will be shown later in Chap. 8, the condition $\overline{\Delta\chi^2}_{IO} \simeq \overline{\Delta\chi^2}_{NO}$ only holds for the lower octant of θ_{23}. In the upper octant, the evaluation using Eq. (6.17) can lead to an underestimation of the sensitivity. As shown in Ref. [120, 122], compared to the actual PEs method, this effect of underestimation is $\sim 1.5\sigma$. Nevertheless, this approach can still be used as a quick and acceptable estimation for the sensitivity and will be adopted throughout of this thesis.

6.2 Calculation of the parameter sensitivity

Another important physics target of ORCA and also one subject of this thesis is the measurement of atmospheric oscillation parameters Δm^2_{31} and θ_{23}. The potential of full ORCA and ORCA with 7 DUs towards the measurement of these parameters is presented in Chap. 8. Here, we give a brief review of the method used for this study.

The objective of evaluating the sensitivity of the experiment to the oscillation parameters is to construct the confidence intervals. We denote θ as the interest parameter of the measurement and other fitted parameters as p which are so-called *nuisance parameters*. θ can be estimated as the value that minimizes the Poissonian χ^2:

$$\Delta\chi^2_\theta = \text{min}_p[\chi^2(d|\theta, p)] - \text{min}_{\theta,p}[\chi^2(d|\theta, p)], \tag{6.19}$$

where the first term is minimized by fitting both θ and p. The last term is fitted with only nuisance parameters p while keeping θ fixed as an assumed value. The notation $\chi^2(d|\theta, p)$ represents for the defined χ^2 function between data d and a hypothesis which is completely determined by parameters θ and p. One then can generate multiple PEs, similarly to the description in the last section, to obtain the PDF of the best-fit θ, repeat this to a series of the assumed value of θ, and finally apply the Neyman's confidence belt construction as described in detail in Ref. [136] and [137].

In this work, similar to the NMO sensitivity evaluation, we also adopt the Asimov dataset approach as an alternative method in which the pseudo-data is replaced by the expectation under a assumed true resulting in the vanish of the second term in the $\Delta\chi^2$. The confidence level (in term of σ) at a test value θ_{test} with a given true value θ_{true} is

computed as follows:

$$S_{Asimov} = \sqrt{\min_p \chi^2(\mu_{\theta_{test}}|\theta_{true}, p)} \tag{6.20}$$

6.3 Accounting for Monte-Carlo uncertainty

As mentioned in the previous section, fluctuation in the Monte Carlo simulation can be taken into account in the fit by adopting the 'Beeston and Barlow light method'. Assuming the fluctuation leads to the variation of expectation as

$$\mu'_k = \beta_k \mu_k \tag{6.21}$$

with β_k is normally distributed:

$$\beta_k \sim \mathcal{N}(1, \sigma_k^2). \tag{6.22}$$

Hence, the χ^2 terms write:

$$\chi^2 = \chi^2_{stat}(d|\beta_0\mu_0, \beta_1\mu_1, ...) + \sum_k \frac{(\beta_k - 1)^2}{\sigma_k^2} + \chi^2_{syst}(p). \tag{6.23}$$

Here we add the prior terms for the new parameter β_k. The procedure assumes that the fluctuations due to insufficient MC are bin-to-bin uncorrelated and independent of the model parameters. This allows one to solve the values of β_k analytically and separately with the minimisation on hypothesis parameter space.

$$\frac{\partial \chi^2}{\partial \beta_k} = 0 \iff \beta_k = \frac{1}{2}\left[1 - \sigma_k^2 + \sqrt{(1 - \mu_k\sigma_k^2)^2 + 4d_k\sigma_k^2}\right] \tag{6.24}$$

To estimate the variance σ_k of the reconstruction event on each bin, the probabilistic model describes the calculation of response matrix R as a single binomial process [138], [139] is used. To understand the procedure, it is convenient to introduce the simplified notation for the response matrix:

$$R^{[\nu_x \to i]}(E, \theta, y; E', \theta', y') = \frac{N_{sel}^{\nu_x \to i}(E, \theta, y; E', \theta', y')}{N_{gen}^{\nu_x}(E, \theta, y)}. \tag{6.25}$$

$$\to R = \frac{n}{N}. \tag{6.26}$$

The computation of R can be approximately modeled as a selection process of N trials in which each event has a probability p to be selected in a given reconstruction and PID bin. Thus n is then a binomially distributed random variable with the variance of

$$\sigma_k^2 = p(1 - p)n. \tag{6.27}$$

To compute the variance of $R = n/N$, one can replace p by its estimate R. Thus, the variance of R yields:

$$\frac{\sigma_R^2}{R^2} = \frac{1-R}{n}. \tag{6.28}$$

The error on the number of events in each bin of reconstructed variables is a weighted quadratic sum of the errors from all contributions

$$\sigma^2\left(n^i_{reco}(\mathbf{x'})\right) = \sum_{\mathbf{x}}\sum_{\nu_x}\left(n^{\nu_x\to i}_{reco}(\mathbf{x},\mathbf{x'})\right)^2 \times \left(\frac{\sigma\left(R^{\nu_x\to i}(\mathbf{x},\mathbf{x'})\right)}{R^{\nu_x\to i}(\mathbf{x},\mathbf{x'})}\right)^2 \tag{6.29}$$

$$= \sum_{\mathbf{x}}\sum_{\nu_x}\left(n^{\nu_x\to i}_{reco}(\mathbf{x},\mathbf{x'})\right)^2 \times \frac{1-R^{\nu_x\to i}(\mathbf{x},\mathbf{x'})}{N^{\nu_x\to i}_{sel}(\mathbf{x},\mathbf{x'})} \tag{6.30}$$

with the true variables $\mathbf{x} = (E,\theta,y)$, and the reconstruction ones $\mathbf{x}' = (E',\theta',y')$.

Since both β and its variance can be estimated analytically this procedure does not require any additional minimization and can be used directly in the calculation of χ^2.

Chapter 7

Systematic uncertainties

Contents

This chapter presents the systematics considered in ORCA oscillation analyses. By systematics, we refer to the parameters that are not of particular interest for the measurement but describe the uncertainties on the model used for the computation of the expected event distributions. In the case of ORCA, they can be characterized into one of the following three categories:

- Atmospheric neutrino flux systematics
- Neutrino cross-section systematics
- Detector-related systematics

These systematics will be implemented at different stages in the analysis chain in SWIM. Fig. 7.1 presents a comprehensive flowchart of the framework including the different sources of systematics that will be discussed in more detail in this chapter. Sec.7.1 describes the baseline set of systematics used in the oscillation analyses presented in Chap. 8, 9 and 10. The second part of this chapter focuses on the description of a MC-based study that I have conducted to characterize the effect of PMT efficiency uncertainty on the ORCA detector response. The results that I have obtained led to the implementation of a detector-related systematic so-called energy scale.

7.1 Baseline set of systematics for the neutrino oscillation analyses

7.1.1 Atmospheric neutrino flux systematics

The production of atmospheric neutrinos generates various sources of systematics mainly related to uncertainties in the primary cosmic ray fluxes and in hadron production in cosmic ray interactions with the atmosphere. The authors of Ref. [71] have evaluated the uncertainties in the computation of neutrino fluxes that arise from the two abovementioned sources. The paper has defined a set of uncorrelated sources of uncertainty in hadronic production which can be varied independently (often referred to as *Barr parameters*), while the primary cosmic ray fluxes are treated using a parametrization model provided in Ref. [140]. These parameters in both hadronic production and cosmic ray model are assigned with the errors constrained from current experiments. The impact of these uncertainty sources on the atmospheric neutrino fluxes is then evaluated using a Monte-Carlo simulation program. The effects result in the changes of the neutrino fluxes in terms of overall normalization,

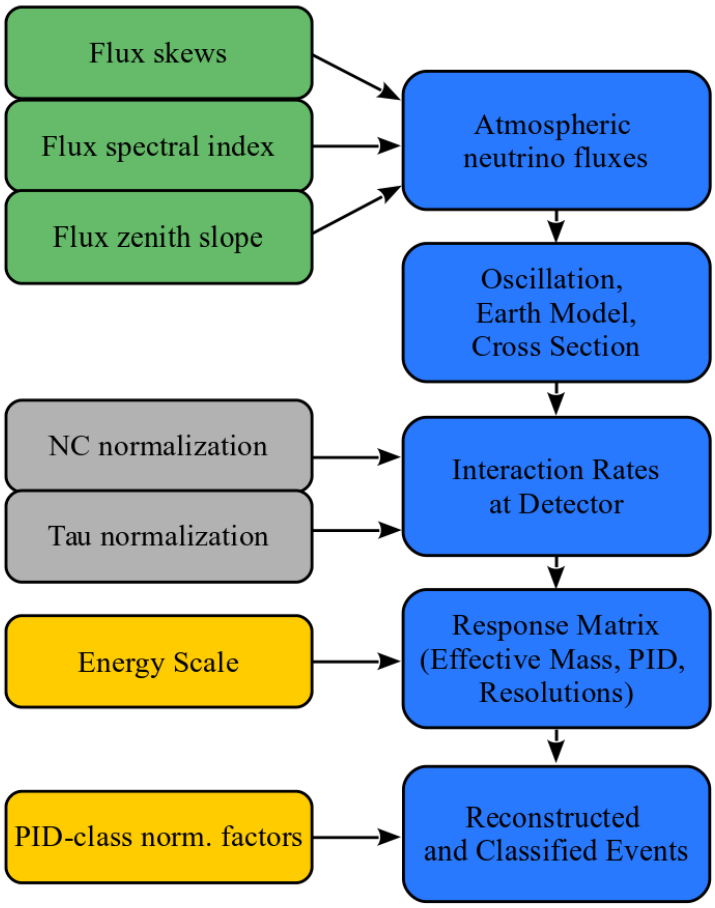

Figure 7.1: The baseline systematics in SWIM and their implementation stages in the computation flow of SWIM. The color code corresponds to three categories of systematics: atmospheric neutrino flux systematics (green), neutrino cross-section systematics (grey), and detector-related systematics (orange).

composition and spectrum shape. In KM3NeT, the flux systematics are currently applied directly at the neutrino flux with the prior taken from the results of Ref. [71].

Flux normalization

The first flux systematic is an overall normalization factor f_{all} applied on the total flux for each flavor:

$$I'_{\nu_\alpha} = f_{all} I_{\nu_\alpha}. \tag{7.1}$$

f_{all} is treated as flavor-independent factor so that it accounts for any global normalization effect on the total neutrino flux. Possible flavor-dependent variations of the flux are taken care of by the other systematics introduced in the next section.

In the current baseline implementation of ORCA systematics, the overall normalization factor is however not applied at the flux level, but rather at the very final stage of the reconstructed and classified event distributions. This approach is believed to also capture the normalization uncertainties at flux or cross-section. Such systematics will therefore be further discussed in the section dedicated to the detector-related systematics.

Flux composition

Figure 7.2 shows the uncertainty of neutrino composition of the atmospheric neutrino fluxes: the $\nu_\mu/\bar{\nu}_\mu$, $\nu_e/\bar{\nu}_e$, and $(\nu_\mu+\bar{\nu}_\mu)/(\nu_e+\bar{\nu}_e)$ ratios as computed in Ref. [71]. The $\nu_\mu/\bar{\nu}_\mu$ ratio exhibits a small uncertainty at low energy since ν_μ and $\bar{\nu}_\mu$ are usually produced as a pair in a charged pion (or kaon) decay in which one comes directly from the pion while the other is from the daughter muon. Any hadronic uncertainty effects, which would cause an under or overproduction of pions, will increase or decrease both the denominator and numerator of the ratio and thus have a small net impact. At high energy, this cancellation is reduced and the uncertainty rapidly increases because high-energy muons tend to reach the ground before they decay, resulting in pion decays producing only one polarisation type of neutrino. The $\nu_e/\bar{\nu}_e$ ratio is not subject to the same cancellation as only one electron neutrino of a given polarisation is produced for each pion decay. The uncertainty on this ratio is therefore much higher, in particular at low energies. For $(\nu_\mu+\bar{\nu}_\mu)/(\nu_e+\bar{\nu}_e)$ ratio, the same cancellation effect as $\nu_\mu/\bar{\nu}_\mu$ is expected at low energy since each pion decay typically produces 2 muon neutrinos and 1 electron neutrino. The uncertainty on this ratio increases at high energy since the cancellation is less effective, but the increase is still lower than $\nu_\mu/\bar{\nu}_\mu$.

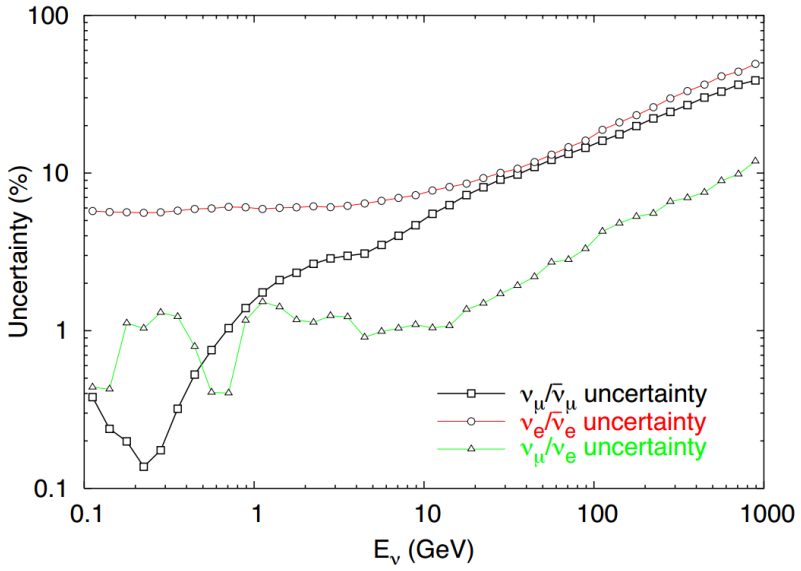

Figure 7.2: Atmospheric neutino flux composition uncertainties averaged over all direction taken from Ref. [71]

To account for the flux composition uncertainties described above, we introduce a set of systematics called the skewness. The skew parameters are defined in such a way that they change the flux composition ratios while preserving the total normalization of each flavor component. This is to avoid the degeneracies with the total normalisation factor f_{all} which is handled as a different systematics. The skew parameters associated with the three different flux composition ratios introduced above are: *the* $(\nu_\mu + \bar{\nu}_\mu)/(\nu_e + \bar{\nu}_e)$ *flavor skew* $s_{\mu e}$, *the* $\nu_e/\bar{\nu}_e$ *skew* $s_{e\bar{e}}$, *and the* $\nu_\mu/\bar{\nu}_\mu$ *skew* $s_{\mu\bar{\mu}}$. These systematics modify the total nominal flux of flavor/polarity α, I_{ν_α}, into the varied one I'_{ν_α} as:

$$I'_{\nu_\alpha} = w_{\nu_\alpha} I_{\nu_\alpha}, \tag{7.2}$$

where the w_{ν_α} are parametrized in function of the skew parameters in order to satisfy the following conditions:

- the flavor skew $s_{e\mu}$ changes the $(\nu_\mu + \bar{\nu}_\mu)/(\nu_e + \bar{\nu}_e)$ ratio in a way that preserves the total flux:

$$I'_{\nu_e} + I'_{\bar{\nu}_e} + I'_{\nu_\mu} + I'_{\bar{\nu}_\mu} = I_{\nu_e} + I_{\bar{\nu}_e} + I_{\nu_\mu} + I_{\bar{\nu}_\mu} \tag{7.3}$$

- In the absence of a flavor skew, the polarity skews $s_{e\bar{e}}$ and $s_{\mu\bar{\mu}}$ should modify the $\nu_e/\bar{\nu}_e$, $\nu_\mu/\bar{\nu}_\mu$ ratios in a way that preserves each flavor flux $\nu_\alpha + \bar{\nu}_\alpha$:

$$I'_{\nu_e} + I'_{\bar{\nu}_e} = I_{\nu_e} + I_{\bar{\nu}_e} \tag{7.4}$$

$$I'_{\nu_\mu} + I'_{\bar{\nu}_\mu} = I_{\nu_\mu} + I_{\bar{\nu}_\mu} \tag{7.5}$$

The parametrization[1] then yields:

$$w_{\nu_e} = (1+s_{e\bar{e}})\frac{I_{\nu_e}+I_{\bar{\nu}_e}}{I_{\nu_e}(1+s_{e\bar{e}})+I_{\bar{\nu}_e}} \times\frac{I_{\nu_\mu}+I_{\bar{\nu}_\mu}+I_{\nu_e}+I_{\bar{\nu}_e}}{(I_{\nu_\mu}+I_{\bar{\nu}_\mu})(1+s_{\mu e})+I_{\nu_e}+I_{\bar{\nu}_e}}, \tag{7.6}$$

$$w_{\bar{\nu}_e} = \frac{I_{\nu_e}+I_{\bar{\nu}_e}}{I_{\nu_e}(1+s_{e\bar{e}})+I_{\bar{\nu}_e}} \times\frac{I_{\nu_\mu}+I_{\bar{\nu}_\mu}+I_{\nu_e}+I_{\bar{\nu}_e}}{(I_{\nu_\mu}+I_{\bar{\nu}_\mu})(1+s_{\mu e})+I_{\nu_e}+I_{\bar{\nu}_e}}, \tag{7.7}$$

$$w_{\nu_\mu} = (1+s_{\mu\bar{\mu}})\frac{I_{\nu_\mu}+I_{\bar{\nu}_\mu}}{I_{\nu_\mu}(1+s_{\mu\bar{\mu}})+I_{\bar{\nu}_\mu}} \times(1+s_{e\mu})\frac{I_{\nu_\mu}+I_{\bar{\nu}_\mu}+I_{\nu_e}+I_{\bar{\nu}_e}}{(I_{\nu_\mu}+I_{\bar{\nu}_\mu})(1+s_{\mu e})+I_{\nu_e}+I_{\bar{\nu}_e}}, \tag{7.8}$$

$$w_{\bar{\nu}_\mu} = \frac{I_{\nu_\mu}+I_{\bar{\nu}_\mu}}{I_{\nu_\mu}(1+s_{\mu\bar{\mu}})+I_{\bar{\nu}_\mu}} \times(1+s_{\mu e})\frac{I_{\nu_\mu}+I_{\bar{\nu}_\mu}+I_{\nu_e}+I_{\bar{\nu}_e}}{(I_{\nu_\mu}+I_{\bar{\nu}_\mu})(1+s_{\mu e})+I_{\nu_e}+I_{\bar{\nu}_e}}. \tag{7.9}$$

Results of Ref. [71] presents the uncertainties on the ratios between flux compositions as shown in Fig. 7.2 while in SWIM framework the priors are applied directly on the skew parameters. Then, one needs to derive the relation between the ratios and the skew parameters. From Eqs. (7.2), (7.6), (7.7), (7.8), (7.9), such relations read:

$$r'_{e\bar{e}} = \frac{I'_{\nu_e}}{I'_{\bar{\nu}_e}} = (1+s_{e\bar{e}})\frac{I_{\nu_e}}{I_{\bar{\nu}_e}}, \tag{7.10}$$

$$r'_{\mu\bar{\mu}} = \frac{I'_{\nu_\mu}}{I'_{\bar{\nu}_\mu}} = (1+s_{e\bar{e}})\frac{I_{\nu_\mu}}{I_{\bar{\nu}_\mu}}, \tag{7.11}$$

$$r'_{\mu e} = \frac{I'_{\nu_\mu}+I'_{\bar{\nu}_\mu}}{I'_{\nu_e}+I'_{\bar{\nu}_e}} = (1+s_{\mu e})\frac{I_{\nu_\mu}+I_{\bar{\nu}_\mu}}{I_{\nu_e}+I_{\bar{\nu}_e}}, \tag{7.12}$$

The perturbation in the ratios finally yields:

$$\frac{r'_{e\bar{e}}}{r_{e\bar{e}}} = 1+s_{e\bar{e}}, \tag{7.13}$$

$$\frac{r'_{\mu\bar{\mu}}}{r_{\mu\bar{\mu}}} = 1+s_{\mu\bar{\mu}}, \tag{7.14}$$

$$\frac{r'_{\mu e}}{r_{\mu e}} = 1+s_{\mu e}. \tag{7.15}$$

[1]This parametrization is different from the one presented in Ref. [122] which is used for the previous version of the SWIM framework. The current SWIM uses this one which provides better synchronization with other analysis frameworks in the Collaboration.

Thus, the constraint priors on the ratios lead to the same one for the corresponding skew parameters. For the case of NMO analysis in which the main sensitivity region is $\sim 3-10$ GeV as will be shown in Chap. 8, Fig. 7.2 gives the set of constraints as follows:

- 7% for $s_{e\bar{e}}$
- 5% for $s_{\mu\bar{\mu}}$
- 2% for $s_{\mu e}$

Flux shape systematics

Other sources of systematics that need to be considered at the flux level are the uncertainties in the shape distribution. They are introduced as a multiplying factor which depends on the energy and zenith angle $w_{\nu_\alpha,\text{shape}}(E,\theta)$ that modifies the flux according to:

$$\phi'_{\nu_\alpha}(E,\theta) = w_{\nu_\alpha,\text{shape}}(E,\theta) \times \phi_{\nu_\alpha}(E,\theta). \tag{7.16}$$

We also ensure that it preserves the total flux integral of each flavor/polarization ν_α:

$$\int\int w_{\nu_\alpha,\text{shape}}(E,\theta) \times \phi_{\nu_\alpha}(E,\theta) dE d\theta = \int\int \phi_{\nu_\alpha}(E,\theta) dE d\theta, \tag{7.17}$$

where the integration runs on the whole defined range of interest for the analysis. In the SWIM framework, the implementation of the flux shape systematics is in the form of generic polynomial functions of $\ln E$ and $\cos\theta$, which are respectively denoted as X and Y. This approach is based on the fact that the atmospheric neutrino flux is almost linear in $\ln E$ and $\cos\theta$ so that one can assume that the shape variation is continuous and slow enough to be well approximated by a finite degree polynomial. The framework allows up to 4 degrees of the polynomial which gives us:

$$w_{\nu_\alpha,\text{shape}}(E,\theta) = \text{Norm}_{\nu_\alpha}(\{c_{ij}\}) \cdot \left(1 + \sum_{1\leq i+j\leq 4} c_{ij} (\ln E)^i (\cos\theta)^j\right) \tag{7.18}$$

$$= \text{Norm}_{\nu_\alpha}(\{c_{ij}\}) \cdot \left(1 + \sum_{1\leq i+j\leq 4} c_{ij} (X)^i (Y)^j\right), \tag{7.19}$$

where $\text{Norm}(c_{ij})_{\nu_\alpha}$ is a renormalization factor that ensures the preservation of each flux composition. This factor is calculated as:

$$\text{Norm}_{\nu_\alpha}(\{c_{ij}\}) = \frac{I_{\nu_\alpha}}{I_{\nu_\alpha} + \sum_{i,j} c_{ij} I_{\nu_{\alpha,ij}}}, \tag{7.20}$$

with $I_{\nu_\alpha,00} = I_{\nu_\alpha}$ and

$$I_{\nu_\alpha,ij} = \int\int X^i Y^i \phi_{\nu_\alpha}(X,Y) dX dY \tag{7.21}$$

Throughout the works presented in this manuscript, two specific shape systematics are used: the *spectral index uncertainty* and the *zenith slope uncertainty*.

The *spectral index uncertainty*, which is also referred to as the *energy slope systematics*, is introduced as a modification on the 'tilt' of the flux shape in terms of energy dependence:

$$\phi'_{\nu_\alpha}(E,\theta) = E^{-\gamma} \times \phi_{\nu_\alpha}(E,\theta). \tag{7.22}$$

Considering the small value of γ, the modification factor $E^{-\gamma}$ is calculated by its fourth-order series expansion:

$$w_{\nu_\alpha,\text{Eslope}} = \text{Norm}_{\nu_\alpha}(\gamma) \cdot \left(1 + \gamma \ln E + \frac{1}{2}\gamma^2 \ln^2 E + \frac{1}{3}\gamma^3 \ln^3 E + \frac{1}{4}\gamma^4 \ln^4 E)\right). \tag{7.23}$$

where $\text{Norm}(\gamma)$ is the aforementioned renormalization factor introduced in order to preserve the total normalization of the flux.

The *zenith slope systematics* is also implemented with the same philosophy. As shown in Fig. 5.1, the flux is approximately linear in $\cos\theta$. Hence, the perturbation can be well described as the first order of the expansion series:

$$w_{\nu_\alpha,\text{zenithslope}} = \text{Norm}_{\nu_\alpha}(\epsilon) \cdot (1 + \epsilon \cos\theta)\,. \tag{7.24}$$

Further prospects on the treatment of flux systematics

Atmospheric neutrino flux systematics are one of the main uncertainty sources in the context of ORCA oscillation analysis since they relate directly to the flavour content of the initial neutrino source. The current treatment of these systematics is considered to be conservative in the sense that they are based on observed characteristics of the neutrino fluxes. They are assumed to be uncorrelated, while actually they should be all directly connected to the uncertainties in the primary cosmic ray fluxes or hadronic interactions.

A future improvement of the treatment of flux systematics would be to fit the event distribution directly with the physical parameters related to the primary cosmic ray flux and hadronic processes in the air shower development (the aforementioned uncorrelated Barr

parameters). This approach requires the ability to perform a fast computation of changes in the neutrino fluxes when a given source of uncertainty is varied. One possibility to achieve this goal is through the use of MCEq (Matrix Cascade Equations), a tool which quickly solves the cascade equations that describe the evolution of the cosmic ray-induced air showers [141]. In Ref. [142], a computation of the gradient of the neutrino flux on Barr parameters with MCEq has been performed which allowed a minimizer to fit directly on hadronic production uncertainties. Thus, this approach could be foreseen to be the next improvement of flux systematic treatment in ORCA oscillation analysis.

7.1.2 Neutrino cross-section systematics

The cross-section systematics involved in this work include the NC normalization and tau normalization which are implemented as the scaling factors on NC event rate and ν_τ CC event rate respectively.

The current treatment on neutrino cross-section systematics is quite limited at the time of writing of this manuscript. One other approach is to introduce a set of normalization and skew parameters similar to the treatment at the flux level. Such an implementation has been shown to have a negligible impact, as the skew parameters applied at the cross-section are mostly degenerate with the one at the flux level, as discussed in Ref. [122]. Hence, for simplification, we do not use it in this work. Another effort aiming at a more precise study of the cross-section uncertainty sources using GENIE and propagating it to the oscillation fit is being carried out within the Collaboration. Nevertheless, it is out of the scope of this thesis.

7.1.3 Detector-related systematics

Various sources of detector-related systematics can be introduced for example the uncertainties in detection medium regarding the absorption length, scattering properties,... or mis-characterizing the PMT response, triggering, reconstruction, and PID performance,... They can result in the variation in the detector response functions or final normalization and shape of the detected event distribution. The two systematics are introduced as an effort for capturing such effects.

The separate total normalization factors are applied for each of the PID classes. The parameters can conservatively account for any detector-related uncertainties which cause normalization effects as well as capturing such effects in flux or cross-section level.

Another detector systematics considered is the uncertainty of PMT efficiency which is the result of intrinsic ageing of PMTs as well as the uncertainty related to calibration method used for monitoring this quantity. The time dependence of PMT efficiencies is currently monitored using ^{40}K decays in seawater - the method which is applied at ANTARES [85] and also described in Sec. 2.2.3. The experience with ANTARES shows a slow decrease in the PMT efficiency over time, which could be mitigated by regular calibration procedures to retune the PMT gain and thresholds. This also shows the importance of being able to monitor the efficiency over time. Nevertheless, some uncertainties may subsist and have to be accounted for as systematics.

By comparing MC samples produced with different PMT efficiencies, previous KM3NeT studies reported in the LoI [61] have shown that wrongly characterizing the PMT efficiency can lead to a wrong evaluation of the detector response to neutrino-induced light signals. To capture this effect, I have worked on the implementation of a systematics called *energy scale*, which has been shown to have a non-negligible impact on the measurement of Δm^2_{31}, hence the necessity to include it in all ORCA physics analyses. This original work is further described in the next subsection.

7.2 The energy scale systematic and effects of PMT efficiency uncertainty

This section presents the description of a MC-based study to characterize the effect of PMT efficiency variance on the ORCA detector response. This effect had been first described in the KM3NeT LoI [61], but only including electron-neutrino signals and using an old simulation chain of the detector. The work presented here is a collaborative work to confirm the LoI results with the latest MC chain and detector configuration, in which I was in charge of analyzing and producing the final results. Based on this MC study, I have implemented the energy scale systematic in SWIM, to capture the expected effects of PMT efficiency uncertainty.

In this section, the implementation of the energy scale in SWIM is first presented. Then a comparison between this parametric approach and the predictions from the MC-based study is also illustrated. Finally the impact of this systematic on physics analyses, and in particular on the Δm^2_{31} parameter, will be shown.

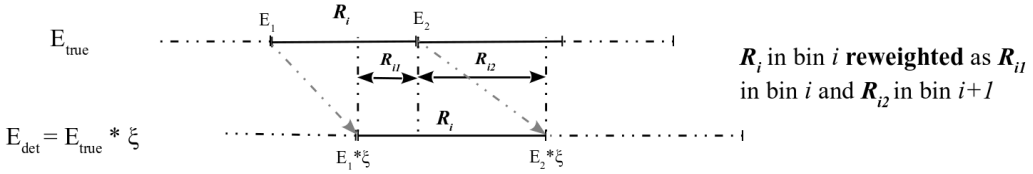

Figure 7.3: Illustration of the energy scale implementation on the response matrix in SWIM. Each entry R_i of the matrix in bin i of true energy E_{true} binning is shifted into a new bin with $E_{det} = E_{\text{true}} * \xi$ and then redistributed into the original bins i and $i+1$ of E_{true}.

7.2.1 Implementation of energy scale systematic in SWIM

Inspiring from the LoI study, the energy scale systematics is applied in SWIM as a global shift in the energy distribution of the Response Matrix. This implementation is illustrated in Fig. 7.3 and develops according to the following steps:

- Consider the response matrix entry R_i at bin i in the true energy variable E_{true}, with bin edges denoted as E_1 and E_2;
- The energy scale systematic ξ acts as a global shift on the true energy of the response matrix so that the response associated to a given energy E_{true} becomes actually the one associated to the energy $E_{det} = E_{true} \times \xi$. Therefore, R_i becomes the entry associated to a new bin with shifted edges $E_1 \times \xi$ and $E_2 \times \xi$.
- The original content of the entry R_i is then redistributed into the true energy bins i and $i+1$, proportionally to their respective overlap with the shifted bin, as described in the figure.
- The whole process is repeated for all entries of the response matrix.

Since the response matrix can be decoupled into effective mass, reconstruction and PID p.d.fs as pointed out in Sec. 5.2.1:

$$R^{[\nu_x \to i]}(E, \theta, y; E', \theta', y') = p_{reco}^{\nu_x \to i}(E, \theta, y, E', \theta', y') \cdot P_{PID}^{\nu_x \to i}(E, \theta, y) \cdot \frac{M_{eff}^{\nu_x}(E, \theta, y)}{M_{ref}}. \tag{7.25}$$

A global shift in the response matrix will correspond to a shift applied on each of these components. In the following, we will therefore also examine the impact of the energy scale systematic onto each of the response functions, for the sake of comparison with the MC-based study as well as for the study of its impact on the Δm^2_{31} measurement.

7.2.2 The Monte-Carlo samples with modified PMT efficiencies

In order to study the impact of uncertainties in the PMT efficiencies, specific MC samples with modified PMT efficiency have been produced. Ten percent of the MC sample 'ORCA115_20x9_190222' presented in Sec. 3.4 have been rerun from the trigger level with a PMT quantum efficiency (QE) modified by $\pm 10\%$ compared to the standard one. In the following, the standard and the two modified PMT efficiency MC samples will be referred to as *nominal*, *QE 90%* and *QE 110%*.

The study has been performed for $\nu_\mu + \bar{\nu}_\mu$ CC and $\nu_e + \bar{\nu}_e$ CC as they are representative of the two topological event types: tracks and showers. ν NC and $\nu_\tau + \bar{\nu}_\tau$ CC are expected to yield similar results as $\nu_e + \bar{\nu}_e$ CC.

7.2.3 Impact of PMT efficiency uncertainties on the effective mass

Fig. 7.4 compares the effective mass as obtained from the $\nu_e + \bar{\nu}_e$ CC and $\nu_\mu + \bar{\nu}_\mu$ CC samples for different PMT efficiencies (nominal, QE 90% and QE 110%), and from an energy scale systematic of $\pm 10\%$ applied on the nominal MC sample.

First, the values of the effective mass in the range 1 - 10 GeV increase (resp. decrease) with a higher (resp. lower) PMT efficiency, while their variation in the plateau, starting from ~ 10 GeV, is almost negligible. This effect is expected due to a better PMT efficiency leading to more sensitivity of the detector to the light induced from neutrino interactions, and vice versa for the case of worse efficiency.

The energy scale systematic implementation here captures relatively well the effect of varying the PMT efficiencies. The energy scale $\xi = 1.1$ shifts the effective mass towards higher energies and matches well the trend induced by a worse PMT efficiency (QE 90%). A similar matching is observed for the case of $\xi = 0.9$ and QE 110%. Both approaches yield a difference in effective masses of $\sim 5\%$ at low energy compared to the nominal, which steadily decreases with increasing energies. Above 10 GeV, the difference with the nominal effective mass is $< 2\%$. One might also notice that there is a fluctuation in the plateau of the modified QE effective mass. This is not a physical effect but the result of the limited statistics in the sample (10 times smaller than the original 'ORCA115_20x9_190222' MC).

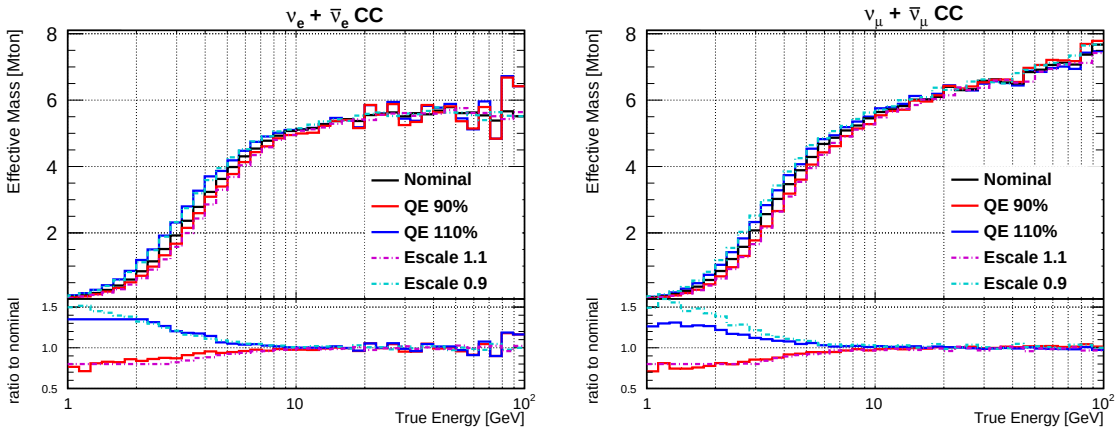

Figure 7.4: Effective mass as a function of E_{true} for different PMT quantum efficiencies (QE) in comparison with the implementation of an energy scale systematic.

7.2.4 Impact of PMT efficiency uncertainties on the energy reconstruction

The effect of PMT efficiency uncertainty and energy scale systematics on the mean reconstructed energy is illustrated in Fig. 7.5. Here, we considered both Dusj and JGandalf reconstruction tools for ν_μ and only Dusj for ν_e.

In the case of Dusj, the variation of PMT efficiencies leads to a global shift of the mean reconstructed energy. A 10% decrease or increase in QE respectively induces also a 10% under- or overestimation of the neutrino energy with Dusj for both ν_μ and ν_e. This effect stems from the fact that Dusj energy reconstruction relies mainly on the total number of observed hits, which should change linearly with the variation in PMT efficiencies. In contrast, JGandalf exhibits a different behavior in which the variation of reconstructed energy steadily increases to reach 30% above 15 GeV.

The shift on the mean reconstructed energy due to the energy scale systematics is evaluated by applying the energy scale shift on the true energy dimension in the p.d.fs of reconstructed vs true energy shown in Fig. 5.7. The mean reconstructed energy is then computed for each true energy bin of the distribution.

The effect of energy scale systematics is in good agreement with the QE variation for the Dusj reconstructed energy of $\nu_e + \bar{\nu}_e$ CC (shower-like) event sample. A similar conclusion holds for Dusj reconstruction in the case of $\nu_\mu + \bar{\nu}_\mu$ CC (track-like) events where the energy scale systematics can capture well the effect of QE variation up to about 20 GeV though it systematically underestimate the QE-induced variations by 5% to 10% at higher energies.

In the case of $\nu_\mu + \bar{\nu}_\mu$ CC events reconstructed with JGandalf, the energy scale correction

fails to capture the effect of varying QE even at low energies and does not reproduce the 30% variation in reconstructed energy observed from 15 GeV upwards. These large variations might however be ascribed to the suboptimal performance of JGandalf for the energy reconstruction of track-like events, as discussed in Sec.5.2.1, rather than to a shortcoming of the energy scale procedure.

At this point, it is worth recalling that in the recent KM3NeT publication on the estimated performance of ORCA for the measurement of NMO and oscillation parameters [98], Dusj energy reconstruction is used for both track-like and shower-like event types. Thus the current implementation of the energy scale systematics can be considered as satisfactory for an NMO analysis in which the sensitivity region lies below 10 GeV.

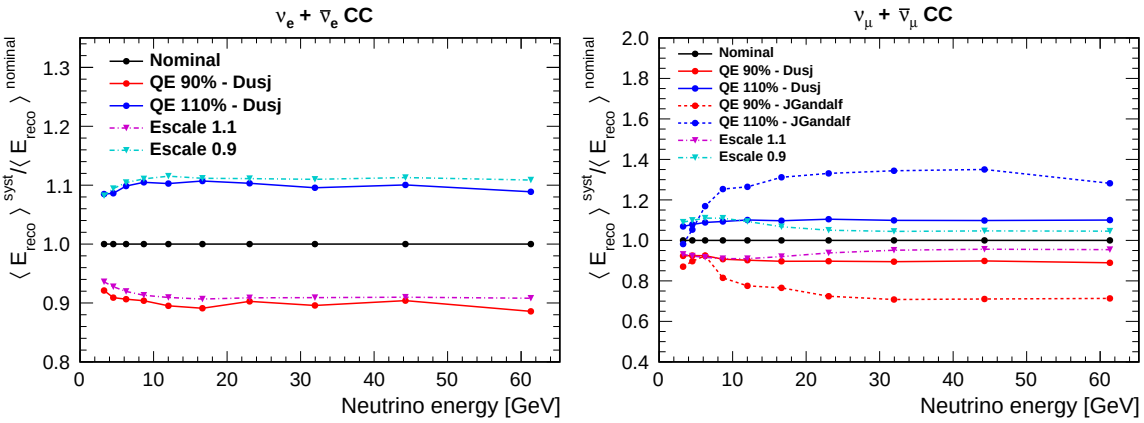

Figure 7.5: Ratio of the mean reconstructed energy for nominal, varied PMT efficiencies and energy scale values.

7.2.5 Impact of PMT efficiency uncertainties on the PID

Fig. 7.6 illustrates the effect of QE variation and energy scale systematics on the PID probability distribution functions. One can see that varying the PMT QE also leads to a shift in true energy of this response function, which is well captured by the energy scale systematics.

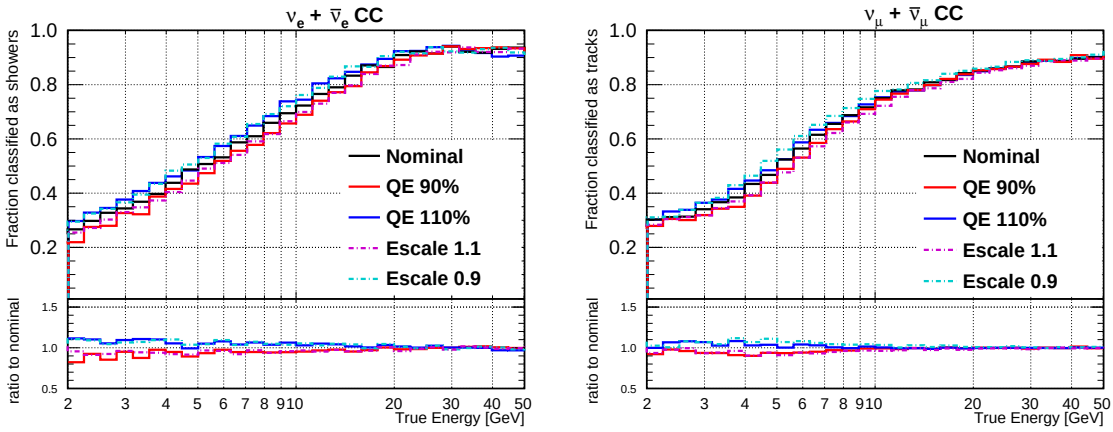

Figure 7.6: Fraction of $\nu_e + \bar{\nu}_e$ CC events classified as showers (left) and $\nu_\mu + \bar{\nu}_\mu$ classified as tracks (right) for nominal, varied PMT efficiencies and energy scale.

7.2.6 Impact of the energy scale systematics on the Δm^2_{31} measurement

The determination of Δm^2_{31} relies on the precise measurement of the phase $\frac{\Delta m^2_{31} L}{E}$ of the oscillation pattern. Therefore, the energy scale systematics, which affect the detector response to the neutrino energy, are expected to have a significant impact on this measurement[2].

This effect is shown in Fig. 7.7 (left panel), where the incremental impact of the energy scale systematics applied on each detector response function is studied. The dominant sources of degradation of the Δm^2_{31} measurement come from the energy scale systematics applied on the PID and effective mass, while its application on the reconstruction p.d.f seems to have negligible impact. The right panel of Fig. 7.7 also confirms that the Δm^2_{31} sensitivity does not degrade much when varying the energy scale factor from 3% to 10%.

Once real data becomes available, the energy scale uncertainty can be constrained by the monitoring of PMT efficiencies using coincident signals from ^{40}K decays as described in Sec. 2.2.3. Based on current estimations, a standard deviation of 5% around the nominal efficiency seems a reasonable estimate of this effect. This value will be adopted for all sensitivity studies described in the manuscript, while a more conservative value of 10% will be chosen for the analysis of the first data sample described in Chap. 10.

[2]It can be mentioned here that the impact of variations in the PMT efficiencies on the reconstructed $\cos\theta$ accuracy, which could affect the factor L in the oscillation phase, has been shown to be negligible [61].

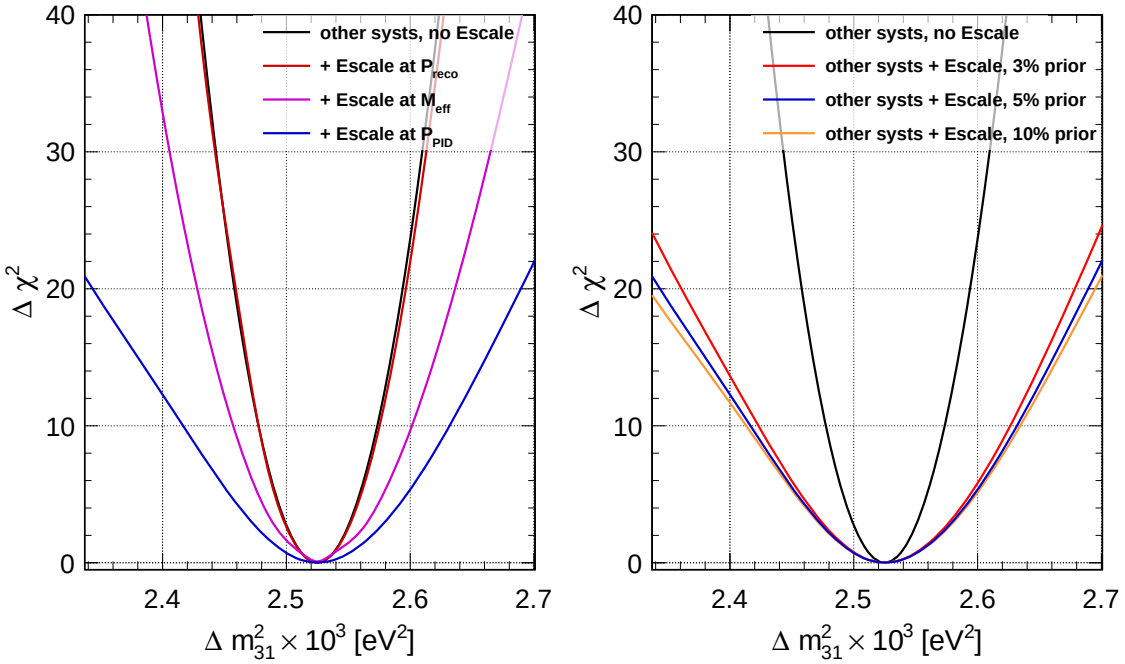

Figure 7.7: The profiled $\Delta\chi^2$ as the function of Δm^2_{31} with 6 years of exposure of full ORCA detector. The figures show the effects of energy scale systematic: applied at each response functions (reconstruction, effective mass, PID) in incremental order (left) and applied with different priors (right).

7.3 Conclusion

This chapter presents the baseline set of systematics used for oscillation analysis in this work. Part of the systematics have been developed within SWIM through previous work of Ref. [122]. The further development from the contribution of this thesis includes the implementation of the energy scale systematic to capture the effect of PMT QE uncertainty. Through the MC-based study, I have also validated the consistency of this systematic implementation as well as confirming and extending the similar study presented in Ref. [61] with the up-to-date KM3NeT simulation chain.

The current status of systematics treatment still allows room for improvement regarding the fact that most of the systematics presented here are not real physics parameters but just effective ones introduced to approximately capture the observed or expected effects of possible uncertainty sources. Thus the possibility of fitting the expected event distribution directly on the parameter space of more physics-related uncertainty sources should be deemed as a priority for further developments.

Part IV

Physics Results

Chapter 8

KM3NeT/ORCA sensitivity to the neutrino mass ordering and oscillation parameters.

Contents

This chapter presents the sensitivity of the KM3NeT/ORCA detector to the neutrino mass ordering and the oscillation parameters in the atmospheric sector: Δm^2_{31} and θ_{23}. I have performed this analysis within the SWIM framework, based on the simulation tools, statistical and systematics treatment described in Chap. 3, 5, 6 and 7. First, Sec. 8.1 describes the general analysis settings which include the MC samples, binning scheme, event selection, PID cuts, and parameter treatment. Then the sensitivity of ORCA for the measurement of the NMO and atmospheric oscillation parameters is presented. Those results have been used as an internal cross-check for the official KM3NeT results described in Ref. [98] and Ref. [143].

8.1 Analysis framework

8.1.1 Monte Carlo samples

The MC samples 'ORCA115_20x9_190222' and 'ORCA7_23x9_190222' introduced in Sec. 3.4 are used in this sensitivity study, and referred to as ORCA115 and ORCA7 respectively. The 'ORCA7_23x9_190222' sample is used for the study of an early measurement of oscillation parameters with a 7 DUs sub-array of ORCA that would be representative of the first construction phase. The sample 'ORCA115_20x9_190222' is for the study with the full detector. This sample is based on the latest geometry configuration of 20 m average horizontal spacing and 9 m vertical spacing between DOMs. In the following, this 20 m x 9 m configuration will be used as the default for the full ORCA detector unless specified otherwise. A comparison between 20 m and 23 m configurations on the performance toward NMO determination will be presented in the next section. As will be shown there, the 20 m horizontal configuration proves to be more suitable in terms of NMO measurement, while equally feasible from the deployment point of view, compared to the 23 m one used in previous works of Ref. [120] and [122].

8.1.2 Binning scheme

The binning scheme of the analysis is described in Tab. 8.1. The neutrino true energy is binned uniformly in $\log_{10} E$ due to the fact that the atmospheric neutrino flux approximately follows a power law in energy. The same binning scheme is also applied for the reconstruction energy because the relative energy resolution of ORCA above 10 GeV is approximately constant: $\delta E/E \simeq \delta(\log E) \simeq 25 - 35\%$ (depending on the channel) [98].

The zenith angle is binned uniformly in $\cos\theta_z$. This is motivated by the fact that the

Table 8.1: Binning scheme used for the oscillation analysis. Only up-going events are considered for the reconstructed $\cos\theta$, while additional 10 bins of down-going are used for the true $\cos\theta$.

Binning	True	Reco
Energy	40 [1-100 GeV]	20 [2-80 GeV]
$\cos\theta$	40 up +10 down	20 up

solid angle covered by the interval $\theta_1 \leq \theta \leq \theta_2$ is proportional to the factor $|\cos\theta_2 - \cos\theta_1|$. Furthermore, the oscillation probability depends on the L/E_ν factor, in which the oscillation baseline $L = R\cos\theta$ (with R the Earth radius). Thus, it is also reasonable to compute the oscillation probability at points equally sampled in $\cos\theta$. In the reconstruction space of $\cos\theta$, we only use the up-going events ($-1 \leq \cos\theta \leq 0$) since these events are of particular interest for the oscillation analysis. Additionally, 10 bins in the range $0 \leq \cos\theta \leq 1$ are considered for the true space to account for the down-going events that are mis-reconstructed as up-going. The bin width of reconstructed variables is adjusted so that it is comparable to the typical detector resolution.

The inelasticity (Bjorken-y variable) is included in the framework as presented in Chap. 5. Nevertheless, it will not be used in this analysis due to the current reconstruction tools can not achieve a good resolution on this variable. In practice, one single bin is set for both true and reconstructed Bjorken-y.

8.1.3 Event selection and classification

The reconstruction tools described in Chap. 3 are used for simulated events. Then an event preselection is applied based on the output of these reconstruction algorithms. Only upgoing events are selected, which also satisfy the requirements of good reconstruction quality and containment criteria. A detailed description of this event preselection can be found in Ref. [94] and Ref. [61]. For each of the used reconstruction algorithms, *Dusj* and *JGandalf*, we refer to the corresponding preselection criteria as: *shower_preselection* and *track_preselection* respectively.

Based on the output score to distinguish track-like events from shower-like events (*track_score*) provided by the RDF classifier, the event samples are classified into three PID classes for the optimization of the NMO sensitivity as described previously in Chap. 3. The PID classes are summarized here with the corresponding applied reconstruction algorithm:

- **Tracks**: $0.7 <$ *track_score* ≤ 1.0 and pass *track_preselection*

Energy: *Dusj*, $\cos\theta$: *JGandalf*.

- **Intermediate**: $0.3 <$ *track_score* ≤ 0.7 and pass *shower_preselection*
  Energy: *Dusj*, $\cos\theta$: *Dusj*.

  Showers: $0.0 <$ *track_score* ≤ 0.3, and pass *shower_preselection*
  Energy: *Dusj*, $\cos\theta$: *Dusj*.

These three-class cuts are the result of an optimization for the sensitivity of the full ORCA115 detector to the NMO [118].

In the **Tracks** class, *Dusj* energy reconstruction is used instead of *JGandalf*, as it yields a better sensitivity to the NMO. Additionally, the study of PMT efficiency variation in Chap 7 has shown a non-linear effect (Fig. 7.5) in the JGandalf energy estimator, that the energy scale systematic cannot capture well. Therefore, the Dusj energy is used for the study in this chapter, in accordance with the choice adopted in Ref. [98].

The condition of selecting only up-going events allows for a first rejection of the atmospheric muon background using the Earth as the natural filter. Furthermore, as mentioned in Chap. 3, the RDF classifier provides two additional scores for the suppression of noise and atmospheric muons: *pure_noise_score* and *atmospheric_muon_score*. Ref. [98] shows that a hard cut on *atmospheric_muon_score* < 0.05 further removes atmospheric muons to a contamination level of ~ 3 % and that a cut on *pure_noise_score* < 0.1 sufficiently rejects the noise events while only resulting in a loss in neutrino efficiency of about $\sim 5\%$. These two suppression cuts are applied for all three defined PID classes. Since the contamination of atmospheric muon background and pure noise events are negligible, they are not included in this work.

8.1.4 Parameters and systematics treatment

The sensitivity study for the NMO and oscillation parameters presented in this chapter is performed based on a simulated Asimov dataset following the procedure described in Chap. 6. If not specified otherwise, the assumed true values of oscillation parameters are taken from Ref. [128].

The detailed treatment of systematics and oscillation parameters is presented in Tab. 8.2. ORCA measures the atmospheric neutrino oscillation at L/E values much smaller than the ones required for a sensitivity to the oscillation with the frequency given by Δm^2_{21}. As a result, ORCA has a negligible sensitivity to θ_{12} and Δm^2_{21} and those parameters are kept fixed in the analysis. Current data from reactor neutrino experiments [49, 144, 145] yield a

very good precision on θ_{13} compared to the one that could be achieved with ORCA. Hence, a prior is used for θ_{13} whose mean and variance are taken from Ref. [128]. Three remaining oscillation parameters are relevant for ORCA and are fitted without any constraint: $\theta_{23}, \Delta m^2_{31}, \delta_{CP}$.

In the case of θ_{23}, a degeneracy in the octant arises from the fact that the dominant terms of the oscillation probability are driven by $\sin^2\theta_{23}$. In order to ensure that the minimization finds the true global minimum, the fit is performed twice, each time with a different starting point located in either the upper or lower octant, and the smallest χ^2 is kept eventually.

Priors on the flux systematics are assigned based on the current knowledge on atmospheric neutrino flux uncertainties reported in Ref. [71]. A prior of 10% is adopted on the NC normalization, while the PID normalization in each topological class is left free. As mentioned in Chap. 7 (Sec. 7.1.3), the time-dependent PMT efficiency can be monitored using coincidence signals from ^{40}K decays. Such a study also gives the uncertainty on the PMT quantum efficiency of 5%. This results in a conservative prior of 5% applied for the energy scale systematic.

Table 8.2: Parameter treatment in ORCA oscillation analysis. The true values of oscillation parameters are taken from the global fits of Ref. [128]. The priors are applied as Gaussian constraints with mean μ and variance σ. The cross mark $\times$ means no prior applied.

Parameter	True value	Treatment	Prior
$\theta_{23}(\mathrm{deg})$	48.6 (NO) 48.8 (IO)	*Fitted*	$\times$
$\theta_{13}(\mathrm{deg})$	8.60 (NO) 8.64 (IO)	*Fitted*	$\mu = 8.60, \sigma = 0.13$
$\theta_{12}(\mathrm{deg})$	33.82	Fixed	$\times$
$\Delta m^2_{31}(10^{-3}\mathrm{eV}^2)$	2.528 (NO) -2.510 (IO)	*Fitted*	$\times$
$\Delta m^2_{21}(10^{-5}\mathrm{eV}^2)$	7.39	Fixed	$\times$
$\delta_{CP}(\mathrm{deg})$	221 (NO) 282 (IO)	*Fitted*	$\times$
Flux $\nu_e/\bar{\nu}_e$ skew	0	*Fitted*	$\mu = 0, \sigma = 0.07$
Flux $\nu_\mu/\bar{\nu}_\mu$ skew	0	*Fitted*	$\mu = 0, \sigma = 0.05$
Flux $\nu_e/\bar{\nu}_\mu$ skew	0	*Fitted*	$\mu = 0, \sigma = 0.02$
Flux spectral index	0	*Fitted*	$\times$
Flux zenith slope	0	*Fitted*	$\mu = 0, \sigma = 0.05$
NC normalization	1	*Fitted*	$\mu = 1, \sigma = 0.1$
Energy scale	1	*Fitted*	$\mu = 1, \sigma = 0.05$
PID class norm.	1	*Fitted*	$\times$

8.2 Sensitivity study of KM3NeT/ORCA to the neutrino mass ordering

In this section, an updated study of the sensitivity of the KM3NeT/ORCA detector to the NMO is presented. As mentioned before, compared to the older results presented in Ref. [120] and Ref. [122], a configuration of 20 m average horizontal spacing is adopted instead of 23 m. The improvement due to this change in the detector layout is illustrated in the following, and the updated sensitivity is also discussed.

8.2.1 Sensitivity region

To have an idea of how ORCA can distinguish the different NMO scenarios, it is necessary to investigate how the measured event distribution changes with different NMO hypotheses. The difference is not easily visible by just looking directly into the distribution (e.g Fig. 5.8) but requires computing the statistical separation between the two distributions.

To visualize the difference in $(E, \cos\theta)$ distribution, we define the so-called *signed*-χ^2 function computed in each bin of the two expected distributions from two corresponding hypotheses A and B as:

$$\chi^2_s(A|B) = \frac{n_A - n_B}{|n_A - n_B|} \times \frac{1}{2}\left(\chi^2(A|B) + \chi^2(B|A)\right), \tag{8.1}$$

where χ^2 is the first term of the test statistics described in Eq. (6.11) of Chap. 6 (also called statistical term):

$$\chi^2(A|B) = 2\left(n_A - n_B + n_A \ln\frac{n_A}{n_B}\right). \tag{8.2}$$

This choice of signed-χ^2 represents the excess in the number of events in each bin as computed with hypothesis A with respect to the number of events obtained with hypothesis B. As discussed in Ref. [122], this convention is suitable for depicting the contribution of each bin into the total statistical contribution of the test statistics used in this work (as defined in Eq. (6.11)), averaged over NO and IO assumptions. It is also worth noting here that the distribution and values computed for this quantity are just to visualize the regions that contribute more, and the relative contribution of each class to the overall sensitivity. The correct sensitivity evaluation is performed with the fit as presented in Chap. 6 and the results will be discussed later.

The effects of the detector on the evolution of the NMO statistical signal, starting from the interacting events up to the final measured distributions, have been discussed extensively in Ref. [122]. Here we concentrate on the NMO signal as obtained from the final expected event distribution, which is shown in Fig. 8.1. The figure depicts the signed-$\chi^2_s(NO|IO)$ distribution in the three defined classes: Tracks, Showers, and Intermediates. The dominant contribution to the NMO signature comes from the Showers class in the energy range of about 3 - 10 GeV, while the contribution of Tracks is notably lower. This is because the NMO sensitivity in the ν_μ CC channel (track-like events) stems from a region of fast oscillations, as one can tell from the rippled structure in Fig. 5.4. This results in a degradation of the sensitivity in the Tracks class because of the effects of energy and angular smearing due to the finite detector resolution. The NMO signal in ν_e CC channel (shower-like events) survives better this effect thanks to the blob-structure spanning a wider energy range in the distribution [122]. The Intermediates class gives a minor con-

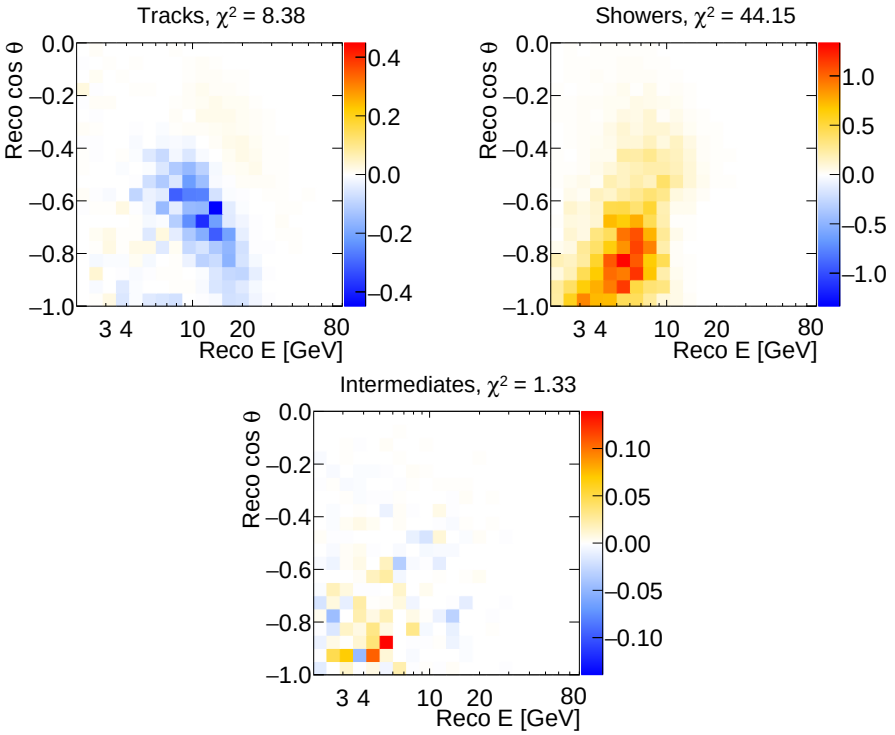

Figure 8.1: The signed-χ^2 distribution between NO and IO assumption in Tracks, Showers and Intermediates classes. The total sum $\sum |\chi_s(NO|IO)|$ is given above each corresponding plot to illustrate the statistical contribution of each class to the total NMO sensitivity.

tribution due to the low purity of flavor information.

8.2.2 Sensitivity study to the neutrino mass ordering

23m vs 20m configuration

As mentioned earlier in this chapter, one of the notable updates in the ORCA NMO sensitivity study is the change in the geometry configuration from 23 m to 20 m horizontal spacing of the DUs. This subsection first describes the evolution in the detector response due to this change, and then its effects on the NMO sensitivity.

Fig. 8.2 shows the effective masses for both detector configurations (20 m and 23 m). Overall, the effective mass of the 20 m configuration is lower than the one of 23 m, except at the lowest (< 4GeV) energies where they are comparable. Moving to a denser detector configuration decreases the effective mass plateau by $\sim 30\%$ and also the plateau is reached earlier. This is expected from the overall reduction of instrumented volume.

Fig. 8.3 and 8.4 respectively depict the energy and angular resolution of the two detector configurations, and their PID performances. The two samples $\nu_\mu + \bar{\nu}_\mu$ CC and $\nu_e + \bar{\nu}_e$

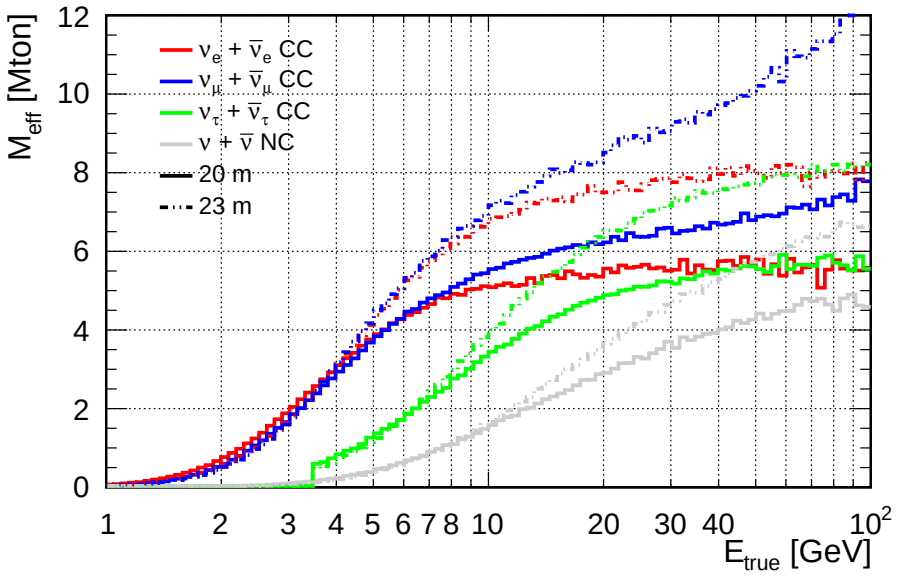

Figure 8.2: ORCA effective masses for different neutrino interaction channels, for the 20 m (solid) and 23 m (dot-dashed) horizontal spacing configurations

CC are used as the two most representative samples contributing respectively to the Track and Shower classes. One can see that the reconstruction accuracy is comparable or, in most cases, slightly improved: the median is closer to zero (as the reconstruction value tends to be closer to the true value) and the resolution is slightly better (as the 90% band is tighter). The same trend is observed in the other channels, not shown here. When going to 20 m spacing, the PID performance improves in both Track and Shower classes, especially for $\nu_\mu + \bar{\nu}_\mu$ CC. This improvement for both PID and reconstruction is somewhat expected because of the denser population of DOMs in the new geometry configuration.

To further explore whether the 20 m is competitive with the old 23 m geometry, the NMO sensitivity of ORCA after 3 years of data taking as the function of θ_{23} true values is shown in Fig. 8.5. The sensitivity is evaluated with the analysis settings described above, except for the value of δ_{CP} which is set to 0, and the statistical method explained in Chap. 6. One can notice that the NMO sensitivity with the new 20 m geometry is better for the 23 m one in all true values of θ_{23}. This demonstrates that the better performance in reconstruction and PID compensates for the loss in effective mass when moving to the denser geometry of 20 m.

SWIM and paramNMH Comparison

To sustain the synchronization of the analysis framework within the collaboration, a comparison between SWIM and paramNMH, the framework used for the results published in

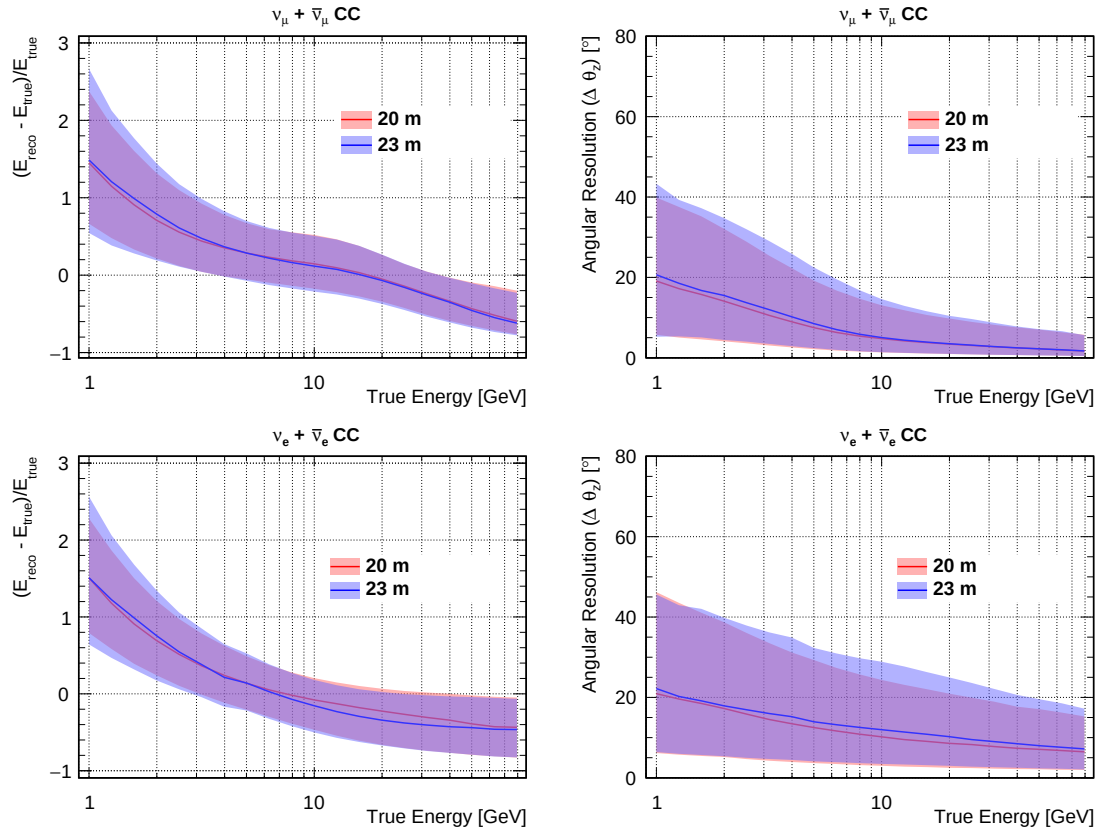

Figure 8.3: Energy (left) and angular (right) resolution of the ORCA 20 m and 23 m configurations for $\nu_\mu + \bar{\nu}_\mu$ CC (top) and $\nu_e + \bar{\nu}_e$ CC (bottom). The line represents the median while the shaded band depicts the 90 % quantile of the distributions.

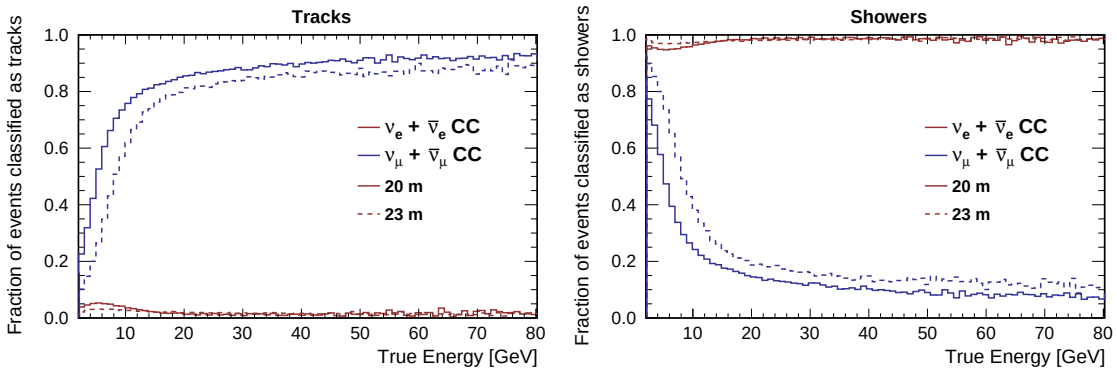

Figure 8.4: Fraction of $\nu_e + \bar{\nu}_e$ CC and $\nu_\mu + \bar{\nu}_\mu$ CC events classified as Tracks (left) and Showers (right) for both 20 m (plain) and 23 m (dashed) geometry.

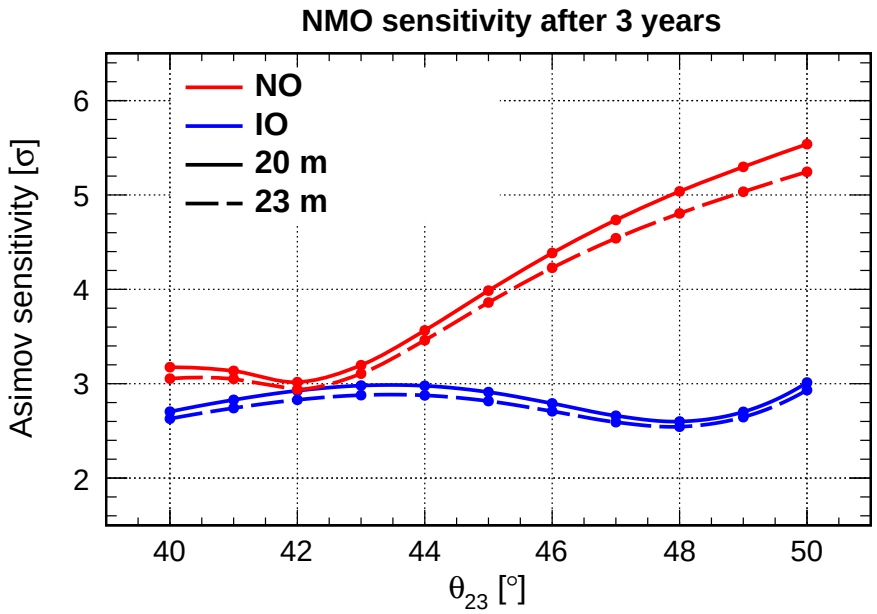

Figure 8.5: Sensitivity to the NMO as a function of true θ_{23}, for 3 years of data taking with the full ORCA detector with either the 20 m (solid) or the 23 m (dashed) geometry, assuming $\delta_{CP} = 0$.

Ref. [98], is performed. The comparison includes a common set of systematics for both frameworks:

- Flux skews (in paramNMH input as flux ratios)
- Flux spectral index
- NC normalization
- PID class normalization

Fig. 8.6 shows the SWIM-paramNMH comparison for the NMO sensitivity of ORCA with 3 years of exposure as the function of true θ_{23}. Since SWIM results are affected by the finite MC problem as discussed in Sec. 6.3 and Ref. [122], the SWIM curve is shown with and without the MC error. The treatment of this error using the 'Beeston and Barlow light method' mentioned in Sec. 6.3 results in a 0.2σ decrease in the sensitivity, reflecting a correction of the overestimation caused by the limited MC sample. As shown in the figure, after correction, SWIM is in really good agreement with paramMNH (which is not affected by the MC fluctuation problem due to the usage of smooth parametrized response functions).

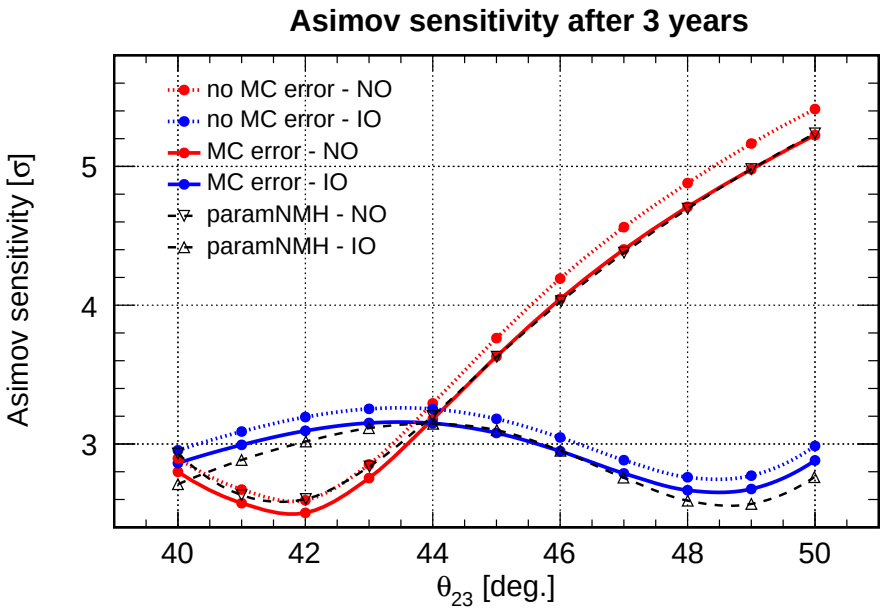

Figure 8.6: NMO sensitivity after 3 years of data taking as the function of true θ_{23} with SWIM (red, blue) and paramNMH (black), assuming the best-fit value for δ_{CP} and the common set of systematics described in the text.

NMO sensitivity with ORCA

The latest results on the NMO sensitivity of ORCA obtained with the SWIM analysis framework are illustrated in Fig. 8.7. The figure shows the NMO sensitivity after 3 years of data taking as the function of true θ_{23}, and the time evolution of NMO sensitivity assuming true values of oscillation parameters following Ref. [128]. The NMO determination potential of ORCA depends strongly on the true value of θ_{23} and true NMO. For the current global best-fit θ_{23} ($\sim 49°$), the NMO sensitivity can reach $\sim 5\sigma$ in case of NO and $\sim 2.8\sigma$ in case of IO after three years of data taking. The dependence in the true value of δ_{CP} can lead to a minor variation of $\sim 0.5\sigma$, with $\delta_{CP} = 0$ giving the most optimistic scenario. With the current global best-fit of oscillation parameters, ORCA can determine the NMO with the significance of 3σ after 1 (4) years of exposure in case of NO (IO) respectively.

The results presented hereabove have been used as an internal cross-check for the KM3NeT Collaboration publication of Ref. [98], which was based on the paramNMH analysis framework. Compared to that publication, the SWIM results give 0.5σ higher NMO sensitivity. The precise reason for that difference is still under investigation. It may be explained by the fact that two more systematics are used in Ref. [98] but currently not used in this analysis: the hadronic energy scale and the up/horizontal neutrino ratio. The hadronic energy scale represents the uncertainties of the light yield in hadronic showers and has been proved internally (using paramNMH) to have a negligible impact on the NMO sensitivity. The up/horizontal neutrino ratio could change the number of events detected

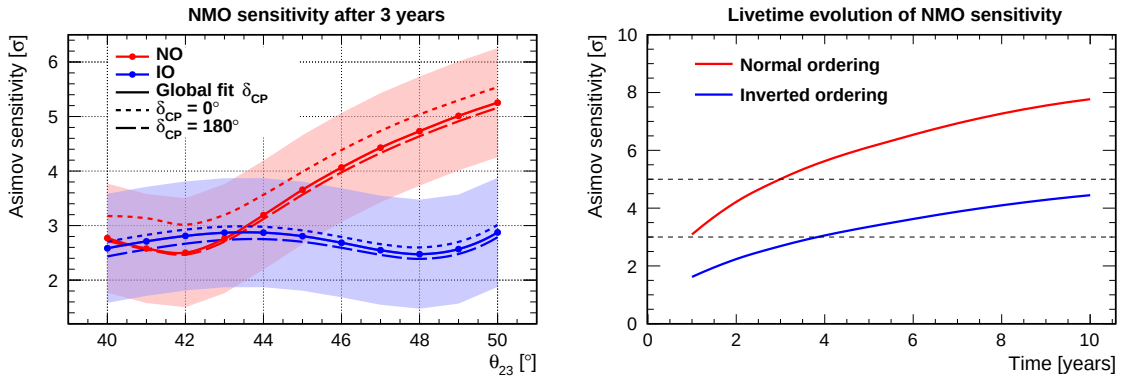

Figure 8.7: Left: NMO sensitivity after 3 years as the function of true θ_{23}, the shaded band shows the sensitivity that 68% ($\pm 1\sigma$) of the experiment realisation would yield, according to the Asimov approach [132]. Right: NMO sensitivity as the function of data taking time with true values of oscillation parameters taken from Ref. [128].

in the NMO sensitivity region, as shown in Fig. 8.1; but it is not clear whether this effect would cause a significant degradation of the signal or if it would remain constrained by the measurements in the regions at higher energy (> 20 GeV) where no NMO signal is expected. The up/horizontal neutrino ratio could in principle be captured by the flux zenith slope systematics in SWIM (as described in Sec. 7.1.1) but this effect has not yet been included in the presented cross-check between the two frameworks. An update of the SWIM framework to account for these systematics is required for reaching a more accurate level of comparison between results obtained with different pipelines.

8.3 Sensitivity for the oscillation parameter measurement

This section presents the sensitivity study for the measurement of the oscillation parameters in the atmospheric sector, θ_{23} and Δm^2_{31}, with ORCA. This goal can also be achieved with the early phase of the detector. Thus, we also investigate the potential for such a measurement with the 7-lines configuration of ORCA (ORCA7).

8.3.1 Sensitivity region

To better understand the origin of the sensitivity, one can take a look at the L/E distribution of the measured events. This stems from the fact that the dominant oscillation term that gives the parameter sensitivity is proportional to $\sin^2\theta_{23}\sin^2\left(\frac{\Delta m^2_{31} L}{4E}\right)$.

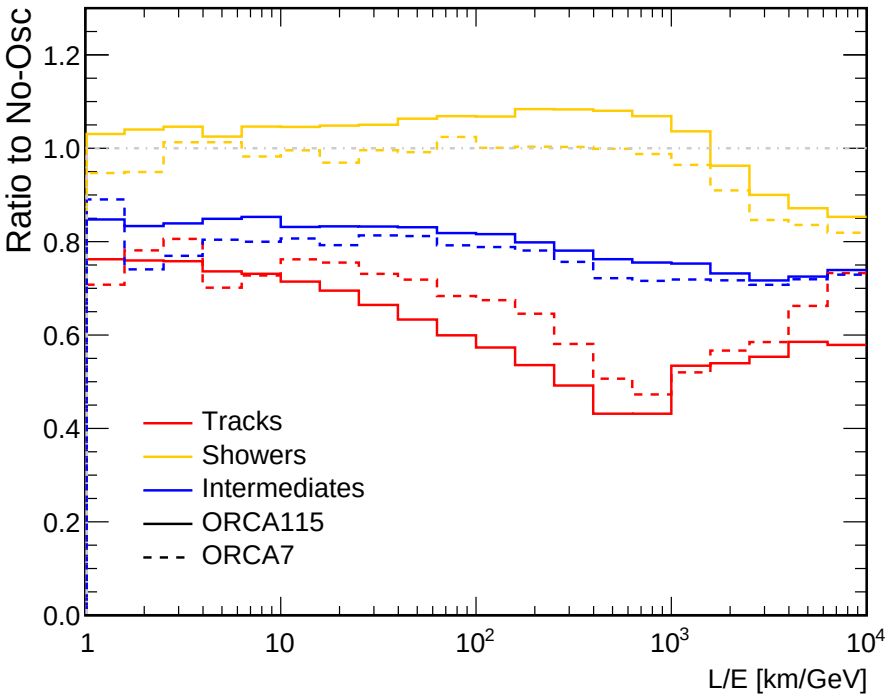

Figure 8.8: L/E distribution of each event class for both ORCA7 (dashed) and ORCA115 (solid), expressed as the ratio between the oscillation and no-oscillation hypothesis, in order to show the origin of the sensitivity.

The ratio of events (after detector response) between oscillation and no-oscillation hypothesis as a function of L/E is shown in Fig. 8.8 for both ORCA115 and ORCA7. The sensitivity to the oscillation mainly originates from the dip observed at $L/E \sim 10^3$[km/GeV], with the largest contribution coming from the Tracks class since $\nu_\mu \to \nu_\mu$ channel plays an important role for this measurement. The figure also shows that with only 7 lines, ORCA is already sensitive to the oscillation parameters.

8.3.2 Sensitivity to Δm^2_{31} and θ_{23}

The sensitivity to Δm^2_{31} and θ_{23} is evaluated following the method described in Chap. 6. For each test value of Δm^2_{31} and θ_{23}, the $\Delta\chi^2$ is evaluated while performing a minimisation on all other parameters, following Tab. 8.2. Then from the Δm^2_{31} surface on the [Δm^2_{31}, θ_{23}] plane, one can extract the excluded region with 90% confidence level.

In Fig. 8.9, the 90% confidence level contours are presented with both ORCA115 and ORCA7. 3 years of data taking for ORCA115 is chosen while just 1 year of ORCA7 is shown since this sub-array of the detector will only be used for an early measurement as the detector configuration will evolve quickly during the construction phase. The results from other experiments are also shown for comparison. After 3 years, the full ORCA detector

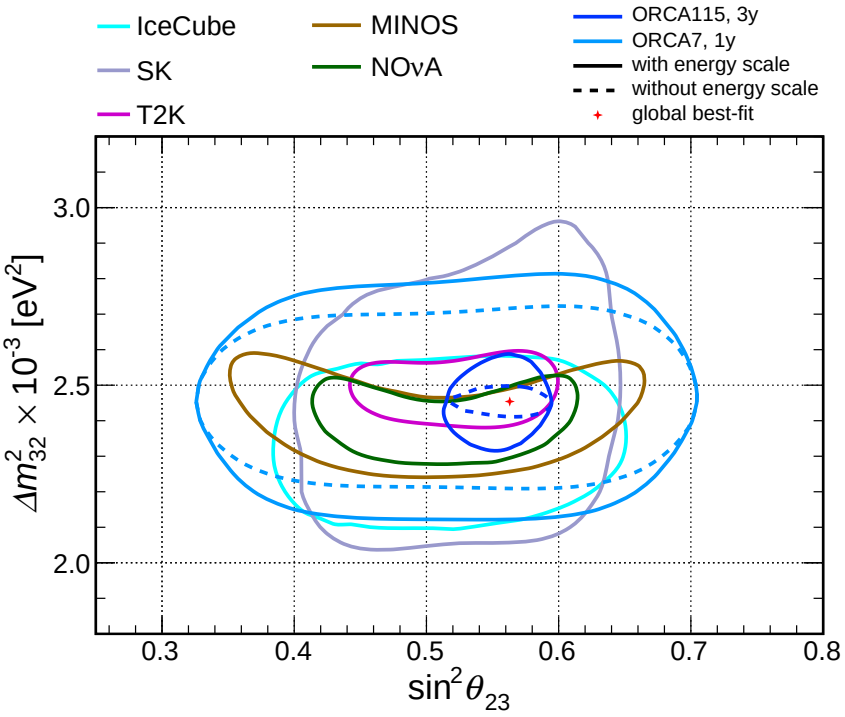

Figure 8.9: Expected 90% confidence level contour on Δm^2_{32} and θ_{23} for NO assumption after 3 (1) years of data taking with ORCA115 (ORCA7) overlaid with the results from other experiments [56, 146–149]. Red cross represents the global best-fit taken from Ref. [128].

can provide a competitive constraint that exceeds the current one from other experiments. Furthermore, ORCA7 with just 1 year of data taking already has the ability to measure Δm^2_{31} and θ_{23}, even though the constraint is still larger than the world data.

As observed in Chap. 7, the energy scale systematics can have a non-negligible impact on the Δm^2_{31} measurement. To illustrate this effect, we show both contours with and without this systematics. The energy scale systematics causes the 90% C.L. contour of $\Delta^2 m_{31}$ to increase by $\sim 10\%$, while it has no impact on the θ_{23} measurement.

8.4 Conclusion

This chapter presents the latest sensitivity of the KM3NeT/ORCA detector to the NMO and oscillation parameters, in particular, the mixing parameters in the atmospheric sector: Δm^2_{31} and θ_{23}, as obtained with the SWIM analysis framework. These results have been used as the internal cross-check for the one presented in Ref. [98] and Ref. [143].

In terms of NMO determination, the analysis presented here has shown that the updated 20 m geometry has slightly better NMO sensitivity due to the improvement in PID

and reconstruction performance. In summary, a significance at the 5σ confidence level can be reached within 3 years, while only 1 year of data taking is required for 3σ if we assume the current global best-fit of θ_{23} and true NO. For the true IO scenario, 3σ can be achieved after 4 years but 5σ will require more than 10 years. However, this time span can be significantly reduced by a combination with the reactor neutrino experiment JUNO, as will be presented in the next chapter.

For the Δm^2_{31} and θ_{23} measurement, a full ORCA detector with 3 years of exposure can improve on the current constraints from world data. In addition, this measurement can already be performed with only 7 lines at an early construction phase of ORCA.

Chapter 9

Neutrino mass ordering sensitivity with the combination of KM3NeT/ORCA and JUNO

Contents

The previous chapter has presented the sensitivity of the KM3NeT/ORCA detector to the NMO, which is obtained by exploiting Earth matter effects on the atmospheric neutrino oscillations in the GeV energy range. Another experiment also aiming at the NMO determination is JUNO (Jiangmen Underground Neutrino Observatory). It is a medium-baseline ($\sim$ 53 km) reactor neutrino experiment that probes the NMO through the interplay between the fast oscillations driven by Δm^2_{31} and Δm^2_{32} in the $\bar{\nu}_e$ disappearance channel, where matter effects play only a small role [150].

This Chapter presents a study on the combination of ORCA and JUNO for the NMO determination, which led to the publication in Ref. [65]. This is a collaborative work in which the JUNO analysis is provided by the JUNO group at the Hubert Curien Pluridisciplinary Institute (IPHC). This combination is motivated by the boost in NMO sensitivity resulting from the expected tension between JUNO and ORCA in the best-fit of Δm^2_{31} when assuming the wrong ordering. The tension arises from the fact that each experiment measures the oscillation parameters in different channels: $\bar{\nu}_e$ disappearance for JUNO and ν_μ disappearance as the main channel for ORCA. The effect has been first mentioned in relation to accelerator neutrino experiments [151, 152]. The reassessment of this effect in the context of the combination of a reactor experiment (Daya Bay II, now evolved into JUNO) and an atmospheric neutrino experiment (PINGU [62], a proposed low-energy extension of the IceCube neutrino telescope), is discussed in Ref. [63] which shows that a strong boost in NMO sensitivity can indeed be reached with a combined fit. In Ref. [64], the same conclusion is reached by performing the combination with detailed simulation tools for JUNO and PINGU.

ORCA is in construction phase with an incremental deployment until 2025, with currently 6 out of total 115 lines installed and taking data [123], while JUNO is planned to be completed in 2022. Their almost simultaneous timelines further motivate the combination.

This Chapter first presents the theoretical aspects of determining NMO by comparing $\bar{\nu}_e$ and ν_μ disappearance in Sec. 9.1. The JUNO detector and the JUNO analysis are described in Sec. 9.2, while Sec. 9.3 presents the ORCA settings for this combination. The combination strategy and results are shown in Sec. 9.4 and Sec. 9.5 respectively. Sec. 9.6 extends the study to evaluate the impact of possible variations in the configuration of each experiment, as well as the dependence of the combination on the true values of oscillation parameters. Conclusions are drawn in Sec. 9.7.

9.1 The determination of NMO by comparing $\bar{\nu}_e$ and ν_μ disappearance

In this section, we illustrate from a phenomenological point of view how one can determine the NMO by measuring Δm^2_{31} from two different oscillation channels ($\bar{\nu}_e$ and ν_μ disappearance). This section is a short summary from [152] - Section III.

We start with the $\nu_\alpha \to \nu_\alpha$ surviving oscillation probabilities in vacuum:

$$P_{\alpha\alpha} = 1 - 4|U_{\alpha1}|^2|U_{\alpha2}|^2 \sin^2\left(\frac{\Delta_{21}L}{2}\right) - 4|U_{\alpha1}|^2|U_{\alpha3}|^2 \sin^2\left(\frac{\Delta_{31}L}{2}\right) - 4|U_{\alpha2}|^2|U_{\alpha3}|^2 \sin^2\left(\frac{\Delta_{32}L}{2}\right), \tag{9.1}$$

where $\Delta_{ij} = \Delta m^2_{ij}/2E = (m^2_i - m^2_j)/2E$.

Next, we try to find out for a given value of Δm^{2+}_{31} in NO scenario, if there is a value of Δm^{2-}_{31} in IO that will reproduce the oscillation probability (9.1) for all values of L/E, assuming the same mixing matrix and Δm^2_{21}. One can then define $\Delta m^{2-}_{31} = -\Delta m^{2+}_{31} + x$ ($x < \Delta m^{2+}_{31}$). The difference in oscillation probability for NO and IO is computed as:

$$P^+_{\alpha\alpha} - P^-_{\alpha\alpha} = -4|U_{\alpha3}|^2 \left\{ |U_{\alpha1}|^2 \left[\sin^2\left(\frac{\Delta_{31}L}{2}\right) - \sin^2\left(\frac{(\Delta_{31} - X)L}{2}\right)\right] + |U_{\alpha2}|^2 \left[\sin^2\left(\frac{(\Delta_{31} - \Delta_{21})L}{2}\right) - \sin^2\left(\frac{(\Delta_{31} + \Delta_{21} - X)L}{2}\right)\right]\right\}, \tag{9.2}$$

with $X = x/(2E)$. One can see that there is no solution for x satisfying $P^+_{\alpha\alpha} - P^-_{\alpha\alpha} = 0$ except in the special case of $U_{\alpha2} = U_{\alpha1}$ and $x = \Delta m^2_{21}$, which does not correspond to reality. Instead, we can consider a realistic case where we probe the oscillation probability in conditions such that $\Delta_{31}L \sim 1$ and $\Delta_{21}L \ll 1$, which is the case for long-baseline experiments. Under such assumption, one can expand the $\sin^2$ terms in Eq. (9.2), neglecting the higher order terms $O((\Delta_{21}L)^2)$ and $O((XL)^2)$. The solution for $P^+_{\alpha\alpha} - P^-_{\alpha\alpha} = 0$ then yields:

$$x_{\alpha\alpha} = \frac{2|U_{\alpha2}|^2}{|U_{\alpha1}|^2 + |U_{\alpha2}|^2}\Delta m^2_{21}. \tag{9.3}$$

This means that if NO is true and we measure Δm^2_{31} under the abovementioned circumstances ($\Delta_{31}L \sim 1$ and $\Delta_{21}L \ll 1$), we could end up with two different values: Δm^{2+}_{31} if assuming the right ordering and $\Delta m^{2-}_{31} = -\Delta m^{2+}_{31} + x$ if assuming the wrong ordering. A similar derivation can also be performed with IO assumed to be true.

The presented inverted-normal ordering degeneracy can be eliminated if one compares

the measurement of Δm^2_{31} in two different oscillation channels. Since $x_{\mu\mu} \neq x_{ee}$ as long as $U_{\alpha 1} \neq U_{\alpha 2}$, the measurement of Δm^2_{31} in $\bar{\nu}_e$ and ν_μ disappearance when assuming wrong ordering can be different.

The formulas derived above are valid for long-baseline accelerator experiments and show, in principle, how a tension in Δm^2_{31} best-fit can arise from measuring different oscillation channels with wrong ordering assumption. A similar effect is expected for the case of JUNO and ORCA. JUNO is a reactor experiment which measures Δm^2_{31} from $\bar{\nu}_e$ disappearance channel. On the other hand, the main contribution of Δm^2_{31} sensitivity in ORCA comes from ν_μ disappearance channel. Thus, a combination between JUNO and ORCA would improve the NMO sensitivity due to the tension in Δm^2_{31} when assuming wrong ordering.

In the realistic cases of JUNO and ORCA, more complicated effects can be involved as discussed in [130]. The measurement of Δm^2_{31} in ORCA also uses other channels apart from $\nu_\mu \rightarrow \nu_\mu$; both ν and $\bar{\nu}$ as well as electron neutrinos are taken into account. The measurement is also sensitive to matter effects. JUNO will measure the Δm^2_{31} by probing the fast oscillation component on the energy spectrum of which an analytical form can be found in Ref. [153]. Despite these differences compared to the presented formulas, we will still see that the tension in Δm^2_{31} appears between JUNO and ORCA when assuming wrong ordering. Thanks to the good resolution in the Δm^2_{31} measurement of the two experiments, this tension enhances the NMO sensitivity.

9.2 JUNO - Jiangmen Underground Neutrino Observatory

The Jiangmen Underground Neutrino Observatory [58, 154, 155] (JUNO) is a multipurpose experiment being built in the south of China. One of its main goals is the determination of the NMO via the precise measurement of reactor neutrino $\bar{\nu}_e$ from the Yangjiang and the Taishan Nuclear Power Plants (NPP) located 53 km away from the detector. The location of the JUNO detector and its schematic view are shown in Fig. 9.1.

The JUNO detector contains 3 parts: the Central Detector, the Water Cherenkov Detector and the Top Tracker. The Central Detector is composed of 35.4 m diameter acrylic sphere and 20 kton of liquid scintillator placed inside. Around the acrylic sphere, about 18 000 20" and 26 000 3" PMTs monitor the liquid scintillator volume to detect the Inverse Beta Decay (IBD) interactions produced by $\bar{\nu}_e$ from the NPPs. When an IBD happens inside the JUNO Central Detector, the prompt signal is detected as the scintillation light created

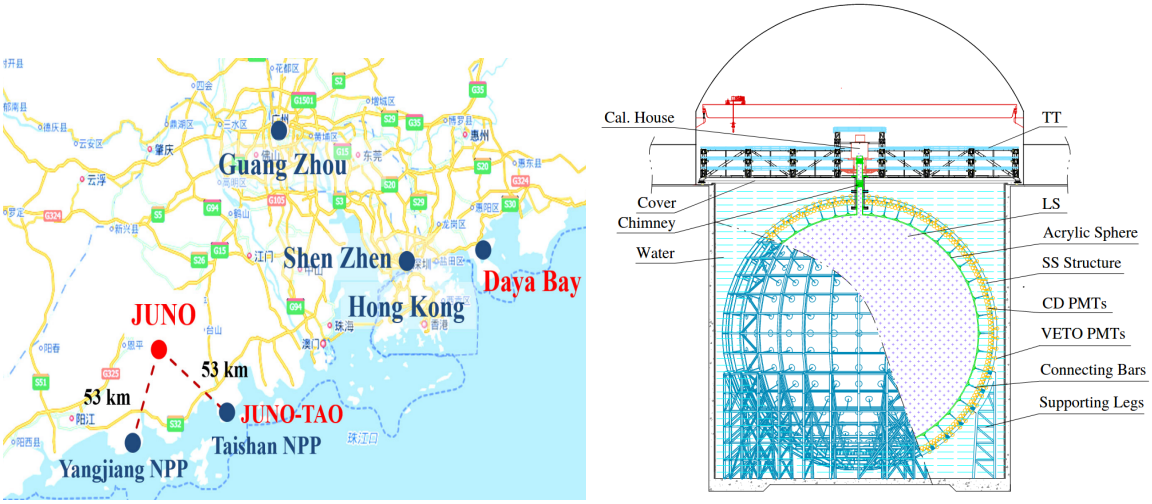

Figure 9.1: JUNO location (left) and the schematic view of JUNO detector (right). Figures are taken from Ref. [155]. The acronym used in the figures: LS (Liquid Scintillator), SS (Stainless Steel), CD (Central Detector), TT (Top Tracker).

from the produced positron and its subsequent annihilation develop. After that, there is the delayed detection of a 2.2 MeV gamma-ray produced via the neutron capture on hydrogen and subsequent de-excitation of the deuteron. Most of the available energy of the incident $\bar{\nu}_e$ is transferred to the positron because of the kinematics of the IBD. As a result, a precise measurement of neutrino oscillations requires a good energy resolution to detect the visible energy of the prompt signal, as will be discussed later. The measured visible energy is smaller than the incident $\bar{\nu}_e$ energy by about 0.8 MeV, due to the mass difference between the initial and final particles (-1.8 MeV) and to the light emitted in the positron annihilation ($+1.0$ MeV). The Central Detector is placed at the center of the Water Cherenkov Detector which is a cylindrical ultra-pure water pool (44 m height, 43.5 m diameter). It serves as a shield for the Central Detector from external radioactivity and provides a veto for atmospheric muons as well as for muon-induced background such as cosmogenic nuclei and fast neutrons. This Water Cherenkov Detector and the Top Tracker, located on top of it to track atmospheric muons, together, form the Veto System of JUNO.

Along with the JUNO detector described above, the project also includes the Taishan Antineutrino Observatory (JUNO-TAO) detector [156]. This detector will be located at a baseline of 30 m from one of the Taishan's reactors to measure the reactor $\bar{\nu}_e$ spectrum with a better energy resolution than JUNO. This measurement would effectively reduce the impact of possible unknown substructures in the reactor neutrino spectra [157] on the measurement of neutrino oscillations.

In this study, the precise distance of the JUNO detector to each reactor core of the Yangjiang and Taishan NPPs is used following Ref. [58] rather than just the distance to the NPP complex. Additionally, the NPPs of Daya-Bay at 215 km and Huizhou at 265 km will

also contribute to the total number of detected reactor neutrinos. Nevertheless, given the much larger distance compared to the Yangjiang and Taishan NPPs, the oscillation pattern will not be the same and these neutrinos are treated as part of JUNO's intrinsic background.

The initial proposal in Ref. [58] contains 10 reactor cores distributed between the Yangjiang and Taishan sites. For the moment, the Yangjiang NPP is already fully operational, with 6 reactor cores for a total of 17.4 GW of thermal power. The Taishan NPP has already 2 reactor cores operational out of the 4 initially foreseen, with a total thermal power of 9.2 GW. Nevertheless, the plan for building the last 2 of Taishan cores, which would bring another additional 9.2 GW of thermal power, is currently uncertain. The Huizhou NPP is under construction and expected to be ready by about 2025 [155] with 17.4 GW thermal power.

The JUNO analysis in this work is performed with the framework developed by the JUNO group at IPHC. The description of the model for JUNO detector and the sensitivity evaluation used in this framework are given below.

9.2.1 Modeling JUNO for the study

This section presents the model used for the JUNO detector response in this analysis. The performance of JUNO closely follows the one provided in Ref. [58]. In particular, we assume a 73% IBD detection efficiency and an energy resolution of $3\%/\sqrt{E/\text{MeV}}$ in the Central Detector which contains 1.5×10^{33} target protons. The impact of a $\pm 0.5\%/\sqrt{E/\text{MeV}}$ change in energy resolution is considered in Sec. 9.6.1 as the energy resolution is critical for the JUNO sensitivity. Following Ref. [58], the nominal running time of 1000 effective days every 3 years is adopted for the experiment.

The measured $\bar{\nu}_e$ spectrum in JUNO is produced as the net effect from the flux induced by the NPPs, the IBD cross-section [158], and the neutrino oscillations. The spectrum produced by the NPPs is determined by the ILL[1] $\bar{\nu}_e$ spectra [159–161] given that the flux normalization is in better agreement with previous data [162]. The fine structure of the spectrum will be precisely measured independently using JUNO-TAO detector as mentioned before. Therefore, it is not included in the spectrum shape. The reactor neutrino spectrum is calculated using the fraction content of fission fragments as: ^{235}U :^{239} Pu :^{238} U :^{241} Pu $= 0.564 : 0.304 : 0.076 : 0.056$ which is similar to the one used in Ref. [163], and the fission energies for each of these isotopes are taken from Ref. [164].

The backgrounds considered in this analysis are taken from Ref. [58], in terms of their rate, shape, and uncertainties. Three dominant components are considered as follows: cos-

[1]Institut Laue-Langevin

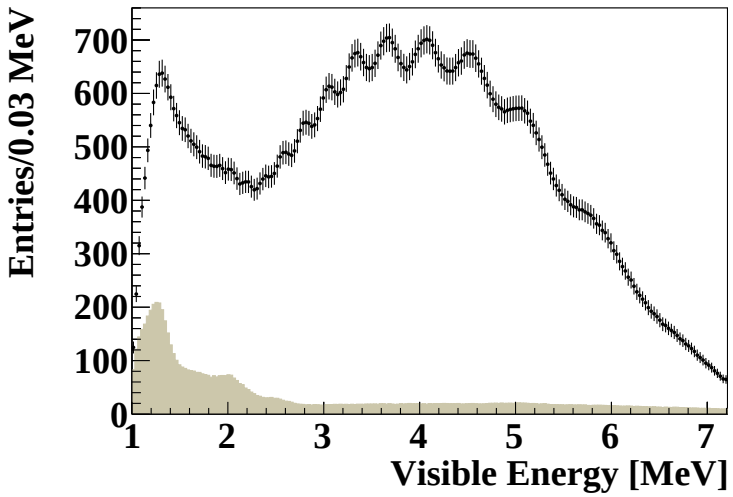

Figure 9.2: Expected event distribution for 6 years of data with JUNO 8 cores as a function of the visible energy of the prompt signal. The current world best-fit [128] oscillation parameters for normal ordering are assumed. The shaded region corresponds to the non-reactor neutrino background events.

mogenic events, geo-neutrinos, and accidental coincidences mainly from the radioactive background, with the rates of about 1.6, 1.1, and 0.9 events per day respectively. As a reference, the expected event rate for Daya-Bay and Huizhou NPPs in total are 4.6 events per day in JUNO while the Taishan and Yangjiang NPPs are 54.3 events per day, assuming the NO world best-fit [128] oscillation parameters, considering all 4 Taishan NPP reactors in operation.

As mentioned, only 2 reactors in the Taishan NPP are currently available while the other 2 reactors are not foreseen. Therefore, the configuration of 8 cores for JUNO (6 at Yangjiang and 2 at Taishan) is used as the baseline in this study and referred to as "JUNO 8 cores". This is a notable difference from Ref. [58] and resulting in 25% less expected signal neutrinos in comparison. Nevertheless, for completeness, the JUNO official configuration with a total of 4 Taishan reactors is also considered in Sec. 9.6.1 and referred to as "JUNO 10 cores". Even though not yet completed, the Huizhou NPP is considered to be active for the whole duration of JUNO in both cases, contributing to the intrinsic background to the neutrino oscillation measurements in JUNO.

Fig. 9.2 shows the expected event distribution as a function of visible energy for 6 years of data taking with 8 cores and the true value of oscillation parameters taken from Ref. [128] in case of NO assumption. The plot also depicts the non-reactor neutrino background. They are mainly distributed in the low-energy region where the energy resolution of JUNO is still not good enough to observe the fast oscillation pattern.

9.2.2 Sensitivity analysis

In JUNO, one can extract the measurement of oscillation parameters and NMO by fitting the measured positron energy spectrum as shown in Fig. 9.2. This figure exhibits two notable features: (i) the slow oscillation governed by θ_{21} and Δm^2_{21} which causes the overall large deficit of the number of events in the whole energy range with a minimum at ~ 2.2 MeV, and (ii) the rapid oscillatory behavior due to Δm^2_{31} and θ_{13} which starts to appear around 2 MeV. If IO were assumed instead of NO in Fig. 9.2, the minima and maxima of the fast oscillation pattern would change position due to the change in oscillation frequencies that produce such pattern [58]. This effect helps JUNO determine NMO. The NMO sensitivity of JUNO is then quantified by the χ^2 difference of the data being fitted under the two ordering hypotheses. The χ^2 function used for evaluating ORCA's NMO sensitivity has been presented explicitly in Chap. 6. Here, we describe the χ^2 function used for JUNO. Then, Sec. 9.4 will show how the combined χ^2 of the two experiments is calculated for the joint analysis.

In this analysis, the measured JUNO visible energy spectrum is linearly binned with $n = 207$ bins of 0.03 MeV between 1.00 MeV and 7.21 MeV. The JUNO analysis adopts a χ^2 function in the following form:

$$\chi^2 = \boldsymbol{\Delta} \times \boldsymbol{\mathcal{M}}^{-1} \times \boldsymbol{\Delta}^T, \tag{9.4}$$

where $\boldsymbol{\Delta}$ is a $1 \times n$ matrix whose content is the difference between the observed and expected rates. $\boldsymbol{\Delta}$ is defined as $\boldsymbol{\Delta} = \boldsymbol{D} - (\boldsymbol{S} + \boldsymbol{B})$, where $\boldsymbol{D}$, $\boldsymbol{S}$, and $\boldsymbol{B}$ correspond to the data, the prediction for a given set of oscillation parameters, and the expected background respectively. $\boldsymbol{\Delta}^T$ is the transpose matrix of $\boldsymbol{\Delta}$. It is worth noting here that we also adopt the Asimov data set approach [132] in coherence with the ORCA analysis as mentioned in Chap. 6. Therefore, $\boldsymbol{D}$ is given by the Asimov sample for the assumed true value of the oscillation parameters, and the NMO significance of JUNO is estimated in a similar way to the one presented in Sec. 6.1: $S_{Asimov} = \sqrt{\overline{\Delta\chi^2}}[\sigma]$.

The matrix $\boldsymbol{\mathcal{M}}$ is a $n \times n$ covariance matrix which is calculated as $\boldsymbol{\mathcal{M}} = \boldsymbol{\mathcal{M}}_{stat} + \boldsymbol{\mathcal{M}}_S + \boldsymbol{\mathcal{M}}_B$. $\boldsymbol{\mathcal{M}}_{stat}$ corresponds to the statistical uncertainty in each bin from the total expected number of events ($\boldsymbol{S} + \boldsymbol{B}$). $\boldsymbol{\mathcal{M}}_S$ and $\boldsymbol{\mathcal{M}}_B$ correspond, respectively, to the covariance matrices of the signal and background as described in Ref. [58].

For consistency, the JUNO analysis in this work has been cross-checked with the previous results in Refs. [58, 64]. With the same set of oscillation parameters and reactor cores as in those references, the NMO sensitivity comparison shows an agreement within 0.1–0.5 χ^2 units.

Table 9.1: Baseline (see Ref. [98]) and optimistic (see Ref. [64]) scenarios for the treatment of systematics considered in the ORCA analysis. The cross (×) indicates that the systematic is not included.

Parameter	Baseline scenario	Optimistic scenario
Flux spectral index	free	
Flux $\nu_e/\bar{\nu}_e$ skew	7% prior	
Flux $\nu_\mu/\bar{\nu}_\mu$ skew	5% prior	
Flux $(\nu_e+\bar{\nu}_e)/(\nu_\mu+\bar{\nu}_\mu)$ skew	2% prior	
NC normalization	10% prior	
Detector energy scale	5% prior	×
PID-class norm. factors	free	×
Effective area scale	×	10% prior
Flux energy scale	×	10% prior

9.3 ORCA settings for the combined analysis

The general settings for the ORCA analysis are similar to what is presented in Chap. 8 with the use of SWIM analysis framework. The evaluation of the NMO sensitivity is exactly the same as the one presented in Chap. 6 and used in Chap. 8, which adopts the Asimov approach. This section mainly focuses on the systematics used for this study.

In this combined study, two sets of systematics are used for ORCA as presented in Tab. 9.1. The “baseline” scenario corresponds to the standard set of ORCA systematics adopted for oscillation analyses, similar to the one used in Chap. 8. The only difference is that the Flux zenith slope is not included here. Because it is observed for SWIM that this systematics has a negligible impact on the NMO sensitivity, we do not include it for the sake of achieving an acceptable computational speed in the combination, while still keeping the ORCA-alone result in agreement with Chap. 8. Other than that, the systematics and their priors are identical to the ones presented in Chap. 8. The energy scale mentioned in the previous chapters (Chap. 7 and Chap. 8) is referred to as the “detector energy scale" to distinguish it from the one of the second systematics scenario described below.

A second, “optimistic” scenario is based on the study in Ref. [64], developed for the PINGU detector. In that analysis, the normalization factors of each PID class are not included. Alternatively, it uses an overall scaling factor that represents a universal systematic uncertainty on all effective areas (or equivalently, on the combined $\nu+\bar{\nu}$ event rate). This effective area scaling, together with an energy scale uncertainty introduced at the flux level, are the only systematics introduced to account, *e.g.*, for potential variations in the detection efficiency of the optical modules. In contrast to the baseline case, these systematics are not applied at the detector response level and are therefore considered as more optimistic in the rest of our study. Fig 9.3 further illustrates the difference between the two

approaches by showing the implementation of each set of systematic uncertainties into the workflow of the SWIM framework. The "baseline" systematic set is believed to be more accurate for the description of the uncertainties in the ORCA detector. It is therefore used for all presented results, unless when stated explicitly that the "optimistic" systematics are used for the sake of cross-checks and comparisons.

It is worth noting here that one would expect the main difference between the two systematic scenarios to arise from the energy scale implementation. As discussed in Sec. 7.2.6, the energy scale applied at the detector level can strongly affect the measurement of Δm^2_{31}. The flux energy scale as described in the optimistic scenario in fact does not produce the same impact due to its implementation in the non-oscillated flux. Fig. 9.4 shows the χ^2 profile as a function of Δm^2_{31} and energy scale systematic, and therefore also demonstrates the correlation between this systematic and Δm^2_{31}. One can see that the detector energy scale shows a strong correlation with Δm^2_{31} which explains the effects observed in Fig. 7.7. In contrast, the flux energy scale shows a weak correlation with Δm^2_{31} and thus would not

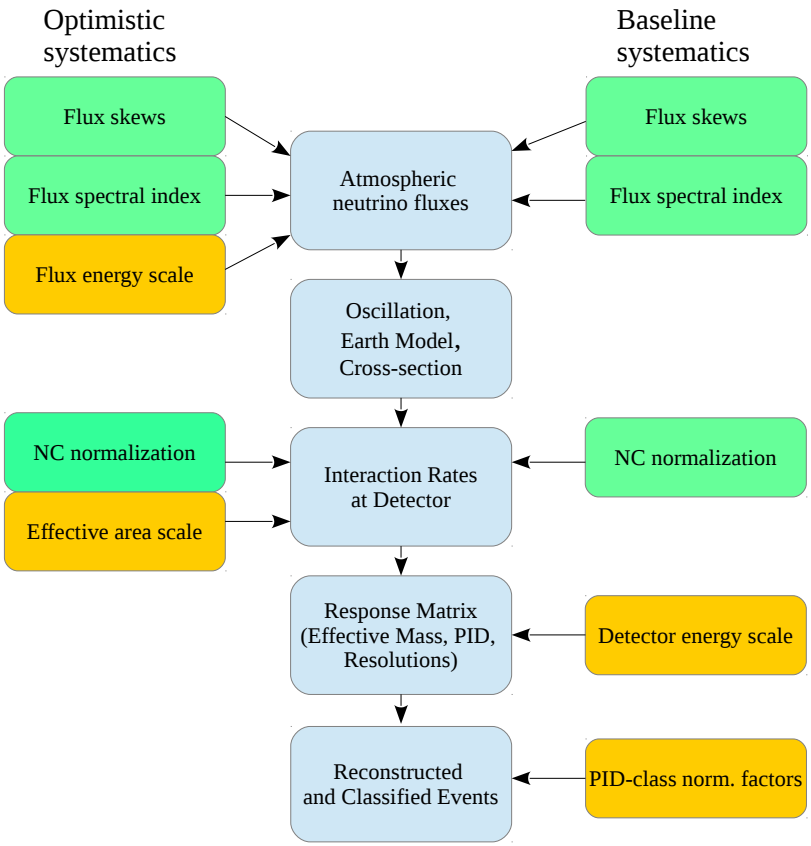

Figure 9.3: Implementation of the two different systematic approaches in the SWIM workflow used in the ORCA analysis.

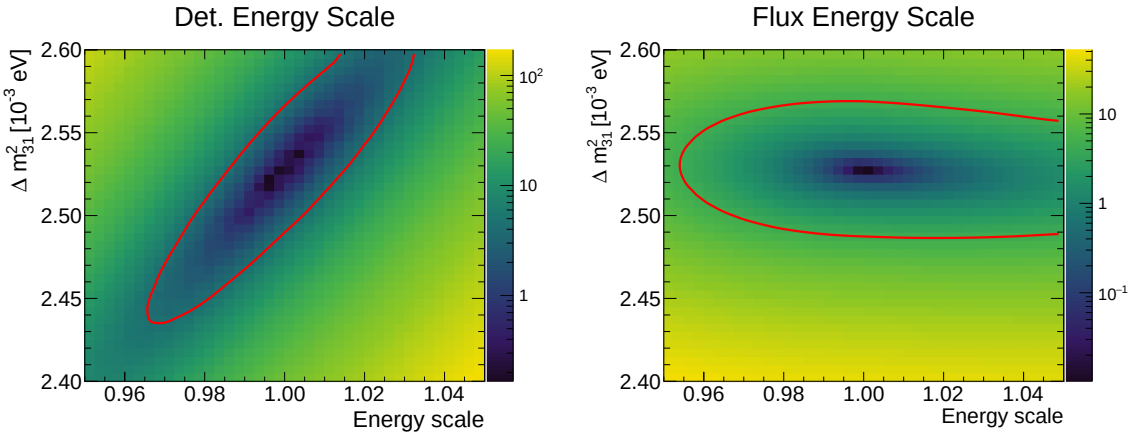

Figure 9.4: χ^2 profile as the function of Δm^2_{31} and energy scale systematic. Left: Detector energy scale, Right: Flux energy scale. The red line illustrates the 90% contour.

affect the precision of Δm^2_{31} measurement. Since the Δm^2_{31} measurement is important for the combined results, one will see later that the two systematic scenarios can have a different impact on the combination.

9.4 Combination strategy

The two detectors involved in this combined analysis work in very different conditions as to their detection techniques and backgrounds, and regarding the sources and energies of neutrinos relevant for each analysis. Therefore, the combination is only performed on the oscillation parameters which are probed by both detectors.

Not all parameters used to describe standard neutrino oscillations have an impact on the results of this analysis. On one hand, the $\bar{\nu}_e$ disappearance channel measured in JUNO does not depend on θ_{23} and δ_{CP} [58] while they are considered for ORCA. On the other hand, ORCA has negligible sensitivity to θ_{12} and Δm^2_{21} as the measured $\nu_\mu + \bar{\nu}_\mu$ oscillations happen at a much smaller L/E than the one required for the development of oscillations with a frequency given by Δm^2_{21} [61]. JUNO, in fact, can measure them at a sub-percent level. These four oscillation parameters that impact a single experiment are accounted for implicitly in the χ^2 function computation for each experiment following the prescription outlined below. The remaining two oscillation parameters, Δm^2_{31} and θ_{13}, have to be considered explicitly in the joint analysis as both experiments are sensitive to them.

In JUNO, for every value of Δm^2_{31} and θ_{13}, the χ^2 is minimized using a grid of 61 uniformly spaced values in $\sin^2\theta_{12}$ between 0.30225 and 0.31775. Δm^2_{21} is kept fixed at the assumed true value given that JUNO will be able to determine this parameter quickly. Stud-

ies have shown that profiling or keeping this parameter fixed would have an impact smaller than about 0.1 units of χ^2, which is negligible in this joint analysis.

In ORCA, for every value of Δm^2_{31} and θ_{13}, we keep θ_{12} and Δm^2_{21} values fixed to their assumed true values given that ORCA has negligible sensitivity to them. The parameters θ_{23} and δ_{CP} are relevant and minimized without any constraints. Similarly to the process used for the ORCA analysis in Chap. 8, the minimization is performed twice, with each time the initial value of θ_{23} being located in a different octant for each minimization. After that, only the smallest value is kept as the global minimum of the χ^2. This approach ensures that the minimizer is not trapped in a possible local minimum.

For the combination, the obtained χ^2 values of each experiment at a fixed test value of Δm^2_{31} and θ_{13} are calculated and summed. The true value of the oscillation parameters considered are the global best-fit values from Ref. [128] obtained "with SK data", unless it is explicitly stated otherwise. For added clarity, those parameters are shown in Tab. 9.2. Because neither JUNO nor ORCA are as sensitive to θ_{13} as the current reactor neutrino experiments [49, 144, 145], a prior on that parameter is added to the combined χ^2 based on the constraint from Ref. [128]. Eq. (9.5) shows the full expression for the combined χ^2 function where Δm^2_{31} and θ_{13} are the tested values of those oscillation parameters. The last term of the formula corresponds to the added prior with $\sin^2\theta^{\text{GF}}_{13}$ being the current global best fit for $\sin^2\theta_{13}$ and $\sigma_{\sin^2\theta^{\text{GF}}_{13}}$ represents its uncertainty.

$$\chi^2\left(\Delta m^2_{31}, \theta_{13}\right) = \chi^2_{\text{JUNO}}\left(\Delta m^2_{31}, \theta_{13}\right) + \chi^2_{\text{ORCA}}\left(\Delta m^2_{31}, \theta_{13}\right) + \frac{\left(\sin^2\theta_{13} - \sin^2\theta^{\text{GF}}_{13}\right)^2}{\sigma^2_{\sin^2\theta^{\text{GF}}_{13}}}. \quad (9.5)$$

For each set of true parameters studied, the combined χ^2 from Eq. (9.5) is computed for each NMO in a 101×21 grid in the $\left(\Delta m^2_{31}, \sin^2\theta_{13}\right)$ space, called the χ^2 map. The grid is defined such that the center is around the assumed true values of the oscillation parameters and spanning uniformly a $\pm 10\%$ interval in Δm^2_{31} from the central value and a $\pm 6\%$ interval in $\sin^2\theta_{13}$ from the central value. More explicitly, in case of assuming true normal ordering with the best-fit values from Ref. [128], the tested values of Δm^2_{31} in the grid runs from -2.78080×10^{-3} eV^2 to -2.27520×10^{-3} eV^2 and from 2.27520×10^{-3} eV^2 to 2.78080×10^{-3} eV^2 with step of 0.00506×10^{-3} eV^2, and those of $\sin^2\theta_{13}$ in the grid is from 0.0210278 to 0.0237122 with a step of 0.0001342. It is worth noting that when the true value of the oscillation parameters is changed, as in Sec. 9.6, or when assuming IO, the described grid is changed such that the central value corresponds to the true values of oscillation parameters.

Table 9.2: Global best-fit values for the oscillation parameters (from Ref. [128]) and assumed to be the "true value" in this analysis. Uncertainties are shown for the parameter where a prior based on the global best-fit value was used.

Parameter	Normal Ordering	Inverted Ordering
$\sin^2\theta_{23}$	0.563	0.565
$\sin^2\theta_{13}$	$0.02237^{+0.00066}_{-0.00065}$	0.02259 ± 0.00065
Δm^2_{31}	2.528×10^{-3} eV^2	-2.435×10^{-3} eV^2
δ_{CP}	221°	282°
$\sin^2\theta_{12}$	0.310	
Δm^2_{21}	7.39×10^{-5} eV^2	

Using the χ^2 map above, for each set of true oscillation parameters tested, the NMO sensitivity is computed as presented in Chap. 6, in particular: $\overline{\Delta\chi^2} = \chi^2_{WO} - \chi^2_{TO}$, where χ^2_{WO} (χ^2_{TO}) is the minimum value of χ^2 in the χ^2 map in the wrong (true) ordering region of the map. The $\overline{\Delta\chi^2}$ is then converted into a median sensitivity $S(\sigma) = \sqrt{\overline{\Delta\chi^2}}$ [131]. The same procedure is also used separately for ORCA and JUNO to obtain the corresponding non-combined sensitivities, computed for each experiment alone.

9.5 Combination results

Fig. 9.5 presents the profile $\overline{\Delta\chi^2}$ scan on the test values of Δm^2_{31} with 6 years of JUNO and ORCA data taking. The four profiles correspond to true normal (top) and inverted (bottom) orderings while fitting the true or wrong ordering. Due to the use of the Asimov dataset, when assuming the true ordering on the fit both experiments show the same best-fit values at the true Δm^2_{31} and their $\overline{\Delta\chi^2}$ minima yield zero. However, when assuming wrong ordering, the minima of $\overline{\Delta\chi^2}$ are no longer at zero and this difference represents the obtained sensitivity to the NMO. After 6 years, JUNO will be able to exclude the wrong ordering with the significance of $\sim 2.3\sigma$ for either NMO. In case of ORCA, it is expected to reach a significance of more than 6σ (3σ) for true NO (IO).

Fig. 9.5 also illustrates how the combination of JUNO and ORCA would exceed the NMO sensitivity of each experiment alone. The key advantage comes from the tension in Δm^2_{31} best fits of the two experiments when assuming the wrong ordering. As explained, this tension arises from the fact that each experiment observes neutrino oscillations starting from a different neutrino flavor ($\bar{\nu}_e$ for JUNO, $\nu_\mu + \bar{\nu}_\mu$ for ORCA). Due to this difference the effective oscillation frequency is the result of a different combination of the various Δm^2_{ij} for each experiment [151, 152]. In the combination, only one single resulting Δm^2_{31} best-fit is allowed. Hence, this tension together with strong constraints in Δm^2_{31} from both

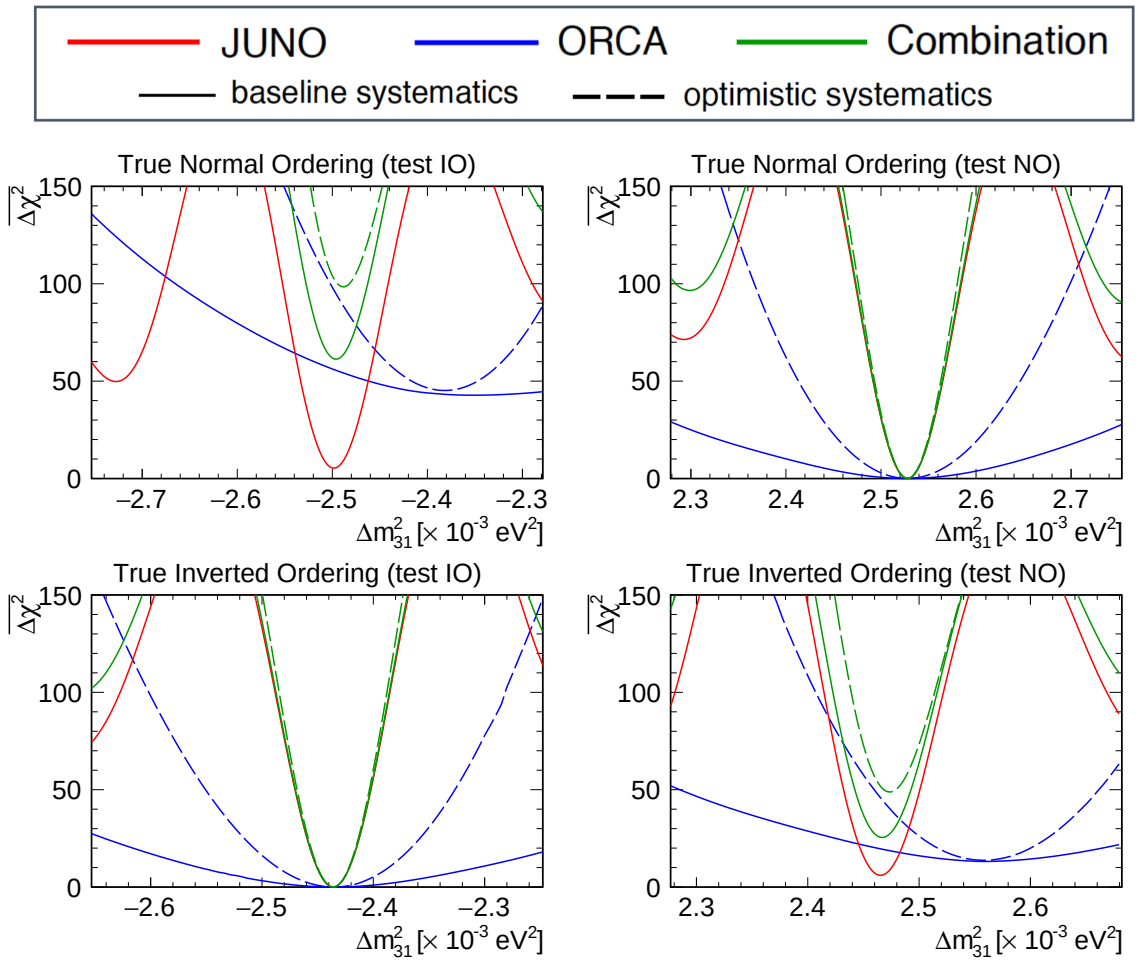

Figure 9.5: $\overline{\Delta\chi^2}$ profile for only JUNO (red), only ORCA (blue), and the combination of JUNO and ORCA (green) as a function of test values of Δm^2_{31} for 6 years of data taking assuming baseline (solid) or optimistic (dashed) systematics.

experiments (especially from JUNO) provides the synergy effect in which the combined $\overline{\Delta\chi^2}$ minimum is boosted to a higher value than simply adding the $\overline{\Delta\chi^2}$ minima of each experiment. The latter scenario, in which the median sensitivity can be obtained as the square root of the sum, will be referred to as "simple sum" in the following discussion. It is shown only to highlight the benefit from doing the combination between JUNO and ORCA properly with the Δm^2_{31} tension taken into account.

In Tab. 9.3, the NMO sensitivities after 6 years of data taking are presented for the combination, each experiment standalone, and the "simple sum" of their sensitivities. The combination reaches 8σ for true NO and 5σ for true IO. This combined sensitivity exceeds the "simple sum" case, which only obtains 7σ for true NO and 4σ for true IO. More important, a 5σ significance is obtained for both NMO scenarios within 6 years of combined analysis while each experiment alone, or the "simple sum" of sensitivities, cannot achieve the same performance.

Table 9.3: Asimov median sensitivity to NMO after 6 years of data taking for each experiment alone, the "simple sum", and the combination of the two experiments, assuming the baseline scenario for systematics.

True NMO	JUNO, 8 cores	ORCA	Simple Sum	Combination
NO	2.3σ	6.5σ	6.9σ	7.8σ
IO	2.4σ	3.6σ	4.3σ	5.1σ

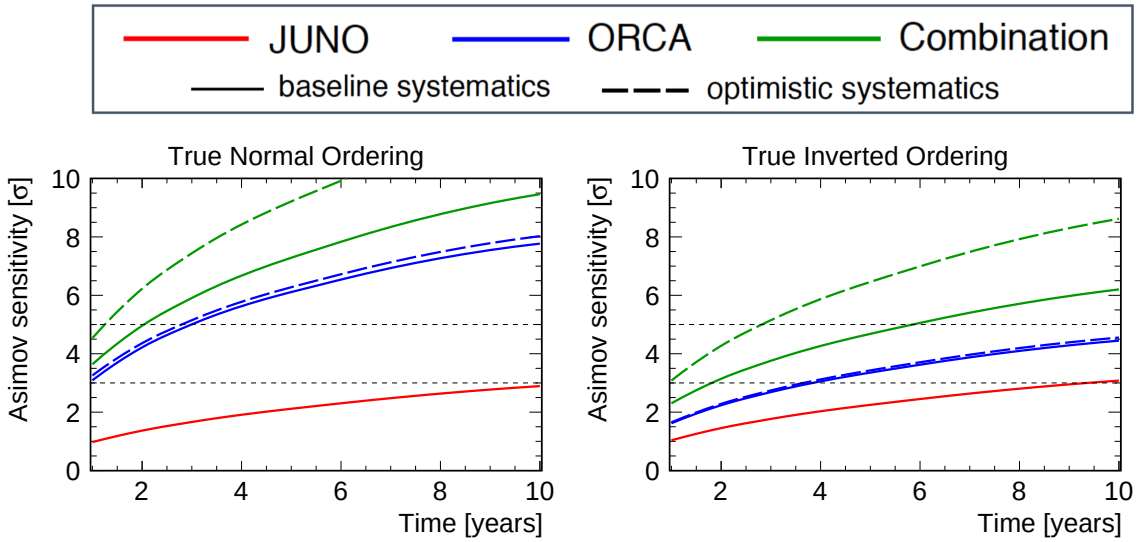

Figure 9.6: NMO sensitivity as a function of time for only JUNO (red), only ORCA (blue), and the combination of JUNO and ORCA (green), assuming baseline (solid) or optimistic (dashed) systematics.

In Fig. 9.6, we study the time evolution of the NMO sensitivity for JUNO, ORCA, and their corresponding combination with the assumption that the two experiments start at the same time. JUNO alone would need 6–10 years of operation to obtain the NMO sensitivity of 3σ. ORCA can determine the NMO at 5σ significance after 3 years in the case of true NO. Nevertheless, more than 10 years of exposure is required to reach 5σ sensitivity in the case of IO. Thanks to the synergy effect discussed above, the combination would help significantly to reduce the time required to reach a 5σ NMO sensitivity when compared to ORCA standalone, especially if IO is true.

As mentioned earlier in Sec. 9.3, ORCA analysis is also performed with a set of systematics similar to those of Ref. [64], as a cross-check for an optimistic approach. Both Fig. 9.5 and Fig. 9.6 show that the two systematic scenarios depicts a very similar $\Delta\chi^2$ minimum value and thus yield the same NMO sensitivity for the ORCA-only analysis. However, Fig. 9.5 also shows that the optimistic approach provides a much tighter constraint on Δm^2_{31}. This causes the combination to reach sensitivities that are 1–2σ higher than in the case of the baseline scenario. As pointed out in Sec. 9.3 and Fig. 9.4, the difference lies in the implementation of the energy scale systematics in which the energy scale applied at

the detector response (baseline) is more strongly correlated with Δm^2_{31} compared to the energy scale at the unoscillated flux (optimistic).

9.6 Further sensitivity studies

9.6.1 Impact of energy resolution in JUNO and 10 reactor cores scenario

One of the most challenging aspects for the design of JUNO is to reach the required energy resolution of the Central Detector. In particular, a level of about $3\%/\sqrt{E/\text{MeV}}$ is essensial for JUNO to be able to determine the NMO by itself. If the energy resolution is decreased to $3.5\%/\sqrt{E/\text{MeV}}$, the required time to reach a 3σ sensitivity would be delayed by more than a factor of 2 [58]. Significant effort within the JUNO collaboration has been made to obtain the goal of $3\%/\sqrt{E/\text{MeV}}$. A description of how to achieve such goal using a data-driven approach relying on calibration data has been discussed in Ref. [165] with a $3.02\%/\sqrt{E/\text{MeV}}$ energy resolution has been achieved and a worsening to $3.12\%/\sqrt{E/\text{MeV}}$ after considering some imperfections in the detector. However, it is interesting to explore the impact of the JUNO energy resolution to the combined NMO analysis.

In this study, a $\pm 0.5\%/\sqrt{E/\text{MeV}}$ variation of the JUNO energy resolution is considered. Although this is a larger departure from the JUNO targeted energy resolution than what described above, it is good for testing the robustness of the combination procedure. In Fig. 9.7, it is illustrated that the variation of the energy resolution has a fairly small impact on the combined sensitivity compared to the impact on the JUNO-only analysis. This can be explained as the benefit of enhancing the NMO sensitivity in the combination comes mainly from the displacement between the Δm^2_{31} best-fit values obtained by ORCA and JUNO for the wrong ordering assumption rather than from the direct measurement of the NMO in JUNO. In more detail, the considered variation in JUNO energy resolution only affect slightly the precision of JUNO to measure Δm^2_{31} while the best-fit value of Δm^2_{31} in both ordering assumption does not change significantly. As a result, the tension in Δm^2_{31} best-fit between the two experiments remains which help preserving the combined sensitivity.

Sec. 9.2 has mentioned the possibility that 2 additional reactors could be built at the Taishan NPP, as originally planned. This could help double the number of neutrinos produced by NPP. This 10 core scenario could help JUNO to reach 3σ about 3 years earlier, as depicted in Fig. 9.8. However, the impact of this change to the combination is still neg-

ligible in the case of assuming true normal ordering, at the current best-fit value. In the IO scenario, going up to 10 cores for JUNO helps to reduce by about 9 months the time required for the combined sensitivity to reach 5σ. Nevertheless, this is still a significantly smaller impact than for the standalone JUNO. The reason is also the same as the case of the JUNO energy resolution dependency in which due to the boost in the combination relies on the difference between the JUNO and ORCA best-fit values for Δm^2_{31} in the wrong ordering scenario, rather than due to the precision of each experiment to measure the NMO separately.

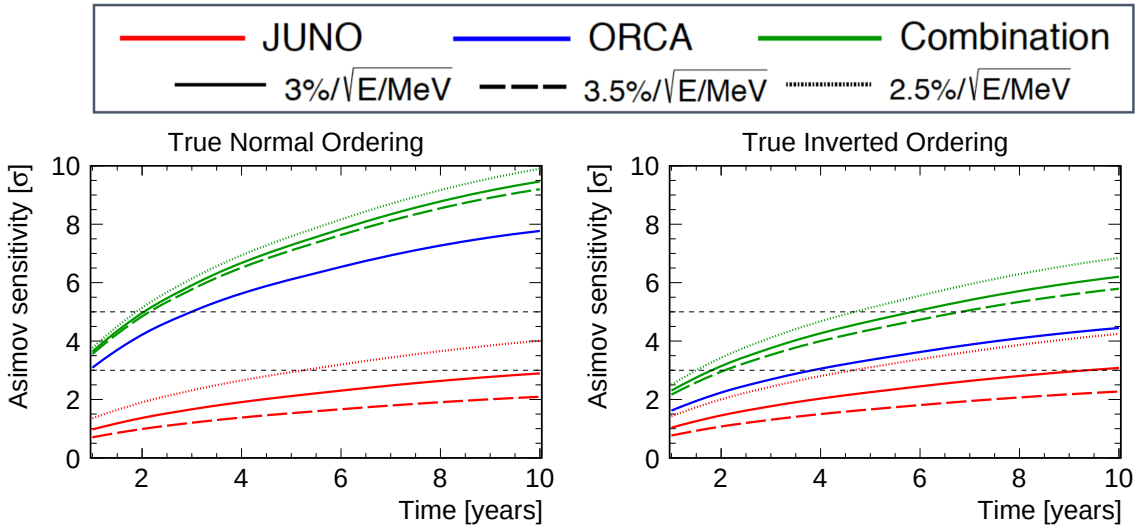

Figure 9.7: NMO sensitivity as a function of time for only JUNO (red), only ORCA (blue), and the combination of JUNO and ORCA (green), considering a better (dotted) and worse (dashed) energy resolution for JUNO than the nominal one (solid) by $\pm 0.5\%/\sqrt{E/\text{MeV}}$.

9.6.2 Combination study with ORCA7 and half-ORCA sub-array

The ORCA detector is planned to be incrementally deployed till 2025 while JUNO is planned to start data taking in 2022. By the starting time of JUNO, ORCA can already have a part of the detector taking data. Therefore, it is particularly interesting to explore the combination potential with just a sub-array of ORCA. Two early phase configurations of ORCA are considered in this study: ORCA7 and half-ORCA ($\sim$ 60 DUs). For ORCA7, we use the presented MC sample: 'ORCA7_23x9_190222'. In the case of half-ORCA, we make use of the full ORCA MC sample ('ORCA115_20x9_190222') with a simple approximation such that NMO sensitivity of half-ORCA after x years will be equal to the sensitivity of full ORCA after $x/2$ years.

Fig. 9.9 depicts the lifetime evolution of NMO sensitivity for the combination of JUNO and ORCA7. With just a sub-array of 7 DUs, ORCA has already a competitive performance

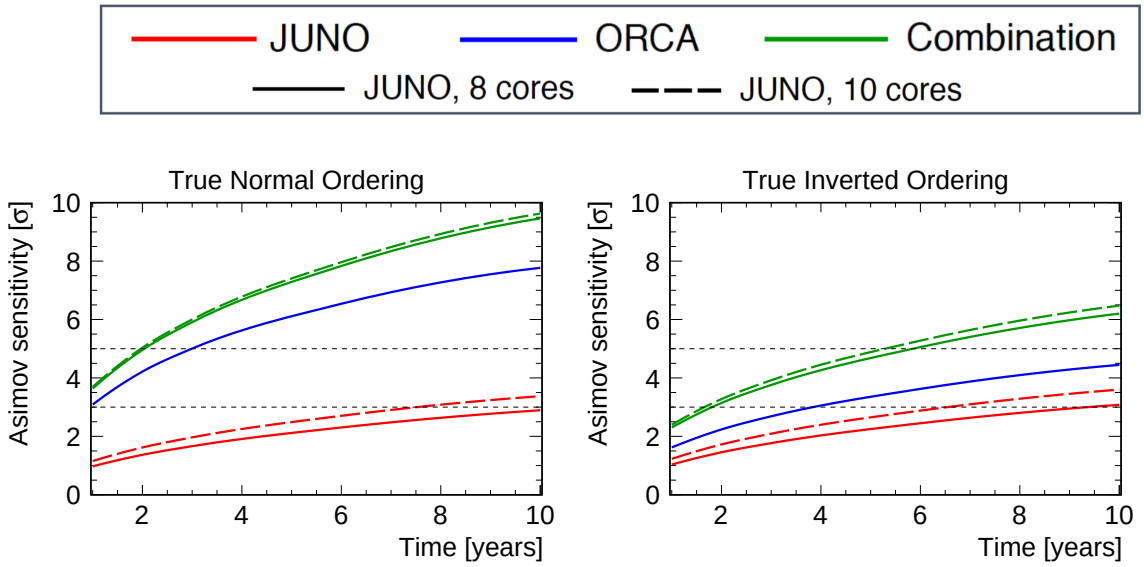

Figure 9.8: NMO sensitivity as a function of time for only JUNO (red), only ORCA (blue), and the combination of JUNO and ORCA (green), considering 2 (solid) or 4 (dashed) Taishan NPP reactors, corresponding respectively to 8 or 10 reactor cores at 53 km from JUNO.

with JUNO in terms of NMO determination. In the combination, 3σ can be guaranteed after 5 years of data taking with the current global best-fit of oscillation parameters and in both NMO scenarios. Even though, it should be noted here that considering ORCA7 with more than 1 year should not make much sense due to the quick growth of ORCA in the construction phase with already 6 lines taking data by now [123].

In Fig. 9.10, an evaluation of the NMO sensitivity for the combination between JUNO and half-ORCA is presented. A 3σ significance can be reached after ~ 1 (3) year of combination in the case of NO (IO) respectively. In the most optimistic case of NO and the current global best-fit oscillation parameters, The combination can lead to a 5σ significance after 4 years of data-taking which reduces by about 2 years the time needed compared to just half-ORCA alone. Given that the combined performance can already be feasible with just a sub-array of ORCA and ORCA will start taking data with its incremental configuration during the construction phase, this study shows that the NMO determination can be obtained even in earlier timescale than what is presented in Sec. 9.5.

9.6.3 Δm^2_{31} and θ_{23} dependence

In this section, the dependence of the analysis on the true values of oscillation parameters is presented, focusing on two relevant parameters: Δm^2_{31} and θ_{23}. The true values of θ_{23} is known to have a strong influence on the ORCA's sensitivity (see Fig. 8.7). In the case of

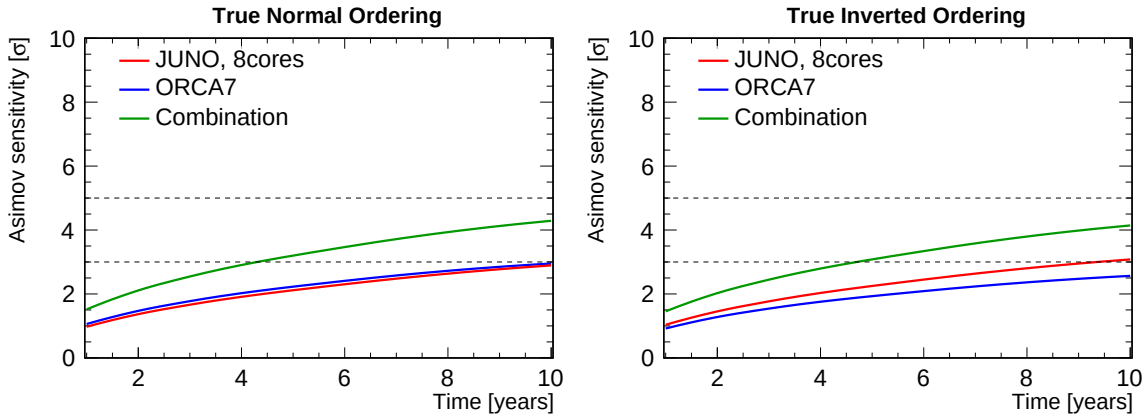

Figure 9.9: NMO sensitivity as a function of time for only JUNO (red), only ORCA7 (blue), and the combination of JUNO and ORCA7 (green).

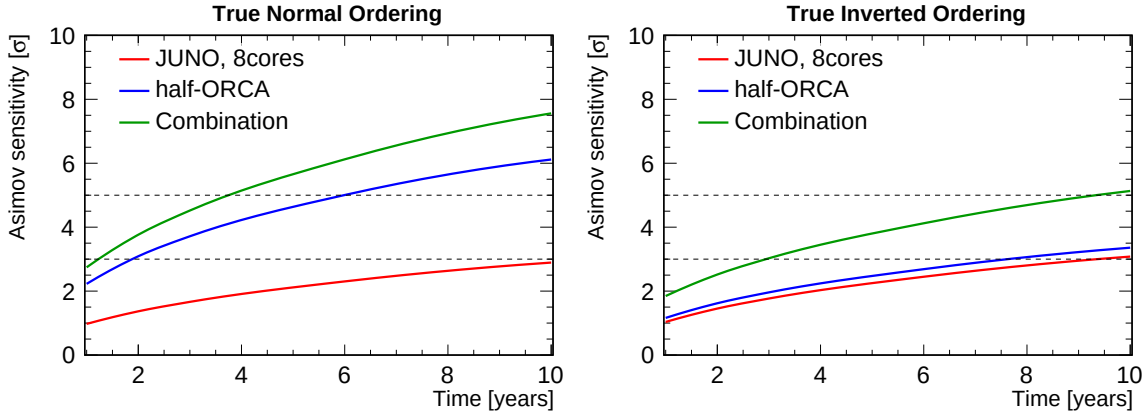

Figure 9.10: NMO sensitivity as a function of time for only JUNO (red), only half-ORCA (blue), and the combination of JUNO and half-ORCA (green).

Δm^2_{31}, the enhancement obtained in the combination is strongly tied to the measurement of this parameter. Therefore, it is necessary to ensure that the boost is stable for any true values of Δm^2_{31}.

The dependence of the NMO sensitivity on the true value of θ_{23} is shown in Fig. 9.11 with 6 years of data taking assumed. JUNO has no sensitivity to θ_{23} as mentioned earlier. For ORCA, the sensitivity depends strongly on the true value of θ_{23} as this parameter affects the amplitude of the detected oscillation pattern. After 6 years of data taking, ORCA can determine the NMO with a significance of 3–7σ and only reaches a 5σ sensitivity for true NO with θ_{23} in the second octant. The combination curve follows a similar θ_{23} dependence as the ORCA-standalone curve, however thanks to the boost in the combination with JUNO, it is shifted to higher sensitivities which ensures a 5σ discovery after about 6 years regardless of the true value of θ_{23} and of the true NMO.

It is worth noting here that the current global best-fit value of θ_{23} is in the upper octant with the values of about $49°$ for both orderings [128]. In the previous studies of Secs. 9.5, 9.6.2, and 9.6.1, this value is used which explains why in those studies the sensitivity for true NO is always much higher than 5σ after 6 years of data taking.

Fig. 9.12 demonstrates the dependence of NMO sensitivity on the true value of Δm^2_{31}. Both JUNO and ORCA standalone sensitivities depict a slight dependence on the true value of Δm^2_{31}. The combination is quite stable with respect to the true values of Δm^2_{31}, reaching a significance of 8σ in the case of NO and 5σ in the case of IO. The figure shows that the boost gained from the tension in Δm^2_{31} is preserved over the whole range of assumed true Δm^2_{31}.

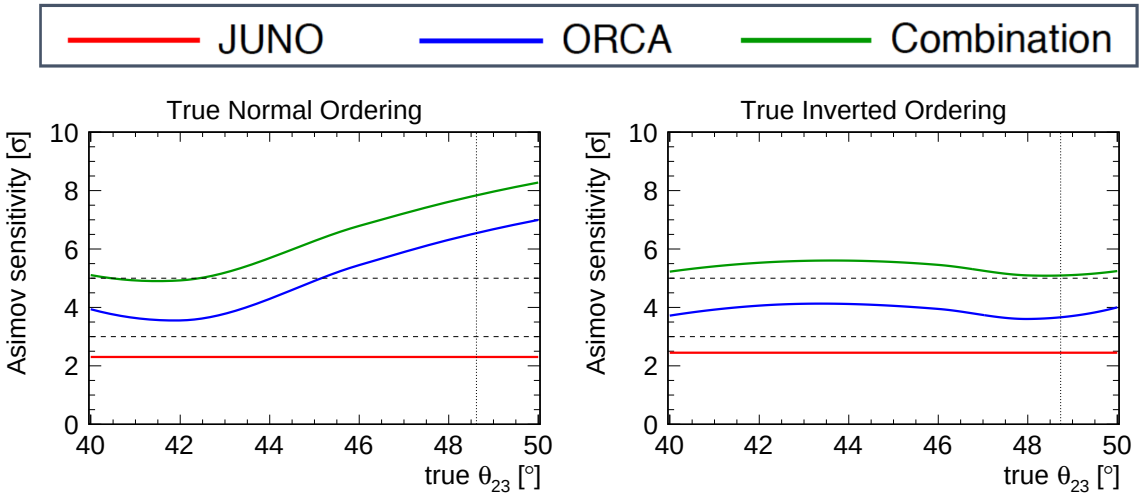

Figure 9.11: NMO sensitivity as a function of the true θ_{23} value for 6 years of data taking for only JUNO (red), only ORCA (blue), and the combination of JUNO and ORCA (green). The vertical lines indicate the global best-fit values used in this analysis (from Ref. [128]).

9.7 Conclusion

In this chapter, an evaluation of the sensitivity to the NMO achieved by a combined analysis of the JUNO and KM3NeT/ORCA experiments is presented. This work results in the paper of Ref. [65]. The most valuable result of this study is that in all cases the combined analysis is more powerful than simply adding the sensitivities for both experiments together. As discussed above, the enhancement in the combined sensitivity comes from the tension of the Δm^2_{31} best-fit between JUNO and ORCA when the wrong neutrino mass ordering is assumed.

With the combination, the time required to reach a 5σ determination of the NMO for any value of the oscillation parameters is significantly reduced. In all cases, a 5σ signifi-

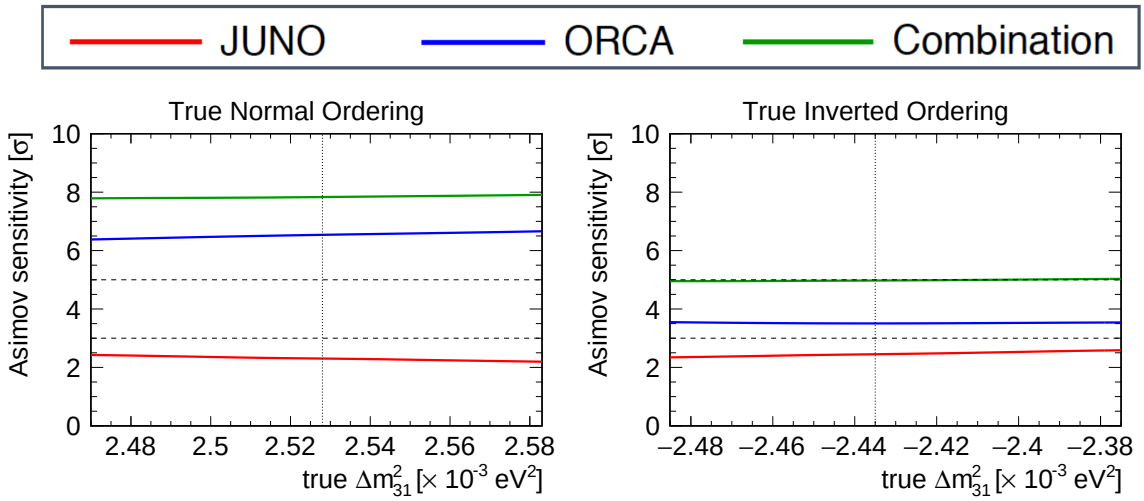

Figure 9.12: NMO sensitivity as a function of the true Δm^2_{31} value for 6 years of data taking for only JUNO (red), only ORCA (blue), and the combination of JUNO and ORCA (green). The vertical lines indicate the global best-fit values used in this analysis (from Ref. [128]).

cance can be obtained within 6 years for the combined analysis, while it could take more than 10 years using only ORCA data, depending on the true ordering. Additionally, the study also shows that the combination can already be made at the early phase of ORCA with very promising results which could potentially further reduce the time required for determining NMO.

The results would strongly depend on the true value of θ_{23}. In the case of true NO and θ_{23} in the upper octant, a 5σ NMO determination would be feasible after less than 2 years of data taking with the combined analysis which is a year ahead of what can be done using only ORCA data. This favorable scenario also corresponds to the current global best-fit value.

The boost for the NMO sensitivity obtained by combining JUNO and ORCA presented in this study is in line with the results of previous studies considering the combination of JUNO with the IceCube Upgrade or with PINGU in Refs. [63, 64]. However, given the differences between PINGU and ORCA, it is important to confirm the result also for the combination of JUNO and ORCA. One of particular interest is the different treatment of the energy scale systematics between this and the previous studies. This systematic when applied at the detector response level can impact directly the Δm^2_{31} measurement with ORCA and thus also the combined result. As shown in this work, changing the treatment of this systematic uncertainty from an optimistic to a more realistic scenario can significantly affect the power of the combination of JUNO and ORCA. Nevertheless, a 5σ determination of the NMO can be effectively reached even in the ORCA baseline scenario of systematics.

Since the gain in the combination does not come exclusively from each experiment's

ability, the dependence of the combination results in systematic uncertainties and the detector effects can be different from what each experiment does independently. For instance, JUNO energy resolution is critical for the JUNO alone sensitivity to the NMO while it has only a weak impact on the combined result. Alternatively, both baseline and optimistic systematics of ORCA yield a very similar NMO sensitivity of ORCA alone but they depict a large difference in the combined sensitivity. These differences arise from the fact that the combination depends strongly on the measurement of Δm^2_{31} of each experiment rather than simply on their measurements of the NMO. In the cases where the required time to reach 5σ is of only a few years, this JUNO-ORCA combination is of particular interest to provide independent validation of the result obtained by the ORCA alone, with a different dependency on the systematic uncertainties.

Chapter 10

Early measurement with KM3NeT/ORCA

Contents

Extensive efforts are ongoing within the KM3NeT Collaboration to deploy their two deep-sea Cherenkov detectors: ORCA and ARCA. Even though the completion is not reached yet, both detectors have been starting their measurements steadily during the construction phase. ARCA has been in operation with 6 DUs since the end of April 2021 with the very first analysis of the collected data reported at ICRC2021 [166] and two more DUs have been added in September 2021, while ORCA is also taking data with 6 DUs since January 2020 [123].

This chapter presents the first oscillation measurement, in particular the sensitivity to θ_{23} and Δm^2_{31}, performed with KM3NeT/ORCA using the data sample from the currently deployed 6 DUs. A joint team effort has been performed in the collaboration for extracting the measurement from this data sample, in which I contributed with the results from SWIM. These results have been used as an internal cross-check for the recent collaboration results shown at ICRC2021 [123].

The outline of this chapter is the following. We first illustrate the data sample used for this study in Sec. 10.1. The analysis settings are described in Sec. 10.2 and the sensitivity results are presented in Sec. 10.3.1. The chapter ends with the conclusion in the final section.

10.1 ORCA6 data sample and run-by-run Monte Carlo for ICRC2021

The ORCA detector started taking data during the early construction phase, and a measurement using its first DU deployed in 2017 can be found in Ref. [167,]. In 2019, following the refurbishment of the main electro-optical cable to shore, 4 DUs were deployed to form ORCA4 with the first results shown in Neutrino2020 [169]. At the beginning of 2020, 2 more lines were installed, bringing the detector to its current configuration with 6 active DUs. As shown in Ref. [169] at Neutrino2020, ORCA4 already has some sensitivity to observe the neutrino oscillation pattern but is still relatively small compared to the one obtained with ORCA6. Therefore, the study presented here uses only the data taken by 6 DUs and with a total exposure of 385.8 days.

The data taking in ORCA is performed in consecutive runs typically lasting for several hours. For each run, a corresponding MC sample is produced following the description in Chap. 3 and taking into account the specific environmental and detector conditions at that moment. In particular, the measured rates in each PMT are used in order to simulate a realistic optical background during the run. Additionally, the detector calibrations provide

the information for simulating the PMT response, with PMT efficiencies obtained from the study of K40 coincidence rates in data. This approach is referred to as run-by-run MC; it results in a MC sample corresponding to each run and therefore suitable for describing the detector response in real-time.

For the time being, only the track reconstruction (JGandalf) is applied for both MC and data. The reconstructed energy used in this study is based on the reconstructed track length from JGandalf. Assuming muons with a minimum ionization potential of 0.25 GeV·m^{-1}, the energy estimation yields $1/4 \cdot Tracklength$ which is an acceptable approximation in the considered energy range of 1-100 GeV. The PID is still in development and not yet used for this study. In the following sections, the event selection is discussed, and a data-MC agreement is also investigated.

10.1.1 Event Selection

In the Collaboration, multiple studies are developed in order to define the data quality criteria for selecting good runs to be used for physics analyses. These criteria are based on multiple parameters which lead to the selection of physics runs with sufficient duration, timing accuracy, and trigger rate. The final run selection results in a dataset of 354.2 days, used in this analysis. This dataset yields a good coverage of 91.9% of the total exposure time (385.8 days).

The events in the selected runs are then passed through an event selection which is designed for significantly rejecting atmospheric muons while keeping a sufficient statistic of neutrinos with a good reconstruction quality. The impact of this event selection is demonstrated in Fig. 10.1. In this figure, the expected neutrino distribution is computed assuming NO with oscillation parameters taken from Ref. [36] and atmospheric muons are added with a weight computed as the ratio between the true data-taking time (354.6 days) and the simulation livetime of the atmospheric muons. The same procedure is also applied for other results of this chapter unless otherwise specified.

In Fig. 10.1, only events reconstructed with an up-going direction (with zenith angle $\theta > 90°$) are shown since they are interesting for the oscillation studies. Additionally, selecting up-going events allows to remove the background of up-going atmospheric muons, which will be filtered by the Earth. The large number of atmospheric muons observed before applying the selection criteria corresponds to down-going atmospheric muons which are misreconstructed as upgoing. The multiple selection criteria on the quality of the reconstruction allows to reject this atmospheric muon background to a very small contamination level, as depicted in Fig. 10.1. The total event numbers of the distributions in Fig. 10.1 are

Table 10.1: Number of events (up-going) detected with ORCA6 after 354.6 days

	Data	Atm. μ	Atm. ν
Without selection	4.2E6	4.8E6	6052.5
With selection	1247	38.9	1240.5

presented in Tab. 10.1. One can see that after the selection the main contribution to the data sample comes from neutrinos while atmospheric muon contamination is reduced to only $\sim 3\%$.

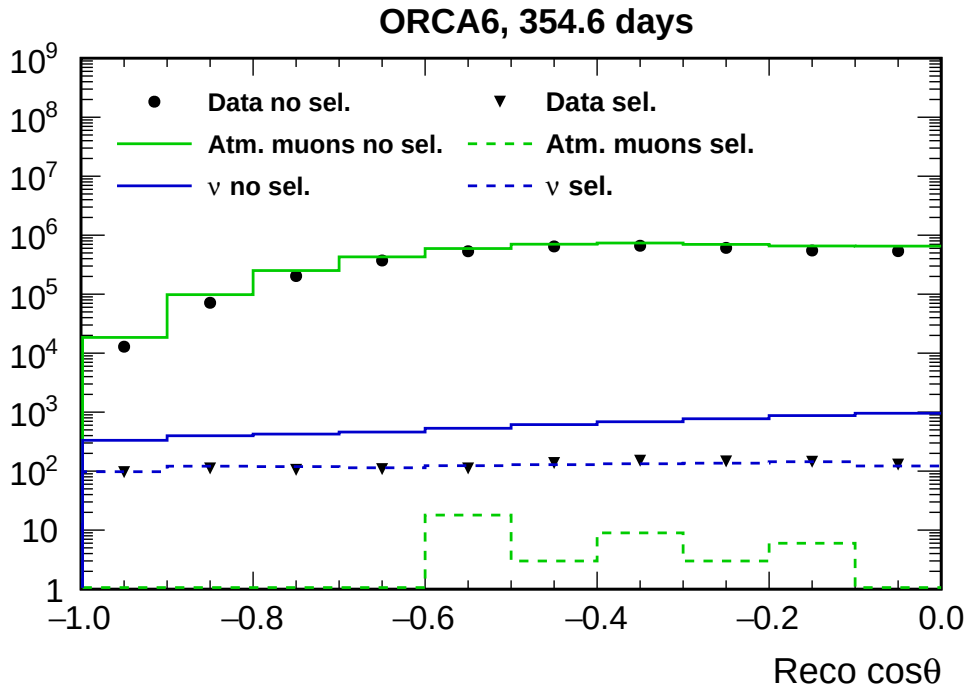

Figure 10.1: Cosine zenith distribution of the events from the selected runs. The distributions before and after applying the event selection are shown.

10.1.2 Data and MC comparison

Multiple studies are ongoing within the collaboration in order to reach a very good data-MC agreement. In this section, a comparison between data and MC is presented at the level of the event distribution after applying all the selection cuts.

Fig. 10.2 shows the event distribution after selection of both data and MC as functions of the reconstructed energy and cosine zenith angle. The main contribution to the detected events comes from the muon neutrino CC channel as the current selection criteria are based on the quality cuts for the track reconstruction. The energy distribution exhibits a peak at ~ 10 GeV, mainly due to the muon neutrino CC contribution. This can be explained by

Table 10.2: Parameter treatment in ORCA6 oscillation analysis. The nominal values of oscillation parameters are taken from Ref. [36]. The priors are applied as Gaussian constraints with mean μ and variance σ. The cross mark $\times$ means no prior applied.

Parameter	True value	Treatment	Prior
$\theta_{23}(\mathrm{deg})$	49.2 (NO) 49.3 (IO)	*Fitted*	$\times$
$\theta_{13}(\mathrm{deg})$	8.57 (NO) 8.60 (IO)	*Fixed*	$\times$
$\theta_{12}(\mathrm{deg})$	33.44	Fixed	$\times$
$\Delta m^2_{31}(10^{-3}\mathrm{eV}^2)$	2.517 (NO) -2.572 (IO)	*Fitted*	$\times$
$\Delta m^2_{21}(10^{-5}\mathrm{eV}^2)$	7.42	Fixed	$\times$
$\delta_{CP}(\mathrm{deg})$	197 (NO) 282 (IO)	*Fixed*	$\times$
Flux $\nu_e/\bar{\nu}_e$ skew	0	*Fitted*	$\mu = 0, \sigma = 0.1$
Flux $\nu_\mu/\bar{\nu}_\mu$ skew	0	*Fitted*	$\mu = 0, \sigma = 0.1$
Flux $\nu_e/\bar{\nu}_\mu$ skew	0	*Fitted*	$\mu = 0, \sigma = 0.03$
Flux spectral index	0	*Fitted*	$\mu = 0, \sigma = 0.1$
Flux zenith slope	0	*Fitted*	$\mu = 0, \sigma = 0.07$
NC normalization	1	*Fitted*	$\mu = 1, \sigma = 0.1$
Energy scale	1	*Fitted*	$\mu = 1, \sigma = 0.1$
Tau normalization	1	*Fitted*	$\mu = 1, \sigma = 0.2$
Normalisation	1	*Fitted*	$\times$

Table 10.3: The binning scheme used for the oscillation analysis with the ORCA6 dataset. Only up-going events are considered for the reconstructed $\cos\theta$ while additional 10 bins of down-going events are used for the true $\cos\theta$.

Binning	True	Reco
Energy	100 [1-1000 GeV]	20 [1-100 GeV]
$\cos\theta$	40 up+10 down	10 up

the current, small geometry of the detector which limits the visible track length detected and causes a decline at higher energy. The cosine zenith angle distribution shows the expected effect of oscillation which is more visible for the more vertical events. Finally, the data shows a favor for oscillation and the very good agreement between data and MC demonstrates a good knowledge of the detector performance in the Collaboration.

10.2 Analysis settings

The parameter treatment in this analysis is presented in Tab. 10.2. Due to the small size of the detector, only Δm^2_{31} and θ_{23} are relevant and fitted while the other oscillation pa-

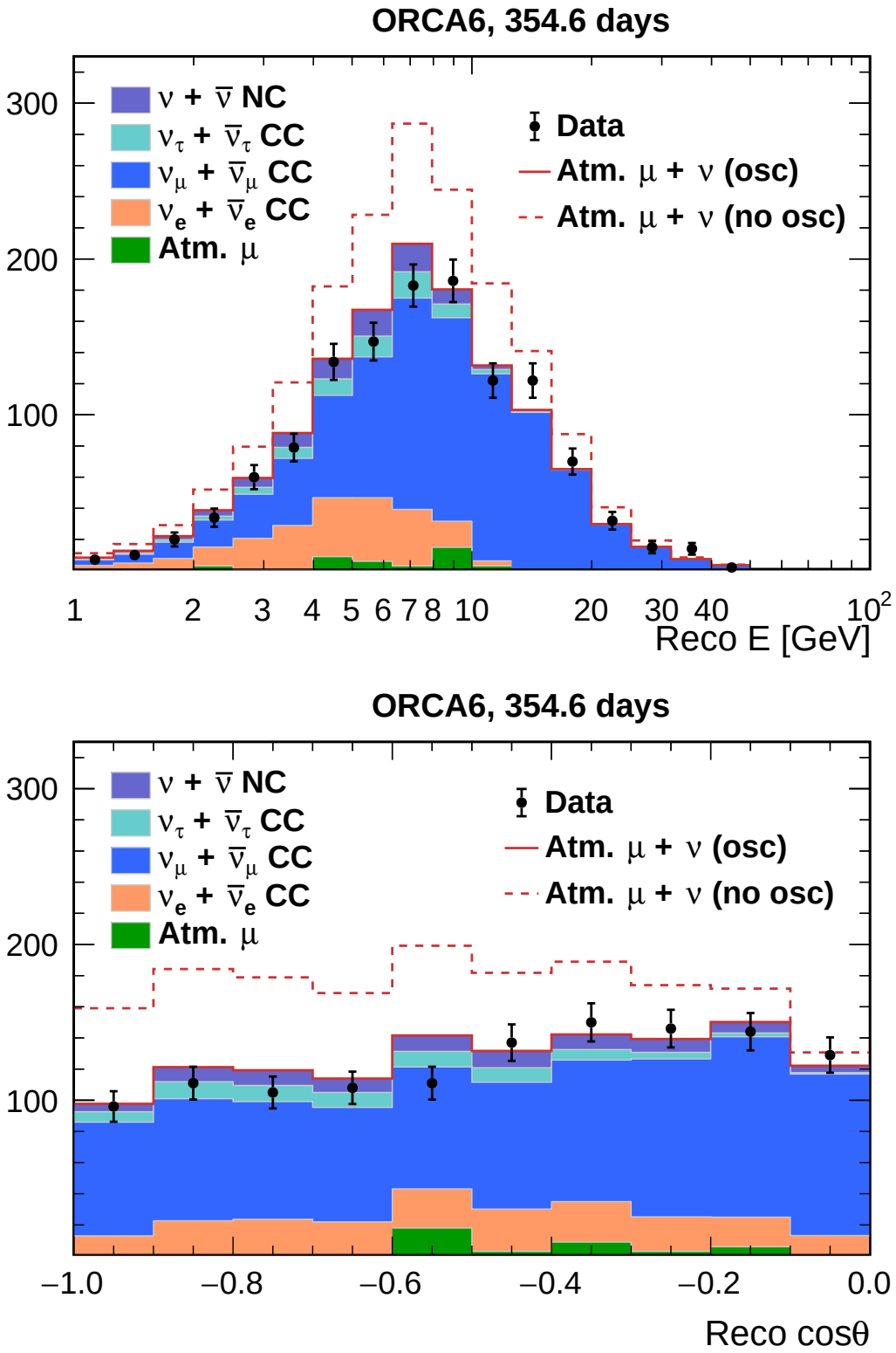

Figure 10.2: Reconstructed energy distribution (top) and cosine zenith angle distribution (bottom) after event selection for data and MC. For the MC, both no oscillation and oscillation hypothesis is shown. When assuming oscillation, the composition of the distribution is illustrated by incrementally stacking all the channels.

rameters have a negligible impact so that they are fixed at the nominal values taken from Ref. [36]. The systematics included here are similar to the analysis performed in Chap. 8 with slightly larger, more conservative priors.

The binning scheme is shown in Tab. 10.3. The true energy range is 1-1000 GeV to make use of the full available MC sample, while reconstructed energies are considered only up to 100 GeV due to the limitation in the energy response of the detector as shown in Fig. 10.2. The number of bins in energy and cosine zenith angle are decided based on the resolution of the detector and the necessity to maintain sufficient statistics in the MC.

10.3 First neutrino oscillation measurement with ORCA6

10.3.1 Sensitivity to the neutrino oscillation

The sensitivity is evaluated following the method described in Chap. 6. Nevertheless, unlike in Chap. 8 and Chap. 9, the Asimov data set is replaced by the real data of ORCA6. In particular, the sensitivity of the data to the hypothesis η_0 in comparison with the hypothesis η_1 can be evaluated as:

$$\Delta\chi^2_{\eta_0} = \min_{\eta_0}\left[\chi^2(d|\eta_0)\right] - \min_{\eta_1}\left[\chi^2(d|\eta_1)\right], \tag{10.1}$$

which is similar to Eq. 6.10. Both models η_0 and η_1 are then fitted to the data to achieve the $\Delta\chi^2$ for rejecting η_1 when assuming η_0 which then can be approximately converted into the significance as $S = \sqrt{\Delta\chi^2}$.

In the context of ORCA6, we want to see if the data favor the oscillation hypothesis instead of no oscillation. Using the formula 10.1, the $\Delta\chi^2$ between oscillation and no oscillation hypothesis yields 44.7 which corresponds to 6.7σ significance of rejecting no oscillations in comparison with oscillations.Fig. 10.3 shows the L/E distribution of the ORCA6 data which demonstrates a clear preference of the data for the oscillation with a main contribution coming from a dip related to the first oscillation minimum at $\sim 10^3$ [km/GeV]. The fit has a tension of about 1.9σ with respect to the one obtained in the current global fit (NuFIT 5.0 [36]).

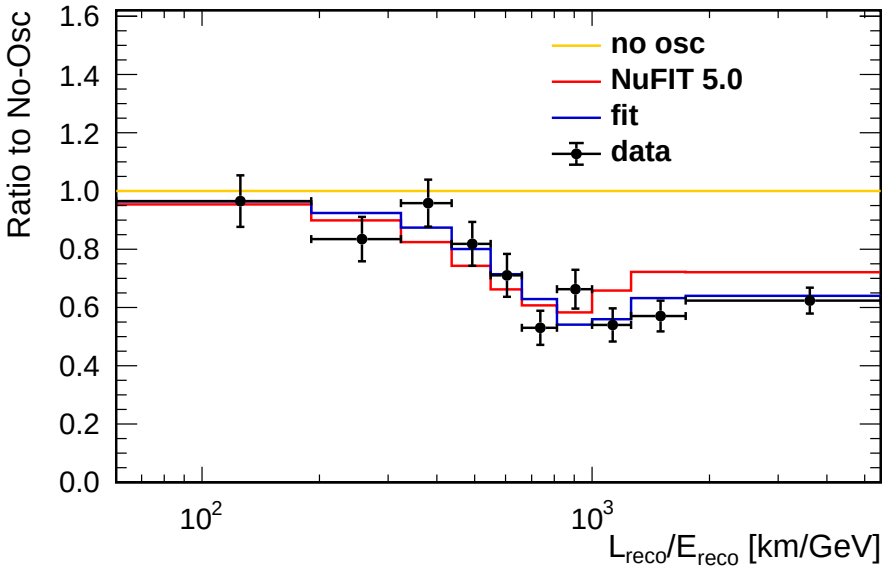

Figure 10.3: L/E distribution of ORCA6 data and expected from oscillation hypothesis relative to the no-oscillation hypothesis. Oscillation hypothesis is shown for both the best-fit to the ORCA6 data and the current global best-fit taken from NuFIT 5.0 [36].

10.3.2 Sensitivity to the oscillation parameters Δm^2_{31} and θ_{23}

The sensitivity of ORCA6 to the oscillation parameters Δm^2_{31} and θ_{23} is evaluated with the procedure presented in Sec. 6.2. The best-fit values are defined in such a way that they minimize the $\Delta\chi^2$ following Eq. 6.19. The error is estimated using the Minos error calculator which is implemented in ROOT [170]. The results yield:

- NO: $\Delta m^2_{31} = 1.94^{+0.30}_{-0.28}$ $[10^{-3}\text{eV}^2]$; $\sin^2\theta_{23} = 0.51^{+0.10}_{-0.10}$
- IO: $\Delta m^2_{31} = -1.84^{+0.27}_{-0.27}$ $[10^{-3}\text{eV}^2]$; $\sin^2\theta_{23} = 0.50^{+0.10}_{-0.10}$

The errors provided include both statistical and systematic ones. Compared to the current world data in which the values are also shown in Tab. 10.2, ORCA6 data prefer a smaller $|\Delta m^2_{31}|$ value, which is coherent with what is observed in the L/E distribution of Fig. 10.3. Since the oscillation is driven by the phase $(\Delta m^2_{31} L)/E$, the ORCA6 data and their best-fit present a dip at a slightly higher value of L/E, which explains the smaller value obtained for $|\Delta m^2_{31}|$. The sensitivity of ORCA6 to each of these parameters is also illustrated with the 1D $\Delta\chi^2$ profiles on Δm^2_{31} and θ_{23} in Fig. 10.4.

Finally, we present the 90% confidence level contour on Δm^2_{31} and $\sin^2\theta_{23}$ obtained with ORCA6 data in Fig. 10.5. The NuFIT best-fit is contained within the ORCA6 contour

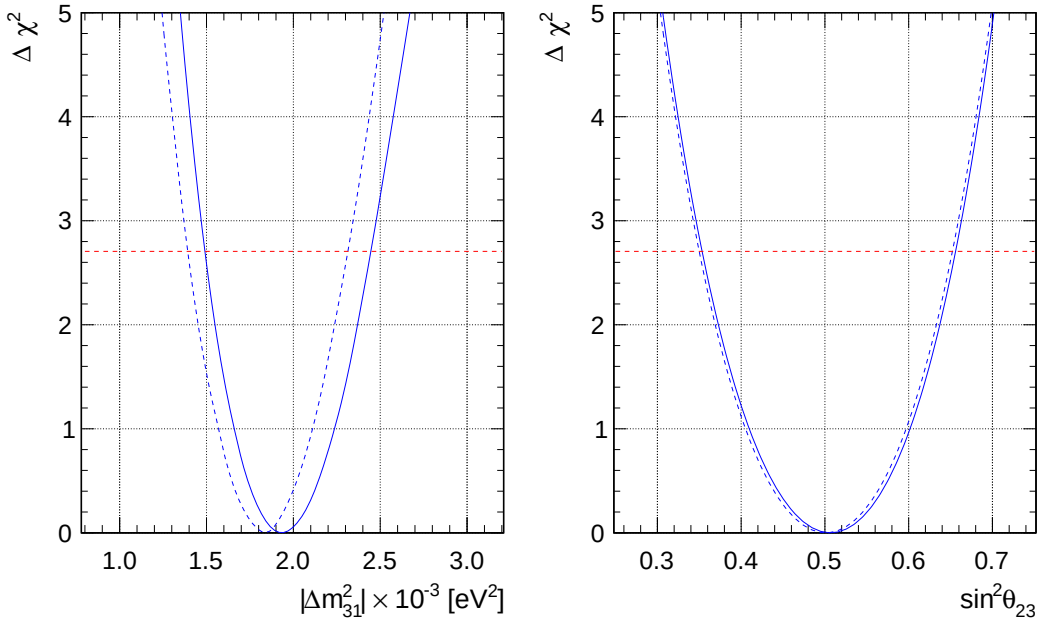

Figure 10.4: $\Delta\chi^2$ profile as a function of Δm^2_{31} (left) and $\sin^2\theta_{23}$ (right) for both NO (solid) and IO (dashed). The dashed red line stands for the 90% confidence level.

even though there is a notable tension in Δm^2_{31}. With only 6 DUs and $\sim$ 1 year of data, ORCA has already reached a sensitivity level that can be compared with that of other current experiments. As the detector is continuously growing and more effort is performed on improving the data-MC agreement as well as the data quality and processing, ORCA is expected to yield a promising future measurement and soon contribute to the current neutrino global picture.

10.4 Conclusion

In this chapter, the sensitivity of the first ORCA sub-array (ORCA6) to the neutrino oscillation has been studied using SWIM. This work has been used as an internal cross-check for the recent collaboration results presented at ICRC2021 [123].

The data quality criteria have been applied to select good physics runs for the analysis, resulting in a final data sample covering 354.6 days of data-taking (91.9% of total exposure time). The corresponding run-by-run Monte Carlo has been produced taking into account the information on the environmental conditions and the detector status during each run. Based on the MC sample, the event selection has been optimized to sufficiently reject the atmospheric muon background while still keeping large statistics of neutrinos. A very good data-MC agreement has been obtained demonstrating a good understanding of the detector. Both data and MC are then injected into SWIM framework for the evaluation of

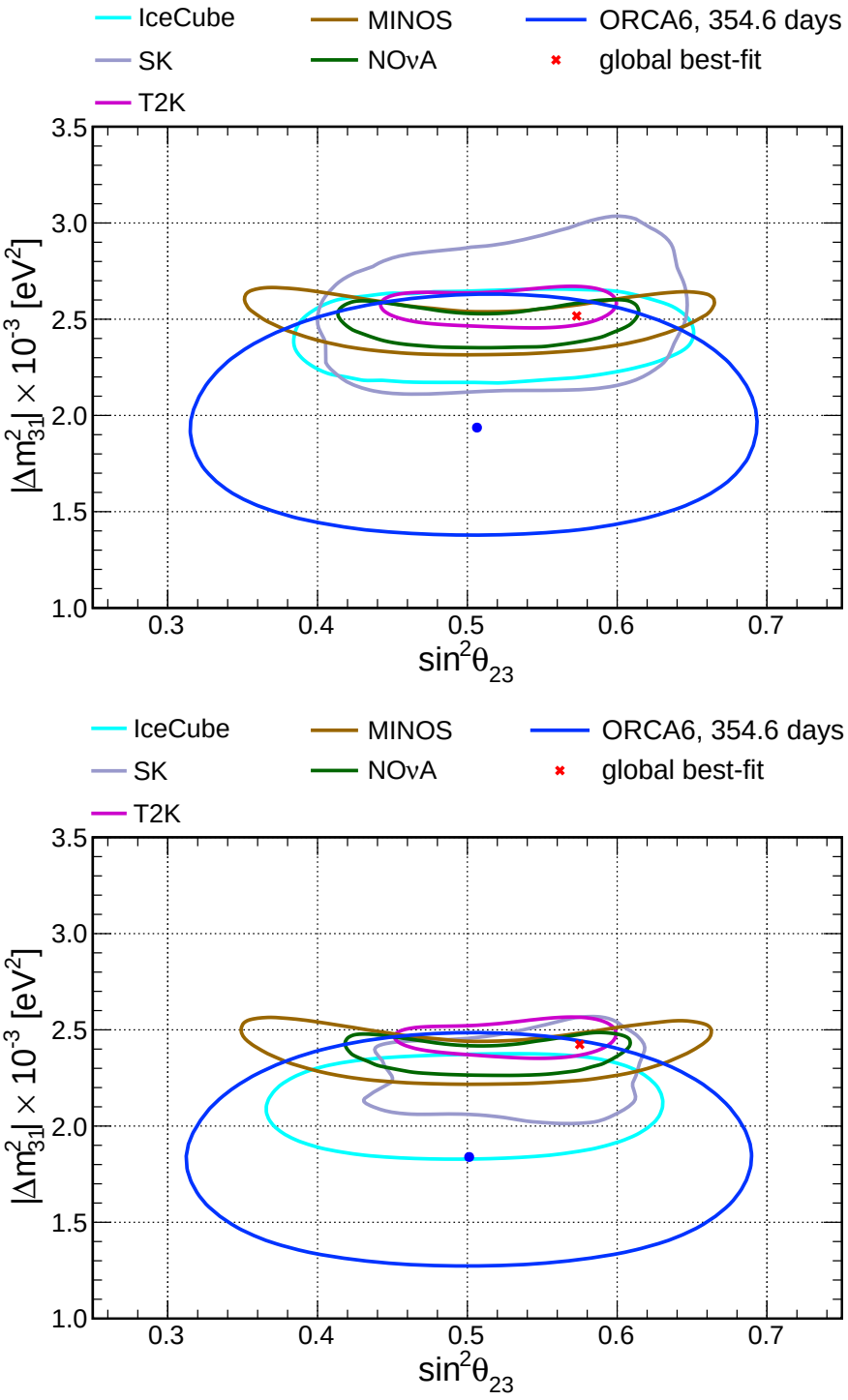

Figure 10.5: 90% confidence level contour on Δm^2_{31} and $\sin^2\theta_{23}$ with ORCA6's data for NO (top) and IO (bottom) assumptions. Contours from other experiments [56, 146–149] and the current values of NuFit [36] are added for comparison.

sensitivity.

With just about 1 year of data from ORCA6, a clear preference for the oscillation scenario has been obtained with the rejection of no oscillation hypothesis at 6.7σ. Additionally, the ORCA6 dataset can already provide a constraint on θ_{23} and Δm^2_{31} which is comparable to that of other current measurements.

While these are promising results, there is still room for multiple improvements in future analyses as the detector is still taking data and growing in size. First, the current MC and data sample are only processed with the track reconstruction and no PID is used yet. The current energy estimator used in this work is not optimized and further development is required. The shower reconstruction and PID will need to be included to further improve the sensitivity of the detector. Second, more effort should be put into characterizing the systematics as well as constraining them with control regions. This will be particularly important for achieving more precise measurements in the future. Finally, it should be noted that multiple studies are in progress for improving the data-MC agreement, reconstruction and event selection and classification. These efforts are all important for extending the potential of the detector.

Conclusions and outlook

Summary on the main results

This thesis investigates the potential for neutrino physics of the KM3NeT/ORCA detector, a water-Cherenkov neutrino telescope being deployed in the depth of the Mediterranean Sea as part of the KM3NeT infrastructure. The ORCA detector will comprise 115 identical Detection Units (DU) each hosting 18 optical modules as elementary detection component. The results can be arranged into two main parts: the contributions to the neutrino simulations, and the evaluations of the sensitivity to neutrino oscillation parameters and mass ordering using SWIM, a KM3NeT analysis framework that uses a full MC approach to build the detector response.

The KM3NeT Collaboration has developed extensive MC simulation chains to produce the MC samples used for evaluating the detector response to the neutrino signals. I have contributed to this effort through, in particular, the production of an MC sample of neutrino events at high energy (50-5000 GeV) for a sub-array with 7 DUs i.e the ORCA7 configuration. This sample will be useful for astrophysical neutrino searches with ORCA in its early phase of construction. This work constitutes my service task for the Collaboration and I have also been in charge of using this production for checking the ORCA simulation chain and for performing the standard quality control of the production. Another simulation-based study presented in this thesis is the production of samples with different PMT efficiencies to study the impact of such uncertainties on ORCA systematics. Based on this MC study, I have validated the implementation of a systematics called energy scale, which has been shown to have a non-negligible impact on the measurement of Δm^2_{31}, hence the necessity to include it in all ORCA physics analyses. As the current maintainer of SWIM, I have also implemented this systematics into the framework.

The next result is the updated sensitivity of ORCA to the neutrino mass ordering (NMO) and oscillation parameters, in particular, the mixing parameters in the atmospheric sector: Δm^2_{31} and θ_{23}. In terms of NMO determination, my analysis confirms the sensitivity improvement obtained by densifying the ORCA geometry from a 23m to a 20m horizontal

spacing between DUs, thanks to the related improvement in particle identification and reconstruction performance. In the most optimistic case, a 5σ significance can be reached within 3 years while only 1 year of data taking is required for 3σ. For the measurement of oscillation parameters, a full ORCA detector with 3 years of exposure can improve on the current world data constraint. An early measurement can already be performed with only 7 DUs during the construction phase.

The manuscript also presents an evaluation of the NMO sensitivity expected by a combined analysis of data from ORCA and JUNO, the new generation reactor neutrino experiment being built in China. This combination is motivated by the boost in NMO sensitivity resulting from the expected tension between the two experiments in the best-fit of Δm^2_{31} when assuming the wrong ordering. This effect has been theoretically discussed already 8 years ago in the context of a possible combination of atmospheric and reactor neutrino data, and ORCA and JUNO may well be the first to provide an experimental confirmation. With the combination, the time required to reach a 5σ NMO determination for any value of the oscillation parameters is significantly reduced. The dependence of the combination results in systematic uncertainties and detector effects are also discussed.

Finally, the thesis presents the results of a first measurement of the oscillation parameters θ_{23} and Δm^2_{31} with KM3NeT/ORCA, using the data sample from the current 6 deployed DUs (ORCA6). A very good data-MC agreement is found, demonstrating a good understanding of the detector. With just about 1 year of data from ORCA6, the no-oscillation hypothesis is already rejected at 6.7σ, and the measurements of the θ_{23} and Δm^2_{31} parameters obtained with the ORCA6 data set are in good agreement with those of other experiments.

Outlook

The quality check performed for the case of ORCA7 high energy production in this work has contributed to the validation of the MC simulation. As we start to have the very first data, it is a unique chance to check and extend our understanding of the detector. To this aim, further developments of the MC chain will be important to reach an increasingly improved data-MC agreement. In such a scenario, quality checks and validation procedures like the ones presented in this work on ORCA7 are necessary. It is worth developing automatic scripts installed within the MC simulation chain to create reports or plots on the features of simulation tools. This would facilitate the validation of the new MC production or new features developed for the MC tools.

The oscillation studies in this PhD using SWIM have contributed actively to the internal cross-checks between analysis frameworks (paramNMH and MONA) for publication

results on NMO sensitivity and oscillation parameter measurements. Even though a fairly good agreement has been obtained, improvements could be achieved especially on the implementation of the systematics. The covariance matrices, which can describe how much each pair of parameters correlated, produced by each analysis framework could be a good start to see if they all agree on the impact of the implemented systematics.

Additionally, the treatment of systematics should be deemed as one of the main objectives that require more investigation in the oscillation analyses of ORCA. The current set of systematics is believed to be conservative. Nevertheless, we could be more accurate by using more realistic parameters for modeling the uncertainties. One example is the Bars parameters for the atmospheric neutrino fluxes mentioned in Chap. 7. For cross-section and detector-related systematics, more effort in modeling the uncertainties is obviously necessary. In my perspective, it is possible and might be helpful to have a common package for all analysis frameworks that models the uncertainties and migrates them into the different physics components used for the analysis i.e fluxes, cross-sections, detector response,...

ORCA will soon contribute to the global picture of neutrino oscillations especially the project gives an optimistic potential to the determination of NMO. In this work, we have shown that the NMO can be resolved even earlier with the combination between ORCA and JUNO. Thus a preparation to facilitate this combination with real data from both experiments should be considered. Looking at the global picture, it is exciting to imagine how ORCA, both alone and in combination with other concomitant experiments, will contribute to improve our understanding of the nature and properties of the neutrino through the detailed study of its flavor oscillations.

List of Abbreviations

ARCA . . . . . Astroparticle Research with Cosmics in the Abyss

CC . . . . . Charged Current

CCQE . . . . . Charged Current Quasi-Elastic Scattering

CR . . . . . Cosmic Ray

DIS . . . . . Deep Inelastic Scattering

DOM . . . . . Digital Optical Module

DU . . . . . KM3NeT Detection Unit

ES . . . . . Elastic Scattering

IBD . . . . . Inverse Beta-Decay

IO . . . . . Inverted Ordering

JUNO . . . . . Jiangmen Underground Neutrino Observatory

MC . . . . . Monte Carlo

MEOC . . . . . Main electro-optical cable

NC . . . . . Neutral Current

NMO . . . . . Neutrino Mass Ordering

NO . . . . . Normal Ordering

NPP . . . . . Nuclear Power Plan

ORCA . . . . . Oscillation Research with Cosmics in the Abyss

PDF . . . . . Probability Density Function

PE . . . . . Pseudo Experiment

PID . . . . . Particle Identification

PINGU . . . . . Precision IceCube Next Generation Upgrade

PMT . . . . . photomultiplier tube

QE . . . . . Quantum Efficiency of the PMT

RDF . . . . . Random Decision Forrest

RES . . . . . Resonant Production Scattering

SK . . . . . Super-Kamiokande

SM . . . . . Standard Model of particle physics

SNO . . . . . Sudbury Neutrino Observatory

SSM . . . . . Standard Solar Model

List of Figures

List of Tables

Bibliography

[1] C. Giunti and C.W. Kim, *Fundamentals of Neutrino Physics and Astrophysics* (2007). [Cited on pages 6, 17, and 21.]

[2] K. Zuber, *Neutrino Physics*, CRC (2020). [Cited on pages 6 and 17.]

[3] J. Chadwick, *Possible Existence of a Neutron*, *Nature* **129** (1932) 312. [Cited on page 6.]

[4] E. Fermi, *Trends to a Theory of beta Radiation. (In Italian)*, *Nuovo Cim.* **11** (1934) 1. [Cited on page 6.]

[5] F. Reines and C.L. Cowan, *A proposed experiment to detect the free neutrino*, *Phys. Rev.* **90** (1953) 492. [Cited on page 7.]

[6] F. Reines, C.L. Cowan, F.B. Harrison, A.D. McGuire and H.W. Kruse, *Detection of the free antineutrino*, *Phys. Rev.* **117** (1960) 159. [Cited on page 7.]

[7] S. Christine, "Ghosts in the machine." https://cerncourier.com/a/ghosts-in-the-machine/. [Cited on page 7.]

[8] C.S. Wu, E. Ambler, R.W. Hayward, D.D. Hoppes and R.P. Hudson, *Experimental Test of Parity Conservation in β Decay*, *Phys. Rev.* **105** (1957) 1413. [Cited on page 8.]

[9] M. Goldhaber, L. Grodzins and A.W. Sunyar, *Helicity of Neutrinos*, *Phys. Rev.* **109** (1958) 1015. [Cited on page 8.]

[10] G. Danby, J.M. Gaillard, K.A. Goulianos, L.M. Lederman, N.B. Mistry, M. Schwartz et al., *Observation of High-Energy Neutrino Reactions and the Existence of Two Kinds of Neutrinos*, *Phys. Rev. Lett.* **9** (1962) 36. [Cited on page 8.]

[11] S.L. Glashow, *Partial-symmetries of weak interactions*, *Nuclear Physics* **22** (1961) 579. [Cited on page 9.]

[12] S. Weinberg, *A Model of Leptons*, *Phys. Rev. Lett.* **19** (1967) 1264. [Cited on page 9.]

[13] A. Salam, *Weak and Electromagnetic Interactions*, *Conf. Proc. C* **680519** (1968) 367. [Cited on page 9.]

[14] P.W. Higgs, *Broken symmetries, massless particles and gauge fields*, *Phys. Lett.* **12** (1964) 132. [Cited on page 9.]

[15] P.W. Higgs, *Broken Symmetries and the Masses of Gauge Bosons*, *Phys. Rev. Lett.* **13** (1964) 508. [Cited on page 9.]

[16] P.W. Higgs, *Spontaneous Symmetry Breakdown without Massless Bosons*, *Phys. Rev.* **145** (1966) 1156. [Cited on page 9.]

[17] F. Englert and R. Brout, *Broken Symmetry and the Mass of Gauge Vector Mesons*, *Phys. Rev. Lett.* **13** (1964) 321. [Cited on page 9.]

[18] ATLAS collaboration, *Observation of a new particle in the search for the Standard Model Higgs boson with the ATLAS detector at the LHC*, *Phys. Lett. B* **716** (2012) 1 [1207.7214]. [Cited on page 9.]

[19] CMS collaboration, *Observation of a New Boson at a Mass of 125 GeV with the CMS Experiment at the LHC*, *Phys. Lett. B* **716** (2012) 30 [1207.7235]. [Cited on page 9.]

[20] UA1 collaboration, *Experimental Observation of Lepton Pairs of Invariant Mass Around 95-GeV/c**2 at the CERN SPS Collider*, *Phys. Lett. B* **126** (1983) 398. [Cited on page 9.]

[21] UA1 collaboration, *Experimental Observation of Isolated Large Transverse Energy Electrons with Associated Missing Energy at* $\sqrt{s} = 540$ *GeV*, *Phys. Lett. B* **122** (1983) 103. [Cited on page 9.]

[22] M.L. Perl et al., *Evidence for Anomalous Lepton Production in e+ - e- Annihilation*, *Phys. Rev. Lett.* **35** (1975) 1489. [Cited on page 9.]

[23] DONUT collaboration, *Observation of tau neutrino interactions*, *Phys. Lett. B* **504** (2001) 218 [hep-ex/0012035]. [Cited on page 9.]

[24] A. Dar and G. Shaviv, *Standard solar neutrinos*, *Astrophys. J.* **468** (1996) 933 [astro-ph/9604009]. [Cited on page 10.]

[25] "Solar Neutrinos." https://neutrino-history.in2p3.fr/solar-neutrinos/. [Cited on page 10.]

[26] R. Davis, Jr., D.S. Harmer and K.C. Hoffman, *Search for neutrinos from the sun*, *Phys. Rev. Lett.* **20** (1968) 1205. [Cited on page 11.]

[27] Kamiokande-II collaboration, *Observation of B-8 Solar Neutrinos in the Kamiokande-II Detector*, *Phys. Rev. Lett.* **63** (1989) 16. [Cited on page 11.]

[28] SAGE collaboration, *Measurement of the solar neutrino capture rate with gallium metal*, *Phys. Rev. C* **60** (1999) 055801 [astro-ph/9907113]. [Cited on page 11.]

[29] GALLEX collaboration, *GALLEX solar neutrino observations: Results for GALLEX IV*, *Phys. Lett. B* **447** (1999) 127. [Cited on page 11.]

[30] Super-Kamiokande collaboration, *Measurements of the solar neutrino flux from Super-Kamiokande's first 300 days*, *Phys. Rev. Lett.* **81** (1998) 1158 [hep-ex/9805021]. [Cited on page 11.]

[31] SNO collaboration, *Direct evidence for neutrino flavor transformation from neutral current interactions in the Sudbury Neutrino Observatory*, *Phys. Rev. Lett.* **89** (2002) 011301 [nucl-ex/0204008]. [Cited on page 12.]

[32] Super-Kamiokande collaboration, *Establishing atmospheric neutrino oscillations with Super-Kamiokande*, *Nucl. Phys. B* **908** (2016) 14. [Cited on pages 13 and 14.]

[33] E. Majorana and L. Maiani, *A symmetric theory of electrons and positrons*, in *Ettore Majorana Scientific Papers: On occasion of the centenary of his birth*, G.F. Bassani, ed., (Berlin, Heidelberg), pp. 201–233, Springer Berlin Heidelberg (2006), DOI. [Cited on page 15.]

[34] S.T. Petcov, *The Nature of Massive Neutrinos*, *Adv. High Energy Phys.* **2013** (2013) 852987 [1303.5819]. [Cited on page 15.]

[35] J.J. Gomez-Cadenas, J. Martin-Albo, M. Mezzetto, F. Monrabal and M. Sorel, *The Search for neutrinoless double beta decay*, *Riv. Nuovo Cim.* **35** (2012) 29 [1109.5515]. [Cited on page 18.]

[36] I. Esteban, M.C. Gonzalez-Garcia, M. Maltoni, T. Schwetz and A. Zhou, *The fate of hints: updated global analysis of three-flavor neutrino oscillations*, *JHEP* **09** (2020) 178 [2007.14792]. [Cited on pages 18, 25, 26, 155, 157, 159, 160, and 162.]

[37] L. Wolfenstein, *Neutrino Oscillations in Matter*, *Phys. Rev. D* **17** (1978) 2369. [Cited on page 20.]

[38] M.C. Gonzalez-Garcia and M. Maltoni, *Phenomenology with Massive Neutrinos*, *Phys. Rept.* **460** (2008) 1 [0704.1800]. [Cited on page 21.]

[39] T. Ohlsson and H. Snellman, *Neutrino oscillations with three flavors in matter of varying density*, *Eur. Phys. J. C* **20** (2001) 507 [hep-ph/0103252]. [Cited on page 22.]

[40] S.P. Mikheev and A.Y. Smirnov, *Resonant amplification of neutrino oscillations in matter and solar neutrino spectroscopy*, *Nuovo Cim. C* **9** (1986) 17. [Cited on page 23.]

[41] SNO collaboration, *Electron energy spectra, fluxes, and day-night asymmetries of B-8 solar neutrinos from measurements with NaCl dissolved in the heavy-water detector at the Sudbury Neutrino Observatory*, *Phys. Rev. C* **72** (2005) 055502 [nucl-ex/0502021]. [Cited on pages 24 and 25.]

[42] M. Maltoni and A.Y. Smirnov, *Solar neutrinos and neutrino physics*, *Eur. Phys. J. A* **52** (2016) 87 [1507.05287]. [Cited on page 24.]

[43] A.Y. Smirnov, *Solar neutrinos: Oscillations or No-oscillations?*, 1609.02386. [Cited on page 24.]

[44] KamLAND collaboration, *Precision Measurement of Neutrino Oscillation Parameters with KamLAND*, *Phys. Rev. Lett.* **100** (2008) 221803 [0801.4589]. [Cited on page 25.]

[45] KamLAND collaboration, *Measurement of neutrino oscillation with KamLAND: Evidence of spectral distortion*, *Phys. Rev. Lett.* **94** (2005) 081801 [hep-ex/0406035]. [Cited on page 25.]

[46] Daya Bay collaboration, *Observation of electron-antineutrino disappearance at Daya Bay*, *Phys. Rev. Lett.* **108** (2012) 171803 [1203.1669]. [Cited on page 25.]

[47] Daya Bay collaboration, *A Precision measurement of the neutrino mixing angle θ_{13} using reactor antineutrinos at Daya-Bay*, hep-ex/0701029. [Cited on page 25.]

[48] Double Chooz collaboration, *Indication of Reactor $\bar{\nu}_e$ Disappearance in the Double Chooz Experiment*, *Phys. Rev. Lett.* **108** (2012) 131801 [1112.6353]. [Cited on page 25.]

[49] Double Chooz collaboration, *Double Chooz θ_{13} measurement via total neutron capture detection*, *Nature Phys.* **16** (2020) 558 [1901.09445]. [Cited on pages 25, 118, and 142.]

[50] RENO collaboration, *Observation of Reactor Electron Antineutrino Disappearance in the RENO Experiment*, *Phys. Rev. Lett.* **108** (2012) 191802 [1204.0626]. [Cited on page 25.]

[51] RENO collaboration, *Measurement of Reactor Antineutrino Oscillation Amplitude and Frequency at RENO*, *Phys. Rev. Lett.* **121** (2018) 201801 [1806.00248]. [Cited on page 25.]

[52] A. Himmel, *New oscillation results from the nova experiment*, July, 2020. 10.5281/zenodo.3959581. [Cited on page 26.]

[53] MINOS collaboration, *Combined analysis of ν_μ disappearance and $\nu_\mu \to \nu_e$ appearance in MINOS using accelerator and atmospheric neutrinos*, *Phys. Rev. Lett.* **112** (2014) 191801 [1403.0867]. [Cited on page 26.]

[54] T2K collaboration, *Search for Electron Antineutrino Appearance in a Long-baseline Muon Antineutrino Beam*, *Phys. Rev. Lett.* **124** (2020) 161802 [1911.07283]. [Cited on page 26.]

[55] Super-Kamiokande collaboration, *Atmospheric neutrino oscillation analysis with external constraints in Super-Kamiokande I-IV*, *Phys. Rev. D* **97** (2018) 072001 [1710.09126]. [Cited on pages 26 and 34.]

[56] IceCube collaboration, *Measurement of Atmospheric Neutrino Oscillations at 6–56 GeV with IceCube DeepCore*, *Phys. Rev. Lett.* **120** (2018) 071801 [1707.07081]. [Cited on pages 26, 129, and 162.]

[57] P.F. de Salas, D.V. Forero, S. Gariazzo, P. Martínez-Miravé, O. Mena, C.A. Ternes et al., *2020 global reassessment of the neutrino oscillation picture*, *JHEP* **02** (2021) 071 [2006.11237]. [Cited on pages 26 and 27.]

[58] JUNO collaboration, *Neutrino Physics with JUNO*, *J. Phys. G* **43** (2016) 030401 [1507.05613]. [Cited on pages 26, 134, 135, 136, 137, 138, 141, and 146.]

[59] DUNE collaboration, *Long-baseline neutrino oscillation physics potential of the DUNE experiment*, *Eur. Phys. J. C* **80** (2020) 978 [2006.16043]. [Cited on page 27.]

[60] Hyper-Kamiokande Working Group collaboration, *T2HK: J-PARC upgrade plan for future and beyond T2K*, in *15th International Workshop on Neutrino Factories, Super Beams and Beta Beams*, 11, 2013 [1311.5287]. [Cited on page 27.]

[61] KM3Net collaboration, *Letter of intent for KM3NeT 2.0*, *J. Phys. G* **43** (2016) 084001 [1601.07459]. [Cited on pages 28, 45, 52, 57, 107, 112, 113, 117, and 141.]

[62] IceCube collaboration, *PINGU: A Vision for Neutrino and Particle Physics at the South Pole*, *J. Phys. G* **44** (2017) 054006 [1607.02671]. [Cited on pages 28 and 132.]

[63] M. Blennow and T. Schwetz, *Determination of the neutrino mass ordering by combining PINGU and Daya Bay II*, *JHEP* **09** (2013) 089 [1306.3988]. [Cited on pages 28, 132, and 151.]

[64] JUNO Collaboration members and IceCube Gen2 collaboration, *Combined sensitivity to the neutrino mass ordering with JUNO, the IceCube Upgrade, and PINGU*, *Phys. Rev. D* **101** (2020) 032006 [1911.06745]. [Cited on pages 28, 132, 138, 139, 145, 151, and 173.]

[65] KM3NeT collaboration, *Combined sensitivity of JUNO and KM3NeT/ORCA to the neutrino mass ordering*, 2108.06293. [Cited on pages 28, 132, and 150.]

[66] G.T. Zatsepin and V.A. Kuzmin, *Neutrino production in the atmosphere*, *Zhur. Eksptl'. i Teoret. Fiz.* **Vol: 41** (1961) . [Cited on page 28.]

[67] M.A. Markov and I.M. Zheleznykh, *On high energy neutrino physics in cosmic rays*, *Nucl. Phys.* **27** (1961) 385. [Cited on pages 28 and 34.]

[68] M. Honda, M. Sajjad Athar, T. Kajita, K. Kasahara and S. Midorikawa, *Atmospheric neutrino flux calculation using the NRLMSISE-00 atmospheric model*, *Phys. Rev. D* **92** (2015) 023004 [1502.03916]. [Cited on pages 29, 77, and 78.]

[69] G.D. Barr, T.K. Gaisser, P. Lipari, S. Robbins and T. Stanev, *A Three - dimensional calculation of atmospheric neutrinos*, *Phys. Rev. D* **70** (2004) 023006 [astro-ph/0403630]. [Cited on page 29.]

[70] M. Honda, T. Kajita, K. Kasahara and S. Midorikawa, *A New calculation of the atmospheric neutrino flux in a 3-dimensional scheme*, *Phys. Rev. D* **70** (2004) 043008 [astro-ph/0404457]. [Cited on page 29.]

[71] G. Barr, T. Gaisser, S. Robbins and T. Stanev, *Uncertainties in Atmospheric Neutrino Fluxes*, *Phys. Rev. D* **74** (2006) 094009 [astro-ph/0611266]. [Cited on pages 29, 99, 100, 101, 102, 103, and 119.]

[72] M. Freund, *Analytic approximations for three neutrino oscillation parameters and probabilities in matter*, *Phys. Rev. D* **64** (2001) 053003 [hep-ph/0103300]. [Cited on page 30.]

[73] E.K. Akhmedov, *Parametric resonance in neutrino oscillations in matter*, *Pramana* **54** (2000) 47 [hep-ph/9907435]. [Cited on page 31.]

[74] P.I. Krastev and A.Y. Smirnov, *Parametric Effects in Neutrino Oscillations*, *Phys. Lett. B* **226** (1989) 341. [Cited on page 31.]

[75] J.A. Formaggio and G.P. Zeller, *From eV to EeV: Neutrino Cross Sections Across Energy Scales*, *Rev. Mod. Phys.* **84** (2012) 1307 [1305.7513]. [Cited on page 32.]

[76] M.A. Markov, *On high energy neutrino physics*, in *10th International Conference on High Energy Physics*, pp. 578–581, 1960. [Cited on page 34.]

[77] ANTARES collaboration, *ANTARES: the first undersea neutrino telescope*, *Nucl. Instrum. Meth. A* **656** (2011) 11 [1104.1607]. [Cited on page 34.]

[78] BAIKAL collaboration, *The prototyping/early construction phase of the BAIKAL-GVD project*, *Nucl. Instrum. Meth. A* **742** (2014) 82 [1308.1833]. [Cited on page 34.]

[79] IceCube collaboration, *The IceCube Data Acquisition System: Signal Capture, Digitization, and Timestamping*, *Nucl. Instrum. Meth. A* **601** (2009) 294 [0810.4930]. [Cited on page 34.]

[80] P.A. Cerenkov, *Visible radiation produced by electrons moving in a medium with velocities exceeding that of light*, *Phys. Rev.* **52** (1937) 378. [Cited on page 35.]

[81] J.D. Jackson, *Classical Electrodynamics*, Wiley (1998). [Cited on page 35.]

[82] Particle Data Group collaboration, *Review of Particle Physics*, *PTEP* **2020** (2020) 083C01. [Cited on page 36.]

[83] J. Hofestädt, *Measuring the neutrino mass hierarchy with the future KM3NeT/ORCA detector*, Ph.D. thesis, Friedrich-Alexander-Universität Erlangen-Nürnberg, 2017. [Cited on pages 36 and 53.]

[84] A. Trovato, *Development of reconstruction algorithms for large volume neutrino telescopes and their application to the KM3NeT detector*, Ph.D. thesis, Catania U., SSC, 2014. [Cited on page 37.]

[85] ANTARES collaboration, *Long-term monitoring of the ANTARES optical module efficiencies using* ^{40}K *decays in sea water*, *Eur. Phys. J. C* **78** (2018) 669 [1805.08675]. [Cited on pages 37, 42, and 107.]

[86] S. Haddock, M. Moline and J. Case, *Bioluminescence in the sea.*, *Annual review of marine science* **2** (2010) 443. [Cited on page 37.]

[87] ANTARES collaboration, *First results of the Instrumentation Line for the deep-sea ANTARES neutrino telescope*, *Astropart. Phys.* **26** (2006) 314 [astro-ph/0606229]. [Cited on page 38.]

[88] ANTARES collaboration, *The ANTARES detector: background sources and effects on detector performance*, in *30th International Cosmic Ray Conference*, vol. 5, pp. 1349–1352, 7, 2007 [0710.0527]. [Cited on page 38.]

[89] KM3NeT collaboration, *Characterisation of the Hamamatsu photomultipliers for the KM3NeT Neutrino Telescope*, *JINST* **13** (2018) P05035. [Cited on page 38.]

[90] "KM3NeT home page." https://www.km3net.org/. [Cited on page 39.]

[91] J. Reubelt, *Hardware studies, in-situ prototype calibration and data analysis of the novel multi-PMT digital optical module for the KM3NeT neutrino telescope*, Ph.D. thesis, Erlangen - Nuremberg U., 2019. [Cited on page 39.]

[92] IceCube collaboration, *A multi-PMT Optical Module for the IceCube Upgrade*, *PoS* **ICRC2019** (2020) 855 [1908.10802]. [Cited on page 40.]

[93] Hyper-Kamiokande Proto collaboration, *Performances of multi-PMT photodetector for the Hyper-Kamiokande experiment*, *PoS* **EPS-HEP2019** (2020) 179. [Cited on page 40.]

[94] S. Hallman, *Sensitivity to atmospheric tau-neutrino appearance and all-flavour search for neutrinos from the Fermi Bubbles with the deep-sea telescopes KM3NeT/ORCA and ANTARES*, Ph.D. thesis, Friedrich-Alexander-Universität Erlangen-Nürnberg, 2021. [Cited on pages 41, 45, 55, and 117.]

[95] KM3NeT collaboration, *KM3NeT Time Calibration*, *PoS* **ICRC2019** (2021) 868. [Cited on page 42.]

[96] KM3NeT collaboration, *The Positioning system for KM3NeT*, *EPJ Web Conf.* **207** (2019) 07005. [Cited on page 42.]

[97] K. Melis, *In-Situ Calibration of KM3NeT*, in *Proceedings of 35th International Cosmic Ray Conference — PoS(ICRC2017)*, vol. 301, p. 1059, 2017, DOI. [Cited on page 42.]

[98] KM3NeT collaboration, *Determining the Neutrino Mass Ordering and Oscillation Parameters with KM3NeT/ORCA*, 2103.09885. [Cited on pages 45, 55, 77, 82, 111, 116, 118, 125, 126, 129, 139, and 173.]

[99] KM3NeT collaboration, *Sensitivity to light sterile neutrino mixing parameters with KM3NeT/ORCA*, 2107.00344. [Cited on page 45.]

[100] ANTARES, KM3NeT collaboration, *Search for neutrino non-standard interactions with ANTARES and KM3NeT-ORCA*, in *9th Very Large Volume Neutrino Telescopes Workshop 2021*, 7, 2021 [2107.14296]. [Cited on page 45.]

[101] KM3NeT collaboration, *Dark Matter Searches from the Sun with the KM3NeT-ORCA detector*, *PoS* **ICRC2019** (2020) 536. [Cited on page 45.]

[102] L. Maderer, J. Coelho, E. Kaminski and V. Van Elewyck, *KM3NeT performance on oscillation and absorption tomography of the Earth*, in *Proceedings of 37th International Cosmic Ray Conference — PoS(ICRC2021)*, vol. 395, p. 1172, 2021, DOI. [Cited on page 45.]

[103] KM3NeT collaboration, *The KM3NeT potential for the next core-collapse supernova observation with neutrinos*, *Eur. Phys. J. C* **81** (2021) 445 [2102.05977]. [Cited on page 46.]

[104] KM3NeT collaboration, *KM3NeT sensitivity to low energy astrophysical neutrinos*, in *9th Very Large Volume Neutrino Telescopes Workshop 2021*, 8, 2021 [2108.07062]. [Cited on page 46.]

[105] G. de Wasseige, *Multi-detector approach to enhance the sensitivity of neutrino telescopes to low-energy astrophysical sources*, in *9th Very Large Volume Neutrino Telescopes Workshop 2021*, 8, 2021 [2108.07067]. [Cited on page 46.]

[106] ANTARES collaboration, *Monte Carlo simulations for the ANTARES underwater neutrino telescope*, *JCAP* **01** (2021) 064 [2010.06621]. [Cited on page 49.]

[107] KM3NeT collaboration, *gSeaGen: The KM3NeT GENIE-based code for neutrino telescopes*, *Comput. Phys. Commun.* **256** (2020) 107477 [2003.14040]. [Cited on page 50.]

[108] GENIE collaboration, *The GENIE Neutrino Monte Carlo Generator*, *Nucl. Instrum. Meth. A* **614** (2010) 87 [0905.2517]. [Cited on page 50.]

[109] NEMO collaboration, *Deep seawater inherent optical properties in the Southern Ionian Sea*, *Astropart. Phys.* **27** (2007) 1 [astro-ph/0603701]. [Cited on page 50.]

[110] ANTARES collaboration, *Transmission of light in deep sea water at the site of the ANTARES Neutrino Telescope*, *Astropart. Phys.* **23** (2005) 131 [astro-ph/0412126]. [Cited on page 50.]

[111] Y. Becherini, A. Margiotta, M. Sioli and M. Spurio, *A Parameterisation of single and multiple muons in the deep water or ice*, *Astropart. Phys.* **25** (2006) 1 [hep-ph/0507228]. [Cited on page 51.]

[112] G. Carminati, A. Margiotta and M. Spurio, *Atmospheric MUons from PArametric formulas: A Fast GEnerator for neutrino telescopes (MUPAGE)*, *Comput. Phys. Commun.* **179** (2008) 915 [0802.0562]. [Cited on page 51.]

[113] A. Tsirigotis, A. Leisos and S. Tzamarias, *HOU Reconstruction & Simulation (HOURS): A complete simulation and reconstruction package for very large volume underwater neutrino telescopes*, *Nucl. Instrum. Meth. A* **626-627** (2011) S185. [Cited on page 51.]

[114] GEANT4 collaboration, *GEANT4–a simulation toolkit*, *Nucl. Instrum. Meth. A* **506** (2003) 250. [Cited on page 51.]

[115] KM3NeT collaboration, *Dependence of atmospheric muon flux on seawater depth measured with the first KM3NeT detection units: The KM3NeT Collaboration*, *Eur. Phys. J. C* **80** (2020) 99 [1906.02704]. [Cited on page 52.]

[116] L. Quinn, *Determining the Neutrino Mass Hierarchy with KM3NeT/ORCA*, Ph.D. thesis, Aix-Marseille Université, Centre de Physique des Particules de Marseille, 2018. [Cited on pages 53 and 82.]

[117] A. Domi, *Shower reconstruction and sterile neutrino analysis with KM3NeT/ORCA and ANTARES*, Ph.D. thesis, Friedrich-Alexander-Universität Erlangen-Nürnberg, 2021. [Cited on page 54.]

[118] N. Lodewijk, *To be updated*, Ph.D. thesis, 2021. [Cited on pages 56 and 118.]

[119] KM3NeT collaboration, *Neutrino oscillation research with KM3NeT/ORCA*, *PoS* **ICRC2019** (2020) 1019. [Cited on pages 56 and 77.]

[120] S. BOURRET and L. QUINN, *Sensitivity of ORCA to the neutrino mass ordering and oscillation parameters*, June, 2018. 10.5281/zenodo.1300771. [Cited on pages 57, 86, 95, 116, and 120.]

[121] ANTARES collaboration, *First all-flavor neutrino pointlike source search with the ANTARES neutrino telescope*, *Phys. Rev. D* **96** (2017) 082001 [1706.01857]. [Cited on page 71.]

[122] S. Bourret, *Neutrino oscillations and earth tomography with KM3NeT-ORCA*, Ph.D. thesis, APC, Paris, 2018. [Cited on pages 77, 80, 89, 92, 93, 95, 103, 106, 113, 116, 120, 121, and 125.]

[123] KM3NeT collaboration, *First neutrino oscillation measurement in KM3NeT/ORCA*, in *Proceedings of 37th International Cosmic Ray Conference — PoS(ICRC2021)*, vol. 395, p. 1123, 2021, DOI. [Cited on pages 77, 82, 132, 148, 154, and 161.]

[124] J. Coelho, "Oscprob neutrino oscillation calculator." [Cited on page 78.]

[125] A.M. Dziewonski and D.L. Anderson, *Preliminary reference earth model*, *Phys. Earth Planet. Interiors* **25** (1981) 297. [Cited on page 78.]

[126] W. Verkerke and D.P. Kirkby, *The RooFit toolkit for data modeling*, *eConf* **C0303241** (2003) MOLT007 [physics/0306116]. [Cited on page 82.]

[127] R.J. Barlow and C. Beeston, *Fitting using finite Monte Carlo samples*, *Comput. Phys. Commun.* **77** (1993) 219. [Cited on page 86.]

[128] I. Esteban, M. Gonzalez-Garcia, A. Hernandez-Cabezudo, M. Maltoni and T. Schwetz, *Global analysis of three-flavour neutrino oscillations: synergies and tensions in the determination of θ_{23}, δ_{CP}, and the mass ordering*, *JHEP* **01** (2019) 106 [1811.05487]. [Cited on pages 87, 118, 119, 120, 126, 127, 129, 137, 142, 143, 150, 151, 170, and 173.]

[129] F. James and M. Winkler, "Minuit2 user manual." [Cited on page 92.]

[130] M. Blennow, P. Coloma, P. Huber and T. Schwetz, *Quantifying the sensitivity of oscillation experiments to the neutrino mass ordering*, *JHEP* **03** (2014) 028 [1311.1822]. [Cited on pages 93, 94, and 134.]

[131] S. Wilks, *The Large-Sample Distribution of the Likelihood Ratio for Testing Composite Hypotheses*, *Annals Math. Statist.* **9** (1938) 60. [Cited on pages 94 and 143.]

[132] G. Cowan, K. Cranmer, E. Gross and O. Vitells, *Asymptotic formulae for likelihood-based tests of new physics*, *Eur. Phys. J. C* **71** (2011) 1554 [1007.1727]. [Cited on pages 94, 127, and 138.]

[133] E. Ciuffoli, J. Evslin and X. Zhang, *Confidence in a neutrino mass hierarchy determination*, *JHEP* **01** (2014) 095 [1305.5150]. [Not cited.]

[134] IceCube-PINGU collaboration, *Letter of Intent: The Precision IceCube Next Generation Upgrade (PINGU)*, 1401.2046. [Cited on page 94.]

[135] X. Qian, A. Tan, W. Wang, J.J. Ling, R.D. McKeown and C. Zhang, *Statistical Evaluation of Experimental Determinations of Neutrino Mass Hierarchy*, *Phys. Rev. D* **86** (2012) 113011 [1210.3651]. [Cited on page 94.]

[136] G. Cowan, *Statistical data analysis* (1998). [Cited on page 95.]

[137] G.J. Feldman and R.D. Cousins, *A Unified approach to the classical statistical analysis of small signals*, *Phys. Rev. D* **57** (1998) 3873 [physics/9711021]. [Cited on page 95.]

[138] D. Casadei, *Estimating the selection efficiency*, *Journal of Instrumentation* **7** (2012) P08021. [Cited on page 96.]

[139] M. Paterno, *Calculating efficiencies and their uncertainties*, . [Cited on page 96.]

[140] T.K. Gaisser, T. Stanev, M. Honda and P. Lipari, *Primary spectrum to 1-TeV and beyond*, in *27th International Cosmic Ray Conference*, 8, 2001. [Cited on page 99.]

[141] A. Fedynitch, R. Engel, T.K. Gaisser, F. Riehn and T. Stanev, *Calculation of conventional and prompt lepton fluxes at very high energy*, *EPJ Web Conf.* **99** (2015) 08001 [1503.00544]. [Cited on page 106.]

[142] J.-P. Yáñez, A. Fedynitch and T. Montgomery, *Calibration of atmospheric neutrino flux calculations using cosmic muon flux and charge ratio measurements*, *PoS* **ICRC2019** (2020) 881 [1909.08365]. [Cited on page 106.]

[143] KM3NeT collaboration, *Neutrino oscillation research with KM3NeT/ORCA*, *PoS* **ICRC2019** (2020) 1019. [Cited on pages 116 and 129.]

[144] Daya Bay collaboration, *Measurement of the Electron Antineutrino Oscillation with 1958 Days of Operation at Daya Bay*, *Phys. Rev. Lett.* **121** (2018) 241805 [1809.02261]. [Cited on pages 118 and 142.]

[145] RENO collaboration, *Measurement of Reactor Antineutrino Oscillation Amplitude and Frequency at RENO*, *Phys. Rev. Lett.* **121** (2018) 201801 [1806.00248]. [Cited on pages 118 and 142.]

[146] T2K collaboration, *Constraint on the matter–antimatter symmetry-violating phase in neutrino oscillations*, *Nature* **580** (2020) 339 [1910.03887]. [Cited on pages 129 and 162.]

[147] NOvA collaboration, *First Measurement of Neutrino Oscillation Parameters using Neutrinos and Antineutrinos by NOvA*, *Phys. Rev. Lett.* **123** (2019) 151803 [1906.04907]. [Cited on pages 129 and 162.]

[148] Super-Kamiokande collaboration, *Atmospheric neutrino oscillation analysis with external constraints in Super-Kamiokande I-IV*, *Phys. Rev. D* **97** (2018) 072001 [1710.09126]. [Cited on pages 129 and 162.]

[149] A. Aurisano, *Recent results from minos and minos+*, June, 2018. 10.5281/zenodo.1286760. [Cited on pages 129 and 162.]

[150] Y.-F. Li, Y. Wang and Z.-z. Xing, *Terrestrial matter effects on reactor antineutrino oscillations at JUNO or RENO-50: how small is small?*, *Chin. Phys. C* **40** (2016) 091001 [1605.00900]. [Cited on page 132.]

[151] H. Nunokawa, S.J. Parke and R. Zukanovich Funchal, *Another possible way to determine the neutrino mass hierarchy*, *Phys. Rev. D* **72** (2005) 013009 [hep-ph/0503283]. [Cited on pages 132 and 143.]

[152] A. de Gouvea, J. Jenkins and B. Kayser, *Neutrino mass hierarchy, vacuum oscillations, and vanishing |U(e3)|*, *Phys. Rev. D* **71** (2005) 113009 [hep-ph/0503079]. [Cited on pages 132, 133, and 143.]

[153] X. Qian et al., *Mass Hierarchy Resolution in Reactor Anti-neutrino Experiments: Parameter Degeneracies and Detector Energy Response*, *Phys. Rev. D* **87** (2013) 033005 [1208.1551]. [Cited on page 134.]

[154] JUNO collaboration, *JUNO Conceptual Design Report*, 1508.07166. [Cited on page 134.]

[155] JUNO collaboration, *JUNO Physics and Detector*, 2104.02565. [Cited on pages 134, 135, and 136.]

[156] JUNO collaboration, *TAO Conceptual Design Report: A Precision Measurement of the Reactor Antineutrino Spectrum with Sub-percent Energy Resolution*, 2005.08745. [Cited on page 135.]

[157] D.A. Dwyer and T.J. Langford, *Spectral Structure of Electron Antineutrinos from Nuclear Reactors*, *Phys. Rev. Lett.* **114** (2015) 012502 [1407.1281]. [Cited on page 135.]

[158] P. Vogel and J.F. Beacom, *Angular distribution of neutron inverse beta decay, $\bar{\nu}_e + p \to e^+ + n$*, *Phys. Rev. D* **60** (1999) 053003 [hep-ph/9903554]. [Cited on page 136.]

[159] F. von Feilitzsch, A. Hahn and K. Schreckenbach, *Experimental beta spectra from Pu-239 and U-235 thermal neutron fission products and their correlated anti-neutrinos spectra*, *Phys. Lett. B* **118** (1982) 162. [Cited on page 136.]

[160] K. Schreckenbach, G. Colvin, W. Gelletly and F. Von Feilitzsch, *Determination of the anti-neutrino spectrum from U-235 thermal neutron fission products up to 9.5-MeV*, *Phys. Lett. B* **160** (1985) 325. [Cited on page 136.]

[161] A. Hahn, K. Schreckenbach, G. Colvin, B. Krusche, W. Gelletly and F. Von Feilitzsch, *Anti-neutrino Spectra From ^{241}Pu and ^{239}Pu Thermal Neutron Fission Products*, *Phys. Lett. B* **218** (1989) 365. [Cited on page 136.]

[162] Daya Bay collaboration, *Improved Measurement of the Reactor Antineutrino Flux at Daya Bay*, *Phys. Rev. D* **100** (2019) 052004 [1808.10836]. [Cited on page 136.]

[163] Daya Bay collaboration, *Spectral measurement of electron antineutrino oscillation amplitude and frequency at Daya Bay*, *Phys. Rev. Lett.* **112** (2014) 061801 [1310.6732]. [Cited on page 136.]

[164] V. Kopeikin, L. Mikaelyan and V. Sinev, *Reactor as a source of antineutrinos: Thermal fission energy*, *Phys. Atom. Nucl.* **67** (2004) 1892 [hep-ph/0410100]. [Cited on page 136.]

[165] JUNO collaboration, *Calibration Strategy of the JUNO Experiment*, 2011.06405. [Cited on page 146.]

[166] KM3NeT collaboration, *Atmospheric neutrinos with the first detection units of KM3NeT/ARCA*, 2107.12721. [Cited on page 154.]

[167] KM3NeT collaboration, *Dependence of atmospheric muon flux on seawater depth measured with the first KM3NeT detection units: The KM3NeT Collaboration*, *Eur. Phys. J. C* **80** (2020) 99 [1906.02704]. [Cited on page 154.]

[168] J. Hofestädt, R. Coniglione, A. Sinopoulou, E. Tzamariudaki and D. Zaborov, *Atmospheric Neutrinos Detected with the First KM3NeT Detection Units of ARCA and ORCA*, in *Proceedings of 36th International Cosmic Ray Conference — PoS(ICRC2019)*, vol. 358, p. 910, 2019, DOI. [Not cited.]

[169] J. Hofestädt, L.A. Fusco and D. Stavropoulos, *Detection of the atmospheric neutrino flux with the first detection units of KM3NeT/ORCA*, June, 2020. 10.5281/zenodo.4122661. [Cited on page 154.]

[170] F. James and M. Winkler, *MINUIT User's Guide*, . [Cited on page 160.]